

ПРИМЉЕНО: 7 п. 01-2025			
Рад.јед.	б р о ј	Арх.шифра	Прилог
	0801 - 0811		

Научном већу Института за физику у Београду

Предмет: Молба за покретање поступка за реизбор у звање виши научни сарадник

Молим Научно веће Института за физику у Београду да у складу са Правилником о поступку и начину вредновања и квантитативном исказивању научно-истраживачких резултата истраживача покрене поступак за мој реизбор у звање виши научни сарадник.

У прилогу достављам:

1. Мишљење руководиоца пројекта са предлогом чланова комисије;
2. Биографске податке;
3. Преглед научне активности;
4. Елементе за квалитативну оцену научног доприноса;
5. Елементе за квантитативну оцену научног доприноса;
6. Списак објављених радова и њихове копије;
7. Податке о цитираности;
8. Фотокопију решења о претходном избору у звање;
9. Додатне прилоге.

С поштовањем,

Тинка Мартина

др Мартина Гилић
виши научни сарадник

ПРИМЉЕНО: Z П -01- 2025			
Рад.јед.	б р о ј	Арх.шифра	Прилог
0801	-68/2		

Научном већу Института за физику у Београду

Предмет: Мишљење руководиоца пројекта за реизбор др Мартине Гилић у звање виши научни сарадник

Др Мартина Гилић запослена је у Лабораторији за истраживања у области електронских материјала Института за физику у Београду, где је првенствено ангажована на задацима везаним за оптичке и структурне особине нанодимензионалних материјала уз помоћ различитих спектроскопских и микроскопских техника. Период између 09.2020 и 07.2023 кандидаткиња је провела на постдоку на Freie Univeristät-у у Берлину. Др Гилић испуњава услове прописане Правилником за избор у научна звања Министарства просвете, науке и технолошког развоја, те сам сагласан да Научно веће Института за физику у Београду покрене поступак за реизбор кандидаткиње у звање виши научни сарадник.

Руководилац лабораторије,



др Небојша Ромчевић
научни саветник

Предлог чланова комисије за писање извештаја

1. др Анђелија Илић, научни саветник Института за физику Београд
2. др Зорица Лазаревић, научни саветник Института за физику Београд
3. др Бранка Хаџић, виши научни сарадник Института за физику Београд
4. др Милица Ђурчић, виши научни сарадник Института за физику Београд
5. др Душан Поповић, редовни професор Физичког факултета Универзитета у Београду

2. БИОГРАФСКИ ПОДАЦИ

Др Мартина Гилић рођена је 22.07.1983. године у Београду, где је завршила Основну школу “Светозар Марковић” а затим и Трећу београдску гимназију. Факултет за физичку хемију Универзитета у Београду уписује школске 2002/03 године, који завршава априла 2008. године као једна од најбољих студената у генерацији, са просечном оценом 9,1. Дипломски рад под називом “Раманова спектроскопија DX-примесних центара у $Pb_{1-x}Sn_xTe(In)$ ” урадила је под менторством др Миљенка Перића и др Небојше Ромчевића. Исте године уписује и докторске студије Факултета за физичку хемију, које завршава јуна 2014. године, одбраном тезе “Оптичке особине нанодимензионих система формираних у пластично деформисаном бакру, танким филмовима CdS и хетероструктурама CdTe/ZnTe”, под менторством др Небојше Ромчевића, научног саветника Института за физику у Београду.

Кандидаткиња је од септембра 2008. године запослена у Институту за физику у Београду. Основни предмет истраживања јој је оптичка спектроскопија и карактеризација различитих врста наноматеријала.

2011. године стиче звање истраживач сарадник, затим је у мају 2015. године изабрана у звање научни сарадник, те јула 2020. године у звање виши научни сарадник (доказ дат у прилогу).

Кандидаткиња је од 2008. до 2010. године активно учествовала на пројекту Министарства просвете, науке и технолошког развоја број 141028Б, под називом “Спектроскопија елементарних екситација у полуманетним полупроводницима”, а од 2011. до 2020. године била је ангажована на пројекту истог Министарства број III45003 “Оптоелектронски нанодимензиони системи- пут ка примени”, где је руководила потпројектом “Синтеза наноматеријала и структура”.

Од септембра 2020. закључно са јулом 2023. године др Гилић је првела на научном усавршавању на Freie Universität-у у Берлину, где је била запослена као научни радник (постдок) на Институту за експерименталну физику, AG Reissig, на DFG пројекту „Diatom frustules as nature-designed building blocks for photonic applications”.

Др Гилић је до сада објавила 45 радова у међународним часописима, који су цитирани 575 пута, са h фактором 14 (списак радова дат је у прилогу 1 овог извештаја), као и 7 поглавља у монографијама (доказ у прилогу). Кандидаткињини резултати су презентовани на десетинама конференција у земљи и иностранству. Одржала је више усмених предавања, од којих су два по позиву (доказ дат у прилогу), као и бројне семинаре групе AG Reissig на Freie Universität-у Berlin. Коауторка је једног патентног решења. Кандидаткиња је чланица едиторијалног одбора часописа American Journal of Optics and Photonics, и рецезент у више међународних часописа (доказ дат у прилогу).

3. ПРЕГЛЕД НАУЧНЕ АКТИВНОСТИ

Научно – истраживачка активност др Мартине Гилић је првенствено везана за експерименталну физику чврстог стања и физику наноматеријала, као и синтезу наноматеријала и структура у оквиру пројектних задатака којима руководи. Истраживања су првенствено усмерена на утврђивање оптичких, структурних и електричних својстава поменутих система различитим спектроскопским и микроскопским методама. Научне активности обухватају формулацију проблема, експериментални рад, обраду резултата и теоријску анализу испитиваних материјала. Кандидаткиња у оквиру матичне лабораторије изводи мерења на уређајима за Раманову и фотолуминесцентну спектроскопију и спектроскопску елипсометрију, док са колегама из Института за мултидисциплинарна истраживања врши мерења на УВ-ВИС спектрометру. Добијени експериментални резултати се анализирају, при чему се примењују постојећи или се развијају нови модели, и долази се до јасне слике о својствима испитиваних материјала.

У наставку је дат преглед области истраживања кандидаткиње, разврстан углавном по изучаваним материјалима.

Оптичке и структурне особине нанодимензионих система:

- **Танки филмови**

Изучавани су танки филмови CdS и CuSe различите дебљине добијени једноставном техником вакуумског напаравања. У случају CdS, инфрацрвени спектри су анализирани коришћењем нумеричког модела за израчунавање коефицијента рефлексije сложених система који укључују филм и супстрат. Диелектрична функција танког филма CdS анализирана је помоћу Maxwell-Garnet-ове формуле као смеша хомогених сферних инклузија CdS у ваздуху. Интензитети Раманових спектра су анализирани помоћу исте формуле, и добило се веома добро слагање између примењеног модела и експерименталних података. Интересантно је напоменути да су филмови високог квалитета добијени једноставном методом вакуумског напаравања, што смањује цену производње за потенцијалну примену у оптоелектроници и пиезоелектроници.

У другом случају (CdS) се ради о двофазним филмовима. Раманова и инфрацрвена спектроскопија су коришћене за идентификацију и квантификацију две фазе. Помоћу модела за конфајнмент оптичких фонона одређиване су величине честица CuSe₂ фазе, при чему је утврђено да се димензије честица повећавају са повећањем дебљине филма. Иако је овај модел ограничен на наночестице правилног сферног облика, показало се да он даје добре резултате и код реалних нанокристала који су неправилног облика. УВ-ВИС спектроскопијом су добијене вредности забрањених зона обе фазе, при чему је утврђено да оне незнатно опадају са повећањем дебљине филма. Фотолуминесцентним мерењима на ниским температурама је детектован дефектни ниво селена – негативни У-центар.

- **Самоорганизујуће квантне тачке**

Изучаване су хетероструктуре CdTe/ZnTe. Због велике разлике у параметрима решетке, овакве структуре погодују формирању квантних тачака. Утврђено је да уочени мултифононски процеси

зависе од температуре и енергије побуде (тј. таласне дужине ласера). Када се енергија расејаног фотона приближи енергији забрањене зоне ZnTe, одговарајући Раманов мод постаје резонантно појачан. Даље, апроксимацијом ефективне масе, израчунат је дијаметар квантних тачака CdTe – 4.3 nm, што је знатно мање од Боровог радијуса ексцитона CdTe који износи 10 nm.

- **Оксидни нанопрахови допирани Eu^{3+} , Dy^{3+} и недопирани**

Луминесценција јона ретких земаља налази велику примену у активним супстанцама белих фосфора код равних екрана, плазма дисплеја, ЛЕД диода итд. Оксидне наноструктуре допирани јонима ретких земаља показују побољшана оптичка својства. Нанопрахови YVO_4 са и без допирања јонима Eu^{3+} , испитивани су методом Раманове спектроскопије. Утврђено је да допирање овим јонима резултује променама Раманових спектра. Код допираног узорка се појављује нов мод, уз промену интензитета постојећих модова. Јон Eu замењује јон Y у решетки. Изотопски ефекат је детаљно разматран и израчунаван. У другом раду је за исти материјал изучавана кинетика и временски разложена анализа луминесценције, при чему је закључено да је нанопрах $\text{YVO}_4:\text{Eu}^{3+}$ погодан материјал за примену у различитим оптоелектронским направама. У трећем раду је утврђено постојање површинског оптичког фонона и различитих мултифононских процеса, што мења спектар балк YVO_4 .

Еуропијумом је допиран и нанопрах $\text{Gd}_2\text{Zr}_2\text{O}_7$, материјал познат као домаћин (хост) за фотолуминесцентну примену. Рамановом спектроскопијом су уочена два фонона која до сада нису била регистрована, и њихова позиција је у складу са уоченом електрон-фонон интеракцијом. Регистровани мултифононски процеси су директна последица допирања, а то условљава и појаву бочне траке фонона.

Нанопрах YAG:Dy испитиван је Рамановом и фотолуминесцентном спектроскопијом. Утврђено је да постоји јако купловање између јона ретке земље и вибрација решетке. Раманови спектри YAG:Dy су нешто шири од одговарајућих спектра монокристала YAG, а неки модови показују и плави помак. Закључује се да се материјал YAG:Dy може користити као извор беле светлости (бели фосфори).

Нанопрах YFeO_3 је добијен механохемијском синтезом, и својства су му испитивана дифракцијом X-зрака, Рамановом и инфрацрвеном спектроскопијом, те Mössbauer-овом спектроскопијом. Шереровом једначином је израчуната величина кристалита и она износи 12 nm. Уочено је 7 Раманових и 10 инфрацрвених модова. Mössbauer-ова мерења су потврдила суперпарамагнетни карактер ортоферита.

- **Квантне тачке у полимерној матрици**

Испитивана су својства нанокомпозита CdSe/ZnS-PMMA и ZnS-PMMA . Циљ је очувати оптичку активност квантних тачака у нанокомпозиту, уз побољшање механичких својстава. У случају core/shell структура (CdSe/ZnS-PMMA), Рамановом спектроскопијом је утврђено да матрица није утицала на фононске модове CdSe језгра квантних тачака, тј спектри CdSe/ZnS-PMMA и CdSe/ZnS су готово идентични. Може се рећи да су кристалити сулфида и селенида ушли у поре мреже PMMA без ремећења континуалне 3D структуре полимерне матрице.

Што се тиче нанокомпозита ZnS-PMMA , анализа Раманових спектра је вршена моделом заснованим на теорији ефективног медијума. Утврђено је присуство површинског оптичког фонона, чији облик и позиција зависе од врсте композита.

Код мултикомпонентног полимерног нанокомпозита титан-карбид/PMMA, који садржи TiC, TiC MXene и остатке TiC и TiO у PMMA матрици, извршена је карактеризација уз помоћ XRD, инфрацрвене и Раман спектроскопије, као и упоредне анализе вибрационих својстава путем DFT прорачуна. SEM мерења су показала да су произведене честице титан-карбида добро дефинисане и раздвојене у наноскалне зрна. Примењен је Maxwell–Garnett модел за анализу инфрацрвеног спектра, што је омогућило одређивање модификације оптичких својстава полимерне матрице за запремински удео од 0.25.

- **Наночестице**

Изучаване су оптичка и структурна својства разних наночестица добијених различитим методама: честице CdSe у стакленој матрици добијене оригиналном техником која комбинује загревање и озрачивање УВ ласером; честице NiO добијене комбинацијом копреципитације и одгревања; честице ZnO допиране CoO добијене копреципитацијом/калцинацијом, честице Cd_{1-x}Mn_xS добијене методом колоидне хемије.

Фрустуле дијатомеја као природни 2D фотонски кристали

Ово је била кандидаткињина главна тема истраживања за време њеног боравка на Freie Univeristät-у у Берлину. Изучаване су силикатне фрустуле дијатомејских микроорганизама које поседују веома правилну структуру на дужинским скалама које се простиру од нанометарског до микрометарског опсега, при чему структурни обрасци и димензије зависе од врсте дијатомеја. Ова структура има јединствена оптичка својства, слична онима код 2D (или 3D) фотонских кристала. Коришћењем хибридних супстрата дијатомеја пресвученим ултратанким слојем злата постигнуто је знатно повећање интензитета Површински појачане Раманове спектроскопије (SERS). Анализирана су три хибридна супстрата са фрустулама три различите врсте дијатомеја, при чему су цилиндричне фрустуле врсте *Aulacoseira sp.* показали највеће повећање сигнала, до 14 пута. Нумеричка анализа методом коначних елемената потврдила је експерименталне резултате. Резултати показују да фрустуле дијатомеја различитих облика могу побољшати SERS сигнал, при чему повећање зависи од геометрије и ултраструктуре фрустуле.

Неоргански филмови на флексибилним полимерима

У сарадњи са др Нерингом Петраушкиене са Технолошког Универзитета Каунас у Литванији, изучавани су флексибилни полимери модификовани халкогенидима бакра, конкретно бакар-сулфидом (Cu_xS) и бакар-селенидом (Cu_{2-x}Se), који представљају обећавајућу класу материјала за флексибилну електронику и оптоелектронске примене. Коришћене су различите методе депозиције, укључујући хемијско таложење из купке, сорпционо-дифузиони процес и SILAR методу, како би се произвели висококвалитетни танки филмови са подесивим структурним, оптичким и електричним својствима.

У првом случају ради се о депозицији танких филмова Cu_xS на полиамидним (PA) и полипропиленским (PP) подлогама коришћењем методе хемијског таложења из купке. Филмови добијени након два или три циклуса депозиције показали су уједначену морфологију и хексагоналну ковелитну структуру, потврђену XRD анализом. Вредности енергетског опсега од 2,75–2,78 eV (директни) и 1,29–1,41 eV (индиректни) указују на одлична полупроводна својства.

Помоћу Раманове спектроскопије идентификовани су карактеристични пикови ковелитне и Cu_{2-x}S фазе, при чему су структурне разлике зависиле од броја циклуса депозиције и типа подлоге, што ове материјале чини погодним за фотонапонске примене.

Друга студија представља економичну сорпционо-дифузиону методу за таложњење Cu_2S филмова на предтретираним полиамидним (РАБ) подлогама. Методе предтретмана значајно су утицале на електрични отпор филмова, који је варирао од $7 \text{ k}\Omega/\text{sq}$ до $6 \text{ M}\Omega/\text{sq}$. XRD анализа показала је орторомбичну кристалну структуру, док је предтретман унапредио кристалиничност филмова. Директни и индиректни енергетски опсези од $2,61\text{--}2,67 \text{ eV}$ и $1,4\text{--}1,44 \text{ eV}$ указују на добра оптичка и електрична својства погодна за оптоелектронске примене. Резултати истичу важност једноставних предтретмана у побољшању квалитета филмова.

Трећа студија истражује Cu_{2-x}Se танке филмове депоноване на полиамиду коришћењем SILAR методе при различитим температурама. Повишене температуре довеле су до побољшане величине зрна и смањења густине дислокација, чиме су побољшани уједначеност и проводљивост филмова. XRD и Раман спектроскопија потврдиле су кубну структуру Cu_{2-x}Se , са енергетским опсезима од $1,98\text{--}2,28 \text{ eV}$. Филмови депоновани при $80 \text{ }^\circ\text{C}$ показали су најбољу комбинацију уједначености, проводљивости и оптичких својстава, наглашавајући важност контроле температуре за прилагођавање перформанси материјала.

Метални комплекси са Шифовим базама

У овом раду описана је синтеза два нова комплекса 2-ацетилпиридин-аминогуанидина (L) са цинком(II) и кадмијумом(II), односно $[\text{Zn}(\text{L})(\text{NCO})_2]$ и $[\{\text{Cd}(\text{L})\text{Cl}(\mu\text{-NCO})\}_2]$. Њихова структура је одређена XRD анализом, док је спектроскопска карактеризација обухватила и два претходно синтетисана комплекса: $[\text{Zn}(\text{L})(\text{NSC})_2]$ и $[\text{Cd}(\text{L})\text{Cl}_2]$. IR и Раман спектри открили су фонске модове са повећаним интензитетима у опсегу $1000\text{--}1700 \text{ cm}^{-1}$ за сва четири узорка. Анализа фотолуминесценције је показала три пика, при чему се интензитет значајно мењао заменом $[\text{Cl}]^-$ лиганда са $[\text{NCO}]^-$. Други $[\text{NCO}]^-$ лиганд је додатно појачао фотолуминесценцију у целом опсегу. Ови резултати пружају бољи увид у интеракцију електрона и фона и проширују могућности примене металних комплекса.

Оптичка и електрична својства монокристала раслих техником Чохралски и Бриџман

Проучавани су монокристали добијени методом раста кристала по Чохралском (Czochralski) и по Бриџману (Bridgman). Израчунати су критични дијаметар и критична стопа ротације, а одређени су и погодни раствори за полирање и нагризање. При карактеризацији добијених монокристала је коришћен низ експерименталних метода: дифракција X - зрака, инфрацрвена и Раманова спектроскопија, спектроскопска елипсометрија. Ови материјали, захваљујући великој разноврсности физичких особина имају велику примену у електронским и оптоелектронским уређајима, где је неопходно да кристали имају малу густину дислокација и велику оптичку хомогеност. Стога се велика пажња посвећује начину и условима добијања узорака. $\text{Bi}_{12}\text{GeO}_{20}$ кристали су добијени по методи Чохралског из високо чистих полазних Bi_2O_3 and GeO_2 оксида и оксида мање чистоће и анализирани су уз помоћ XRD, Раман и ИЦ спектроскопије. Индекси преламања су одређени методом елипсометрије. $\text{Bi}_{12}\text{GeO}_{20}$ кристал прозирно жуте боје је на основу магнетно оптичког квалитета чак 10 пута бољи од комерцијалног материјала. Сврха је била да се утврди минимална чистоћа оксида неопходних за производњу $\text{Bi}_{12}\text{GeO}_{20}$ сензорског кристала. Снижење цена поступка производње кристала је један од главних циљева који треба

да буде испуњен, да би могао да се користи и угради као оптички сензор на основу Фарадејевог ефекта.

Посебно треба истаћи добијање оксидних кристала итријум-алуминијум гарнета (YAG, $Y_3Al_5O_{12}$) и неодимијумом допираног итријум-алуминијум гарнета (Nd:YAG) доброг оптичког квалитета методом Чохралског, и њихову карактеризацију Раман и инфрацрвеном спектроскопијом. Показана је јака метал-кисеоник вибрација карактеристична за везу Al-O.

Модификованом вертикалном методом по Бриџману у вакууму је добијен високо квалитетни монокристал CaF_2 . Добијени кристал је испитиван Раман и инфрацрвеном спектроскопијом. Кристална структура је потврђена ренгеноструктурном анализом. Концентрација дефеката кисеоника у кристалу је испитивана фотолуминесцентном спектроскопијом. Помоћу ових метода је процењен оптички квалитет добијеног монокристала и утврдило се да је добар, јер само монокристал доброг оптичког квалитета може даље да се угради у полимерну матрицу и да се добије композит са побољшаним термичким и механичким, а очуваним оптичким својствима.

Бриџмановом методом су добијени и монокристали $CdTe_{0.97}Se_{0.03}$ и $CdTe_{0.97}Se_{0.03}+1.2 \text{ at.}\%In$, чија карактеризација је вршена далеком инфрацрвеном спектроскопијом на различитим температурама. Анализа спектра је вршена фитовањем базираним на диелектричној функцији која укључује просторну расподелу слободних носилаца као и утицај плазмон-фонон интеракције. Показано је да оптички фонони мешаних кристала показују двомодно понашање, а утврђен је и локални мод индијума. У оба случаја је утврђено присуство површинског слоја са ниском концентрацијом носилаца.

Пластично деформисани метали и металне легуре

Изучавају се оптичка својства бакра и легуре бакар-алуминијум подвргнутих екстремној пластичној деформацији поновљеном употребом једнакоканалне угаоне пресе, у циљу побољшања механичких својстава материјала. Трослојни модел је коришћен за израчунавање дебљине спонтано насталог бакар оксида из елипсометријских мерења. Рамановом спектроскопијом су регистрована два типа линија, уске и широке, што указује на постојање нанокристалних структура бакра и бакар оксида, окружених са свих страна аморфним фазама. Пластична деформација бакра није довела до потпуне аморфизације узорка. Код легуре бакар-алуминијум је утврђено да је степен аморфизације већи у трансверзалној него у лонгитудиналној равни. Финални узорак има полифазну структуру са нехомогеним уређењем фаза.

Четворокомпонентни системи

Изучаване су оптичке особине разблажених магнетних полупроводника $Zn_{1-x}Mn_xGeAs_2$ и $Zn_{1-x}Mn_xSnSb_2$, као и халкогенида Cu_2FeSnS_4 . Наночестице Cu_2FeSnS_4 су синтетисане механохемијским путем, и Раманова спектроскопија је коришћена за систематско одређивање вибрационих својстава ових система и испитивање утицаја времена млевења на исте тј на чистоћу нанокристала материјала. Поред модова основног кристала уочени су и модови који припадају FeS и SnS фазама, који слабе и на крају се губе са повећањем времена млевења. После млевења од 90 минута остају само модови основног кристала.

Рамановом спектроскопијом су изучаване фононске особине и $Zn_{1-x}Mn_xSnSb_2$, не би ли се утврдило како додатак Mn утиче на оптичка и структурна својства $ZnSnSb_2$. Фононска својства $ZnSnSb_2$ као и MnSb су по први пут одређивана. На основу помака фонона $ZnSnSb_2$ нађено је да се одређена количина Mn уградила у решетку кристала и формирала $Zn_{1-x}Mn_xSnSb_2$.

Инфрацрвеном спектроскопијом се изучавао утицај фактора пригушења на интеракцију плазмона и два фонона у $Zn_{1-x}Mn_xGeAs_2$. Откривена је специфична природа фреквенција спрегнутих фонона. При високим пригушењима, постојање фонона у региону између ТО и ЛО фреквенција није примећен за плазмон-два-фонона интеракцију, супротно случају за плазмон-фонон интеракцију.

Слојевити III-V полупроводници допирани јонима прелазних метала

Слојевити полупроводници, па међу њима и γ -InSe, су од великог значаја како за фундаментална, тако и за примењена истраживања јер имају изузетно анизотропне оптичке и електронске особине и инертне базалне пљосни. Због ових особина, слојевити полупроводници се често користе као фотохемијске електроде. Индијум селенид, са директним енергетским процепом у блиском инфрацрвеном опсегу енергија је атрактиван материјал у области конверзије соларне енергије. Овај рад представља допринос истраживању утицаја примеса на оптичке особине γ -InSe, посебно на оптички процеп и електронске нивое. Мерења фотолуминесценције су потврдила плави помак енергијских нивоа у валентној зони и постојање дубоких примесних стања. Енергијски прелази чистог и допираног кристала су изучавани спектроскопском елипсометријом, где је утврђен велики број прелаза у нискоенергијском опсегу, повезаних са дефектним и примесним стањима, док је у нискоенергијском опсегу регистрован плави помак енергијских стања.

Примена неорганских филмова у соларним ћелијама и фотодетекторима

Соларне ћелије осетљиве на боје постају штедљива алтернатива конвенционалним фотоволтаицима заснованим на *p-n* споју. Главна компонента ових ћелија је фотоактивна анода направљена од дебелог филма TiO_2 покривена слојем боје. У овом раду, припремљен је фотоанодни дебео филм TiO_2 који садржи мезопорозне сфере, и изучавана применљивост оваквог филма у соларним ћелијама осетљивим на боју. Рамановом спектроскопијом је утврђено формирање анатас фазе након третирања са $TiCl_4$.

Cr_2O_3 је обећавајући кандидат за примену у новим MIS(I)M фотодетекторима. Одговарајући услови за депоновање ових филмова техником реактивног спатеровања тек треба дефинисати. Ту спадају парцијални притисак кисеоника, температура супстрата, време депоновања, а и одгревање. За сада је изучаван утицај парцијалног притиска на дебљину и нанооптичка својства танких филмова, низом техника: Рамановом, инфрацрвеном и УВ-ВИС спектроскопијом, микроскопијом атомске силе, дифракцијом X-зрака. Ова тема је започета у сарадњи са Louissom Reissig са Frei Universität-a Berlin.

Транспорт јона алкалних метала у DXE гасу

Др Гилић се прикључила колегама из Групе за гасну електронику (др Никитовић, др Стојановић, др Распоповић), који се дуже време баве изучавањем транспорта позитивних јона у гасним пражњењима. Овде су изучаване транспортне особине јона алкалних метала K^+ , Na^+ и Li^+ у DXE (1,2 - диметоксиетан) гасу, који се користи као катализатор у физици чврстог стања и као прекурсор у производњи керамике. Изабране су највероватније реакције јона алкалних метала са молекулом DXE гаса и његовим фрагментима, и израчунате одговарајуће енталпије формирања продуката.

Стакло-керамика на бази титаната

Сфенска стакло-керамика (CaTiSiO_5), перспективан материјал за матрикс керамике и имобилизацију нуклеарног отпада, синтетисана је из мешавине CaCO_3 , TiO_2 и SiO_2 . Након топљења на $1400\text{ }^\circ\text{C}$, хлађења и поновног мљења, материјал је кристализован термичким третманом, при чему је чиста монофазна сфенска стакло-керамика добијена на $800\text{ }^\circ\text{C}$ за 4 сата. Морфологија праха анализирана је помоћу SEM-а, а развој фазног састава праћен XRD, FT-IR, Раман и термичким анализама.

1. ЕЛЕМЕНТИ ЗА КВАЛИТАТИВНУ ОЦЕНУ НАУЧНОГ ДОПРИНОСА КАНДИДАТКИЊЕ

4.1. Квалитет научних резултата

4.1.1. Научни ниво и значај резултата, утицај научних радова

У свом досадашњем раду, др Гилић је објавила 45 научних радова са ISI листе. Од тог броја, 3 рада спадају у категорију M21A (међународни часописи изузетних вредности), 12 су M21 категорије (врхунски међународни часописи), 24 су M22 категорије и 6 спадају у категорију M23. Објављен је и један рад у водећем часопису националног значаја M51, као и 7 поглавља у монографијама. Одржала је више предавања на међународним конференцијама, од којих су два по позиву.

Након избора у научно звање виши научни сарадник, Др Гилић је објавила 10 радова са ISI листе. Од тог броја, 3 рада спадају у категорију M21 (врхунски међународни часописи), док су 7 радова M22 категорије. У овом периоду је кандидаткиња објавила и поглавље у монографији, а и одржала више предавања на међународним конференцијама.

Као пет најзначајнијих радова кандидаткиње издвајамо:

1. **M. Gilic**, M. Ghobara, L. Reissig, "Tuning SERS Signal via Substrate Structuring: Valves of Different Diatom Species with Ultrathin Gold Coating", *Nanomaterials* 13 (2023) 1594.
2. **M. Gilic**, J. Trajic, N. Romcevic, M. Romcevic, D. V. Timotijevic, G. Stanisic, I. S. Yahia, "Optical properties of CdS thin films", *Optical Materials* 35 (2013) 1112-1117.
3. **M. Gilic**, N. Romcevic, M. Romcevic, D. Stojanovic, R. Kostic, J. Trajic, W. D. Dobrowolski, G. Karczewski, R. Galazka, "Optical properties of CdTe/ZnTe self-assembled quantum dots: Raman and photoluminescence spectroscopy", *Journal of Alloys and Compounds* 579 (2013) 330-335.
4. **M. Gilić**, M. Petrović, R. Kostić, D. Stojanović, T. Barudžija, M. Mitrić, N. Romčević, U. Ralević, J. Trajić, M. Romčević, I. S. Yahia, "Structural and optical properties of CuSe₂ nanocrystals formed in thin solid Cu-Se film", *Infrared Physics & Technology* 78 (2016) 276-284.
5. M. Romcevic, **M. Gilic**, L. Kilanski, W. Dobrowolski, I. Fedorchenko, S. F. Marenkin, N. Romcevic, "Phonon properties of ZnSnSb₂+Mn semiconductors: Raman spectroscopy", *Journal of Raman Spectroscopy* 49 (2018) 1678-1685.

У првом раду (*Nanomaterials* 2023) Др Гилић детаљно изучава улогу различитих дијатомеја као хибридних супстрата за Површински појачану Раманову спектроскопију. Супстрати базирани на три врсте дијатомеја са круцијално различитим структурним параметрима, пресвучени танким хомогеним слојем злата, показали су знатно појачање Рамановог сигнала, где степен појачања зависи управо од структурних параметара. Експериментални резултати су потврђени и нумеричком анализом (метода коначних елемената). Утврђено је да резонанција вођених модова вероватно није једини механизам који доприноси појачању сигнала.

У другом раду (*Optical Materials* 2013) кандидаткиња је дала кључни допринос карактеризацији оптичких и структурних својстава танких филмова кадмијум сулфида различите дебљине. Инфрацрвени спектри су анализирани коришћењем нумеричког модела за израчунавање коефицијента рефлексије сложених система који укључују филм и супстрат. По први пут је диелектрична функција танког филма CdS анализирана помоћу Maxwell-Garnet-ове формуле као

смеша хомогених сферних инклузија у ваздуху. Интензитети Раманових спектра су анализирани помоћу исте формуле, и добило се веома добро слагање између примењеног модела и експерименталних података. Интресантно је напоменути да су филмови високог квалитета добијени једноставном методом вакуумског напаравања, што смањује цену производње за потенцијалну примену у оптоелектроници и пиезоелектроници.

У трећем раду (*Journal of Alloys and Compounds* 2013) др Гилић врши детаљну анализу резултата спектроскопских мерења хетероструктура CdTe/ZnTe. Због велике разлике у параметрима решетке, овакве структуре погодују формирању квантних тачака. Научни допринос кандидаткиње у овом раду је расветљавање природе мултифононских процеса уоченим током фотолуминесцентних и Раманових мерења. Утврђено је да зависе од температуре и енергије побуде (тј. таласне дужине ласера). Када се енергија расејаног фотона приближи енергији забрањене зоне ZnTe, одговарајући Раманов мод постаје резонантно појачан. Даље, апроксимацијом ефективне масе израчунат је дијаметар квантних тачака CdTe – 4.3 nm, што је знатно мање од Боровог радијуса ексцитона CdTe који износи 10 nm. Овај и претходни рад резултат су докторске дисертације кандидаткиње.

У четвртом раду (*Infrared Physics and Technology* 2016) кандидаткиња детаљно изучава оптичка и структурна својства овај пут двофазних танких филмова. Раманова и инфрацрвена спектроскопија су коришћене за идентификацију и квантификацију две фазе. Помоћу модела за конфајнмент оптичких фонона одређиване су величине честица CuSe₂ фазе, при чему је утврђено да се димензије честица повећавају са повећањем дебљине филма. Иако је овај модел ограничен на наночестице правилног сферног облика, показало се да он даје добре резултате и код реалних нанокристала који су неправилног облика.

У петом раду (*Journal of Raman Spectroscopy* 2018) кандидаткиња даје кључан допринос карактеризацији четворокомпонентног система Zn_{1-x}Mn_xSnSb₂ Рамановом спектроскопијом. Додатак Mn оваквим материјалима омогућава формирање магнетних кластера, одговорних за високотемпературни феромагнетизам. Показано је да су ово вишефазни материјали. На основу величине и облика сложених микроструктура које се састоје од различитих фаза и кластера, могу се идентификовати дисперзивне, дуплекс и триплекс микроструктуре. Фононска својства ZnSnSb₂ и MnSb су први пут експериментално регистрована. На основу помака фонона ZnSnSb₂, утврђено је да се одређена количина Mn уграђује у решетку основног материјала где формира чврст раствор Zn_{1-x}Mn_xSnSb₂.

4.1.2. Позитивна цитираност научних радова кандидаткиње

На дан 11.12.2024. године, према бази података Scopus др Гилић има 444 цитата. Према овој бази података, њен *h* фактор је 13. Према бази података Google Scholar, број цитата кандидаткиње на исти дан износи 575 (доказ дат у прилогу).

4.1.3. Параметри квалитета часописа

Од последњег избора у звање, тј. у периоду између 2020. и 2024. године, др Гилић је објавила 10 радова, и то: 3 у M21 и 7 у M22. Укупан импакт фактор радова кандидаткиње од последњег избора у звање износи 30,11. Часописи у којима кандидаткиња публикује цењени су и угледни у одговарајућим областима. Даље је дат списак часописа са одговарајућим импакт факторима за одговарајућу годину публикације.

- Physica E: Low - Dimensional Systems and Nanostructures (3,112 – 2021; 3,369 - 2020) M22
- Nanomaterials (5,3 – 2023) M21
- Chemosensors (4,0 – 2022) M21
- Science of Sintering (1,4 -2024; 1,5 – 2022; 1,172 -2020) M22
- Optical Materials (3,69 - 2023) M21
- Optical and Quantum Electronics (2,47 - 2022) M22
- Materials Chemistry and Physics (4,094 - 2020) M22

4.1.4. Степен самосталности и степен учешћа у реализацији радова

Од 45 објављених радова, др Гилић је први аутор на 6 радова, други на 11 радова, док је на једном раду последњи аутор.

На радовима објављеним након избора у тренутно научно звање, др Гилић је водећи аутор на једном раду, други аутор на 2 рада, и последњи аутор на једном научном раду.

На свим радовима на којима се налази, кандидаткиња је учествовала у конкретној формулацији проблема, експерименталном раду-мерењима, обради резултата мерења, тумачењу истих, примени теоријских модела. Др Гилић је од почетка своје научне делатности запослена на Институту за физику у Београду, где у одвиру Лабораторије за истраживања у области електронских материјала изводи већину експеримената. Др Гилић се самостално повезала са групом Др Петраушкиене са Технолошког факултета Каунас, Литванија, што је резултовало објављивањем три научна рада, саопштењима на неколико научних конференција, као и планираном Ерасмус посетом. Сарађивала је и са теоријском групом др Жељке Никитовић око транспортних особина алкалних метала у гасу, где је њен интердисциплинарни приступ доктора физичкохемијских наука посебно дошао до изражаја. Пројектни задатак “Нанооптички ефекти у подешавању радних перформанси диференцијалних фотодетектора сачињених од Cr_2O_3 ” који је иницијано започет ради добијања DAAD стипендије и краћег академског боравка на Freie Universität-у у Берлину отворио је пут за постдок од 2020. до 2023. године и дуготрајну сарадњу ове две престижне институције.

4.2. Ангажованост у формирању научних кадрова

Током свог постдока на Freie Universität-у у Берлину, кандидаткиња је активно учествовала у осмишљавању задатака везаних за докторску тезу студента докторских студија Мохамеда Гхобаре, консултацијама и сугестијама (захвалница из тезе дата у прилогу, теза је предата и чека се датум одбране).

Др Гилић је значајно помогла колегиници (и пријатељици) др Јелени Митрић при изради докторске дисертације (Факултет за Физичку хемију, 2021. године, доказ – захвалница из тезе у прилогу).

Др Мартина Гилић је сарађивала и значајно помогла Николи Тасићу са Института за мултидисциплинарна истраживања при изради докторске дисертације (Технолошко - металуршки факултет, Универзитет у Београду 2017. године, доказ – захвалница из тезе у прилогу).

Др Мартина Гилић је помогла Хани Ибрахим Елсвие око израде докторске дисертације (Технолошко – металуршки факултет, Универзитет у Београду 2017. године, доказ – захвалница из тезе у прилогу).

Др Мартина Гилић је помогла око израде тезе Стевану Димитријевићу (Технички факултет у Бору, Универзитет у Београду 2015. године, доказ – захвалница из тезе у прилогу).

4.3. Нормирање броја коауторских радова, патентних и техничких решења

Као што је већ речено, кандидаткиња је од избора у претходно научно звање објавила 10 научних радова у међународним часописима, од тога 3 у категорији М21 и 7 М22 категорије. Укупан број поена ових радова је 59. Нормирањем ових поена по формули датај у правилнику, њихов број се смањује на 53,5.

4.4. Руковођење пројектима, потпројектима и пројектним задацима

У оквиру националног пројекта из области интегралних и интердисциплинарних истраживања III45003 “Оптоелектронски нанодимензиони системи – пут ка примени”, финансираним од Министарства просвете, науке и технолошког развоја Републике Србије, др Гилић је руководила потпројектом “Синтеза наноматеријала и структура” (доказ дат у прилогу – Анекс 9 уговора о реализацији пројекта ИИИ45003).

Учесник је пројекта који се реализује у оквиру билатералне сарадње, а на основу Споразума о научној сарадњи између Института за физику Пољске академије наука и Института за физику у Београду (доказ у прилогу – споразум о сарадњи).

Током боравка на Frei Universität-у у Берлину, у оквиру DFG пројекта: Diatom frustules as nature-designed building blocks for photonic applications Др Гилић је руководила задацима везаним за примену дијатомеја у Површински појачаној Рамановој спектроскопији.

4.5. Патенти

Др Гилић је коаутор једног патентног решења:

П. Коларж, М. Ђурчић, М. Гилић, Б. Хаџић, *МОДИФИКОВАНИ НОСАЧ ЗА ВЕРТИКАЛНО ПОЗИЦИОНИРАЊЕ ТАБЛЕТНИХ УЗОРАКА ОД ПРАШКАСТИХ МАТЕРИЈАЛА КОЈИ ЈЕ ДЕО КОМОРЕ ЗА ВАКУУМИРАЊЕ И ХЛАЂЕЊЕ КОЈА СЕ КОРИСТИ У СПЕКТРОСКОПСКИМ МЕРЕЊИМА*, Регистар малих патената Завода за интелектуалну својину МП2018/0028 од 19.06.2018. године (доказ у прилогу).

4.6. Активност у научним и научно – стручним друштвима

Др Гилић је чланица Српског керамичког друштва, као и Српског огранка Америчког керамичког друштва.

Др Гилић је чланица едиторијалног одбора часописа *American Journal of Optics and Photonics (AJOP)* (доказ дат у прилогу – сертификат чланства).

Др Гилић је рецезент у већем броју међународних часописа: *Materials Science in Semiconductor Processing, SciFed Journal of Metallurgical Science, Engineering Science and Technology, Processing and Application of Ceramics, Optoelectronics and Advanced Materials – Rapid Communications* (докази дати у прилогу).

Др Гилић је била члан организационег одбора конференције КОНГРЕС МЕТРОЛОГА 2015, Златибор, 12-15. октобар 2015. године (доказ дат у прилогу).

Након избора у претходно звање, др Гилић је одржала предавање по позиву:

M. Gilic, M. Ghobara and L. Reissig, "Photonic crystal behavior of biosilica – influence of frustule's morphology on SERS sensitivity", 15th Photonics Workshop: Kopaonik, March 13 – 16, 2022.

4.7. Утицајност научних резултата

Утицајност научних радова др Мартине Гилић детаљно је описана у одељку 5.1. овог документа. У прилогу је дат списак радова и цитата.

4.8. Конкретан допринос кандидата у реализацији радова у земљи и иностранству

Др Марина Гилић је у својој досадашњој научној каријери објавила 45 научних радова у међународним часописима, 1 рад у часопису националног значаја, 8 поглавља у монографијама. Од тога, 3 рада су категорија M21A, 12 су M21, 25 M22 док их је 6 M23. На 6 публикација др Гилић је први аутор, други је на 11, и кореспондинг аутор на две.

Након избора у тренутно научно звање, Др Гилић је објавила 10 радова са ISI листе. Од тог броја, 3 су M21 категорије (врхунски међународни часописи) и 7 су M22 категорије. Од овог броја, кандидаткиња је први аутор на једној публикацији, други на 2, а на једној публикацији је кореспондинг аутор. У овом периоду је објавила и 2 поглавља у монографијама.

На свим овим радовима др Гилић је активно учествовала, од формулације проблема до финалног решавања уз комуникацију и сарадњу са осталим коауторима, где се истакла као вешт координатор. Пошто је реч о експерименталној физици, постављање и извођење експеримента представља значајан део кандидаткињине научне активности, у шта спада припрема апаратуре и припрема узорака за експеримент, али и обрада резултата мерења уз коришћење одговарајућих теоријских модела, као и теоријске симулације.

4.9. Уводна предавања на конференцијама и друга предавања

Др Гилић је одржала два предавања по позиву:

Martina Gilić and Milica Ćurčić, *Optical and structural properties of nanostructured semiconductors*, The Seventh Serbian Ceramic Society Conference - Advanced Ceramics and Application, September 17-

19, 2018, Belgrade, Serbia, Program and The Book of Abstracts, INV-OGE4, 51-52. (доказ у прилогу – сертификат)

M. Gilic, M. Ghobara and L. Reissig, "*Photonic crystal behavior of biosilica – influence of frustule's morphology on SERS sensitivity*", 15th Photonics Workshop: Kopaonik, March 13 – 16, 2022.

5. ЕЛЕМЕНТИ ЗА КВАНТИТАТИВНУ ОЦЕНУ НАУЧНОГ ДОПРИНОСА КАНДИДАТКИЊЕ

5.1. Остварени резултати након одлуке Научног већа о предлогу за стицање тренутног научног звања:

Категорија	Број радова	Број бодова по раду	Укупан број бодова	Укупан број нормираних бодова
М13	1	7	7	7
М21	3	8	24	20,38
М22	7	5	35	33,12
М32	1	1,5	1,5	1,5
М33	2	2	2	2
М34	4	0,5	2	2
Збир			71,5	66

5.2. Табела са квантитативним показатељима радова категорија М20 објављеним након претходног избора у звање:

Редни број рада	Категорија	М	ИФ	СНИП
1	М21	8	5,3	1,09
2	М21	8	3,69	0,92
3	М21	8	4,0	0,96
4	М22	5	1,4	0,65
5	М22	5	2,47	0,92
6	М22	5	1,5	0,65
7	М22	5	3,112	0,79
8	М22	5	1,172	0,65
9	М22	5	3,369	0,79
10	М22	5	4,094	1,01
Збир		59	30,11	8,43

5.3. Поређење са минималним квантитативним условима за избор у звање виши научни сарадник:

Минималан број М бодова		Остварено	Остварено нормираних
укупно	25	71,5	66
М10+М20+М31+М32+М41+М42	20	68,5	63
М11+М12+М21+М22+М23+М24	15	59	53,5

6. Списак радова и осталих публикација кандидаткиње, разврстаних по важећим категоријама прописаних правилником

M10: МОНОГРАФИЈЕ, МОНОГРАФСКЕ СТУДИЈЕ, ТЕМАТСКИ ЗБОРНИЦИ, ЛЕСКИКОГРАФСКЕ И КАРТОГРАФСКЕ ПУБЛИКАЦИЈЕ МЕЂУНАРОДНОГ ЗНАЧАЈА

M13 - монографска студија/поглавље у књизи M11 или рад у тематском зборнику водећег међународног значаја:

1. Z. Lazarević, **M. Gilic**, A. Milutinović, N. Romcević, H. Elswie, V. Radojević, D. Sekulić, "15 Growth and characterization of calcium fluoride single crystals", *Advanced Ceramics and Applications*, De Gruyter (2021) 179-203.

M20: РАДОВИ ОБЈАВЉЕНИ У НАУЧНИМ ЧАСОПИСИМА МЕЂУНАРОДНОГ ЗНАЧАЈА

M21 – рад у врхунском међународном часопису:

1. **M. Gilic**, M. Ghobara, L. Reissig, „Tuning SERS Signal via Substrate Structuring: Valves of Different Diatom Species with Ultrathin Gold Coating”, *Nanomaterials* 13 (2023) 1594.
2. B. Babic, M. Romcevic, **M. Gilic**, J. Trajic, MM. Radanović, Lj. S. Vojinović-Ješić, MV. Rodić, N. Romcevic, "Phonon assisted charge transfer in complexes of Zn (II) and Cd (II) with 2-acetylpyridine-aminoguanidine", *Optical Materials* 136 (2023) 113445.
3. G. Jakubauskas, **M. Gilic**, E. Paluckiene, J. Mitric, J. Cirkovic, U. Ralevic, E. Usoviene, E. Griskonis, N. Petrasauskiene, "Characterization of Flexible Copper Selenide Films on Polyamide Substrate Obtained by SILAR Method—Towards Application in Electronic Devices", *Chemosensors* 10 (2022) 313-325.

M22 – рад у истакнутом међународном часопису:

4. M. Curcic, **M. Gilic**, N. Petrauskienė, B. Hadzic, J. Mitric, E. Paluckiene, „Nanocomposite CuxS on Flexible Polymers: Raman Study”, *Science of Sintering* (2024) in press.
5. J. Pešić, A. Šolajić, J. Mitrić, **M. Gilić**, I. Pešić, N. Paunović, N. Romčević, "Structural and optical characterization of titanium–carbide and polymethyl methacrylate based nanocomposite", *Optical and Quantum Electronics* 54 (2022) 1-13.
6. N. Petrasauskiene, E. Paluckiene, R. Alaburdaite, **M. Gilić**, „Deposition of copper sulfide films on polyamide surface” *Science of Sintering* 54 (2022) 1-14.
7. J. Mitrić, N. Paunović, M. Mitrić, J. Ćirković, **M. Gilić**, M. Romčević, N. Romčević, "Surface optical phonon and multi–phonon transitions in YVO4: Eu³⁺ nanopowders", *Physica E: Low-dimensional Systems and Nanostructures* 134 (2021) 114923.
8. J. Maletaškić, B. Todorović, **M. Gilić**, M. Marinović-Cincović, K. Yoshida, A. Gubarevich, B. Matović, "Synthesis and characterization of monophase CaO-TiO₂-SiO₂ (sphene) based glass-ceramics", *Science of Sintering* 52 (2020) 41-52.
9. M. Curcic, B. Hadzic, **M. Gilic**, V. Radojevic, A. Bjelajac, I. Radovic, D. Timotijevic, M. Romcevic, J. Trajic, N. Romcevic, „Surface optical phonon (SOP) mode in ZnS/Poly

(methylmethacrylate) nanocomposites“, Physica E: Low-dimensional Systems and Nanostructures 115 (2020) 113708.

10. A. Kalijadis, N. Gavrilov, B. Jokić, **M. Gilić**, A. Krstić, I. Pašti, B. Babić, “Composition, Structure and Potential Energy Application of Nitrogen Doped Carbon Cryogels“, Materials Chemistry and Physics 239 (2020) 122120.

Радови објављени пре избора у тренутно научно звање:

M21A:

1. N. Romcevic, M. Romcevic, W. D. Dobrowolski, L. Kilanski, M. Petrovic, J. Trajic, B. Hadzic, Y. Lazarevic, **M. Gilic**, J. L. Ristic-Djurovic, N. Paunovic, A. Rezska, B. J. Kowalski, I. V. Fedorchenko, S. F. Marenkin, “Far-infrared spectroscopy of $Zn_{1-x}Mn_xGeAs_2$ single crystals: Plasma damping influence on plasmon-Phonon interaction“, Journal of Alloys and Compounds 649 (2015) 375-379.
2. **M. Gilic**, N. Romcevic, M. Romcevic, D. Stojanovic, R. Kostic, J. Trajic, W. D. Dobrowolski, G. Karczewski, R. Galazka, “Optical properties of CdTe/ZnTe self-assembled quantum dots: Raman and photoluminescence spectroscopy“, Journal of Alloys and Compounds 579 (2013) 330-335.
3. N. Romčević, M. Petrović-Damjanović, M. Romčević, **M. Gilić**, L. Klopotoski, W. D. Dobrowolski, J. Kossut, I. A. Janković, M. I. Čomor, “Magnetic field influence on optical properties of $Cd_{1-x}Mn_xS$ ($x = 0; 0.3$)“, Journal of Alloys and Compounds 553 (2013) 75-78.

M21:

4. J. Mitric, U. Ralevic, M. Mitric, J. Cirkovic, G. Krizan, M. Romcevic, **M. Gilic**, N. Romcevic, “Isotope-like effect in $YVO_4:Eu^{3+}$ nanopowders: Raman spectroscopy“, Journal of Raman Spectroscopy (2019) 1-7.
5. M. Romcevic, **M. Gilic**, L. Kilanski, W. Dobrowolski, I. Fedorchenko, S. F. Marenkin, N. Romcevic, “Phonon properties of $YnSnSb_2+Mn$ semiconductors: Raman spectroscopy“, Journal of Raman Spectroscopy 49 (2018) 1678-1685.
6. G. Krizan, **M. Gilic**, J. L. Ristic-Djurovic, J. Trajic, M. Romcevic, J. Krizan, B. Hadzic, B. Vasic, N. Romcevic, “Raman spectroscopy and electron-phonon coupling in Eu^{3+} doped $Gd_2Zr_2O_7$ nanopowders“, Optical Materials 73 (2017) 541-544.
7. D. Sevic, M. S. Rabasovic, J. Krizan, S. Savic-Sevic, M. Mitric, **M. Gilic**, B. Hadzic, N. Romcevic, “Characterization and luminescence kinetics of Eu^{3+} doped YVO_4 nanopowders“, Materials Research Bulletin 88 (2017) 121-126.
8. Ž. Nikitović, **M. Gilić**, Z. Raspopović, V. Stojanović, “Comparison between transport parameters for K^+ and Li^+ in 1,2-dimethoxy ethane (DXE) gas“, EPL 116 (2016) 15002.
9. M. S. Rabasovic, D. Sevic, J. Krizan, S. Savic-Sevic, M. Mitric, M. Petrovic, **M. Gilic**, N. Romcevic, “Structural properties and luminescence kinetics of white nanophosphor $YAG:Dy$ “, Optical Materials 50 (2015) 250-255.
10. N. Romčević, **M. Gilić**, I. Anžel, R. Rudolf, M. Mitrić, M. Romčević, B. Hadžić, D. Joksimović, M. Petrović Damjanović, M. Kos, “DETERMINATION OF MICROSTRUCTURAL CHANGES BY SEVERELY PLASTICALLY DEFORMED COPPER-ALUMINIUM ALLOY: OPTICAL STUDY“, J. Min. Metall. Sect. B-Metall. 50 (1) B (2014) 61-68.
11. **M. Gilic**, J. Trajic, N. Romcevic, M. Romcevic, D. V. Timotijevic, G. Stanisic, I. S. Yahia, “Optical properties of CdS thin films“, Optical Materials 35 (2013) 1112-1117.

12. Z. Ž. Lazarević, P. Mihajlović, S. Kostić, M. J. Romčević, M. Mitrić, S. Petričević, J. Radunović, M. Petrović-Damjanović, **M. Gilić**, N. Ž. Romčević, "Determination of magneto-optical quality and refractive index of bismuth germanium oxide single crystals grown by Czochralski technique", *Optical materials* 34 (2012) 1849-1859.

M22:

13. Z. Ž. Lazarević, G. Križan, J. Križan, A. Milutinović, V. N. Ivanovski, M. Mitrić, **M. Gilić**, A. Umičević, I. Kuryliszyn-Kudelska, N. Ž. Romčević, "Characterization of LiFePO₄ samples obtained by pulse combustion under various conditions of synthesis", *Journal of Applied Physics* 126 (2019) 085109-14.
14. Z. Lazarević, G. Križan, J. Križan, A. Milutinović, **M. Gilić**, I. Kurzliszyn-Kudelska, N. Romčević, "Spectroscopic Characterization of LiFePO₄ as Cathode Material for Li-ion Battery Prepared in the Pulse Thermo-acoustic Reactor", *Science of Sintering* 51 (2019).
15. R. Abozaid, Z. Lazarević, I. Radović, **M. Gilić**, D. Šević, M. Rabasović, V. Radojević, "Optical properties and fluorescence of quantum dots CdSe/ZnS-PMMA composite films with interface modifications", *Optical Materials* 92 (2019) 405-410.
16. N. Tasic, Z. Marinkovic Stanojevic, Z. Brankovic, M. Zunic, U. Lacnjevac, **M. Gilić**, T. Novakovic, G. Brankovic, "Mesoporous TiO₂ spheres as a photoanodic material in dye-sensitized solar cells", *Processing and Application of Ceramics* 12 [4] (2018) 374-382.
17. J. Trajic, M. Romcevic, M. Petrovic, **M. Gilić**, P. Balaz, A. Zorkovska, N. Romcevic, "Optical properties of the mechanochemically synthesized Cu₂FeSnS₄ (stannite) nanocrystals: Raman study", *Optical Materials* 75 (2018) 314-318.
18. Z. Lazarević, Č. Jovalekić, **M. Gilić**, V. Ivanovski, A. Umičević, D. Sekulić, N. Romčević, "Yttrium Orthoferrite Powder Obtained by the Mechanochemical Synthesis", *Science of Sintering* 49 (2017) 277-284.
19. **M. Gilić**, M. Petrović, J. Ćirković, N. Paunović, S. Savić-Šević, Ž. Nikitović, M. Romčević, I. Yahia, N. Romčević, "Low-temperature photoluminescence of CuSe₂ nano-objects in selenium thin films", *Processing and Application of Ceramics* 11 [2] (2017) 127-135.
20. M. Petrović, **M. Gilić**, J. Ćirković, M. Romčević, N. Romčević, J. Trajić, I. Jahia, "Optical properties of CuSe Thin Films – Band Gap Determination", *Science of Sintering* 49 (2017) 167-174.
21. **M. Gilić**, M. Petrović, R. Kostić, D. Stojanović, T. Barudžija, M. Mitrić, N. Romčević, U. Ralević, J. Trajić, M. Romčević, I. S. Yahia, "Structural and optical properties of CuSe₂ nanocrystals formed in thin solid Cu-Se film", *Infrared Physics & Technology* 78 (2016) 276-284.
22. H. I. Elswie, Z. Ž. Lazarević, V. Radojević, **M. Gilić**, M. Rabasović, D. Šević, N. Ž. Romčević, "The Bridgman Method Growth and Spectroscopic Characterization of Calcium Fluoride Single Crystals", *Science of Sintering* 48 (2016) 333-341.
23. Ž. D. Nikitović, **M. D. Gilić**, M. S. Petrović, N. Ž. Romčević, Z. M. Raspopović, V.D. Stojanović, "Cross sections and Transport properties for Na⁺ in (DXE) Gas, *Science of Sintering* 48 (2016) 379-386.
24. A. Milutinović, Z. Ž. Lazarević, M. Jakovljević, B. Hadžić, M. Petrović, **M. Gilić**, W. D. Dobrowolski, N. Ž. Romčević, "Optical properties of layered III-VI semiconductor γ-InSe:M (M=Mn, Fe, Co, Ni)", *Journal of Physics and Chemistry of Solids* 89 (2016) 120-127.
25. J. Trajić, **M. Gilić**, N. Romčević, M. Romčević, G. Stanišić, B. Hadžić, M. Petrović, Y. S. Yahia, "Raman Spectroscopy of Optical Properties In CdS Thin Films", *Science of Sintering*, 47 (2015) 145-152.

26. M. Petrović, N. Romčević, J. Trajić, W. D. Dobrowolski, M. Romčević, B. Hadžić, **M. Gilić**, A. Mycielski, "Far-infrared spectroscopy of CdTe_{1-x}Se_x(In): Phonon properties", *Infrared Physics & Technology* 67 (2014) 323-326.
27. J. Trajić, **M. Gilić**, M. Romčević, G. Stanišić, Z. Lazarević, D. Joksimović, I. S. Yahia, "Far-infrared investigations of the surface modes in CdS thin films", *Phys. Scr. T162* (2014) 014031 (4pp).
28. S. Kostić, Z. Lazarević, M. Romčević, V. Radojević, A. Milutinović **M. Gilić**, "Spectroscopic characterization of YAG and Nd:YAG single crystals", *Phys. Scr. T162* (2014) 014026 (5pp).
29. Z. Lazarević, S. Kostić, V. Radojević, M. Romčević, **M. Gilić**, M. Petrović Damjanović, N. Romčević, "Raman spectroscopy of bismuth silicon oxide single crystals grown by the Czochralski technique" *Phys. Scr. T157* (2013) 014046 (4pp).

M23:

30. **M. Gilić**, R. Kostic, D. Stojanovic, M. Romcevic, B. Hadzic, M. Petrovic, U. Ralevic, Z. Lazarevic, J. Trajic, J. Ristić-Djurovic, J. Cirkovic, N. Romcevic, "Photoluminescence spectroscopy of CdSe nanoparticles embedded in transparent glass", *Optical and Quantum Electronics* 50 (2018) 288-295.
31. S. P. Dimitrijević, Z. Ž. Lazarević, M. Rajčić-Vujasinović, S. B. Dimitrijević, M. Petrović, **M. Gilić**, B. M. Jokić, "Raman spectroscopy study of anodic film on Ag₄₃Cu₃₇Zn₂₀ alloy", *Optoelectronics and advanced materials-rapid communications* 10 (2016) 777-780.
32. M. Petrović, M. Romčević, R. Kostić, N. Romčević, W. D. Dobrowolski, **M. Gilić**, B. Hadžić, J. Trajić, D. Stojanović, Z. Lazarević, "Optical properties of Cd_{1-x}Mn_xS nanoparticles: off-resonance Raman spectroscopy", *Optoelectronics and advanced materials-rapid communications* 10 (2016) 177-179.
33. B. Hadžić, N. Romčević, M. Romčević, I. Kuryliszyn-Kudelska, W. Dobrowolski, **M. Gilić**, M. Petrović Damjanović, J. Trajić, U. Narkiewicz, D. Sibera, "Raman study of surface optical phonons in ZnO(Co) nanoparticles prepared by calcinations method", *Journal of optoelectronics and advanced materials* 16 (2014) 508-512.
34. J. Trajic, N. Romcevic, **M. Gilić**, M. Petrovic Damjanovic, M. Romcevic, V. N. Nikiforov, "Optical properties of PbTe_{0.95}S_{0.5} single crystal at different temperatures: far-infrared study", *Optoelectronics and advanced materials-rapid communications* 6 (2012) 543-546.
35. R. Rudolf, **M. Gilić**, M. Romčević, I. Anžel, "Optical properties of plastically deformed copper: amorphous state with residual nanocrystals", *Optoelectronics and advanced materials-rapid communications* 5 (2011) 932-935.

M50: часописи националног значаја

M51 – водећи научни часопис националног значаја

1. V. Nikolić, **M. Gilić**, V. Spasojević, CHARACTERIZATION OF NiO NANOPARTICLES PREPARED USING GELATIN AND LOW – COST SYNTHESIS, *VOJNOTEHNIČKI GLASNIK* 67 (2019) 36-52.

M30: ЗБОРНИЦИ СА МЕЂУНАРОДНИХ НАУЧНИХ СКУПОВА

M32 – предавање по позиву са међународног скупа штампано у изводу:

1. **Martina Gilić**, Mohamed Ghobara and Louisa Reissig, *Photonic crystal behavior of biosilica – influence of frustule's morphology on SERS sensitivity*, 15th Photonics Workshop: Kopaonik, March 13 – 16, 2022, Program and The Book of Abstracts. (доказ у прилогу – позивно писмо)

M33 – саопштење са међународног скупа штампано у целини:

1. **M. Gilic**, M. Ghobara, L. Reissig, „Boosting Surface-Enhanced Raman Scattering by Ultrathin Golden Film on Bio-Photonic Crystals”, Bragg Gratings, Photosensitivity and Poling in Glass Waveguides and Materials, Optica Publishing Group (2022) JW3A. 52.
2. Ž. Nikitović, **M. Gilić**, J. Mitrić, Z. Raspopović, RATE COEFFICIENTS FOR Ar⁺ IN Ar/BF₃ MIXTURES, 30th Summer School and International Symposium on the Physics of Ionized Gasses, Aug.24-28, 2020, Šabac, Serbia, Publ. Astron. Obs. Belgrade No. 99 (2020), 79 – 82.

M34 – саопштење са међународног скупа штампано у изводу:

1. N. Petrauskiene, **M. Gilic**, E. Paluckiene, ANALYSIS OF Cu_xS THIN FILM DEPOSITED ON SURFACE OF POLYAMIDE – RAMAN SPECTROSCOPY, Baltic Polymer Symposium 2023 JELGAVA, LATVIA SEPTEMBER 20-22, Book of Abstracts pp. 65.
2. E. Paluckiene, **M. Gilic**, N. Petrauskiene, RAMAN ANALYSIS OF Cu_xS THIN FILMS DEPOSITED ON the SURFACE OF POLYPROPYLENE, Baltic Polymer Symposium 2023 JELGAVA, LATVIA SEPTEMBER 20-22, Book of Abstracts pp. 64.
3. **M. Gilic**, R. Adaburdaite, E. Paluckiene, N. Petrauskiene, Effect of Deposition Cycles on the Properties of Copper Sulfide Thin Films Deposited by CBD, CCT-2023, March 10th Vilnius, Lithuania.
4. **M. Gilic**, M. Ghobara, L. Reissig, Boosting surface plasmon resonances of thin golden film by bio photonic crystals, PHOTONICA2021 VIII International School and Conference on Photonics & HEMMAGINERO workshop, Book of Abstracts pp. 105.

Article

Characterization of Flexible Copper Selenide Films on Polyamide Substrate Obtained by SILAR Method—Towards Application in Electronic Devices

Gediminas Jakubauskas ¹, Martina Gilic ^{2,3}, Edita Paluckiene ¹, Jelena Mitric ², Jovana Cirkovic ⁴, Uros Ralevic ², Egle Usoviene ¹, Egidijus Griskonis ¹  and Neringa Petrasauskiene ^{1,*} 

¹ Department of Physical and Inorganic Chemistry, Kaunas University of Technology, Radvilenu 19, 50254 Kaunas, Lithuania

² Institute of Physics Belgrade, University of Belgrade, Pregrevica 118, 11080 Belgrade, Serbia

³ Institut of Experimental Physics, Freie Universität Berlin, Arnimallee 14, 14195 Berlin, Germany

⁴ Institute for Multidisciplinary Research, University of Belgrade, Kneza Visaslava 1, 11000 Belgrade, Serbia

* Correspondence: neringa.petrasauskiene@ktu.lt

Abstract: Thin copper selenide films were synthesized on polyamide sheets using the successive ionic layer adsorption and reaction (SILAR) method at three different temperatures. It was found that elevating the temperature of the solution led to the creation of copper selenide films with different features. X-ray diffraction characterization revealed that all films crystallized into a cubic Cu_{2-x}Se , but with different crystallinity parameters. With elevating the temperature, grain size increased (6.61–14.33 and 15.81 for 40, 60 and 80 °C, respectively), while dislocation density and the strain decreased. Surface topology was investigated with Scanning Electron Microscopy and Atomic Force Microscopy, which revealed that the grains combined into agglomerates of up to 100 nm (80 °C) to 1 μm (40 °C). The value of the direct band gap of the copper selenide thin films, obtained with UV/VIS spectroscopy, varied in the range of 2.28–1.98 eV. The formation of Cu_{2-x}Se was confirmed by Raman analysis; the most prominent Raman peak is located at 260 cm^{-1} , which is attributed to binary copper selenides. The thin Cu_{2-x}Se films deposited on polyamide showed *p*-type conductivity, and the electrical resistivity varied in the range of 20–50 Ω . Our results suggest that elevated temperatures prevent large agglomeration, leading to higher resistance behavior.

Keywords: copper selenide; polyamide; SILAR method



Citation: Jakubauskas, G.; Gilic, M.; Paluckiene, E.; Mitric, J.; Cirkovic, J.; Ralevic, U.; Usoviene, E.; Griskonis, E.; Petrasauskiene, N.

Characterization of Flexible Copper Selenide Films on Polyamide Substrate Obtained by SILAR Method—Towards Application in Electronic Devices. *Chemosensors* **2022**, *10*, 313. <https://doi.org/10.3390/chemosensors10080313>

Academic Editor: Vardan Galstyan

Received: 22 June 2022

Accepted: 1 August 2022

Published: 5 August 2022

Publisher's Note: MDPI stays neutral with regard to jurisdictional claims in published maps and institutional affiliations.



Copyright: © 2022 by the authors. Licensee MDPI, Basel, Switzerland. This article is an open access article distributed under the terms and conditions of the Creative Commons Attribution (CC BY) license (<https://creativecommons.org/licenses/by/4.0/>).

1. Introduction

Copper selenide can be formed in various stoichiometric compositions, such as CuSe , Cu_2Se , CuSe_2 , Cu_3Se_2 , Cu_7Se_4 , Cu_5Se_4 , Cu_3Se_4 , and non-stoichiometric compositions Cu_{2-x}Se [1–3]. The stoichiometric composition of copper selenide strongly influenced its crystalline structure and electronic behavior—it alters its electronic, chemical, and thermal properties [4,5]. Copper-deficient Cu_{2-x}Se is an intrinsic *p*-type semiconductor with direct bandgap energies in the range of 2.0 to 2.4 eV, the work function of 4.17 eV, and high photo-electrochemical conversion efficiency (~14.6%) [3,5–8]. These features of Cu_{2-x}Se can be used as Schottky diodes [9], self-repairable electrodes [10], and photovoltaic devices [8]. Furthermore, the Cu_{2-x}Se columnar superstructures are used as low-cost and highly efficient counter electrodes in quantum dot sensitized solar cells [11,12].

Several decades ago, due to concerns about homeland security, medical and environmental monitoring as well as food safety, a large interest was shown in the development of gas sensors for detecting volatile and toxic gases. Cu_{2-x}Se exhibits good sensitivity and short response and recovery times to Hg^{2+} [13], and organic gases such as ethanol and acetone [14].

Many works have been reported on the formation of Cu_{2-x}Se on substrates, such as glass [1,6,15], and fluorine-doped tin oxide [8,11,12,16].

Flexible electronics is a growing field that is promising to develop various new commercial products such as displays, solar cells, flexible photovoltaics, and biomedical sensors due to their lightweight and low cost [17–21]. Flexible polymer substrates possess unique features such as low cost, low thickness, low mass, and excellent mechanical deformability. They can remain in the environmental, chemical, and thermal environments required for the construction of electronic circuits while maintaining their mechanical flexibility [22,23]. Recently, ferroelectric semiconductors have been increasingly studied [24,25].

When Cu_{2-x}Se is deposited on a flexible transparent polymer substrate (polyvinylchloride, polyvinyl alcohol), the possibility of using thin flexible polymer substrates appears in the fabrication of flexible optoelectronic devices [26]. Cu_{2-x}Se films on polyester sheets can be used as a transparent electrode for inorganic and organic hybrid light emitters, as a possible replacement for indium tin oxide or fluorine-doped tin oxide [7].

This work reports the preparation and characterization of electrically conductive copper selenide onto polyamide 6 (PA) sheets. Polyamide 6 was chosen as a cheap, chemically stable, and flexible substrate. Flexibility is the ability of the material to be bent without mechanical failures such as fracture and plastic deformation. One of the few mechanical parameters that describe the deformation of a material is Young's modulus, which characterizes the resistance of a material to elastic deformation. Young's moduli of polyamide 6 are lower than those of other polymers. For example, polyimide and polyethylene terephthalate have a Young's modulus of 4 GPa and 3 GPa, respectively, while the Young's modulus of polyamide 6 is 2.4 GPa [17,27,28]. As a semihydrophilic flexible polymer, PA is capable of adsorbing molecules or ions of various electrolytes from nonaqueous and aqueous solutions [29,30]. Unlike glass and fluorine-doped tin oxide substrates, on which copper selenide builds a thin film, polymer allows the material to partially diffuse in it, so the final product is a conductive composite (PA with copper selenide nanocrystals embedded in it).

Cu_{2-x}Se films can be prepared by chemical bath deposition [1,7,31], combined electrochemical followed by chemical bath deposition [8], sonochemical synthesis [32], ion beam sputtering deposition [33], electrochemical [12], successive ionic layer adsorption and reaction [15,34], and other methods.

Here, copper selenide nanocrystals were formed on the surface as well as inside the polyamide using the simple and versatile successive ionic layer adsorption and reaction (SILAR) method. The method used differs from other chemical methods, as it does not require specialized equipment or conditions; it is quite inexpensive and simple, convenient for large area deposition, and it can be used at room temperature [34]. As a low-temperature process, it also avoids oxidation [35]. The SILAR method consists of two stages: first, copper ions are adsorbed on the polyamide surface from a precursor solution containing copper ions; second, copper selenide thin films are formed by treating the layer formed in the first stage with a solution containing selenium ions. To the best of our knowledge, the copper selenide/PA composite by employing the SILAR method has never been obtained before. We suggest that slightly elevated solution temperatures could facilitate crystalline formation in the polymer matrix and therefore improve the optical and electric properties of the as-obtained composites. Combined with the natural abundance of material and the low cost of composite production, the copper selenide/PA composite could be a possibility for printable electronics on flexible substrates or in sensors in the future.

Structural characterization of the composites was performed with the help of X-ray diffraction, Scanning electron microscopy combined with Energy-dispersive X-ray spectroscopy, and Raman Spectroscopy, while the optical properties were characterized with UV/VIS spectroscopy. The surface morphology of the films was investigated with Atomic Force Microscopy. The conductivity of the composites was checked with a multimeter.

2. Materials and Methods

2.1. Materials and Film Preparation

The reactive solutions were made with just pure analytical reagents and purified water. All reagents were obtained from Sigma-Aldrich and used as received. Only freshly prepared solutions were used for experiments and were not de-aerated during the experiments.

Thin copper selenide films were deposited on a PA sheet (PA 6, Tecamid 6, density 1.13 g/cm^{-3} , thickness $500 \text{ }\mu\text{m}$, surface resistance $\sim 1 \text{ k}\Omega/\text{m}^2$), which was obtained from Ensinger GmbH (Germany). Before the experiments, the PA films were boiled in distilled water for 2 h to remove the remaining unpolymerized monomer residues. Then, they were dried with filter paper and incubated over anhydrous CaCl_2 for 24 h.

The copper sulfate solution (CuSO_4) was used as the cationic solution and the freshly prepared sodium selenosulfate solution (Na_2SeSO_3) was used as the anionic solution for the deposition of a thin film of copper selenide on PA using the SILAR method.

To prepare the Na_2SeSO_3 solution, selenium powder (99% purity) and anhydrous sodium sulfite were dissolved in distilled water for 8 h at $80 \text{ }^\circ\text{C}$ with constant stirring. It was kept for 24 h in a sealed container, to allow undissolved selenium to settle. A clear solution was obtained after it was filtered [34].

In one SILAR cycle, the substrate was immersed separately in solutions of anionic and cationic precursors. The substrate was washed with an ion exchange solution (distilled water) to avoid a homogeneous deposition between each immersion.

Thin copper selenide films on polyamide substrate were grown by repeating these cycles 30 times at different temperatures ($40 \text{ }^\circ\text{C}$, $60 \text{ }^\circ\text{C}$, and $80 \text{ }^\circ\text{C}$). The proposed reaction mechanism of the obtained film could be found in [34].

2.2. Characterization of Copper Selenide Films

X-ray diffraction (XRD) measurements were performed using a Philips PW 1050 diffractometer equipped with a PW 1730 generator, $40 \text{ kV} \times 20 \text{ mA}$, using Ni filtered $\text{Co K}\alpha$ radiation of 0.1778897 nm at room temperature. Measurements were carried out in the 2θ range of 10 to 70° with a scanning step of 0.05° and a scan time of 10 s per step. The experimental values of d (lattice spacing) for copper selenide are determined using the Bragg relation [36]. The average grain size (D) was calculated based on the full width at the half-maximum intensity (FWHM) of the main reflections by applying Scherrer's formula [37,38]. Furthermore, to have more information on the number of defects in the films, the dislocation density (δ) [34] and the strain (ϵ) values were calculated [39].

Scanning electron microscopy (SEM) was performed using a Raith GMBH e-Line instrument equipped with a field emission gun operating at 10 kV accelerating voltage, magnification: $20,000 \times$. A secondary electron signal was used for imaging. Energy-dispersive X-ray spectroscopy (EDX) imaging was performed using QUANTAX EDS with an X-Flash Detector 3001 and ESPRIT software.

The UV/VIS absorbance and diffusion reflectance spectra were recorded in the wavelength range of 200 – 800 nm on a Shimadzu UV-2600 spectrophotometer equipped with an integrated sphere. The diffuse reflectance and absorbance spectra were measured relative to a reference sample of BaSO_4 . The optical band gap from the diffuse reflectance measurements was calculated using the Tauc plot [40,41]. The acquired diffuse reflectance spectra are converted to Kubelka–Munk function [42]. The optical band gap was estimated by extrapolating the linear portion of a plot of $(\alpha h\nu)^2$ versus $h\nu$ to $\alpha = 0$. Using this function, a plot of $(\alpha h\nu)^2$ against $h\nu$ is obtained.

Raman measurements were performed using TriVista 557 micro-Raman system in backscattering configuration, equipped with a nitrogen-cooled CCD detector. The 514.5 nm line of Ar^+/Kr^+ ion laser was used as the excitation source. The measurements were performed with low laser power to prevent a local overheating of the sample.

The surface morphology of copper selenide samples was investigated by atomic force microscopy (AFM). AFM imaging was performed using the NTEGRA Prima system from NT MDT. AFM measurements were performed at room temperature and under ambient

conditions. The AFM topography and phase images were acquired simultaneously using NSG01 probes with a typical resonant frequency of 150 kHz and a 10 nm curvature radius of the tip apex.

The constant current resistivity of the copper selenide films was measured using a multimeter MS8205F (Mastech, Shenzhen, China) with special electrodes. The electrodes were produced from two nickel-plated copper plates with a 1 cm spacing and the dielectric material between them.

3. Results

3.1. XRD Characterization of Copper Selenide Thin Films

The crystal structures and orientations of the thin copper selenide films on the PA substrate were investigated by X-ray diffraction patterns and are shown in Figure 1. The XRD results revealed that all films have a polycrystalline structure.

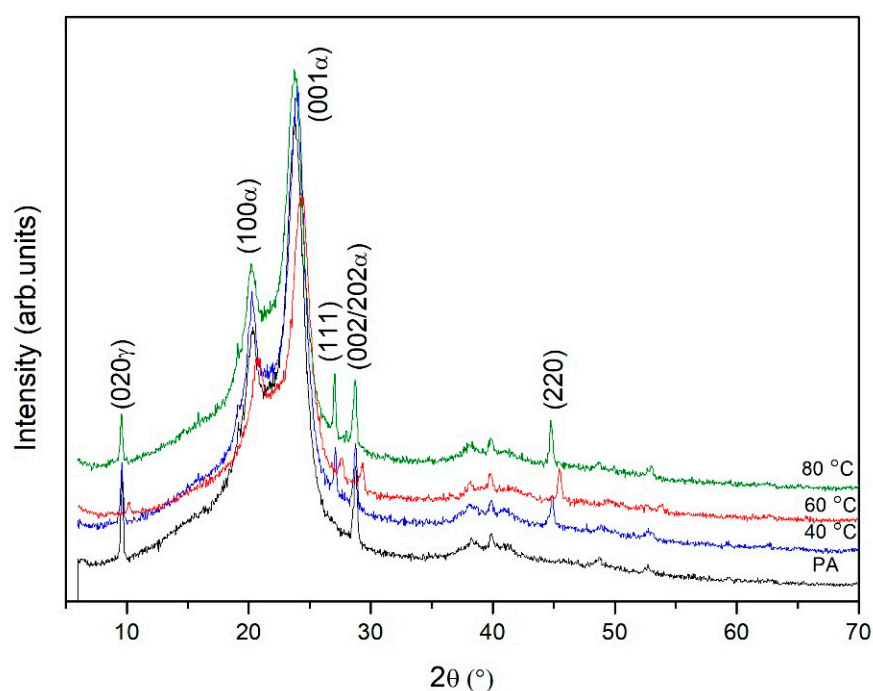


Figure 1. XRD patterns of the initial PA and copper selenide thin films.

Semicrystalline peaks of polyamide were observed between 9° and 30° (in 2θ). These peaks, according to JCPDS 12-923, appear at 20.3° and 23.8° with the corresponding d -spacing of 4.36 and 3.74, respectively. They are attributed to the (100α) and (001α) crystal planes, respectively, showing the presence of a dominant crystalline α -phase [28,43,44]. Two reflections were also observed at around $2\theta = 9.6^\circ$ (020γ) and 28.8° ($002/202\alpha$). XRD analysis showed that the temperature of the solutions of anionic and cationic precursors used in the experiment influenced the composition of the obtained thin films. The X-ray peaks on diffractograms are more intense when the solutions' temperature is higher. The peaks at 28° and 45° are absent in the spectrum of pure PA and they correspond to planes (111) and (220) of a cubic phase of Cu_{2-x}Se Berzelianite (JCPDS 6-680). It is common Cu_{2-x}Se phase [12,15]. The experimental values of the Miller indices d , 2θ and (hkl) of PA and copper selenide thin films are given in Table 1.

Table 1. Values of the Miller indices d , 2θ and (hkl) of PA and copper selenide thin films.

Miller Indices (hkl)		Temperature							
		PA		40 °C		60 °C		80 °C	
		(2 θ)	d (Å)	(2 θ)	d (Å)	(2 θ)	d (Å)	(2 θ)	d (Å)
PA	(020 γ)	9.6	9.21	9.65	9.16	10.2	8.67	9.6	9.21
	(100 α)	20.35	4.36	20.3	4.37	20.95	4.24	20.25	4.38
	(001 α)	23.8	3.74	24	3.70	24.3	3.66	23.75	3.74
Cu _{2-x} Se	(111)	–	–	27.15	3.28	27.7	3.22	27.1	3.28
PA	(002/202 α)	28.75	3.10	28.8	3.10	29.4	3.04	28.75	3.10
Cu _{2-x} Se	(220)	–	–	44.95	2.02	45.5	1.99	44.8	2.02

Changes in the intensities and full width at half maximum (FWHM) values of these peaks were observed with the use of different temperatures of solutions. The intensities of the diffraction peak increased slightly with changing temperature of the solution temperature from 40 to 80 °C. The structural parameters for the (220) peak such as FWHM (β), grain size (D), dislocation density (δ), and strain (ϵ) for all films were evaluated by XRD patterns and presented in Table 2. As shown, grain size increases, while dislocation density and strain decrease with the change in the deposition temperature.

Table 2. Grain size (D), dislocation density (δ), strain (ϵ) and full width at half maximum (FWHM, β) values of copper selenide thin films.

Temperature	2 θ (°)	β (°)	D (nm)	$\delta \cdot 10^{-3}$ (nm ⁻²)	$\epsilon \cdot 10^{-3}$ (nm ⁻²)
40 °C	44.95	1.30	6.61	22.89	13.72
60 °C	45.5	0.60	14.33	4.86	6.25
80 °C	44.8	0.54	15.81	4.00	5.76

These changes can be attributed to the improvement in film crystallization and to the inductive lattice matching, which has a strong impact on structural parameters. The higher values of D , and the smaller β , δ and ϵ values indicate better crystallization of thin films. Regarding the values of D , β , and δ , the best results were obtained for the film made at 80 °C, suggesting that a higher temperature facilitates the crystallization of the film.

3.2. Scanning Electron Microscopy and Energy Dispersive X-ray Analysis

Scanning electron microscopy was used to evaluate the changes in surface morphology of the copper selenide layer on the PA substrate, with the changes in synthesis parameters. The SEM micrographs of the samples are presented on the left-hand side of Figure 2, with a magnification of 20,000 k. The images clearly show that the polymer is well-covered with copper selenide thin films.

Copper selenide grains grow in irregular shapes and sizes. By changing temperature, it could be seen that when the temperature increases, the copper selenide film becomes denser, coated with tightly packed spherical grains that, in turn, were combined into agglomerates of 100 nm to 1 μ m. Micrographs show a compact structure composed of single types of small, densely packed microcrystals. The thin copper selenide films on surface of PA are well dispersed, relatively uniform, and consist of randomly oriented particles. Such morphological forms can produce a very rough surface with high porosity, which leads to increased catalytic activity.

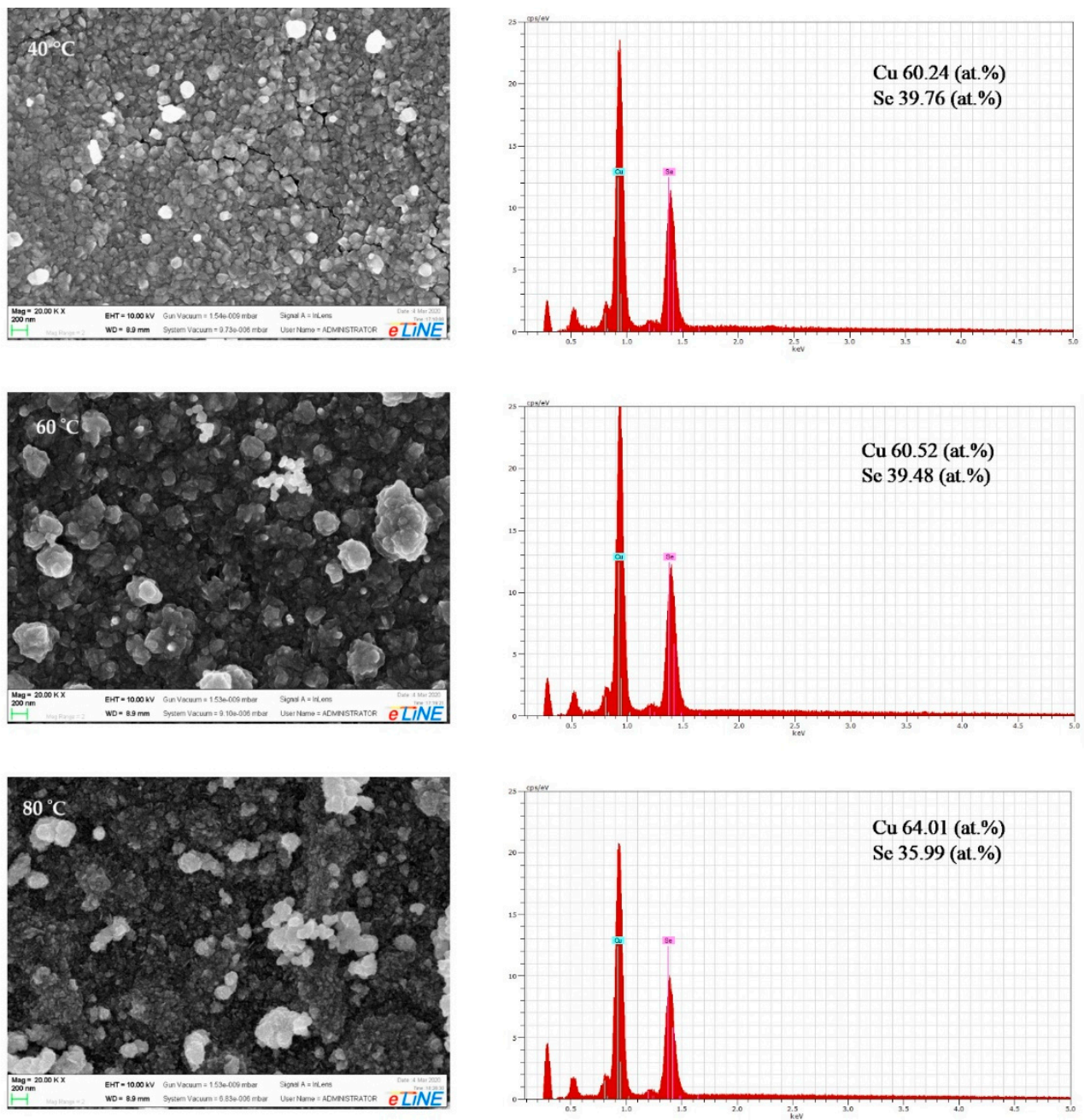


Figure 2. SEM micrographs and EDX spectra of copper selenide/PA thin films.

The elemental analysis of the copper selenide thin films was performed using an EDX micro-analytic unit attached with scanning electron microscopy and shown on the right-hand side of Figure 2. The presence of emission lines in the investigated energy range indicates that copper selenide films were successfully deposited on the polyamide substrates and the expected elements (selenium and copper) were detected. The element analysis revealed the presence of Cu and Se with the average atomic percentages shown on the right side of Figure 2. All films show a higher atomic presence of Cu than Se, which confirms the presence of Cu_{2-x}Se . The Cu/Se ratio measured by EDX analysis was 1.52–1.78, which is in good agreement with the XRD results.

3.3. Measurements of Electrical Resistivity

The resistance of thin films of copper selenide formed on PA plotted in Figure 3 is measured from the close contact up to the 1 cm distance of electrodes, and it includes the contact resistance of the electrode contacts. On the contrary, the pure PA substrate shows no electrical conductivity—the material is a pure insulator.

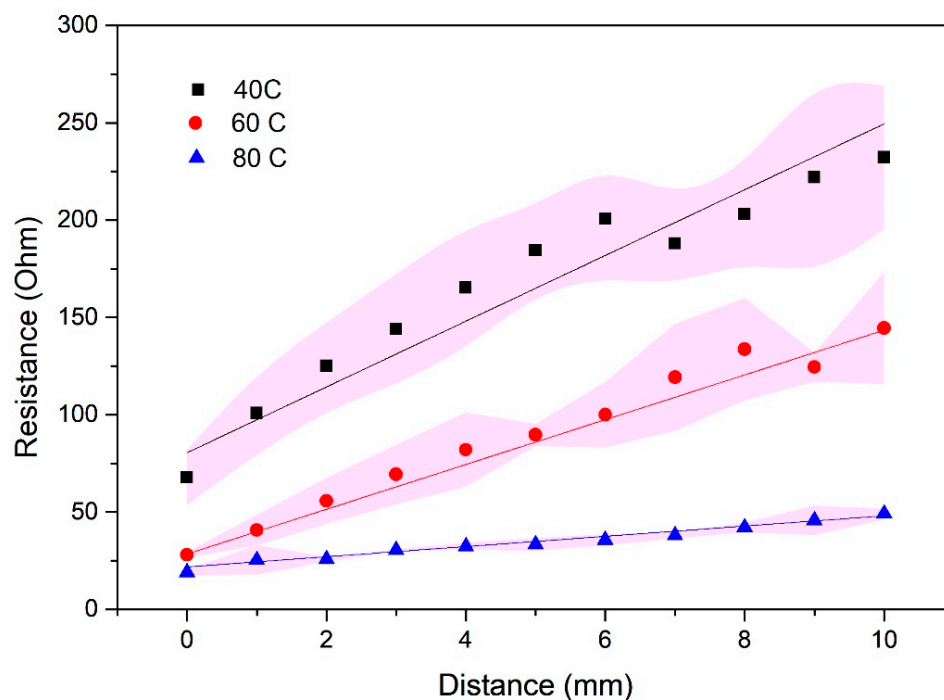


Figure 3. Resistance vs. distance graph for copper selenide films on PA. The results are the averaged values of 4 measurements, and error bars are indicated as the pink area.

At a distance of 1 cm between the electrodes, the resistances of films obtained at 40 °C, 60 °C and 80 °C are 270 Ω, 124 Ω and 49 Ω, while the values for the close contact between the electrodes were obtained to be 50 Ω, 26 Ω and 20 Ω, respectively. The corresponding slopes are 16, 11, and 2.6, which implies that the electrical properties of the film improve with elevating the temperature. Compared to XRD results, the sample obtained at 80 °C has the best crystallinity, which is directly connected with higher conductivity (i.e., lower resistivity). As it can be seen in the graph, the error bar values are minimal for the sample obtained at 80 °C, and they increase with decreasing the temperature.

3.4. Optical Analysis of Copper Selenide Thin Films

The absorbance and diffuse reflectance spectra of thin films of copper selenide on PA in the wavelength range of 200–800 nm are presented in Figure 4. An increase in the absorbance of the copper selenide films is observed with the increased temperature of solutions, as well as the opposite effect of the reflectance.

The determination of band gaps in semiconductors is significant for obtaining basic solid-state physics.

In this study, we used the Tauc plot for the determination of the optical band gap from diffuse reflectance measurements [40–42]. The experimental values of energy gaps for copper selenide thin films are determined to be 2.28 eV for the sample obtained at 80 °C, 2.14 eV for the sample at 60 °C, and 1.98 eV for the sample obtained at 40 °C (Figure 5). This is in good agreement with the values of the reported data [3,5,6].

The obtained band gap values are also consistent with AFM data, according to the rule—the smaller particle size, the bigger the band gap.

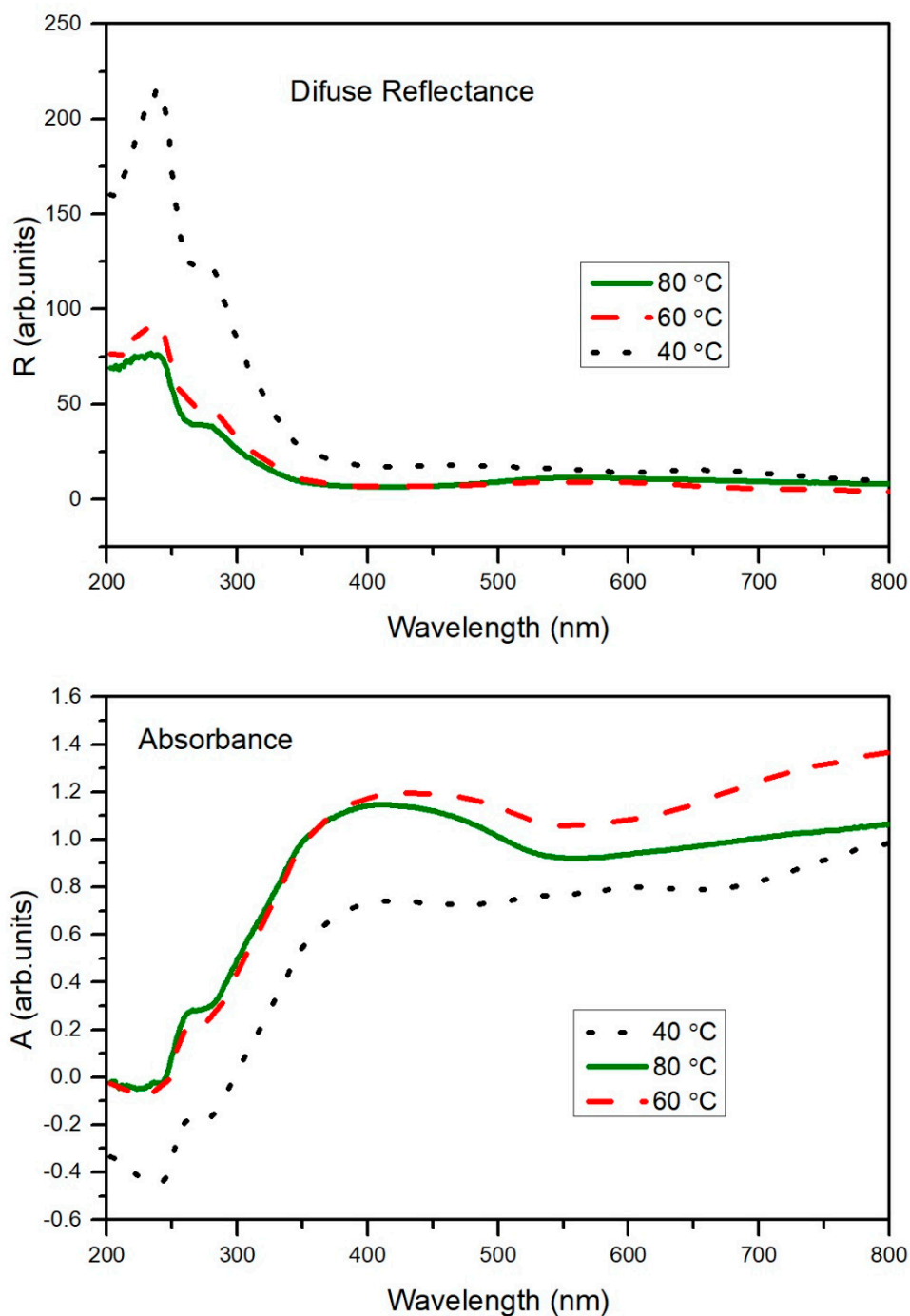


Figure 4. Diffuse reflectance and absorbance spectra of copper selenide/PA thin films.

3.5. Raman Analysis of Copper Selenide Thin Films

Raman spectroscopy is a useful spectroscopic technique for detecting the vibration energy levels of compounds and for further confirming the crystal structure.

Consequently, further clarity on the crystalline phase of the copper selenide thin films was explored by Raman analysis. As shown in Figure 6, the typical Raman spectra of three copper selenide film samples (deposited at different temperatures) exhibit similar peak positions.

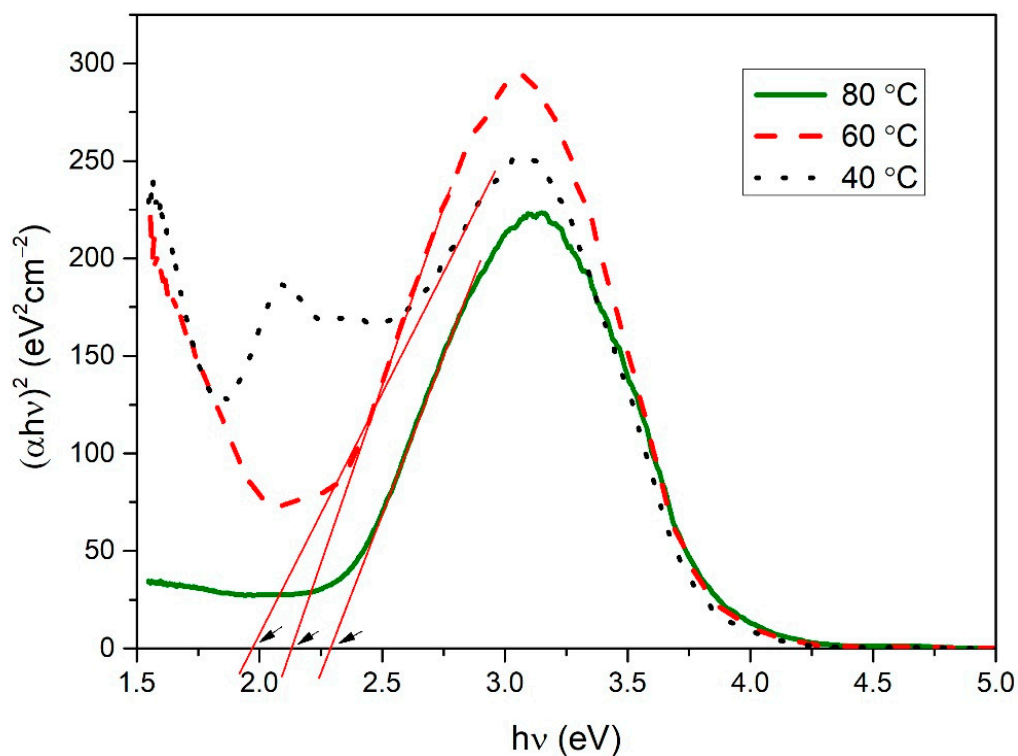


Figure 5. Plots of $(\alpha h\nu)^2$ versus $h\nu$ for copper selenide/PA thin films.

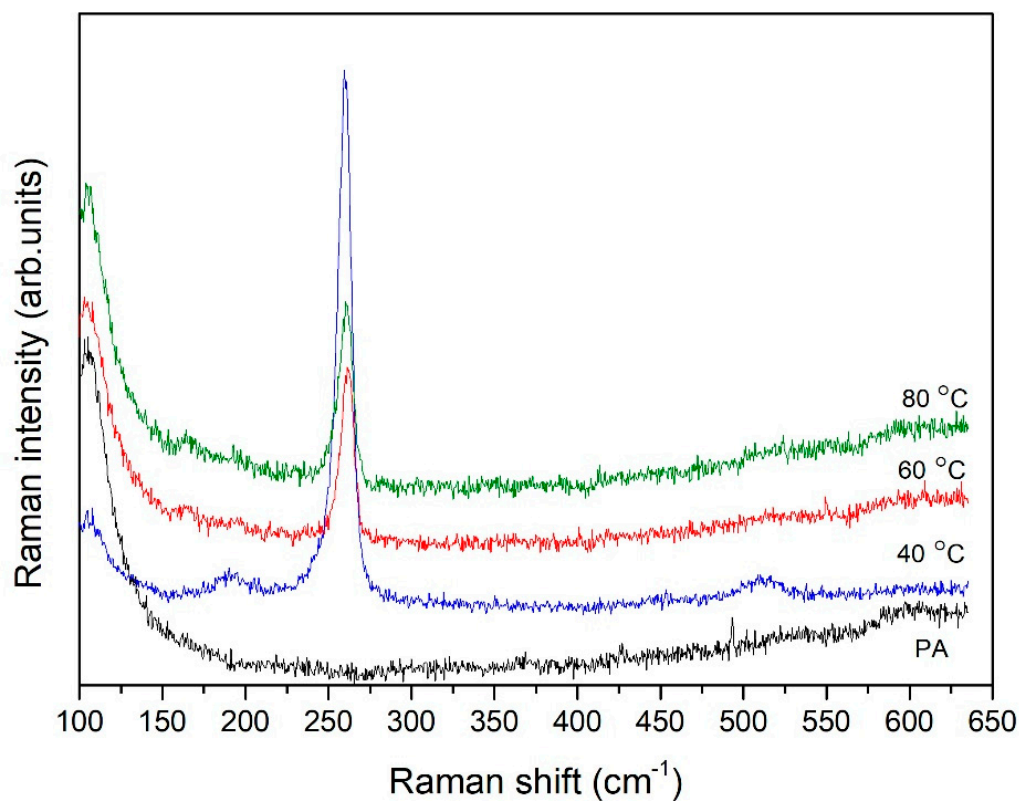


Figure 6. Raman spectra of the copper selenide/PA thin films.

The only strong peak, observed at 260 cm^{-1} , can be assigned to the Se–Se stretching vibration in Cu_{2-x}Se and is consistent with the previous reports [11,45], while the peak at 187 cm^{-1} corresponds to the Cu–Se vibration [46]. The peak at 520 cm^{-1} is the first overtone

of the intensive peak at 260 cm^{-1} . Raman analysis confirms the composition of the copper selenide/PA films. There are no modes of elemental selenium or copper. The background at the beginning of the spectra comes from PA.

3.6. AFM Analysis of Copper Selenide Thin Films

Atomic force microscopy is a very suitable method for visualizing the surface morphology and quantitative analysis of surface roughness. 2D and 3D images, as well as histograms of $5 \times 5\ \mu\text{m}$ areas of copper selenide/PA films, are presented in Figure 7. The height and surface morphology of the copper selenide thin films formed on PA depend on the temperature of the solutions of anionic and cationic precursors used in the experiment: the microstructure of the thin film changes according to the deposition temperature. The surface image shows that the surface of the film is rough with particles gathered into agglomerates. The typical parameters of the quantitative analysis of AFM images are presented in Table 3. With an increase in the precursor solution temperature, the surface roughness decreases and the film becomes more compact and dense. Average roughness is $\sim 194\text{ nm}$ at a precursor solution temperature of $40\text{ }^\circ\text{C}$ and decreases to $\sim 16\text{ nm}$ and $\sim 13\text{ nm}$ in case of the temperature of $60\text{ }^\circ\text{C}$ and $80\text{ }^\circ\text{C}$. As can be seen, a thin film of copper selenide deposited at $80\text{ }^\circ\text{C}$ temperature solution has greater uniformity and homogeneity than other films.

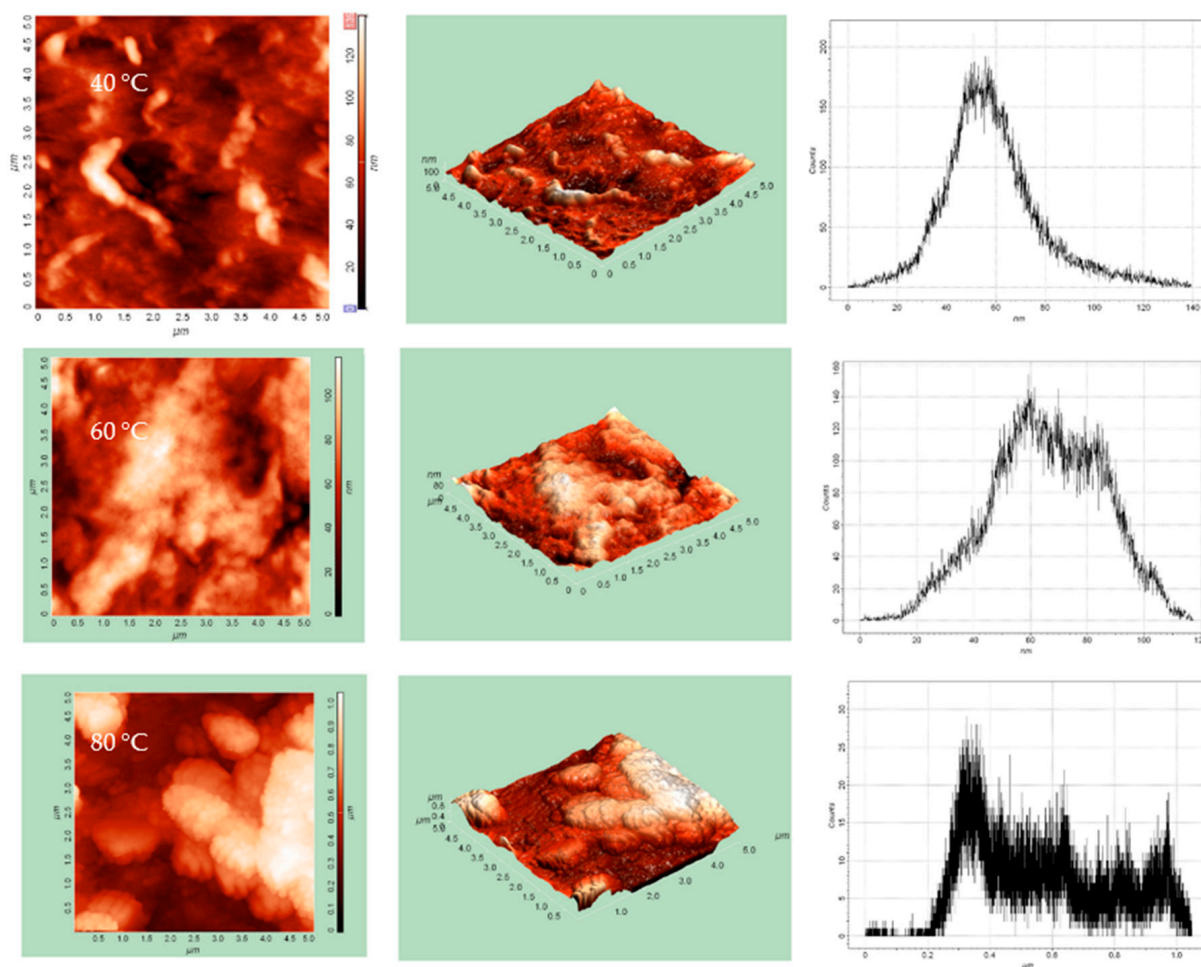


Figure 7. 2D and 3D AFM images and histograms of copper selenide/PA films.

Table 3. Surface roughness parameters of copper selenide thin films.

Parameters	Temperature		
	40 °C	60 °C	80 °C
Maximum height of peaks, h_{max} , nm	1048.41	117.32	123.16
Average height, h_{mean} , nm	565.57	65.64	49.99
Average Roughness, R_a , nm	194.62	16.24	13.32
RMS Roughness, R_q , nm	227.76	19.90	17.21
Surface skewness, R_{sk}	0.42	−0.13	0.58

4. Conclusions

$Cu_{2-x}Se$ thin films can be deposited on a flexible polyamide substrate by using the SILAR method, while by adjusting the temperature of precursor solutions we can affect and tune the optical, structural, and electrical properties of as obtained films. XRD analysis revealed that $Cu_{2-x}Se$ exists in the cubic crystal structure. The band gap energy of $Cu_{2-x}Se$ films was found to be in the order of 1.98–2.28 eV. Raman analysis confirmed the formation of the $Cu_{2-x}Se$ phase (260 cm^{-1}) without any elemental selenium or copper phase. A thin film of copper selenide deposited at 80 °C temperature solution has greater uniformity and homogeneity than other films, the largest grain size, but with the smallest agglomerates, the largest band gap value, and the best conductivity.

Author Contributions: Conceptualization, N.P. and G.J.; methodology, N.P., G.J. and E.P.; validation, M.G., N.P. and G.J.; formal analysis, N.P., G.J. and E.P.; investigation, G.J., J.M., J.C. and U.R.; data curation, M.G., J.C., U.R. and E.G.; writing—original draft preparation, G.J. and N.P.; writing—review and editing, N.P., M.G. and E.P.; visualization, G.J. and E.U.; supervision, N.P. and M.G. All authors have read and agreed to the published version of the manuscript.

Funding: This research received no external funding.

Institutional Review Board Statement: Not applicable.

Informed Consent Statement: Not applicable.

Data Availability Statement: Not applicable.

Conflicts of Interest: The authors declare no conflict of interest.

References

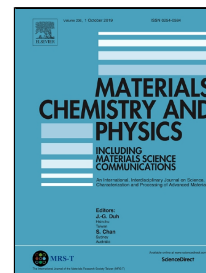
- García, V.M.; Nair, P.K.; Nair, M.T.S. Copper Selenide Thin Films by Chemical Bath Deposition. *J. Cryst. Growth* **1999**, *203*, 113–124. [[CrossRef](#)]
- Tyagi, K.; Gahtori, B.; Bathula, S.; Jayasimhadri, M.; Singh, N.K.; Sharma, S.; Haranath, D.; Srivastava, A.K.; Dhar, A. Enhanced Thermoelectric Performance of Spark Plasma Sintered Copper-Deficient Nanostructured Copper Selenide. *J. Phys. Chem. Solids* **2015**, *81*, 100–105. [[CrossRef](#)]
- Thirumavalavan, S.; Mani, K.; Sagadevan, S. Investigation of the Structural, Optical and Electrical Properties of Copper Selenide Thin Films. *Mater. Res.* **2015**, *18*, 1000–1007. [[CrossRef](#)]
- Zhao, L.; Wang, X.; Yun, F.F.; Wang, J.; Cheng, Z.; Dou, S.; Wang, J.; Snyder, G.J. The Effects of Te^{2-} and I^- Substitutions on the Electronic Structures, Thermoelectric Performance, and Hardness in Melt-Quenched Highly Dense $Cu_{2-x}Se$. *Wiley Online Libr.* **2015**, *1*, 1400015. [[CrossRef](#)]
- Hussain, R.A.; Hussain, I. Copper Selenide Thin Films from Growth to Applications. *Solid State Sci.* **2020**, *100*, 106101. [[CrossRef](#)]
- Hankare, P.P.; Khomane, A.S.; Chate, P.A.; Rathod, K.C.; Garadkar, K.M. Preparation of Copper Selenide Thin Films by Simple Chemical Route at Low Temperature and Their Characterization. *J. Alloy. Compd.* **2009**, *469*, 478–482. [[CrossRef](#)]
- Silva, S.F.C.; Zanatta, B.S.; Rabelo, A.C.; Bottecchia, O.L.; Tozoni, J.R.; Oliveira, O.N.; Marletta, A. Flexible and Transparent Electrodes of $Cu_{2-x}Se$ with Charge Transport via Direct Tunneling Effect. *Adv. Electron. Mater.* **2021**, *7*, 2001189. [[CrossRef](#)]
- Zyoud, A.; Murtada, K.; Kwon, H.; Choi, H.J.; Kim, T.W.; Helal, M.H.S.; Faroun, M.; Bsharat, H.; Park, D.H.; Hilal, H.S. Copper Selenide Film Electrodes Prepared by Combined Electrochemical/Chemical Bath Depositions with High Photo-Electrochemical Conversion Efficiency and Stability. *Solid State Sci.* **2018**, *75*, 53–62. [[CrossRef](#)]
- Kalenga, M.P.; Govindraju, S.; Airo, M.; Moloto, M.J.; Sikhwivhilu, L.M.; Moloto, N. Fabrication of a Schottky Device Using CuSe Nanoparticles: Colloidal versus Microwave Digestive Synthesis. *J. Nanosci. Nanotechnol.* **2015**, *15*, 4480–4486. [[CrossRef](#)]
- Singh, S.C.; Li, H.; Yao, C.; Zhan, Z.; Yu, W.; Yu, Z.; Guo, C. Structural and Compositional Control in Copper Selenide Nanocrystals for Light-Induced Self-Repairable Electrodes. *Nano Energy* **2018**, *51*, 774–785. [[CrossRef](#)]

11. Xu, J.; Yang, Q.; Kang, W.; Huang, X.; Wu, C.; Wang, L.; Luo, L.; Zhang, W.; Lee, C.S. Water Evaporation Induced Conversion of CuSe Nanoflakes to Cu_{2-x}Se Hierarchical Columnar Superstructures for High-Performance Solar Cell Applications. *Part. Part. Syst. Charact.* **2015**, *32*, 840–847. [[CrossRef](#)]
12. Zhou, R.; Huang, Y.; Zhou, J.; Niu, H.; Wan, L.; Li, Y.; Xu, J.; Xu, J. Copper Selenide (Cu₃Se₂ and Cu_{2-x}Se) Thin Films: Electrochemical Deposition and Electrocatalytic Application in Quantum Dot-Sensitized Solar Cells. *Dalton Trans.* **2018**, *47*, 16587. [[CrossRef](#)] [[PubMed](#)]
13. Zhang, H.; Xia, Y. Ratiometry, Wavelength, and Intensity: Triple Signal Readout for Colorimetric Sensing of Mercury Ions by Plasmonic Cu_{2-x}Se Nanoparticles. *ACS Sens.* **2016**, *1*, 384–391. [[CrossRef](#)]
14. Wang, Z.; Peng, F.; Wu, Y.; Yang, L.; Zhang, F.; Huang, J. Template Synthesis of Cu_{2-x}Se Nanoboxes and Their Gas Sensing Properties. *Cryst. Eng. Comm.* **2012**, *14*, 3528–3533. [[CrossRef](#)]
15. Astam, A.; Akaltun, Y.; Yildirim, M. Conversion of SILAR Deposited Cu₃Se₂ Thin Films to Cu_{2-x}Se by Annealing. *Mater. Lett.* **2016**, *166*, 9–11. [[CrossRef](#)]
16. Bhuse, V.M.; Hankare, P.P.; Garadkar, K.M.; Khomane, A.S. A Simple, Convenient, Low Temperature Route to Grow Polycrystalline Copper Selenide Thin Films. *Mater. Chem. Phys.* **2003**, *80*, 82–88. [[CrossRef](#)]
17. Li, X.; Li, P.; Wu, Z.; Luo, D.; Yu, H.-Y.; Lu, Z.-H. Review and Perspective of Materials for Flexible Solar Cells. *Mater. Rep. Energy* **2021**, *1*, 100001. [[CrossRef](#)]
18. Yoon, H.; Kang, S.M.; Lee, J.K.; Choi, M. Hysteresis-Free Low-Temperature-Processed Planar Perovskite Solar Cells with 19.1% Efficiency. *Energy Environ. Sci.* **2016**, *9*, 2262–2266. [[CrossRef](#)]
19. Aernouts, T.; Vanlaeke, P.; Geens, W.; Poortmans, J.; Heremans, P.; Borghs, S.; Mertens, R.; Andriessen, R.; Leenders, L. Printable Anodes for Flexible Organic Solar Cell Modules. *Thin Solid Film.* **2004**, *451–452*, 22–25. [[CrossRef](#)]
20. Fonrodona, M.; Escarré, J.; Villar, F.; Soler, D.; Asensi, J.M.; Bertomeu, J.; Andreu, J. PEN as Substrate for New Solar Cell Technologies. *Sol. Energy Mater. Sol. Cells* **2005**, *89*, 37–47. [[CrossRef](#)]
21. Chen, H.; Gu, Z.G.; Zhang, J. Chiral-Induced Ultrathin Covalent Organic Frameworks Nanosheets with Tunable Circularly Polarized Luminescence. *J. Am. Chem. Soc.* **2022**, *144*, 7245–7252. [[CrossRef](#)] [[PubMed](#)]
22. Hassan, M.; Abbas, G.; Li, N.; Afzal, A.; Haider, Z.; Ahmed, S.; Xu, X.; Pan, C.; Peng, Z. Significance of Flexible Substrates for Wearable and Implantable Devices: Recent Advances and Perspectives. *Adv. Mater. Technol.* **2022**, *7*, 2100773. [[CrossRef](#)]
23. Wang, K.; Cheng, S.; Hu, Q.; Yu, F.; Cheng, Y.; Huang, K.; Yuan, H.; Jiang, J.; Li, W.; Li, J.; et al. Vertical Graphene-Coated Cu Wire for Enhanced Tolerance to High Current Density in Power Transmission. *Nano Res.* **2021**, *14*, 1–7. [[CrossRef](#)]
24. Chen, Y.; Gao, C.; Yang, T.; Li, W.; Xu, H.; Sun, Z.; Chen, Y.; Gao, C.; Yang, T.; Li, W.; et al. Research Advances of Ferroelectric Semiconductors of 2D Hybrid Perovskites toward Photoelectronic Applications. *Chin. J. Struct. Chem.* **2022**, *41*, 2204001–2204011. [[CrossRef](#)]
25. Chang, H.B.; Liu, J.B.; Dong, Z.; Wang, D.D.; Xin, Y.; Jiang, Z.L.; Tang, S.S. Enhancement of Photocatalytic Degradation of Polyvinyl Chloride Plastic with Fe₂O₃ Modified AgNbO₃ Photocatalyst under Visible-Light Irradiation. *Jiegou Huaxue* **2021**, *40*, 1595–1603. [[CrossRef](#)]
26. Vikulov, S.; di Stasio, F.; Ceseracciu, L.; Saldanha, P.L.; Scarpellini, A.; Dang, Z.; Krahne, R.; Manna, L.; Lesnyak, V. Fully Solution-Processed Conductive Films Based on Colloidal Copper Selenide Nanosheets for Flexible Electronics. *Adv. Funct. Mater.* **2016**, *26*, 3670–3677. [[CrossRef](#)]
27. Qu, C.; Hu, J.; Liu, X.; Li, Z.; Ding, Y. Morphology and Mechanical Properties of Polyimide Films: The Effects of UV Irradiation on Microscale Surface. *Materials* **2017**, *10*, 1329. [[CrossRef](#)]
28. Parodi, E.; Peters, G.W.M.; Govaert, L.E. Structure-Properties Relations for Polyamide 6, Part 1: Influence of the Thermal History during Compression Moulding on Deformation and Failure Kinetics. *Polymers* **2018**, *10*, 710. [[CrossRef](#)]
29. Janickis, V.; Petraškauskienė, N.; Žalėnkiene, S.; Morkvenaite-Vilkociene, I.; Ramanavicius, A. Morphology of CdSe-Based Coatings Formed on Polyamide Substrate. *J. Nanosci. Nanotechnol.* **2018**, *18*, 604–613. [[CrossRef](#)]
30. Ivanauskas, R.; Milasiene, D. Fabrication of Polyamide-Ag₂Se Composite Films with Controllable Properties by an Adsorption–Diffusion Method. *J. Phys. Chem. Solids* **2020**, *145*, 109533. [[CrossRef](#)]
31. Lakshmi, M.; Bindu, K.; Bini, S.; Vijayakumar, K.P.; Sudha Kartha, C.; Abe, T.; Kashiwaba, Y. Chemical Bath Deposition of Different Phases of Copper Selenide Thin Films by Controlling Bath Parameters. *Thin Solid Film.* **2000**, *370*, 89–95. [[CrossRef](#)]
32. Xu, S.; Wang, H.; Zhu, J.J.; Chen, H.Y. Sonochemical Synthesis of Copper Selenides Nanocrystals with Different Phases. *J. Cryst. Growth* **2002**, *234*, 263–266. [[CrossRef](#)]
33. Li, Y.D.; Fan, P.; Zheng, Z.H.; Luo, J.T.; Liang, G.X.; Guo, S.Z. The Influence of Heat Treatments on the Thermoelectric Properties of Copper Selenide Thin Films Prepared by Ion Beam Sputtering Deposition. *J. Alloy. Compd.* **2016**, *658*, 880–884. [[CrossRef](#)]
34. Güzeldir, B.; Sağlam, M. Using Different Chemical Methods for Deposition of Copper Selenide Thin Films and Comparison of Their Characterization. *Spectrochim. Acta Part A Mol. Biomol. Spectrosc.* **2015**, *150*, 111–119. [[CrossRef](#)]
35. Pathan, H.M.; Lokhande, C.D. Deposition of Metal Chalcogenide Thin Films by Successive Ionic Layer Adsorption and Reaction (SILAR) Method. *Bull. Mater. Sci.* **2004**, *27*, 85–111. [[CrossRef](#)]
36. Bragg, W.H.; Bragg, W.L.; Bragg, B.W.; Professor of Physics, C. The Reflection of X-Rays by Crystals. *Proc. R. Soc. London. Ser. A Contain. Pap. A Math. Phys. Character* **1913**, *88*, 428–438. [[CrossRef](#)]
37. Patterson, A.L. The Scherrer Formula for X-Ray Particle Size Determination. *Phys. Rev.* **1939**, *56*, 978. [[CrossRef](#)]

38. Nath, D.; Singh, F.; Das, R. X-Ray Diffraction Analysis by Williamson-Hall, Halder-Wagner and Size-Strain Plot Methods of CdSe Nanoparticles—A Comparative Study. *Mater. Chem. Phys.* **2020**, *239*, 122021. [[CrossRef](#)]
39. Ashraf, M.; Akhtar, S.M.J.; Khan, A.F.; Ali, Z.; Qayyum, A. Effect of Annealing on Structural and Optoelectronic Properties of Nanostructured ZnSe Thin Films. *J. Alloy. Compd.* **2011**, *509*, 2414–2419. [[CrossRef](#)]
40. Tauc, J.; Grigorovici, R.; Vancu, A. Optical Properties and Electronic Structure of Amorphous Germanium. *Phys. Status Solidi (B)* **1966**, *15*, 627–637. [[CrossRef](#)]
41. Makuła, P.; Pacia, M.; Macyk, W. How To Correctly Determine the Band Gap Energy of Modified Semiconductor Photocatalysts Based on UV-Vis Spectra. *J. Phys. Chem. Lett.* **2018**, *9*, 6814–6817. [[CrossRef](#)] [[PubMed](#)]
42. Petrović, M.; Gilić, M.; Ćirković, J.; Romčević, M.; Romčević, N.; Trajić, J.; Yahia, I. Optical Properties of CuSe Thin Films—Band Gap Determination. *Sci. Sinter.* **2017**, *49*, 167–174. [[CrossRef](#)]
43. Banerjee, S.S.; Janke, A.; Gohs, U.; Heinrich, G. Electron-Induced Reactive Processing of Polyamide 6/Polypropylene Blends: Morphology and Properties. *Eur. Polym. J.* **2018**, *98*, 295–301. [[CrossRef](#)]
44. Zhao, X.Y.; Zhang, B.Z. The Effects of Annealing (Solid and Melt) on the Time Evolution of the Polymorphic Structure of Polyamide 6. *J. Appl. Polym. Sci.* **2010**, *115*, 1688–1694. [[CrossRef](#)]
45. Minceva-Sukarova, B.; Najdoski, M.; Grozdanov, I.; Chunnillal, C.J. Raman Spectra of Thin Solid Films of Some Metal Sulfides. *J. Mol. Struct.* **1997**, *410–411*, 267–270. [[CrossRef](#)]
46. Malavekar, D.B.; Bulakhe, R.N.; Kale, S.B.; Patil, U.M.; In, I.; Lokhande, C.D. Synthesis of Layered Copper Selenide on Reduced Graphene Oxide Sheets via SILAR Method for Flexible Asymmetric Solid-State Supercapacitor. *J. Alloy. Compd.* **2021**, *869*, 159198. [[CrossRef](#)]

Journal Pre-proof

Composition, Structure and Potential Energy Application of Nitrogen Doped Carbon Cryogels



Ana Kalijadis, Nemanja Gavrilov, Bojan Jokić, Martina Gilić, Aleksandar Krstić, Igor Pašti, Biljana Babić

PII: S0254-0584(19)30937-X
DOI: <https://doi.org/10.1016/j.matchemphys.2019.122120>
Article Number: 122120
Reference: MAC 122120
To appear in: *Materials Chemistry and Physics*
Received Date: 23 May 2019
Accepted Date: 31 August 2019

Please cite this article as: Ana Kalijadis, Nemanja Gavrilov, Bojan Jokić, Martina Gilić, Aleksandar Krstić, Igor Pašti, Biljana Babić, Composition, Structure and Potential Energy Application of Nitrogen Doped Carbon Cryogels, *Materials Chemistry and Physics* (2019), <https://doi.org/10.1016/j.matchemphys.2019.122120>

This is a PDF file of an article that has undergone enhancements after acceptance, such as the addition of a cover page and metadata, and formatting for readability, but it is not yet the definitive version of record. This version will undergo additional copyediting, typesetting and review before it is published in its final form, but we are providing this version to give early visibility of the article. Please note that, during the production process, errors may be discovered which could affect the content, and all legal disclaimers that apply to the journal pertain.

© 2019 Published by Elsevier.

Composition, Structure and Potential Energy Application of Nitrogen Doped Carbon Cryogels

*Ana Kalijadis*¹, Nemanja Gavrilov², Bojan Jokić³, Martina Gilić⁴, Aleksandar Krstić¹, Igor Pašti², Biljana Babić⁴,*

*¹Vinča Institute of Nuclear Sciences, University of Belgrade, Mike Petrovića Alasa 12-14,
11351 Belgrade, Serbia*

*²Faculty of Physical Chemistry, University of Belgrade, Studentski trg 12-16, 11158
Belgrade, Serbia.*

*³Faculty of Technology and Metallurgy, University of Belgrade, Karnegijeva 4, 11000
Belgrade, Serbia*

*⁴Institute of Physics Belgrade, University of Belgrade, Pregrevica 118, 11000 Belgrade,
Serbia*

Abstract

Resorcinol–formaldehyde (RF) cryogels were synthesized by sol–gel polycondensation of resorcinol with formaldehyde and freeze-drying was carried out with t-butanol. Carbon cryogel (CC) was obtained by pyrolyzing RF cryogels in an inert atmosphere to 950 °C. Nitrogen doped CCs (CCN) were synthesized by introducing melamine into RF precursor mixture solution to obtain nitrogen concentration 2, 6 and 10 wt. %. Material was characterized by elemental analysis, nitrogen adsorption– desorption measurements, scanning electron microscopy (SEM), Raman spectroscopy, FT-IR Spectroscopy. Cyclic voltammetry

* Corresponding author. Fax: + 381 11 3408224

E-mail address: anautovicic@vinca.rs (A. Kalijadis).

(CV) was used to investigate capacitive and electrocatalytic properties. Conductivity measurement was also performed. Elemental analysis results confirmed presence of nitrogen in CCN samples in the range from 0.45 to 1.15 wt.%. Raman spectroscopy of the samples showed increase of D and G peak integrated intensity ratio (I_D/I_G) with nitrogen doping suggesting that the structural disorder as well as edge plane density increase, but according to similar I_D/I_G values for CCN samples, their share is not directly related to the amount of incorporated N. Characterization by nitrogen adsorption showed that overall specific surface and maximum mesopores are achieved in CCN sample with medium nitrogen concentration. Results of cyclic voltammetry experiments demonstrated maximum capacitance for CCN sample with smallest N wt.% indicating that narrow pore size distribution and high specific surface area are dominant factors to achieve good capacitive behavior. The relatively low doping level of nitrogen reached in CCN samples may be the reason for the incomplete reduction of oxygen to hydroxide and furthermore it turned out that presence of N in the structure of CC had a negligible effect on the otherwise relatively high conductivity of CC.

Keywords: Carbon cryogel; Nitrogen doping; Structure; Porosity; Energy application

1. Introduction

Carbon aerogels, cryogels and xerogels are carbon materials which are usually obtained from the sol–gel polycondensation of organic compounds, followed by drying, and subsequent pyrolysis at an elevated temperature (ca. 1050 °C) in an inert atmosphere. In 1989, Pekala firstly described procedure for the preparation of the organic gels by polycondensation of resorcinol (R) and formaldehyde (F) in water solutions, in the presence of sodium carbonate (C) as basic catalyst [1, 2]. Drying of wet RF gels can be provided by supercritical drying (aerogels), freeze drying (cryogels) and conventional evaporation of the solvent at atmospheric conditions (xerogels). Supercritical drying or freeze drying is used in order to keep the porous structure of RF gels. Following the procedure recommended by Tamon and co-workers [3, 4], we developed a synthesis procedure for the carbon cryogels (CC) with a tortuous open-cell structure, ultrafine particle (cell) and pore size (<50 nm), and high surface area (400–1000 m² g⁻¹) [5]. The resulting materials are nanostructured sp² carbons with good electrical conductivity, environmental compatibility and chemical inertness. These unique properties make them promising materials for applications such as electrodes, adsorbents, catalyst supports, hydrogen storage, supercapacitors or for solar applications [6-10]. Previously, we used carbon cryogels for removal of ionic species from water [11] and as a catalyst support [12, 13].

Design of carbon materials properties and their precise control are essential if the aim is to improve and extend their application. For instance, optimization of the morphology and structure as well as direct introduction of porosity to enlarge the share of edge sites are proven to be important for adsorption and electrochemical applications of carbon materials. Many studies have shown that heteroatom doping (e.g., boron, sulfur, phosphorous, and nitrogen) of sp² carbon materials could influence their physicochemical properties as well as electrical conductivity and electrochemical properties [14-18]. Nitrogen doping has a significant

influence on the electronic structure and chemical properties of carbon materials due to its comparable atomic size and five valence electrons available to form strong valence bonds with carbon atoms [19]. Nitrogen species in the carbon materials can not only act as an electron donor, but also introduce functional groups containing nitrogen and oxygen atoms [20, 21]. A previously theoretical study has shown that nitrogen incorporation in carbon structure results in the higher positive charge on a carbon atom adjacent to the nitrogen atoms [22], and a positive shift of Fermi energy at the apex of the Brillouin zone of graphene [23]. Also, it is mainly believed that lone-pair of electrons of nitrogen can infuse an additional negative charge in to the graphene π electron system which leads to an enhanced conductive behavior along with stronger interaction with foreign molecules (i.e. ions, acidic compounds). [24, 25].

Substitutionally incorporated nitrogen has received focused attention because of significant changes in hardness, electrical conductivity, and chemical reactivity, which have been theoretically predicted and experimentally observed [25-28]. It is well known that N-doped carbon materials work well as the support for Pt catalysis by resulting in the improvement of Pt nanoparticle dispersion in terms of catalytic activity and durability [29]. Many authors reported that N-doping improved the activity and performance of different carbon materials (GO foams, single-wall carbon nanohorns, various porous carbons and commercially carbon black) as the electrode for fuel cells [30-34]. Incorporation of N into structurally and porously different carbon materials improved the cycling performance of Li-S batteries [35- 37].

Different types of carbon gels produced using Pekala's method have been mostly used in adsorption and energy storage and due to their versatility in terms of surface area, pore texture and surface chemistry they have got a considerable attention among the researchers now a day. It was shown that N doping improved catalytic and adsorption properties of

modified carbon xerogels [24, 38–40]. Enhancing the adsorption properties is related to nitrogen functional groups introduction on carbon xerogels surface which are responsible for the increase of surface basicity and hydrophilicity. Nitrogen-doped (1.2–4.5 wt%) carbon xerogels synthesized in an ammonia atmosphere showed good performances for hydrogen storage and strong correlation was observed between hydrogen uptakes and N/C ratio [41]. A chitosan based nitrogen doped carbon cryogel shows significantly enhanced performance as supercapacitor and lithium ion battery electrodes in terms of capacity and rate capability due to its quasi two-dimensional structure with reduced thickness [42].

Although many studies have evaluated the relation between N content, structure and property of N-doped carbons, the influence of nitrogen doping on final physicochemical properties has not been fully delineated. The reason for that lay in the fact that family of carbon materials is very reach with different variation of structural, textural and morphological properties which makes comparison of the effects induced by N doping quite difficult. Also, utilization of different doping methods combined with the effects of a different nitrogen source can modify physicochemical properties of the resulting doped carbon in many various and unexpected ways [15-18]. Therefore, nitrogen doping of carbon materials should be considered as non-straightforward process which success, as well as the final concentration of incorporated nitrogen, strongly depends on the type of carbon material, doping method and selected chemical taken as a nitrogen source. Among different carbon materials, CC is material that has good characteristics for application in the field of energy conversion, intensely developed porous structure, chemical inertness and electrical conductivity. In accordance to that, the aims of this work were to determine the extent to which nitrogen can be incorporated in CC structure, by adding N-containing compound into resorcinol - formaldehyde mixture and to examine influence of incorporated N on CC's characteristics and its potential energy application. In particular, possible use of these materials for charge

storage and electrocatalysis of oxygen reduction reaction (ORR) is addressed. Nitrogen doped CC samples were synthesized by introducing melamine into precursor mixture to obtain nitrogen concentration of 2, 6 and 10 wt. %. The efficiency of nitrogen incorporation studied by various characterization techniques: scanning electron microscopy (SEM), nitrogen adsorption– desorption measurements, Raman spectroscopy, as well as electrocatalytic, capacitance and conductivity measurements.

2. Material and methods

2.1. Sample preparation and characterization

Carbon cryogel (CC) was synthesized by the method previously described by Babic et al. [5]. Briefly, it is a polycondensation reaction of resorcinol (R) with formaldehyde (F) in water solution with sodium carbonate as a basic catalyst, followed by freeze-drying and carbonization in the inert atmosphere at 900 °C. Melamine (Sigma-Aldrich, St. Louise, MO, USA) was used as a source of nitrogen and it was added to the precursor solution to obtain nitrogen concentration of 2, 6, and 10 wt. %. The very important step prior to drying is rinsing of RF gels in t-butanol (99.5 %, Acros Organics, USA) so that water solvent could be replaced with organic one which does not exhibit significant changes in the volume of solvent during the freezing process. After that all synthesized R-F gels were pre-frozen at -30 °C and then freeze dried for 24 h under vacuum (0.4 mbar). N doped CC samples were marked as CCN₁, CCN₂ and CCN₃ (subscripts 1, 2 and 3 denote nominal nitrogen content in the precursor solution of 2, 6 and 10 wt.%).

The LECO Elemental Analyzer CHNS-628 Model was used for the elemental analysis of CC samples.

The morphology of samples has been investigated by SEM using high resolution electron microscope MIRA3 FEG-SEM, Tescan at accelerating voltage lower than 29 kV.

The micro-Raman spectra were taken in backscattering configuration and analyzed by TriVista 557 spectrometer, equipped with the nitrogen cooled charged-coupled-device detector. As an excitation source, the 532 nm line of Ti: Sapphire laser was used, with the laser power 50 mW. In order to analyze changes in bonding structure deconvolution of spectra was performed using Gaussian fitting.

The specific surface area and the pore size distribution (PSD) of carbon cryogel samples doped with different amount of nitrogen were analyzed using the Surfer (Thermo Fisher Scientific, USA). PSD was estimated by applying BJH method [43] to the desorption branch of isotherms and mesopore surface and micropore volume were estimated using the t-plot method [44].

Analyses of surface oxygen groups were performed by Fourier Transform Infrared (FT-IR) Spectroscopy (Bomem MB-Series, Hartmann & Braun).

2.2. Electrochemical measurements and electrode preparation

Carbon sample quantity, measuring 5.0 mg, was suspended in 1 cm³ 40 v/v% ethanol/water solution, followed by 15 minute homogenization in an ultrasonic bath. Droplet of the catalytic ink was transferred onto the glassy carbon (GC) disk electrode (cross-section surface – 0.196 cm²) and dried under N₂ flow to obtain overall loading of the catalyst was 250 μg cm⁻² per geometric surface area. Upon drying, the surface was covered with 10 μL of 0.05 wt% Nafion in ethanol to ensure the integrity of the thin film during electrochemical testing. The solvent was removed by evaporation.

Cyclic voltammetry (CV) was used to investigate electrocatalytic and capacitive properties of doped carbons in a conventional one compartment three-electrode electrochemical cell with wide Pt foil serving as a counter electrode and a saturated calomel electrode (SCE) as a reference electrode. The capacitive performance was trialed in 3M KOH solution while electrocatalytic activity toward ORR was investigated in oxygen saturated 0.1

mol dm⁻³ KOH aqueous solution using rotating disk electrode (RDE) voltammetry.

Measurements were done using Gamry PCI4/750 Potentiostat/Galvanostat equipped with a Pine rotator. Before and during the capacitive measurements, a gentle gas flow of N₂ was kept just beneath the electrolyte surface while ORR was tested in O₂ purged solution (purity 99.9995 vol%) at room temperature (25.0±0.5 °C). Reported current densities are evaluated with respect to the geometrical cross-section area of the supporting GC disk.

Conductivity was measured on GW instek LCR-6100 with carbon samples pressed into a pellet under 2t pressure at 1000 Hz.

3. Results and Discussion

Results obtained by elemental analysis confirmed presence of nitrogen in CCN samples (Table 1). Adding melamine to precursors solution resulted in the incorporation of nitrogen in the wt.% range from 0.45 to 1.15. The reason for such low content of incorporated N in doped carbon cryogels is presumably due to processes that take place during carbonization. Namely, during carbonization, within formation of porous structure occurs, the majority of N species localized on the surface or near surface of R-F gels burn off and as a consequence of that after carbonization process only nitrogen from the bulk remains in final doped CC samples. A similar phenomenon was observed by Wu et al. [45].

The morphology of the resulting CC samples was characterized by scanning electron microscopy. Fig. 1 shows SEM images of the CC and CCN samples. It is evident that the all 4 presented materials are porous, but the pore size and shape are irregular for each sample. It can be noted that presence of N in CC structure (Fig. b-d) affects the porosity of CCN samples compare to CC to a considerable extent. It seems that nitrogen has direct impact to specific surface area development. Further characterization by nitrogen adsorption gave a

better insight into the changes of the specific surface area and porosity induced by N incorporation into CC structure.

Table 1. Elemental analysis results and calculated intensity ratio I_D/I_G for CC, CCN₁, CCN₂, and CCN₃ samples.

Sample	[C] ^a (wt.%)	[N] ^a (wt.%)	[O] ^b (wt.%)	[H] ^a (wt.%)	I_D/I_G
CC	88.47	0.00	10.04	1.49	0.9
CCN ₁	84.85	0.45	12.80	1.90	1.1
CCN ₂	81.58	0.72	15.82	1.88	1.2
CCN ₃	82.44	1.15	14.72	1.69	1.2

^aMeasured by combustion element analyses, ^bCalculated by the difference

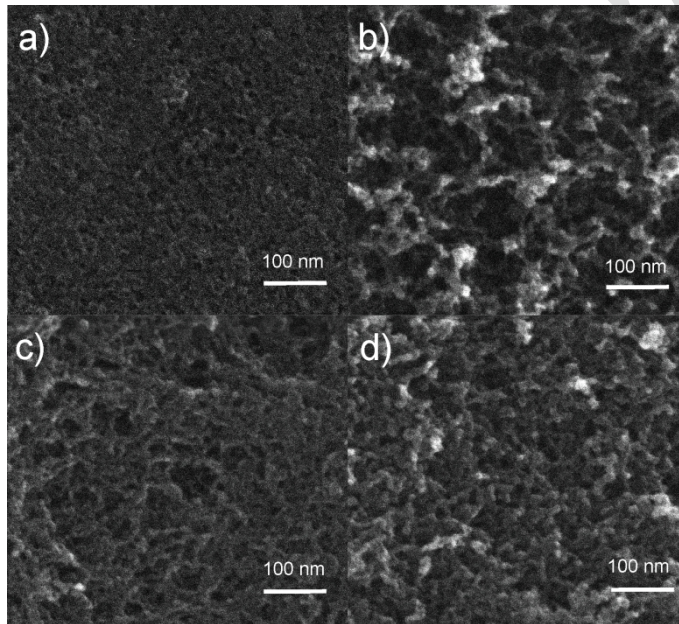


Fig.1. SEM images of undoped CC (a) and nitrogen doped samples: CCN₁ (b), CCN₂ (c) and CCN₃ (d).

In order to evaluate the degree of CC's structural changes induced by N incorporation, Raman spectroscopy was carried out (Fig. 2). Two main peaks can be observed: D band, at $\sim 1340\text{ cm}^{-1}$ originates from disordered structures in the graphitic plane and G band, at

approximately 1570 cm^{-1} , observed for all graphitic based structures, attributed to the E_{2g} vibrational mode present in the sp^2 bonded carbons [46, 47].

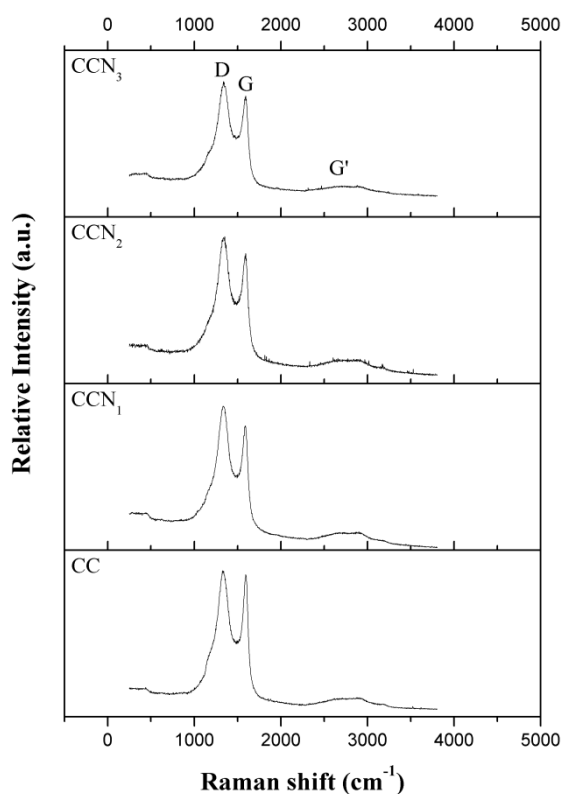


Fig. 2. Raman spectra of CC, CCN₁, CCN₂ and CCN₃ samples

There are also noticeable, but less intense three peaks in the region $2300\text{--}3400\text{ cm}^{-1}$. The most prominent second-order Raman peak G' is located at $\sim 2700\text{ cm}^{-1}$ [48, 49]. Since the frequency of this peak is close to twice that of the D-band frequency, the G' band is an overtone mode of the D band [47]. The second-order peak around 2940 cm^{-1} is a combination of the D and G bands and the peak around 3220 cm^{-1} is attributed to the G band overtone [50, 51]. The most pronounced difference between Raman spectra of CC and CCN samples is a strong increase of D peak intensity with N doping, which influenced the increase of integrated intensity ratio I_D/I_G (derived from deconvolution of Raman spectra) of CCN samples compared to I_D/I_G of CC (Table 1). The higher values of I_D/I_G ratio is the result of the larger share of structural defects and edge plane exposure obviously caused by nitrogen atom

incorporation into CC structure [25, 26]. The similar I_D/I_G values for CCN samples indicate that share of structural defects is independent of the amount of incorporated N. Another difference which can be noticed in Raman spectra is slightly decreasing of G' peak intensity with the increase of doping level. According to Bulusheva et al. the G' band is independent of the structural defects, but the change in its intensity may indicate changes in the electronic structure induced by the N presence in the carbon lattice [49].

Nitrogen adsorption isotherms for carbon cryogel samples doped with different amount of nitrogen, as the amount of N_2 adsorbed as a function of relative pressure at $-196\text{ }^\circ\text{C}$, are shown in Fig. 3. It can be notice that the shape of the isotherms is similar for all samples with well defined hysteresis loops which means that the mesoporous structure is kept for samples with the incorporated nitrogen into CC structure. The shapes of the hysteresis loop indicate the irregular form of the pores in all samples.

According to the IUPAC classification [52] isotherms of samples are of type IV and with a hysteresis loop which is associated with mesoporous materials. In all samples, the shape of hysteresis loop and isotherms are a combination of type H2 and H3. It was found that materials that give rise to H2 hysteresis are often disordered and the distribution of pore size and shape is not well defined. Also, isotherms revealing type H3 hysteresis do not exhibit any limiting adsorption at high P/P_0 , which is observed with non-rigid aggregates of plate-like particles giving rise to slit-shaped pores [53]. Adsorption amounts at low relative pressures showed the presence of the micropores. Specific surface areas calculated by BET equation, S_{BET} , are listed in Table 2.

Table 2. Porous properties of CC and CCN samples.

	S_{BET}	S_{meso}	S_{micro}	V_{tot}	V_{micro}	r_{med}	r_{max}
	m^2/g	m^2/g	m^2/g	cm^3/g	cm^3/g	nm	nm
CC	592	318	274	0.297	0.142	1.94	1.91
CCN ₁	887	513	374	0.665	0.179	2.24	1.99
CCN ₂	928	561	367	0.901	0.193	3.06	3.07
CCN ₃	676	305	371	0.681	0.147	3.81	3.80

Obtained results confirmed that the presence of the nitrogen atoms influences the porous structure of the materials. S_{BET} values, for all samples, lie within $592\text{-}928\text{m}^2\text{ g}^{-1}$. Values of the S_{BET} showed that that all samples have high specific surface, as well as, that the increase of specific surface are not proportional to the amount of incorporated N (Table 1), since the maximum specific surface was achieved at CCN₂ sample. However, the values of the specific surface for the CCN₁ and CCN₂ are similar (the difference is within 5%). Our results showed that the presence of nitrogen atoms up to 1 wt.% increases the specific surface and, after that value, the specific surface starting to decrease but it is still significantly higher than for the pristine sample (CC). These results indicate that the optimal concentration of nitrogen in precursor mixture is below 6 wt. %. when melamine is used as nitrogen source. But, it should keep in mind that the incorporation of the nitrogen into carbon structure strongly depends on the source of the nitrogen which, additionally, complicates the doping process. These changes presumably originated from fact that N atoms during the preparation process of CCN samples can substitute some carbon atoms which are most likely located on the reactive edges and these N atoms could have a catalytic role in the porosity development to some extent. The similar phenomenon was previously reported by Wang et al. [54].

Pore size distribution (PSD) and calculated porosity parameters (S_{meso} , S_{mic} , V_{mic}) of samples are shown in Fig. 4 and Table 2, respectively. The figure shows that samples are mesoporous with most pore radius below 10 nm. Median pore radius, for all samples, presented at Table 2, continuously increased, as well as the maximum pore radius (also presented in Table 2), with the increasing the amount of doped nitrogen, which was previously noted at SEM images (Fig.1). As we mentioned earlier, the presence of nitrogen has the catalytic effect and accelerate the oxidation of the carbon surface. Due to that, the specific surface area and the radius of the pores increase. To a certain limit, the increasement of the specific surface and pore radius is happening simultaneously. At higher amount of nitrogen atoms (above 1 wt.%), the increasement of the pore radius is so high that leads to the decreasing of the specific surface. In that sense, the synthesis of the samples with different amount of nitrogen is necessary to enable us to determine the optimal content of the nitrogen atoms.

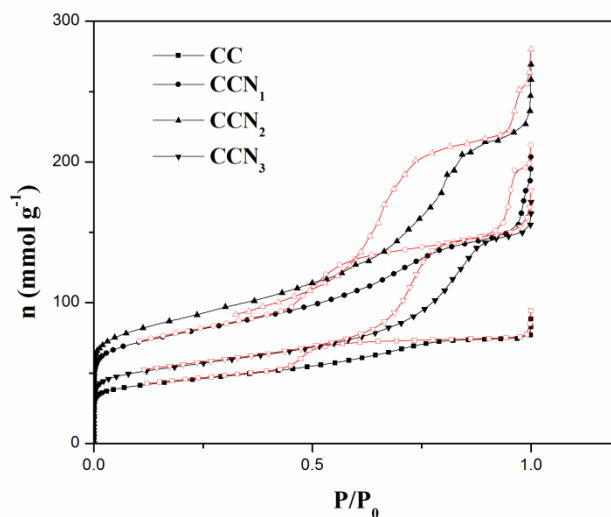


Fig.3. Nitrogen adsorption isotherms, as the amount of N_2 adsorbed as a function of relative pressure for CC and CCN samples. Solid symbols - adsorption, open symbols – desorption.

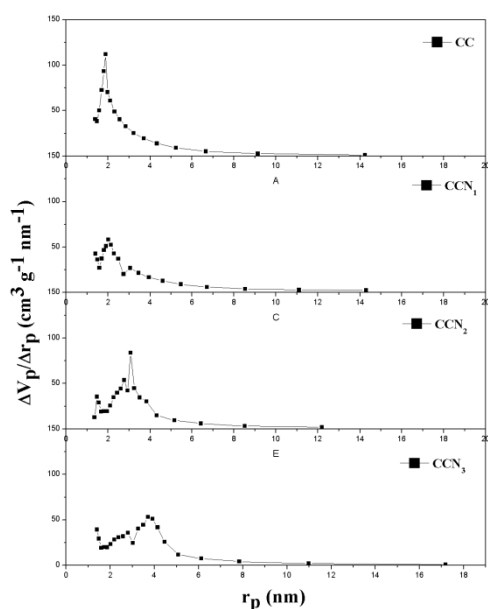


Fig.4. Pore size distribution (PSD) for CC and CCN samples

The FT-IR spectra of the CC samples are shown in Fig. 5. Although carbonization temperature was relative high (900 °C), a quite amount of surface oxygen groups can be noticed for all samples, which was also indicated by the results of the elemental analysis (Table 1). The reasons for such a state of surface chemistry for tested CC samples originate from the structural and porous characteristics. Previously results showed that all CC samples are characterized by disordered structure (Fig. 2) and highly developed specific surface area (Table 2). Both of these characteristics are responsible for the existence of a large number of carbon edge atoms, which represent active sites for surface oxygen group formation [55, 56].

FT-IR spectra for all CC samples show some characteristic bands: wide band near 3400 cm^{-1} , which represents hydroxyl stretching vibration mode in carboxyl, phenol and/or intercalated H_2O . The bands at 2925-2970 cm^{-1} and 2850-2880 cm^{-1} related to symmetric and antisymmetric stretching vibration of C-H bond, respectively, indicates the presence of aliphatic groups [57]. The peak located near 1635 cm^{-1} originated from the skeletal vibration of graphitic domains. For all CC samples, FTIR spectra show high intensity bands in the

range of $1000\text{-}1300\text{ cm}^{-1}$ which include the C-OH stretching and OH bending vibrations, which implying the existence of residual hydroxyl groups. The band around 1380 cm^{-1} can be attributed to carboxyl C-O deformation vibrations [58, 59]. According to the obtained results, nitrogen incorporation into CC structure did not affect the surface chemistry in a qualitative way, probably due to low ratio of nitrogen to carbon atoms and final distribution on N in CCN samples (mainly into the bulk).

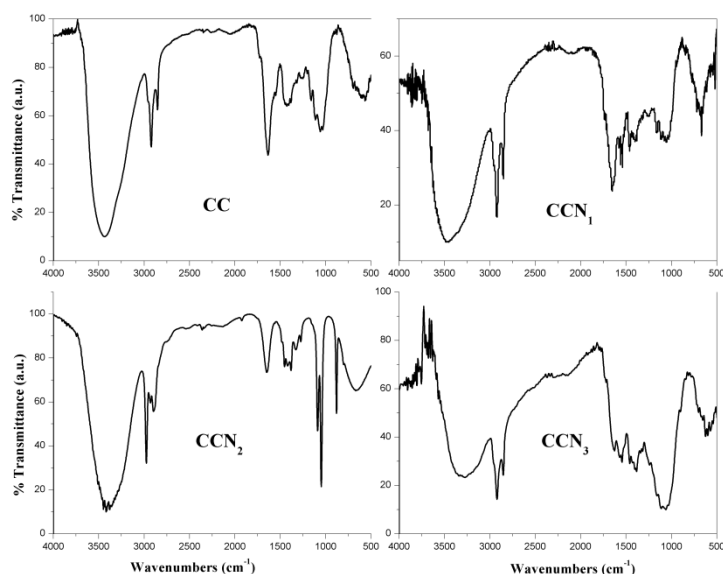


Fig. 5. FT-IR spectra of CC, CCN₁, CCN₂ and CCN₃ samples

Results from conductivity measurements are given in Table 3. Conductivity falls slightly between CC and CCN₃. This trend can be correlated to the increase in nitrogen and oxygen content (Table 1) whose incorporation into the graphite plane is known to lower conductivity. The values of conductivity are roughly half of those measured for similarly prepared materials [5] which can be attributed to the measurement procedure. Namely, in our measurements carbon was subjected to 2t pressure while those in [5] were measured by a four point probe technique. It is well established that the conductivity of cryogel is strongly dependent on the size of grains and their packing and it is presumed that the applied pressure

during measurements influenced grain packing which results in lower conductivity values. However, our previous experience with polyaniline-derived carbons [60, 61] shows that the conductivity values are still sufficiently high to provide good electrochemical behavior of explored materials. In other words, measured conductivities (Table 3) warrant efficient current collection, especially considering that the electrodes are prepared in a thin film configuration (Section 2.2).

Table 3. Conductivity values for CC and CCN samples

Sample	CC	CCN ₁	CCN ₂	CCN ₃
Conductivity (S cm ⁻¹)	14.8 ± 0.5	11.9 ± 0.4	10.1 ± 0.3	9.0 ± 0.3

As an example of recorded CVs at the different sweep rate, CV of CCN₁ sample is presented (Fig. 6, left), while the stored charge for all samples, obtained by CV integration and normalization by the mass on the electrode is subsequently tabulated (Table 4).

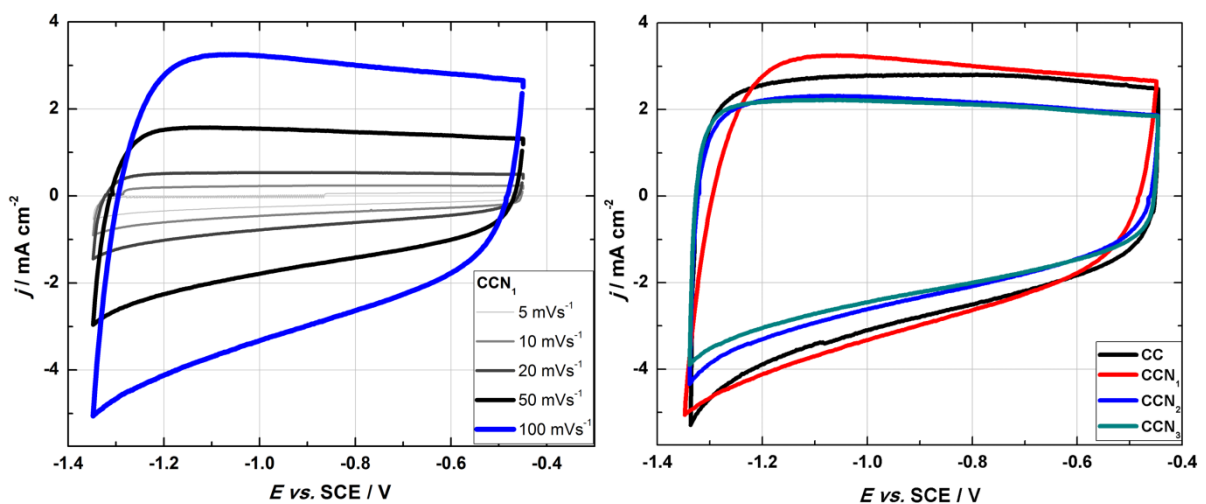


Fig. 6. Cyclic voltammograms of CCN₁ sample recorded in N₂-purged 3M KOH solution recorded at different potential sweep rates (left) and cyclic voltammograms of all four samples recorded at 100 mV s⁻¹.

Nearly rectangular shape, quite often seen for similar types of carbons [18, 60, 61], independent of the sweep rate, characterizes CVs of all samples indicating good capacitive behavior with no discernible Faradaic processes in the form of peaks/humps present. Elemental analysis indicates the presence of small amounts of nitrogen in doped samples, known to show pseudo-capacitive behavior in certain forms, which is well documented as it can significantly contribute to the overall capacitance [60, 61]. However, significant contribution of pseudo-capacitance from nitrogen moieties can be excluded for CCN materials as CV of CC is identical in shape as for CCN, possibly because of relatively low concentration of nitrogen. Hence, we conclude that capacitance comes mainly from electrical double-layer (EDLC), which is known to be highly dependent on the specific surface area. When adjoining the capacitance values with specific surface area linear dependence is not evidenced pointing to the fact that some other factors must come into play and that likely entire S_{BET} is not electrochemically active.

Table 4. Capacitance values (C) at the different sweep rate for CC and CCN samples

Sweep rate (mVs ⁻¹)	C _[CC] (Fg ⁻¹)	C _[CCN1] (Fg ⁻¹)	C _[CCN2] (Fg ⁻¹)	C _[CCN3] (Fg ⁻¹)
5	105	130	85	82
10	90	124	80	75
20	71	117	70.	58
50	65	114	68	54
100	62	106	59	40

Chmiola et al. conducted a detailed study on the correlation between pore size and capacitance which showed capacitance increase with decreasing pore size, which approaches maximum when desolvated ion diffuse into pores [62, 63]. The conclusion is therefore drawn

that the key for achieving high capacitance is to tune the pore sizes to the electrolyte ion size and ensure that the pore volume is accessible to ions without facing transport limitations in addition to the high total surface area. Comparing measured capacitance values at 5 mVs^{-1} we can see that CC and CCN_1 store more charge, 105 and 130 Fg^{-1} , respectively, than CCN_2 (85 Fg^{-1}) and CCN_3 (82 Fg^{-1}) even though they have smaller S_{BET} than CCN_2 . To explain this occurrence we adjoin the average pore size from PSD to S_{BET} values for both CC (1.91 nm ; $592 \text{ m}^2\text{g}^{-1}$; 105 Fg^{-1}) and CCN_1 (1.99 nm ; $887 \text{ m}^2\text{g}^{-1}$; 130 Fg^{-1}) and see that for materials having similar pore size distribution, both are narrow and centered slightly below 2 nm , specific surface area determines the overall capacity.

Looking now at the CCN_2 (3.07 nm ; $928 \text{ m}^2\text{g}^{-1}$; 85 Fg^{-1}) we see that, even though it has the highest S_{BET} , having wider pores is not optimal, as adsorbed ions are now farther away from the surface which leads to a lower capacitance value as it scales inversely proportional to the ion center distance. Finally, CCN_3 (3.80 nm ; $676 \text{ m}^2\text{g}^{-1}$; 82 Fg^{-1}) having the smallest S_{BET} among the doped samples and widest pores results in the lowest measured capacity. These results demonstrate that tuning the carbon porosity in addition to maintaining the large specific surface area is the way of achieving the good capacitive behavior. From Table 4 it can also be seen that the effect of scan rate is rather prominent, when materials with similar pore sizes are considered better rate capabilities are seen for materials with higher S_{BET} (CCN_1 and CCN_2). We note that in all the cases capacitances normalized by S_{BET} are under $20 \mu\text{F cm}^{-2}$, suggesting dominant EDLC contribution.

I-E curves comparing ORR activity of explored materials in 0.1M KOH , with a sweep rate of 20 mVs^{-1} at 600 rpm are presented in Fig. 7a. If onset potential is taken as a measure of materials activity, the most positive onset potential is evidenced for sample CC with the value of -0.15 V vs. SCE , making it the best among explored set of materials. However, all

four have onset potentials spread in a potential window of 100 mVs^{-1} indicating that even for similar materials their activity can vary significantly.

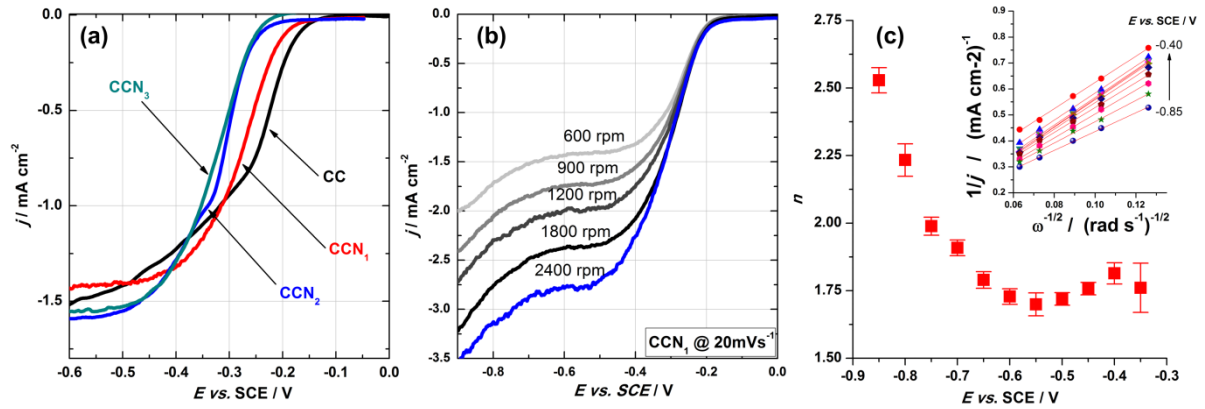


Fig. 7. (a) Background-corrected ORR polarization curves of investigated samples recorded in O_2 -saturated 0.1 KOH (20 mV s^{-1} , electrode rotation rate 600 rpm); (b) Background-corrected ORR polarization curves of CCN_1 samples recorded in O_2 -saturated 0.1 M KOH under different electrode rotation rates (20 mV s^{-1}), and (c) evaluated number of electrons consumed *per* O_2 molecule for CCN_1 sample (inset gives K-L plots).

CCN_1 , as the best doped sample in the series (Fig. 7a), was subjected further to the RDE experiment (Fig. 7b) and K-L analysis to determine the number of apparent electrons exchanged and dominant mechanism (Fig. 7c). Onset potential values are close to those measured for similar types of materials with a small fraction of heteroatoms [18]. The apparent number of electrons is determined from the slope of K-L lines defined by:

$$\frac{1}{j(E)} = \frac{1}{j_k(E)} + \frac{1}{j_d} = \frac{1}{j_k} - \frac{1}{0.62 \cdot n \cdot F \cdot D(\text{O}_2)^{2/3} \cdot \nu^{-1/6} \cdot \omega^{1/2} \cdot c(\text{O}_2)} \quad (1)$$

In Eq. (1), $j(E)$ and $j_k(E)$ are the measured current density and the kinetic current density at a given electrode potential (E), respectively, while j_d is the limiting diffusion

current density (which indirectly depends on E via n). Additionally, ν presents the kinematic viscosity of the solution ($0.01 \text{ cm}^2 \text{ s}^{-1}$) [64], $D(\text{O}_2)$ is the diffusion coefficient of O_2 ($1.9 \times 10^{-5} \text{ cm}^2 \text{ s}^{-1}$) [43] and $c(\text{O}_2)$ is the concentration of dissolved O_2 ($1.2 \times 10^{-6} \text{ mol cm}^{-3}$) [65]. K-L analysis was done in the potential range -0.35 to -0.85 V vs. SCE . Interestingly, n was found to be close to 2 at low overvoltages, while it slightly increased with deeper negative overvoltage and reached 2.55 at -0.85 V vs. SCE (Fig. 7c). This indicates that $2e^-$ is principal pathway in O_2 reduction for CCN_1 which is contrary to N-doped carbon nanotubes and polyaniline derived N-containing nanocarbon [66] which shows a switch from $2e^-$ to predominantly $4e^-$ mechanism at deep negative overvoltages. This discrepancy can be attributed to the level of nitrogen doping as aforementioned materials have about 9 wt.% while CCN_1 has only 0.5 wt.%. Results are analogous to those found for low level doped carbons [13, 18], where n was also between 2 and 3, stressing that high doping level is crucial for good ORR selectivity. However, considering practical application of CCN in the field of electrocatalysis, these materials seems as proper candidates for electrochemical synthesis of hydrogen peroxide due to rather exclusive $2e^-$ reduction of O_2 .

4. Conclusions

In this study, nitrogen doped carbon cryogels were synthesized and characterized. Final nitrogen concentrations in doped samples were found to be in the range of 0.45–1.15 wt.%. Investigation of nitrogen doped carbon cryogel by means of Raman spectroscopy revealed an influence of nitrogen substitution on the structural disorder in carbon cryogel structure. Scanning electron microscopy, as well as characterization by nitrogen adsorption, pointed out that, even with such low nitrogen contents, it is possible to drastically affect morphology and porosity of carbon cryogel. Namely, although the doped samples preserved the dominant mesoporosity, the values of the specific surface area for two samples with lower

nitrogen content increase over 50% compared to the value of pristine carbon cryogel. For the sample with highest nitrogen content, this enhancement of specific surface area is quite lower, indicating that lower content of incorporated nitrogen, has a much more pronounced developing effect to specific surface area. The maximum capacitance value of 130.2 Fg^{-1} at 5 mVs^{-1} is obtained for material concurrently having narrow pore size distribution and high specific surface area reiterating the conclusion that tuning of carbon porosity is the way to achieve good capacitive behavior. Low level nitrogen doping has a small effect on ORR selectivity in the alkaline solution which predominantly goes through $2e^-$ mechanism. To achieve complete reduction of oxygen to hydroxide high level of doping is needed. Obtained results showed that it is possible, using simple doping procedure with low nitrogen content, to affect the morphology, structural and surface characteristics of the carbon cryogel, which further could lead to the expansion of nitrogen doped carbon cryogel application.

Acknowledgements

This work was supported by the Serbian Ministry of Educations, Science and Technological Development through the projects: III45006, III45016, and III45014.

References

- [1] R. W. Pekala, Organic aerogels from the polycondensation of resorcinol with formaldehyde, *J. Mater. Sci.* 24 (1989) 3221–3227.
- [2] R. W. Pekala, C. T. Alviso, X. Lu, J. Gross, J. Fricke, New organic aerogels based upon a phenolic-furfural reaction, *J. Non-Cryst. Solids* 188 (1995) 34–40.
- [3] H. Tamon, H. Ishizaka, T. Yamamoto, T. Suzuki, Preparation of mesoporous carbon by freeze drying, *Carbon* 37 (1999) 2049–2055.

- [4] T. Yamamoto, T. Sugimoto, T. Suzuki, S. R. Mukai, H. Tamon, Preparation and characterization of carbon cryogel microspheres, *Carbon* 40 (2002) 1345–1351.
- [5] B. Babić, B. Kaludjerović, Lj. Vračar, N. Krstajić, Characterization of carbon cryogel synthesized by sol–gel polycondensation and freeze-drying, *Carbon* 42 (2004) 2617–2624.
- [6] A. Kaplan, E. Korin, L. Soifer, A. Bettelheim, Ion-Conductive and Transparent Resorcinol-Formaldehyde Hydrogels for Electrochemical and Solar Applications, *Electrochem. and Solid-State Lett.* 15 (2012) F1–F4.
- [7] J. Fricke., A. Emmerling, Aerogels—Preparation, properties, applications, in: R. Reisfeld, C.K. Jørgensen (Eds.), *Chemistry, Spectroscopy and Applications of Sol-Gel Glasses, Structure and Bonding*, Springer, Berlin, 1992, pp. 37-87.
- [8] Z.M. Marković, B.M. Babić, M.D. Dramićanin, I.D. Holclajtner Antunović, V.B. Pavlović, D.B. Peruško, B.M. Todorović Marković, Preparation of highly conductive carbon cryogel based on pristine graphene, *Synthetic Metals* 162 (2012) 743– 747.
- [9] M. Haro, G. Rasines, C. Maclas, C.O. Ania, Stability of a carbon gel electrode when used for the electro-assisted removal of ions from brackish water, *Carbon* 49 (2011) 3723–3730.
- [10] Z. Jin, Y. Liu, X. Bai, X. Ren, C. Qin, Y. Wang, Electrochemical properties of carbon aerogels derived from resorcinol-formaldehyde-aniline for supercapacitors, *Pigment & Resin Technol.* 40 (2011) 175–180.
- [11] T. Z. Minović, J. J. Gulicovski , M. M. Stoiljković , B. M. Jokić, Lj. S. Zivkovic, B. Z. Matović , B. M. Babić, Surface characterization of mesoporous carbon cryogel and its application in arsenic (III) adsorption from aqueous solutions, *Microporous and Mesoporous Mater.* 201 (2015) 271–276.

- [12] B.M. Babić, Lj.M. Vračar, V. Radmilović, N.V. Krstajić, Carbon cryogel as support of platinum nano-sized electrocatalyst for the hydrogen oxidation reaction, *Electrochim. Acta* 51 (2006) 3820–3826.
- [13] M. Momčilović, M. Stojmenović, N. Gavrilov, I. Pašti, S. Mentus, B. Babić, Complex electrochemical investigation of ordered mesoporous carbon synthesized by the soft-templating method: charge storage and electrocatalytical or Pt-electrocatalyst supporting behavior, *Electrochim. Acta* 125 (2014) 606–614.
- [14] Y. Cao, H. Yu, J. Tan, F. Peng, H. Wang, J. Li, W. Zheng, N.B. Wong, Nitrogen-, phosphorous- and boron-doped carbon nanotubes as catalysts for the aerobic oxidation of cyclohexane, *Carbon* 57 (2013) 433–442.
- [15] Ana Kalijadis, Zoran Jovanovic, Mila Lausevic, Zoran Lausevic, The effect of boron incorporation on the structure and properties of glassy carbon, *Carbon* 49 (2011) 2671–2678.
- [16] Ana Kalijadis, Jelena Đorđević, Tatjana Trtić-Petrović, Marija Vukčević, Maja Popović, Vesna Maksimović, Zlatko Rakočević, Zoran Laušević, Preparation of boron-doped hydrothermal carbon from glucose for carbon paste electrode, *Carbon* 95 (2015) 42–50.
- [17] Ana Kalijadis, Jelena Đorđević, Zsigmond Papp, Bojan Jokić, Vuk Spasojević, Biljana Babić and Tatjana Trtić-Petrović, A novel carbon paste electrode based on nitrogen-doped hydrothermal carbon for electrochemical determination of carbendazim, *J. Serb. Chem. Soc.* 82 (2017) 1–14.
- [18] I. A. Pašti, N. M. Gavrilov, A. S. Dobrota, M. Momčilović, M. Stojmenović, A. Topalov, D. M. Stanković, B. Babić, G. Ćirić-Marjanović, S. V. Mentus, The Effects of a Low-Level

Boron, Phosphorus, and Nitrogen Doping on the Oxygen Reduction Activity of Ordered Mesoporous Carbons, *Electrocatalysis* 6 (2015) 498–511.

[19] D. Geng, S. Yanga, Y. Zhang, J. Yang, J. Liu, R. Li, T.-K. Sham, X. Suna, S. Ye, S. Knights, Nitrogen doping effects on the structure of grapheme, *Appl. Surf. Sci.* 257 (2011) 9193–9198.

[20] D.-W. Wang, F. Li, L.-C. Yin, X. Lu, Z.-G. Chen, I. R. Gentle, G. Q. (Max) Lu, H.-M. Cheng, Nitrogen-doped carbon monolith for alkaline supercapacitors and understanding nitrogen-induced redox transitions, *Chem. Eur. J.* 18 (2012) 5345–51.

[21] Xiaoming Fan, Chang Yu, Juan Yang, Zheng Ling, Jieshan Qiu, Hydrothermal synthesis and activation of graphene-incorporated nitrogen-rich carbon composite for high-performance supercapacitors, *Carbon* 70 (2014) 130–141.

[22] K. Gong, F. Du, Z. Xia, M. Duratock, L. Dai, Nitrogen-Doped Carbon Nanotube Arrays with High Electrocatalytic Activity for Oxygen Reduction, *Science* 323 (2009) 760–764.

[23] S.U. Lee, R.V. Belosludov, H. Mizuseki, Y. Kawazoe, Designing Nanogadgets for Nanoelectronic Devices with Nitrogen-Doped Capped Carbon Nanotubes, *Small* 5 (2009) 1769–1775.

[24] B. Khalid, Q. Meng, J. Li, B. Cao, Nitrogen rich graphene-cross-linked melamine formaldehyde carbon cryogels for supercapacitors, *Electrochim. Acta* 142 (2014) 101–107.

[25] M. C. dos Santos, F. Alvarez, Nitrogen substitution of carbon in graphite: structure evolution toward molecular forms, *Phys. Rev. B* 58(1998) 13918–13924.

[26] S. Maldonado, S. Morin, K. J. Stevenson, Structure, composition, and chemical reactivity of carbon nanotubes by selective nitrogen doping, *Carbon* 44 (2006) 1429–1437.

- [27] D. P. Kim, C. L. Lin, T. Mihalisin, P. Heiney, M.M. Labes, Electronic properties of nitrogen-doped graphite flakes, *Chem. Mater.* 3 (1991) 686–692.
- [28] A. K. Shukla, M. K. Ravikumar, A. Roy, S. R. Barman, D. D. Sarma, A. S. Arico, et al., Electro-oxidation of methanol in sulfuric acid electrolyte on platinized carbon electrodes with several functional-group characteristics, *J. Electrochem. Soc.* 141 (1994) 1517-1522.
- [29] M. Inagaki, M. Toyoda, Y. Soneda, & T. Morishita, Nitrogen-doped carbon materials *Carbon*, 132 (2018) 104–140.
- [30] X. Zhou, S. Tang, Y. Yin, S. Sun, J. Qiao, Hierarchical porous N-doped graphene foams with superior oxygen reduction reactivity for polymer electrolyte membrane fuel cells, *Appl. Energy* 175 (2016) 459-467.
- [31] L. Zhang, N. Zheng, A. Gao, C. Zhu, Z. Wang, Y. Wang, et al., A robust fuel cell cathode catalyst assembled with nitrogen-doped carbon nanohorn and platinum nanoclusters, *J. Power Sources* 220 (2012) 449-454.
- [32] G. A. Ferrero, A. B. Fuertes, M. Sevilla, M. M. Titirici, Efficient metal-free N-doped mesoporous carbon catalysts for ORR by a template-free approach, *Carbon* 106 (2016) 179-187.
- [33] G. Nam, J. Park, S. T. Kim, D.-B. Shin, N. Park, Y. Kim, et al., Metal-free Ketjenblack incorporated nitrogen-doped carbon sheets derived from gelatin as oxygen reduction catalysts. *Nano Lett* 14 (2014) 1870-1876.
- [34] J. Liu, P. Song, W. Xu, Structure-activity relationship of doped-nitrogen (N)-based metal-free active sites on carbon for oxygen reduction reaction, *Carbon* 115 (2017) 763-772.

- [35] L. Li, G. Zhou, L. Yin, N. Koratkar, F. Li, H.-M. Cheng, Stabilizing sulfur cathodes using nitrogen-doped graphene as a chemical immobilizer for Li-S batteries, *Carbon* 108 (2016) 120-126.
- [36] P. Zuo, H. Zhang, M. He, Q. Li, Y. Ma, C. Du, et al., Clew-like N-doped multiwalled carbon nanotube aggregates derived from metal-organic complexes for lithium-sulfur batteries, *Carbon* 122 (2017) 635-642.
- [37] S. Niu, W. Lv, C. Zhang, F. Li, L. Tang, Y. He, et al., A carbon sandwich electrode with graphene filling coated by N-doped porous carbon layers for lithium-sulfur batteries, *J. Mater. Chem. A* 3 (2015) 29218-29224.
- [38] S. Liu, H. Zhang, Z. Xu, H. Zhong, H. Jin, Nitrogen-doped carbon xerogel as high active oxygen reduction catalyst for direct methanol alkaline fuel cell, *Int. J. Hydrog. Energy* 37 (2012) 19065-19072.
- [39] T. Horikawa, N. Sakao, T. Sekida, J. Hayashi, D. D. Do, M. Katoh, Preparation of nitrogen-doped porous carbon by ammonia gas treatment and the effects of N-doping on water adsorption, *Carbon* 50, (2012) 1833-1842.
- [40] P. Veselá, V. Slovák, N-doped carbon xerogels prepared by ammonia assisted pyrolysis: Surface characterisation, thermal properties and adsorption ability for heavy metal ions, *J. Anal. Appl. Pyrol.* 109 (2014) 266-271.
- [41] K. Y. Kang, B. I. Lee, J. S. Lee, Hydrogen adsorption on nitrogen-doped carbon xerogels, *Carbon* 47 (2009) 1171-1180.

- [42] Z. Ling, C. Yu, X. Fan, S. Liu, J. Yang, M. Zhang, et al., Freeze-drying for sustainable synthesis of nitrogen doped porous carbon cryogel with enhanced supercapacitor and lithium ion storage performance, *Nanotechnology* 26 (2015) 374003 (11pp).
- [43] E.P. Barret, L.G. Joyner, P.P. Halenda, The determination of pore volume and area distributions in porous substances. I. Computations from nitrogen isotherms, *J. Am. Chem. Soc.* 73 (1951) 373-380.
- [44] B.C. Lippens, B.G. Linsen, J.H. de Boer, Studies on pore systems in catalysts I. The adsorption of nitrogen; apparatus and calculation, *J. Catalysis* 3 (1964) 32-37.
- [45] Q. Wu, W. Li, S. Liu, C. Jin, Hydrothermal synthesis of N-doped spherical carbon from carboxymethylcellulose for CO₂ capture, *Appl. Surf. Sci.* 369 (2016) 101–107.
- [46] A. C. Ferrari, J. Robertson, Interpretation of Raman spectra of disordered and amorphous carbon, *Phys. Rev. B* 61(2000) 14095–14107.
- [47] M. J. Matthews, M. A. Pimenta, G. Dresselhaus, M. S. Dresselhaus, M. Endo, Origin of dispersive effects of the Raman D band in carbon materials, *Phys. Rev. B* 59(1999) R6585–R6588.
- [48] R. Saito, A. Grüneis, Ge.G. Samsonidze, V.W. Brar, G. Dresselhaus, M.S. Dresselhaus, A. Jorio, L.G. Cançado, C. Fantini, M.A. Pimenta, and A.G. Souza Filho, Double resonance Raman spectroscopy of single-wall carbon nanotubes, *New J. Phys.* 5 (2003) 157.1–157.15.
- [49] L. G. Bulusheva, A. V. Okotrub, I. A. Kinloch, I. P. Asanov, A. G. Kurennya, A. G. Kudashov, X. Chen, and H. Song, Effect of nitrogen doping on Raman spectra of multi-walled carbon nanotubes, *Phys. Stat. Sol. (b)* 245 (2008) 1971–1974.

- [50] A. Gupta, G. Chen, P. Joshi, S. Tadigadapa, and P.C. Eklund, Raman scattering from high-frequency phonons in supported n-graphene layer films, *Nano Lett.* 6 (2006) 2667–2673.
- [51] Y. Kawashima and G. Katagiri, Fundamentals, overtones, and combinations in the Raman spectrum of graphite, *Phys. Rev. B* 52 (1995) 10053–10059.
- [52] K. S. W. Sing, D. H. Everett, R. A. W. Haul, L. Moscou, R. A. Pierotti, J. Rouquerol, T. Siemieniewska, Reporting physisorption data for gas/solid systems with special reference to the determination of surface area and porosity, *Pure Appl. Chem.* 57 (1985) 603-619.
- [53] S. Lowell, J.E. Shields, M. A. Thomas, M. Thommes, *Characterization of Porous Solids and Powders: Surface Area, Pore Size and Density*, Ed. Kluwer Academic Publishers, Dordrecht Netherlands, 2004.
- [54] X. Wang, X. Li, L. Zhang, Y. Yoon, P.K. Weber, H. Wang, J. Guo, H. Dai, N-doping of graphene through electrothermal reactions with ammonia, *Science* 324 (2009) 768–771.
- [55] A. Kalijadis, M. Vukcevic, Z. Jovanovic, Z. Lausevic, M. Lausevic, Characterisation of surface oxygen groups on different carbon materials by the Boehm method and temperature-programmed desorption, *J. Serb. Chem. Soc.* 76 (2011) 757–768.
- [56] H. P. Boehm, Surface oxides on carbon and their analysis: a critical assessment, *Carbon* 40 (2002) 145–149.
- [57] M. Domingo-García, F.J.L. Garzón, M.J. Pérez-Mendoza, On the characterization of chemical surface groups of carbon materials, *J. Coll. Int. Sci.* 248 (2002) 116–122.
- [58] J. H. Zhou, Z. J. Sui, J. Zhu, P. Li, D. Chen, Y. C. Dai, W.-K. Yuan, Characterization of

surface oxygen complexes on carbon nanofibers by TPD, XPS and FT-IR, *Carbon* 45 (2007) 785–796.

[59] C. Laginhas, J. M. Valente Nabais, M. M. Titirici, Activated carbons with high nitrogen content by a combination of hydrothermal carbonization with activation, *Microporous and Mesoporous Mater.* 226 (2016) 125–132.

[60] N. Gavrilov, I. A. Pašti, M. Vujković, J. Travas-Sejdic, G. Ćirić-Marjanović, S. V. Mentus, High-performance charge storage by N-containing nanostructured carbon derived from polyaniline, *Carbon* 50 (2012) 3915–3927.

[61] M. Vujković, N. Gavrilov, I. Pašti, J. Krstić, J. Travas-Sejdic, G. Ćirić-Marjanović, S. Mentus, Superior capacitive and electrocatalytic properties of carbonized nanostructured polyaniline upon a low-temperature hydrothermal treatment, *Carbon* 64 (2013) 472–486.

[62] J. Chmiola, G. Yushin, Y. Gogotsi, C. Portet, P. Simon, P. L. Taberna, Anomalous Increase in Carbon Capacitance at Pore Sizes Less Than 1 Nanometer, *Science* 313 (2006) 1760–1763.

[63] C. Largeot, C. Portet, J. Chmiola, P.-L. Taberna, Y. Gogotsi, and P. Simon, Relation between the Ion Size and Pore Size for an Electric Double-Layer Capacitor, *J. Am. Chem. Soc.* 130 (2008) 2730–2731.

[64] D. W.H. Rankin, CRC handbook of chemistry and physics, in: David R. Lide (Eds.), *Crystallography Reviews*, Taylor and Francis Online, Taylor and Francis Online, Informa PLC, London, 2009, pp. 223–224.

[65] R.E. Davis, G.L. Horvath, C.W. Tobias, The Solubility and Diffusion Coefficient of Oxygen in Potassium Hydroxide Solutions, *Electrochim. Acta* 12 (1967) 287–297.

[66] N. Gavrilov, M. Vujković, I. A. Pašti, G. Ćirić-Marjanović; S. V. Mentus, Enhancement of electrocatalytic properties of carbonized polyaniline nanoparticles upon a hydrothermal treatment in alkaline medium, *Electrochim. Acta* 56 (2011) 9197–9202.

Journal Pre-proof

List of figure captions

Fig.1. SEM images of undoped CC (a) and nitrogen doped samples: CCN₁ (b), CCN₂ (c) and CCN₃ (d).

Fig. 2. Raman spectra of CC, CCN₁, CCN₂ and CCN₃ samples

Fig.3. Nitrogen adsorption isotherms, as the amount of N₂ adsorbed as a function of relative pressure for CC and CCN samples. Solid symbols - adsorption, open symbols – desorption.

Fig.4. Pore size distribution (PSD) for CC and CCN samples

Fig. 5. FT-IR spectra of CC, CCN₁, CCN₂ and CCN₃ samples

Fig. 6. Cyclic voltammograms of CCN₁ sample recorded in N₂-purged 3M KOH solution recorded at different potential sweep rates (left) and cyclic voltammograms of all four samples recorded at 100 mV s⁻¹.

Fig. 7. (a) Background-corrected ORR polarization curves of investigated samples recorded in O₂-saturated 0.1 KOH (20 mV s⁻¹, electrode rotation rate 600 rpm); (b) Background-corrected ORR polarization curves of CCN₁ samples recorded in O₂-saturated 0.1 KOH under different electrode rotation rates (20 mV s⁻¹), and (c) evaluated number of electrons consumed *per* O₂ molecule for CCN₁ sample (inset gives K-L plots).

Highlights

- Nitrogen doped carbon cryogels with nitrogen content to 1.15 wt.% were synthesized
- Drastic changes in doped samples morphology and porosity were obtained
- The maximum capacitance value was obtained for the lowest nitrogen content
- Effects of nitrogen doping on carbon cryogels electrocatalytic properties and conductivity were insignificant
- Low nitrogen content led to sufficiently modified carbon cryogels properties

UDK: 548.73; 549.3: 677.017.5

Deposition of Copper Sulfide Films on Polyamide Surface

Neringa Petrasauskiene¹, Edita Paluckiene¹, Rasa Alaburdaite¹, Martina Gilic^{2,3*}

¹Department of Physical and Inorganic Chemistry, Kaunas University of Technology, Radvilenuj 19, LT-50254 Kaunas, Lithuania

²Institute of Physics Belgrade, University of Belgrade, Pregrevica 118, Zemun 11080, Serbia

³Institut of Experimental Physics, Freie Universität Berlin, Arnimallee 14, 14195 Berlin, Germany

Abstract:

In this paper, we present a novel and low – cost method for preparing copper sulfide films on polyamide. Non-treated as well as pre-treated PA6 films by 3 different methods (in boiled water; in NaOH solution; in boiled water and then in NaOH solution) were used for the formation of Cu₂S layers by the sorption-diffusion method. Molten sulfur has been used as a sulfurization agent. The XRD, FTIR, and UV-VIS methods were used to characterize the structural, optical, and electrical properties of samples and to track changes in samples after each treatment stage. The sheet resistance of Cu₂S layers depends on the pre-treatment method and varied from 7 kΩ/sq to 6 MΩ/sq. The optical band gaps (E_g) for direct and indirect transitions are determined to be 2.61–2.67 eV and 1.40-1.44 eV, respectively. Furthermore, the optical constants n, k, and σ are determined from UV-VIS measurements.

Keywords: *Thin film; Copper sulfide; Polyamide 6; X-ray diffraction; Optical properties.*

1. Introduction

Copper sulfides, Cu_xS, x=1–2, are one of the most important compounds of chalcogenide semiconductor materials due to their low toxicity, versatility, and availability. They can be used as absorbers and p-type semiconductors due to their excellent electrical, optical, and structural properties [1–3]. The electrical conductivity of copper sulfides is decreasing from CuS to Cu₂S, direct bandgap values vary from 2.2 to 2.9 eV in Cu₂S, 2.1 eV in Cu_{1.8}S, and 1.7 eV in CuS [1,4–6].

Copper sulfides are widely applied as thin films and composite materials with technologically important applications in optoelectronic devices [7,8], sensors [9,10], photocatalysis [11,12], photovoltaic cells [10,13], for high-energy supercapacitors [14,15], battery electrodes [7,16,17], and in biomedical fields [18,19]. Recently, they found application as counter electrodes in quantum dot sensitized solar cells [15,20]. For all these applications, the material must be highly accessible; therefore, it is very important to identify simple and inexpensive production technologies on a large scale.

The deposition of a thin layer of copper sulfide on the surface of an organic polymer is one of the simple ways to obtain electrically conductive films for the manufacture of electronic devices, because they can change properties from a semiconductor to a metal conductor. The ability of a polymer to sorb fine particles from a solution provides

*) **Corresponding author:** martina.gilic@fu-berlin.de (M. Gilic)

opportunities for many novel applications [21]. Once the copper sulfide is deposited on a flexible transparent polymer substrate, the resulting coated polymer may be applicable in many areas: as the conductive substrate for the deposition of metals and semiconductors [22,23]; as room temperature gas sensors [24,25]; in thermoelectric applications [26].

Polyamide (PA6 or polycapromamide, Nylon 6) as a semihydrophilic polymer is capable of absorbing ions or molecules of various electrolytes from aqueous and non-aqueous solutions [27]. Polyamide can be characterized as a polymer with high thermal resistance and good mechanical properties.

Polymers with electrically conductive metal chalcogenide layers on their surface can be prepared by the sorption-diffusion method described in our earlier works [27–29]. According to this method, the surface of a polymer is pre-treated by a solution containing a sulfurization agent and subsequently treated by an aqueous solution of metal salt.

This work presents a new low-cost method for preparing good quality Cu_2S thin films on a modified PA6 surface. The structure of the prepared films is studied by X-ray diffraction (XRD), Fourier transform infrared (FTIR), and UV-VIS spectroscopy. The material (composite) structure and the optical and electrical properties of Cu_2S films are discussed.

2. Materials and Experimental Procedures

2.1. Materials

Analytical pure reagents and *distilled water* were used to prepare the reactive solutions. All reagents were obtained from Sigma-Aldrich and used as received. Only freshly prepared solutions were used for experiments and were not de-aerated during the experiments.

The polyamide film (PA6) (Tecamid 6, thickness - 500 μm , density - 1.13 g/cm^{-3} , surface resistance 10^{12} Ω/sq) used in this study was obtained from Ensinger GmbH (Germany).

2.2. Formation of Cu_xS thin layers

According to the bibliography [30], the impregnation of copper sulfide on PA6 or other polymers requires a previous treatment process to facilitate its adhesion. For the experiment, non-treated PA6 samples have been used, as well as the ones pre-treated by 3 different methods: boiled in distilled water for 120 min; exposed to 0.1 M NaOH solution for 120 min at 80°C; boiled in distilled water for 120 min and subsequently exposed to 0.1 M NaOH solution for 120 min at 80°C (Table I). All samples were rinsed and air-dried at room temperature, followed by desiccation with CaCl_2 .

Tab. I Sample labelling and experimental conditions of PA6.

Labelling	Experimental conditions
PA6-0	Non-treated
PA6-1	Boiled in distilled water for 120 min
PA6-2	Exposed to 0.1 M NaOH solution for 120 min at 80°C
PA6-3	Boiled in distilled water for 120 min and subsequently exposed to 0.1 M NaOH solution for 120 min at 80°C.

The formation of copper sulfide layers on PA6 film surface was carried out in two stages. In the first stage, the PA6 films were sulfurized by molten sulfur at 135°C for 1 min in a glass reactor. In the second stage, the samples of sulfurized PA6 films were treated with the aqueous 0.4 M CuSO_4 solution with the reducing agent at 80°C for 10 min. The PA6 substrate

was placed vertically. After the treatment with the solution of Cu(I/II) salts, the samples of PA6 were rinsed and dried in a desiccator.

2.3. Characterization of PA6 and copper sulfide layers

An X-ray diffractometer (D8 Advance diffractometer, Bruker AXS, Karlsruhe, Germany) has been applied to examine the crystal phase of the PA6 and PA6/Cu_xS samples. The samples were scanned over the range $2\theta = 3\text{--}70^\circ$ at a scanning speed of 6°min^{-1} using a coupled two theta/theta scan type. The peaks obtained were identified based on those available in the PDF-2 database.

The optical properties of the PA6 and PA6/Cu_xS samples were measured at room temperature by using UV/VIS spectrometer Lambda 35 UV/VIS (Perkin Elmer, USA) in the range of 200 to 1100 nm.

The FTIR spectra were recorded in the wavenumber range of 3500 to 600 cm^{-1} using the compensation method on Perkin Elmer FTIR Spectrum GX 2000 spectrophotometer by averaging 64 scans with a wavenumber resolution of 1 cm^{-1} at room temperature.

The constant current resistivity of the copper sulfide films was measured using a multimeter MS8205F (Mastech, China) with special electrodes. The electrodes were produced from two nickel-plated copper plates with a 1 cm spacing and the dielectric material between them.

3. Results and Discussion

3.1. X-ray diffraction analysis

Polyamide 6 has the repeating group $[-\text{NH}(\text{CH}_2)_5(\text{CO})-]$ and is characterized by the presence of secondary amide groups CO-NH in the polymer skeleton. The hydrogen bonds formed between neighbouring chains strongly affect the mechanical properties. PA6 is semicrystalline; it consists of crystalline and amorphous phases. The degree of crystallinity of PA6 is 35-45 %. The crystalline regions contribute to the hardness, temperature stability, and chemical resistance. Amorphous areas contribute to the impact of resistance and high elongation [31,32]. PA6 has two well-established crystalline modifications of α phase and γ phase, which can be transformed into each other under certain conditions. The stable monoclinic α phase is dominant in the structure of PA6; while γ form is unstable, and it can be transformed into the α form [33].

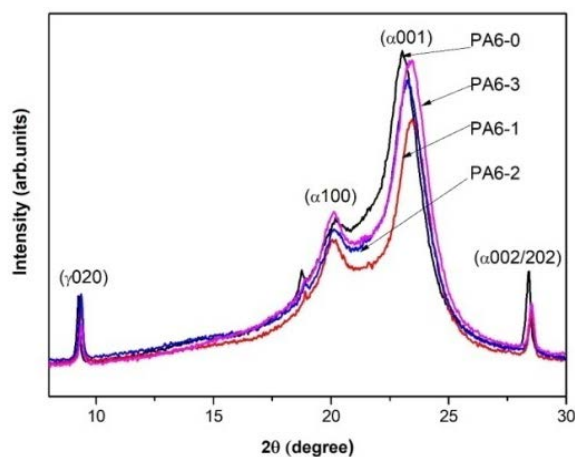


Fig. 1. XRD patterns of PA6.

The first task of our work was to study the influence of the polymer preparation on the formation of the copper sulfide thin films by XRD and FTIR analysis.

The XRD diffraction patterns of the initial polyamide films used in the experiments are presented in Fig. 1.

The experimental values of d (lattice spacing) for the polymer are determined using Bragg's relation [34] by taking the θ value from the peak position of XRD pattern:

$$n\lambda = 2d \sin \theta \quad (1)$$

where n (an integer) is the order of diffraction; λ is the wavelength of incident X-rays; d is the interplanar spacing of the crystal and θ is the angle of incidence. Calculated values of d are shown in Table II.

Tab. II The 2θ , d and (hkl) Miller indices values of PA6.

(hkl)	PA6-0		PA6-1		PA6-2		PA6-3	
	2θ (°)	d (Å)	2θ (°)	d (Å)	2θ (°)	d (Å)	2θ (°)	d (Å)
(γ 020)	9.24	9.56	9.38	9.42	9.36	9.44	9.36	9.44
(α 100)	20.19	4.39	20.05	4.42	20.11	4.41	20.11	4.41
(α 001)	23.03	3.85	23.44	3.79	23.25	3.82	23.44	3.79
(α 002/202)	28.41	3.14	28.52	3.13	28.52	3.13	28.52	3.13

The peaks of semicrystalline PA6 between 8° to 30° (in 2θ) were observed. These peaks, according to JCPDS 12-923, appear at $\sim 20.1^\circ$ and $\sim 23.4^\circ$ with the corresponding d -spacing of ~ 4.4 and ~ 3.8 Å, respectively. They are attributed to the α 100 and α 001 crystal planes, respectively, and showed the presence of the dominant crystalline α -phase [30,32]. Two reflections are also observed at around $2\theta = 9.3^\circ$ (γ 020) and 28.5° α 002/202.

It has been observed that the intensities and full width at half-maximum (FWHM) values of these peaks slightly changed with the preparation of the PA6 before the formation of the copper sulfide thin films. These changes may be attributed to the crystallinity of the films. The structural parameters for the (α 001) peak such as FWHM (β), crystallites size (D), dislocation density (δ) and strain (ε) for all the prepared films were evaluated from XRD patterns and presented in Table III. The grain size of the thin films was calculated by XRD patterns using Debye Scherrer's formula [35]:

$$D = \frac{0.9\lambda}{\beta \cos \theta} \quad (2)$$

where D is the crystallite size; λ is the X-ray wavelength used; β is the angular line width at half-maximum intensity in radians and θ is Bragg's angle.

Additionally, to have more information on the number of defects in the films, the dislocation density (δ) was evaluated using the formula [36]:

$$\delta = \frac{1}{D^2} \quad (3)$$

The strain values were calculated from the following relation [37]:

$$\varepsilon = \frac{\beta \cos \theta}{4} \quad (4)$$

The results in Table III showed that the highest value of crystallite size has the polymer PA6-1, while its dislocation density and strain have the lowest value. The larger D , and the smaller β , δ and ε values indicate better crystallization of the films [38,39].

Tab. III The crystallite size (D), dislocation density (δ), strain (ε) and full width at half maximum (FWHM, β) values of copper sulfide thin films.

	2θ (°)	β (°)	D (nm)	$\delta \cdot 10^{-2}$ (nm ⁻²)	$\varepsilon \cdot 10^{-3}$ (nm ⁻²)
PA6-0	23.03	2.61665	30.98	10.42	11.19
PA6-1	23.44	2.2013	36.86	7.36	9.40
PA6-2	23.25	2.42247	33.48	8.92	10.35
PA6-3	23.44	2.22641	35.69	7.85	9.71

X-ray diffraction analysis of the sulfurized PA6 films showed that elemental hexagonal sulfur was diffused into PA6 surface. The peaks of PA6-0 at 9.27°, 18.78°, 20.07°, 23.1°, and 28.4° are attributed to sulfur S₆ [JCPDS No. 72-2402].

XRD studies of Cu₂S thin films are limited by the polycrystallinity of the layers obtained and by the semicrystallinity of the PA6 film itself. The intensity of the peak maximum of PA6 at $2\theta < 25^\circ$ exceeds few times the intensity of the copper sulfide peaks maxima. The XRD spectrum recorded after treatment of sulfurized PA6-0 film in Cu(I/II) salt solution shows the peaks at 9.37° (attributed to sulfur), 20.22°, 23.24° and 28.5° (attributed to copper sulfide phase) and indicates the formation of chalcocite, Cu₂S [JCPDS No. 12-227]. Although the overlapping of XRD peaks makes their identification difficult, the XRD data for other sulfurized and treated samples with copper sulfate solutions are presented in Table IV. They indicate that the composition of Cu₂S layers does not depend on the pre-treating method of the polymer surface.

Tab. IV Comparison of d -spacing, angle values and their respective planes for Cu₂S layers obtained by different pre-treating methods of polyamide surface.

	PA6-0		PA6-1		PA6-2		PA6-3		(hkl)
	2θ (°)	d (Å)	2θ (°)	d (Å)	2θ (°)	d (Å)	2θ (°)	d (Å)	
S (hexagonal) JCPDS No 72-2402	9.27	9.53	9.27	9.54	9.27	9.54	9.31	9.49	(100)
	18.78	4.72	18.76	4.72	18.76	4.72	18.83	4.71	(200)
	20.07	4.42	20.14	4.4	20.14	4.4	20.05	4.4	
	23.1	3.85	22.95	3.87	22.95	3.87	23.3	3.8	(101)
	28.4	3.14	28.41	3.14	28.41	3.14	28.5	3.13	(300)
Cu₂S (orthorhombic) JCPDS No 12-227	20.22	4.39	20.12	4.41	20.12	4.41	20.03	4.43	(212)
	23.24	3.82	23.20	3.83	23.20	3.83	23.3	3.81	(133)
	28.5	3.13	28.54	3.13	28.54	3.13	28.48	3.14	(351)

3.2. FTIR spectrum analysis

The FTIR spectra of PA6 films are shown in Fig. 2. PA6 has IR active bands: the stretching band of N–H at about ~ 3295 cm⁻¹; at ~ 3077 cm⁻¹ due to the first overtone of amide II; the symmetrical and asymmetrical stretching bands of a methylene group (CH₂) at ~ 2862 and ~ 2932 cm⁻¹, respectively. The band at ~ 1635 cm⁻¹ corresponds to the stretching of the amide carbonyl and the one at ~ 1537 cm⁻¹ is due to the amide II (N–H) in plane bending and C–N stretching [40,41]. In the 650–1400 cm⁻¹ region of the IR spectra, the modes attributed to CH₂ sequences (1478 cm⁻¹ – CH₂ scissor vibration, 1373 cm⁻¹ – amide III and CH₂ wag vibration, 1199 cm⁻¹ – CH₂ twist-wag vibration, 959 cm⁻¹ CO–NH in plane

vibration) and crystalline forms of PA6 films can be distinguished. This confirms that the sample studied consists predominantly of α crystalline form.

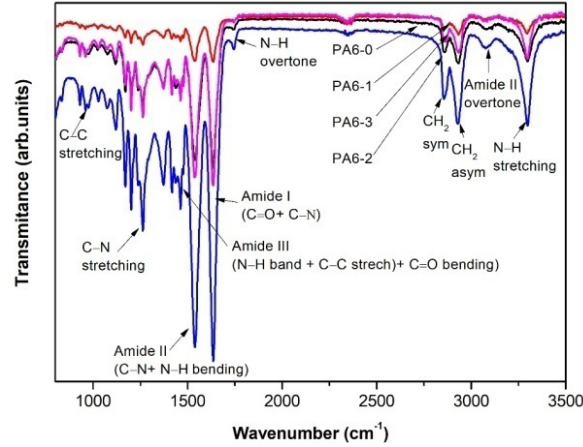


Fig. 2. FTIR spectra of PA6.

All peaks are consistent with the data in the literature [40,42], but the peak intensities differ when PA6 samples are prepared differently. More intensive peaks were obtained by the treatment of PA6 with an alkali solution. However, no significant differences were observed between the spectra of the PA6-0 and PA6-1, PA6-2, or PA6-3. There were no changes in the shape of these peaks compared to the PA6-0 sample.

3.3. UV-VIS absorption spectroscopy

The UV-VIS absorption spectroscopy is a powerful tool for the investigation of the optical properties of the material. In this study we used Tauc plot for the determination of optical band gap from absorbance measurements [43]:

$$\alpha h\nu = A(h\nu - E_g)^n \quad (5)$$

where α is the absorption coefficient; $h\nu$ – photon energy; E_g – energy band gap; A – a constant; n – a constant for a given transition ($n=2$ for direct transition and $n=1/2$ for indirect transition). The optical band gap can be estimated by extrapolating the linear portion of the $(\alpha h\nu)^2$ and, respectively $(\alpha h\nu)^{1/2}$ plots versus $h\nu$ to $\alpha = 0$ [44].

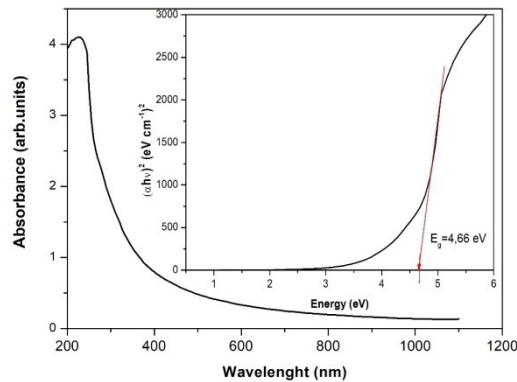


Fig. 3. UV-VIS absorbance spectrum and plot of $(\alpha h\nu)^2$ against $h\nu$ for PA6-0 film (inset).

The energy band gap for pure PA6 is 4.66 eV (Fig. 3), which means that the polymer is an insulator. The variations in UV-VIS absorbance spectra of PA6 boiled in distilled water, exposed to a NaOH solution, and boiled in distilled water for 120 min and subsequently exposed to a NaOH solution for 120 min at 80°C are not pronounced in the shape compared to unaterated polyamide 6.

Fig. 4 illustrates that copper sulfide films show strong absorption in the UV region (maximum at cca 320 nm with a shoulder at cca 350 nm) while in the VIS region the absorbance drastically drops.

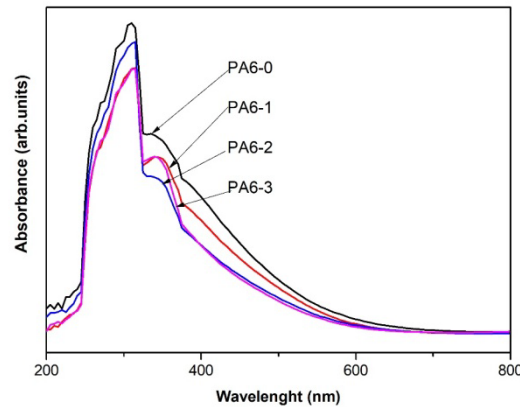


Fig. 4. UV-VIS absorbance spectra of PA6/Cu₂S films.

Both direct- and indirect-allowed transitions are exhibited in the Cu₂S film. The experimentally determined values of energy gaps for Cu₂S thin films slightly differ, their values range from 2.61 to 2.67 eV for direct transitions (Fig. 5), and from 1.40 to 1.44 eV in the case of indirect transitions (Fig. 6). It seems that despite the way the samples of polymer were treated prior to deposition, their optical properties, such as band gap energies, are quite similar.

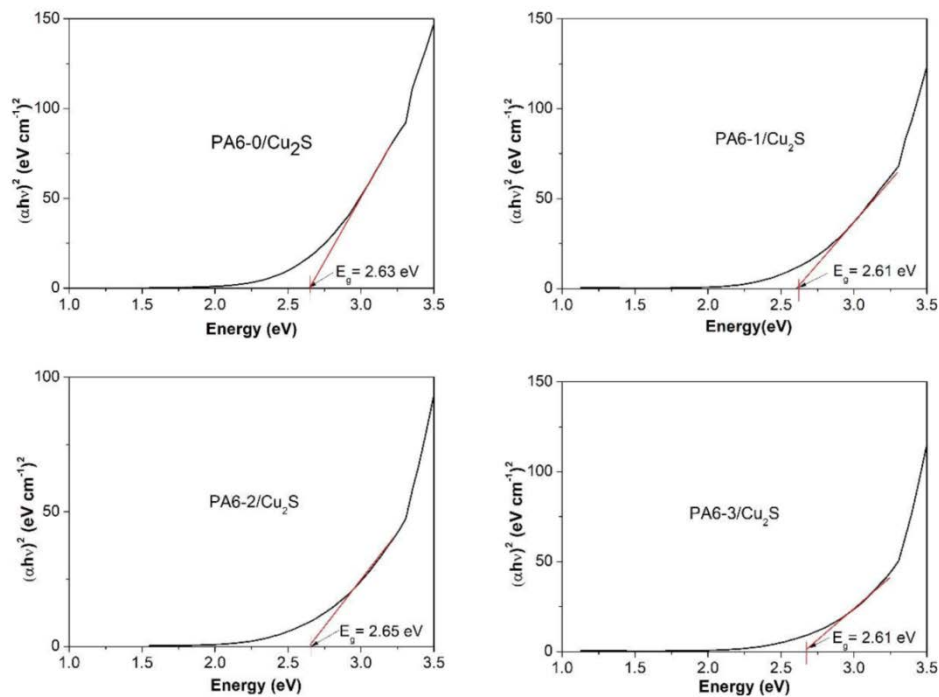


Fig. 5. Plot of $(\alpha h\nu)^2$ against $h\nu$ for PA6/Cu₂S films (Direct transition).

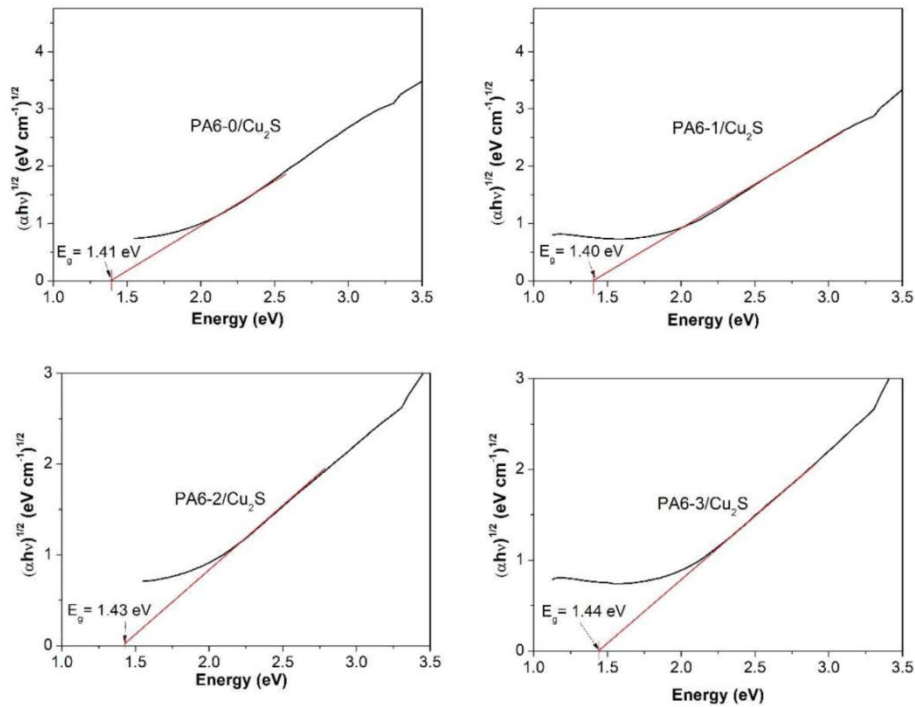


Fig. 6. Plot of $(\alpha hv)^2$ against hv for PA6/Cu₂S films (Indirect transition).

In the literature [6,45,46], we can see that the values obtained for E_g by different authors were not exactly the same: the energy band gap values for Cu₂S vary from 1.0 to 1.5 eV for indirect transitions and from 2.40 to 2.96 eV for direct transitions. Different values of the energy gap may be due to different techniques of preparation, the thickness of the films obtained, the particle size, and the mechanism of light absorption in the film.

Table V gives the values of the energy gaps obtained in the present work. These results are consistent with the literature [6,45,46].

Tab. V The band gap energies of copper sulfide thin films deposited on polymer.

	PA6-0/Cu ₂ S	PA6-1/Cu ₂ S	PA6-2/Cu ₂ S	PA6-3/Cu ₂ S
Direct transition (eV)	2.63	2.61	2.65	2.67
Indirect transition (eV)	1.41	1.40	1.43	1.44

The lowest band gap result was obtained for PA6-1/Cu₂S. A lower bandgap implies higher intrinsic conductivity, i.e. as the energy band gap decreases, the electrical conductivity increases. Therefore, the optical constants were calculated just for PA6-1/Cu₂S film. As mentioned above, this film has also the best crystallinity.

The optical constants of Cu₂S thin films were studied using optical absorption theory [6]. According to the conservation law of energy theory, the relation between reflectance (R), transmittance (T), and absorbance (A) is:

$$R+T+A=1 \quad (6)$$

where transmittance (T) was measured by $T = 10^{(-A)}$. Additionally, the optical constants of Cu₂S thin films such as the refractive index (n) and the extinction coefficient (k) are important parameters for thin films. The extinction coefficient (k) is the attenuation per unit radiation, and it is related to the absorption coefficient by the following relation:

$$k = \frac{\alpha\lambda}{4\pi}. \tag{7}$$

The refractive index (n) is the measure of how fast light propagates through the material. The higher the refractive index is, the slower light travels through the material, which changes its direction. It is a very important optical property in designing optical devices. There are many ways to determine the refractive index of the material. In this work, the approach of H. Pathan et al. is used [6]:

$$n = \frac{1 + \sqrt{R}}{1 - \sqrt{R}}. \tag{8}$$

The plots of absorbance (A), reflectance (R) and transmittance (T) against wavelength (λ) (a) and plots of refractive index (n) and extinction coefficient (k) against $h\nu$ (b) for PA6-1/Cu₂S thin film are shown in Fig. 7.

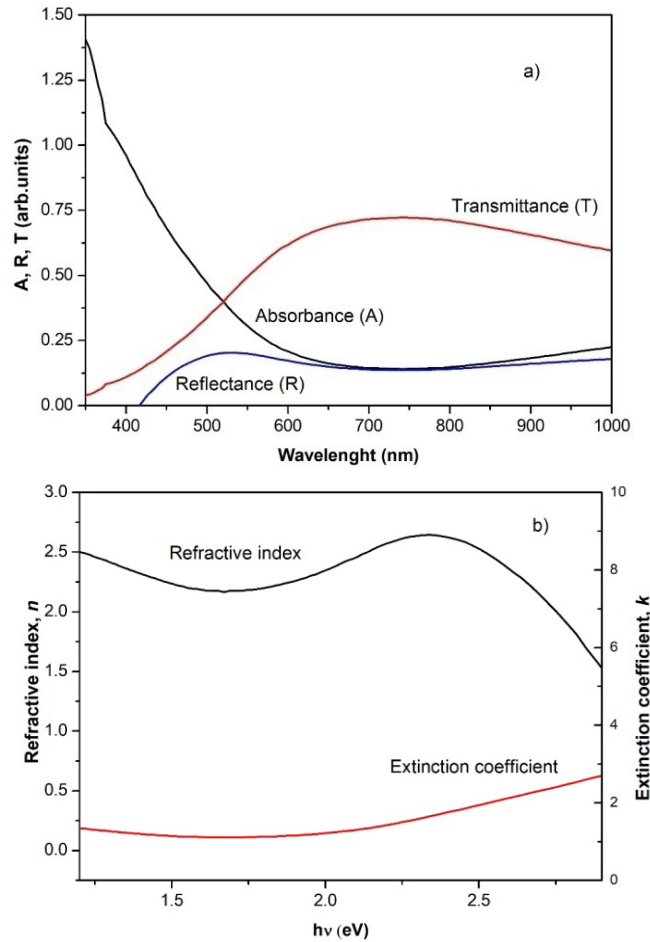


Fig. 7. Plots of absorbance (A), reflectance (R) and transmittance (T) against wavelength (λ) (a) and plots of refractive index (n) and extinction coefficient (k) against $h\nu$ (b) for PA6-1/Cu₂S thin film.

The refractive index value exhibits a minimum at ~ 2.17 for the PA6-1/Cu₂S thin film at the energy equal to 1.68 eV. The extinction coefficient of the Cu₂S thin film at the same energy was found to be 0.11.

The real (ϵ_r) and the imaginary (ϵ_i) part of dielectric constant for the same film were determined using the relations [6]:

$$\epsilon_r = n^2 - k^2, \quad (9)$$

$$\epsilon_i = 2nk. \quad (10)$$

The obtained results were shown in Fig. 8.

The imaginary part confirms the contribution of the free carrier to the absorption. From Fig. 7 and Fig. 8 it can be seen that the real and imaginary dielectric constants have the same behaviour as the refractive index and extinction coefficient.

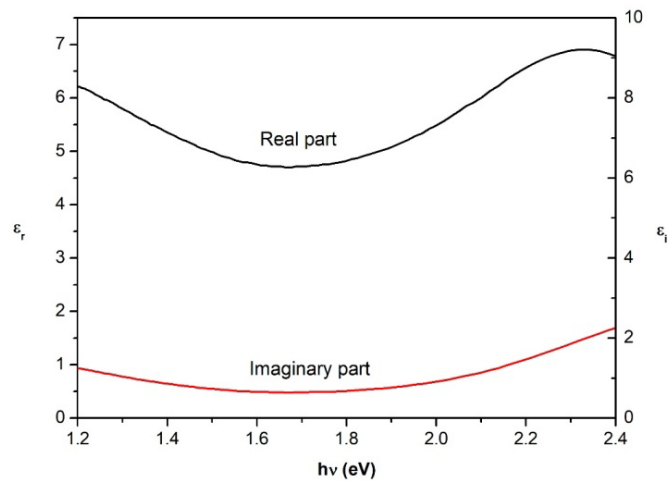


Fig. 8. Plot of real (ϵ_r) and the imaginary (ϵ_i) part of the dielectric constant against $h\nu$ for PA6 - 1/Cu₂S thin film.

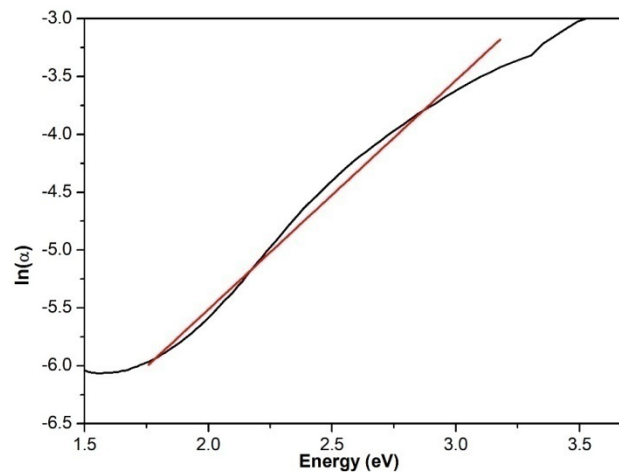


Fig. 9. Plot of $\ln(\alpha)$ against $h\nu$ for PA6-1/Cu₂S thin film.

The defect states in the optical band gap region are represented by Urbach energy, which can be extracted from absorption spectra and can be calculated using the following relation [47,48]:

$$\alpha = \alpha_0 \exp\left(\frac{E}{E_u}\right), \quad (11)$$

where α is the absorption coefficient; α_0 is constant; E is the incident photon energy which is equal to $h\nu$, and E_u is the Urbach energy. The Urbach energy can be obtained from the slope of the straight line of plotting $\ln(\alpha)$ against the incident photon energy $h\nu$. Fig. 9 shows the variation of $\ln(\alpha)$ versus $h\nu$ for the PA6-1/Cu₂S film.

The Urbach energy value was calculated from the reciprocal of the straight line slope of PA6-1, with the obtained value of 0.51 eV.

The optical conductivity (σ) was determined using the relation [46]:

$$\sigma = \frac{\alpha n c}{4\pi} \quad (12)$$

where α is the absorption coefficient; n is the refractive index of the film, and c is the speed of light in a vacuum. Fig. 10 shows the variation of optical conductivity (σ) with energy. The increased optical conductivity is due to the high absorbance of the copper sulfide thin film.

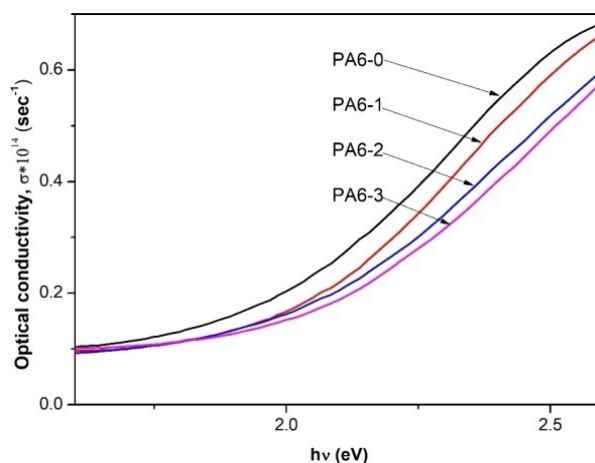


Fig. 10. Plot of optical conductivity (σ) against $h\nu$ for PA6/Cu₂S thin film.

The parameters determined for the thin films were compared to those published for Cu₂S thin films prepared by similar techniques, and it was found that the results of optical constants are consistent with the data from the literature [6].

3.4. Measurements of electrical resistivity

Formed Cu₂S layers changed conductivity of PA6: the surface resistance of pure PA6 is $1.0 \times 10^{12} \Omega/\text{sq}$. The square sheet resistance measurements of Cu₂S layers on PA6 matrix showed that the lowest resistivity was obtained on a sample which was formed on PA6-1 (~7 k Ω/sq), next value was for PA6-3 (~10 k Ω/sq), then on PA6-0 (~60 k Ω/sq), and on PA6-2 electrically conductive layers are not formed (6 M Ω/sq).

4. Conclusion

Copper sulfide thin films are deposited on a polymer substrate using the novel sorption-diffusion method. XRD analysis has revealed that the crystallinity of the non-treated

PA6 sample is the highest. After the pre-treatment of PA6, the position and intensity of the peaks changed slightly in diffractograms. According to the diffractograms, elemental hexagonal sulfur was diffused into PA6 surface after sulfurization. The XRD pattern indicates that the Cu_xS films possess a structure that matches the orthorhombic crystal system of the chalcocite (Cu_2S) phase. Direct and indirect allowed transitions are exhibited for Cu_2S thin films with energy band gaps of 2.61–2.67 eV and 1.4–1.44 eV, respectively. The lowest resistance of copper sulfide thin film was found on PA6-1/ Cu_2S and equals $\sim 7 \text{ k}\Omega/\text{sq}$. It has been proven that films of good quality for optoelectronic application could be produced by implementing a simple and low-cost technique.

Acknowledgments

Neringa Petrasauskiene: Conceptualization, Methodology, Investigation, Visualization, Writing - original draft. Edita Paluckiene: Data curation, Methodology, Investigation, Validation, Writing – review & editing. Rasa Alaburdaite: Methodology, Investigation, Writing – review & editing. Martina Gilic: Data curation, Validation, Writing – review & editing.

5. References

1. N. S. Kozhevnikova, L. N. Maskaeva, V. P. Markov, O. A. Lipina, A. U. Chufarov, M. V. Kuznetsov, *Mater. Chem. Phys.*, 242 (2020) 122447.
2. L. Isac, I. Popovici, A. Enesca, A. Duta, *Energy Procedia*, 2 (2010) 71.
3. I. Grozdanov, M. Najdoski, *J. Solid State Chem.*, 114 (1995) 469.
4. Y. Zhao, C. Burda, *Energy Environ. Sci.*, 5 (2012) 5564.
5. K. R. Nemade, S. A. Waghuley, *Mater. Sci. Semicond. Process.*, 39 (2015) 781.
6. H. M. Pathan, J. D. Desai, C. D. Lokhande, *Appl. Surf. Sci.*, 202 (2002) 47.
7. Y. Du, Z. Yin, J. Zhu, X. Huang, X. J. Wu, Z. Zeng, Q. Yan, H. Zhang, *Nat. Commun.*, 3 (2012) 1.
8. X. Yu, C. Cao, H. Zhu, Q. Li, C. Liu, Q. Gong, *Adv. Funct. Mater.*, 17 (2007) 1397.
9. L. Qiana, J. Maa, X. Tiana, H. Yuan, D. Xiaoa, *Sensors Actuators, B Chem.*, 176 (2013) 952.
10. H. Lee, S.W. Yoon, E.J. Kim, J. Park, *Nano Lett.*, 7 (2007) 778.
11. M. Tanveer, C. Cao, I. Aslam, Z. Ali, F. Idrees, M. Tahir, W.S. Khan, F.K. Butt, A. Mahmood, *RSC Adv.*, 4 (2014) 63447.
12. Z. Cheng, S. Wang, Q. Wang, *B*) 144.
13. Y. Wu, C. Wadia, W. Ma, B. Sadtler, A.P. Alivisatos, *Nano Lett.*, 8 (2008) 2345.
14. D. Majumdar, *J. Electroanal. Chem.*, 880 (2021) 114825.
15. K.P. Ganesan, A.A. Roselin, *Nano-Structures and Nano-Objects.*, 17 (2019) 138.
16. L. Meng, *Mater. Lett.*, 236 (2019) 131.
17. L. Wu, J. Gao, Z. Qin, Y. Sun, R. Tian, Q. Zhang, Y. Gao, *J. Power Sources*, 479 (2020) 228518.
18. S. Roy, J.W. Rhim, L. Jaiswal, *Food Hydrocoll.*, 93 (2019) 156.
19. A.N. Nikam, A. Pandey, G. Fernandes, S. Kulkarni, S.P. Mutalik, B.S. Padya, S.D. George, S. Mutalik, *Coord. Chem. Rev.*, 419 (2020) 213356.
20. *Commun.*, 122 (2020) 108294.
21. M. Nenadovic, D. Kistic, M. Mirkovic, S. Nenadovic, Lj. Kljajevic, *Sci. Sinter.*, 53 (2021) 187.
22. J. Cardoso, O. Gomezdaza, L. Ixtlilco, M.T.S. Nair, P.K. Nair, *Semicond. Sci. Technol.*, 16 (2001) 123.

23. M.T.S. Nair, P.K. Nair, Semicond. Sci. Technol., 4 (1989) 191.
24. A. Galdikas, A. Mironas, V. Strazdiene, A. Setkus, I. Ancutiene, V. Janickis, Sensors Actuators, B Chem., 67 (2000) 76.
25. A. A. Sagade, R. Sharma, I. Sulaniya, J. Appl. Phys. 105 (2009) 043701.
26. Y. He, T. Day, T. Zhang, H. Liu, X. Shi, L. Chen, G.J. Snyder, Adv. Mater., 26 (2014) 3974.
27. V. Janickis, N. Petrašauskiene, S. Žalėnkiene, I. Morkvenaite-Vilkonciene, A. Ramanavicius, J. Nanosci. Nanotechnol., 18 (2018) 604.
28. E. Balciunaite, N. Petrasauskiene, R. Alaburdaite, G. Jakubauskas, E. Paluckiene, Surfaces and Interfaces, 21 (2020) 100801.
29. R. Alaburdaite, E. Paluckiene, Chalcogenide Lett., 15 (2018) 139.
30. S. L. Fávoro, A. F. Rubira, E. C. Muniz, E. Radovanovic, Polym. Degrad. Stab., 92 (2007) 1219.
31. E. Parodi, G.W.M. Peters, L. E. Govaert, Polymers (Basel), 10 (2018) 1.
32. S. S. Banerjee, A. Janke, U. Gohs, G. Heinrich, Eur. Polym. J. 98 (2018) 295.
33. X. Y. Zhao, B.Z. Zhang, J. Appl. Polym. Sci., 115 (2010) 1688.
34. W.H. Bragg, W.L. Bragg, Proc. R. Soc. London. Ser. A, Contain. Pap. a Math. Phys. Character. 88 (1913) 428-438.
35. A.L. Patterson, Phys. Rev., 56 (1939) 978.
36. B. Güzeldir, M. Sallam, Spectrochim. Acta - Part A Mol. Biomol. Spectrosc., 150 (2015) 111.
37. M. Ashraf, S.M.J. Akhtar, A. F. Khan, Z. Ali, A. Qayyum, J. Alloys Compd., 509 (2011) 2414.
38. M. Saadeldin, H. S. Soliman, H.A.M. Ali, K. Sawaby, Chinese Phys. B, 23 (2014) 046803.
39. H. Shashidharagowda, S. Mathad, M. Abbigeri, Sci. Sinter., 53 (2021) 429.
40. J. Maillo, P. Pages, E. Vallejo, T. Lacorte, J. Gacén, Eur. Polym. J., 41 (2005) 753.
41. N. Vasanthan, D. R. Salem, J. Polym. Sci. Part B Polym. Phys., 39 (2001) 536.
42. V. Krylova, N. Dukštienė, Appl. Surf. Sci., 470 (2019) 462.
43. J. Tauc, R. Grigorovici, A. Vancu, Phys. Status Solidi, 15 (1966) 627.
44. M. Petrovic, M. Gilic, J. Cirkovic, M. Romcevic, N. Romcevic, J. Trajic, I. Yahia, Sci. Sinter., 49 (2017) 167.
45. L. Reijnen, B. Meester, A. Goossens, J. Schoonman, Chem. Vap. Depos., 9 (2003) 15.
46. T. Hurma, S. Kose, Optik (Stuttg), 127 (2016) 6000.
47. H. Chamroukhi, Z. Ben Hamed, A. Telfah, M. Bassou, A. Zeinert, R. Hergenröder, H. Bouchriha, Opt. Mater. (Amst), 84 (2018) 703.
48. A. El-Denglawey, M.M. Makhlof, M. Dongol, M.M. El-Nahass, J. Mater. Sci. Mater. Electron., 26 (2015) 5603.

Сажетак: У овом раду је представљена нова и повољна метода припреме филмова бакар сулфида на полиамиду. Нетретирани, као и претходно третирани РАБ филмови помоћу 3 различите методе (у кључалој води; у раствору NaOH; у кључалој води на у раствору NaOH) су коришћени као супстрати за формирање слојева Cu_2S сорпционо – дифузионом методом. Као сулфоризациони агенс коришћен је топљени сумпор. За карактеризацију структурних, оптичких и електричних особина узорака, али и за праћење промена након сваког ступња третирања, коришћене су XRD, FTIR и UV-VIS технике. Површински отпор слојева Cu_2S зависи од методе третирања полимера и креће се између 7 $\text{k}\Omega/\text{sq}$ и 6 $\text{M}\Omega/\text{sq}$. На основу UV-VIS мерења одређене су ширине забрањених зона за директне и индиректне прелазе, и крећу се у опсегу 2.61 – 2.67 eV и 1.40 – 1.44 eV респективно. Одређене су и оптичке константе n , k и σ .

Кључне речи: Танки филмови, бакар сулфид, Полиамид 6, Дифракција рендгенског зрачења, Оптичке особине.

© 2022 Authors. Published by association for ETRAN Society. This article is an open access article distributed under the terms and conditions of the Creative Commons — Attribution 4.0 International license (<https://creativecommons.org/licenses/by/4.0/>).



Submitted: 12.06.2024.

Accepted: 17.08.2024.

Nanocomposite Cu_xS on Flexible Polymers: Raman Study

Milica Curcic^{*1}, Martina Gilic¹, Neringa Petrasauskiene², Branka Hadzic¹, Jelena Mitric¹,
Edita Paluckiene²

¹*Institute of Physics Belgrade, University of Belgrade, Belgrade 11080, Serbia*

²*Department of Physical and Inorganic Chemistry, Kaunas University of Technology, LT-50254 Kaunas, Lithuania*

Milica Curcic – ORCID 0000-0001-9239-0912

Martina Gilic – ORCID 0000-0002-5715-7717

Neringa Petrasauskiene – ORCID 0000-0002-8666-112X

Branka Hadzic – ORCID 0000-0001-5459-7461

Jelena Mitric – ORCID 0000-0002-1526-3976

Edita Paluckiene – ORCID 0000-0002-9957-0497

<https://doi.org/10.2298/SOS240612034C>

Abstract

Flexible polymers modified with copper sulfides have emerged as a novel class of materials, presenting composite structures with remarkable properties suitable for applications in flexible electronics. This study focuses on the deposition of copper sulfide (Cu_xS) layers onto the surfaces of polyamide and polypropylene through the chemical bath deposition method, employing either 2 or 3 deposition cycles. The objective is to explore the impact of deposition cycles and discern the optimal conditions for the deposition process. Comprehensive analysis of the Cu_xS thin films entails techniques such as scanning electron microscopy (SEM), Raman spectroscopy, UV-VIS spectroscopy, and X-ray diffraction to shed light on their structural and optical characteristics.

Keywords: *Copper Sulfide, Nanocomposite, Optical properties, SEM, Raman spectroscopy, UV-VIS spectroscopy, X-ray diffraction*

* Corresponding author: Milica Curcic, Institute of Physics Belgrade, University of Belgrade, Pregrevica 118, Belgrade, Serbia
mail: milicap@ipb.ac.rs

1. INTRODUCTION

The CuS, commonly referred to as covellite, demonstrates both superconducting and metallic behaviour at distinct temperatures, as documented in various studies [1-5]. Notably, this material is environmentally friendly and abundant. Its considerable potential for application in Li-ion rechargeable batteries has been widely recognized [6-8]. Additionally, numerous reports highlight its suitability for use in optoelectronic devices [9], solar cells [2, 5, 9, 10], photo catalytic activity [11], chemical sensing [12], and in the fabrication of gas sensors for devices [8, 13, 14]. The origin of superconductivity in CuS is elucidated by its intriguing crystal symmetry. It possesses two distinct crystalline forms at different temperatures. Under ambient conditions, it adopts a hexagonal structure with the space group $P63/mmc$ ($Z=6$) [15, 16, 17]. However, at a low temperature of approximately 55K, it undergoes a structural phase transition from a hexagonal structure to orthorhombic crystal symmetry ($Cmcm$) [17]. Despite extensive investigations of the structure and associated properties of CuS, the findings exhibit mutual inconsistencies. Notably, there are conflicting reports regarding the transition temperatures from the conducting to the superconducting state in CuS. Raveau et al. [18] have documented superconducting behaviour below 40K, while Buckel et al. and Saito et al. independently observed it at remarkably lower temperatures, specifically 1.2K and 1.72K, respectively [19, 20].

Copper sulfide forms five stable phases at room temperature: covellite (CuS), anilite (Cu_{1.75}S), digenite (Cu_{1.8}S), djurleite (Cu_{1.95}S) and chalcocite (Cu₂S) with a crystal structure varying from orthogonal to hexagonal [13]. Copper sulfide films are interesting absorber materials with their film solar cells with ideal optical characteristics [5, 21, 22]. Copper sulfide thin films maintain transmittance in the infrared region, low reflectance in the visible region, and relatively high reflectance in the near infrared region, which has been used in many applications, including solar control coatings, solar energy conversion, electronic, and low-temperature gas sensor applications [14, 21, 22, 23].

Furthermore, disagreement persists regarding the valence state of the Cu atom within the structure. Several oxidation formalisms propose a valence state for the Cu atom ranging from 1 to 1.4e⁻ [20, 24, 25]. Conversely, X-ray absorption spectroscopy (XAS) and X-ray photoelectron spectroscopy (XPS) assert the ionic state of the Cu atom with a valency of 1e⁻ [10, 26, 27]. Kumar et al.'s XAS investigation [28] reports two oxidation states of the Cu atom, corresponding to two distinct crystallographic positions. Moreover, X-ray emission spectroscopy (XES) and X-ray absorption near-edge spectroscopy (XANES) consistently depict the same valence state of the S atom in solid CuS [29, 30, 31]. Consequently, a consensus on the aforementioned aspects of CuS remains elusive.

Nanocomposites are a class of composites wherein at least one of the constituent phases exhibits dimensions within the nanometer range [6]. These materials have emerged as promising alternatives to address the limitations associated with microcomposites and monolithics. However, their preparation presents challenges, particularly in the precise control of elemental composition and stoichiometry

within the nanocluster phase. Widely regarded as materials defining the 21st century, nanocomposites possess distinctive design characteristics and property combinations not observed in traditional composites.

Polymer nanocomposites consist of two primary elements: an organic polymer matrix and inorganic components, often semiconductors. This category encompasses a variety of structures, including three-dimensional metal matrix composites, lamellar composites, colloids, porous materials, gels, and copolymers where nanosized materials are dispersed within the bulk matrix. The properties of these nanocomposites are intricately linked to the characteristics of their components, morphology, and interfaces. To broaden the potential applications of polymer nanocomposites, enhancements in the thermal, mechanical, and electronic properties of conventional polymer materials are essential [32, 33]. This necessitates a concerted effort to improve and optimize these properties, thereby extending the range of possible applications for these advanced materials.

Usage of polymer films, coated with electroconductive layers, has been increasing in the past years due to their elasticity, resistance against corrosion and low toxicity. Electrically conductive Cu_xS layers on polymers can be prepared by methods of vacuum evaporation, activated reactive evaporation [13], electroless deposition [34], successive ionic layer adsorption and reaction (SILAR) [15], chemical bath deposition [35], and sorption–diffusion methods [36, 37].

Polyamide is a semihydrophilic polymer with the ability to absorb ions and molecules from various electrolytes in both aqueous and non-aqueous solutions [38]. This property makes it useful for a range of applications. Polyamide is known for its high thermal resistance and excellent mechanical properties. Types of Polyamide:

- Nylon 6 (PA 6): This is a widely used polyamide with good mechanical properties and excellent resistance to abrasion.
- Nylon 66 (PA 66): Known for its high melting point and chemical resistance, it is commonly used in the automotive industry.

Nylon is widely used in the textile industry for the production of fabrics, garments, and carpets. Polyamide is used in various automotive components, such as gears, bushings, and engine parts. Nylon is used in the production of durable and heat-resistant plastic parts.

On the other hand, polypropylene (PP) is an economical thermoplastic polymer that boasts outstanding chemical, physical, and mechanical characteristics. These include flame resistance, transparency, a high heat distortion temperature, dimensional stability, and recyclability, making it well-suited for a wide array of applications [39, 40, 41, 42]. Polypropylene is relatively rigid, has a high melting point (160–166 °C), low density (0.91–0.94 g/cm³), and demonstrates good resistance to high temperatures, chemical agents, and impacts [43].

This study aimed to investigate the morphology and optical properties of copper sulfide layers formed on polyamide and polypropylene film using the chemical bath deposition method. Structural characterization of the thin films was performed with the help of X-ray diffraction, and Scanning

Electron Microscopy, while the optical properties were characterized with UV/VIS spectroscopy and Raman spectroscopy.

2. MATERIALS AND METHODS

2.1. Thin films formation

Commercially available PA (PA 6, Tecamid 6, Ensinger GmbH (Germany) and PP (Proline X998, KWH Plast, Finland) films were chosen as flexible substrates for the deposition of thin films of copper sulfide Cu_xS . The nominal characteristics of PP and PA films provided by the manufacturer are given in Table 1.

TABLE 1. Characteristics of PA and PP films

Polymer	Appearance	Thickness (μm)	Density (g/cm^3)	Surface Resistance (Ω)
PA	opaque	500	1.13	10^{12}
PP	clear	150	0.90	10^{16}

Acetone (CH_3COCH_3 , 99.5%), alcohol ($\text{CH}_3\text{CH}_2\text{OH}$, 95%), and all other chemicals used for deposition were purchased from Sigma-Aldrich and were of analytical grade, used without further purification.

Before the experiments, the PA films were boiled in distilled water for 2 h to remove the remaining un-polymerized monomer residues. PP films were etched for 25 min at 90 °C with oxidizing solution ($\text{H}_2\text{SO}_4/\text{H}_3\text{PO}_4$ (1:1), saturated with CrO_3) [39] Then, samples of polymers were dried with filter paper and incubated over anhydrous CaCl_2 for 24 h.

The Cu_xS thin films deposit was carried out at room temperature by using the following procedure: 0.05 M CuCl_2 and 0.05 M $\text{Na}_2\text{S}_2\text{O}_3$ were mixed, and the pH of the resultant solution was adjusted to 3. The pre-treated PA and PP samples were vertically immersed along the wall of the reactor and were left undisturbed for the deposition of Cu_xS films for 16 h at 20 °C. At the end of the deposition time, the samples were taken out and then the substrate was rinsing with distilled water for 30 s to remove the desorbed ions and dried in a desiccator for 8 h. The deposition process was carried out by repeating such deposition cycles 3 times. The formed samples were annealed at 80 °C for 30 minutes in an air atmosphere.

2.2. Thin films characterisation

Structural characterization of polymers coated with films was done by a Scanning Electron Microscope Hitachi SU8030 supported with a secondary electron detector.

Raman measurements were carried out in a backscattering configuration on a Horiba XploRA confocal Raman instrument equipped with a charge-coupled-device (CCD) detector. The spectra acquisition was carried out using an excitation laser wavelength of 532 nm of ca. 100mW power, in a spectral range of 200 – 1100 cm^{-1} .

The UV/VIS diffusion reflectance spectra were recorded in the wavelength range of 300 – 1000 nm on a Shimadzu UV-2600 spectrophotometer equipped with an integrated sphere. The absorbance spectra were measured relative to a reference sample of virgin polymers (PA and PP). The optical band gap from the absorbance measurements was calculated using the Tauc plot.

X-ray diffraction (XRD) measurements were performed using a Philips PW 1050 diffractometer equipped with a PW 1730 generator, 40 kV \times 20 mA, using Ni filtered Co K α radiation of 0.1778897 nm at room temperature. Measurements were carried out in the 2 θ range of 10 to 90° with a scanning step of 0.05° and a scan time of 10 s per step.

3. RESULTS AND DISCUSSION

3.1. Scanning Electron Microscopy

The scanning electron microscopy technique was used to evaluate the changes in the surface morphology of polyamide and polypropylene after 2 or 3 cycles of copper sulfide Cu_xS thin films deposition. The description makes reference to SEM micrographs in Figure 1. In Figure 1(a), the SEM images illustrate the initial state of the polymers, with PA on the left and PP on the right. In Figure 1(b), the SEM images indicate that copper sulfide grains exhibit irregular shapes and varying sizes after 2 cycles of film deposition. Following 3 cycles of film deposition, Figure 1(c) reveals micrographs displaying a dense structure composed of a single type of small, closely packed microcrystals. The thin copper sulfide films on the surfaces of PP and PA are well-dispersed, relatively uniform, and consist of randomly oriented particles. Such morphological characteristics can result in a highly rough surface with significant porosity, potentially leading to increased catalytic activity. The pronounced agglomeration on the surface of thin films indicates semiconductor characteristics of Cu_xS .

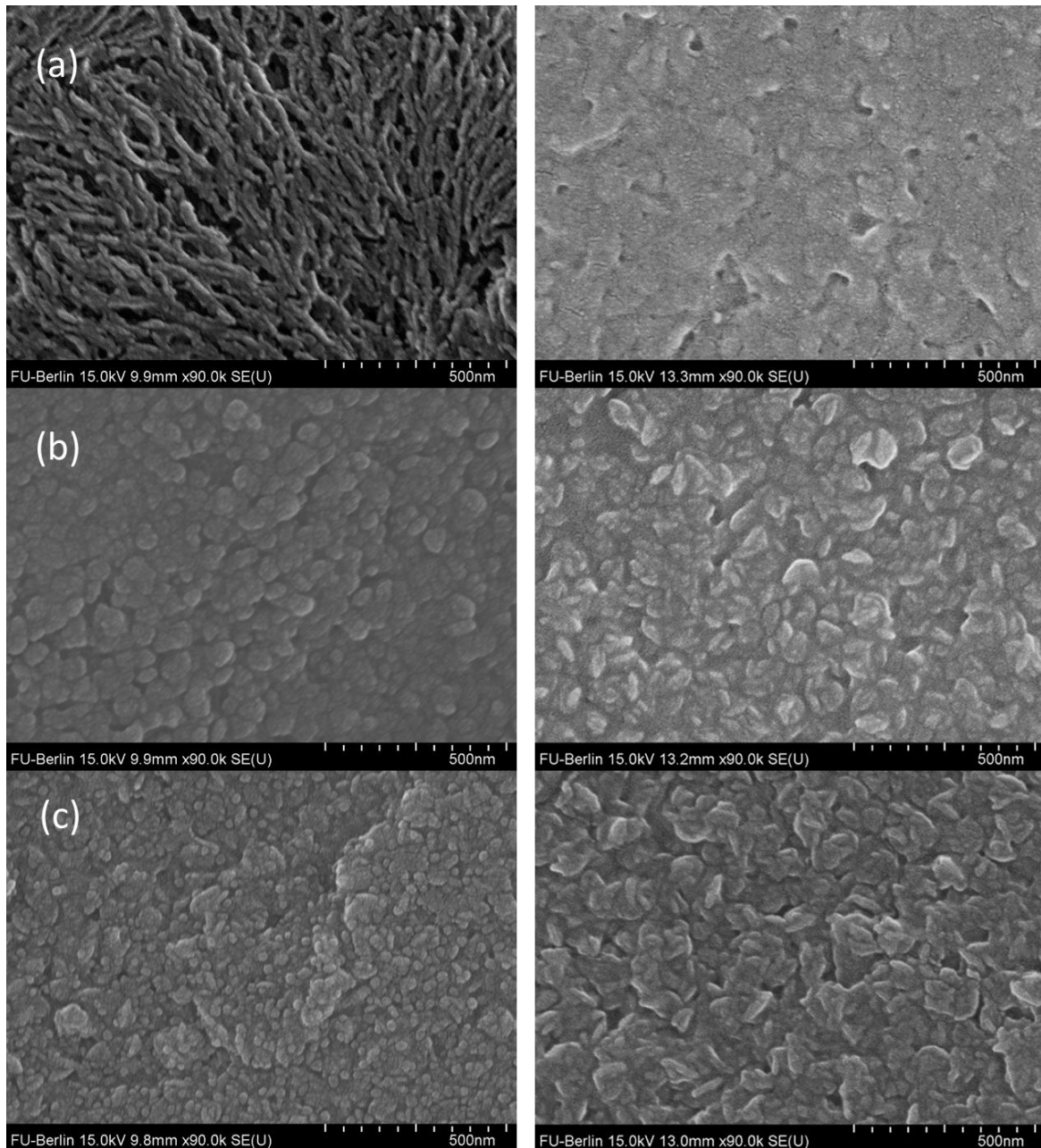


Figure 1. SEM micrographs of PA (left) and PP (right) polymers: (a) virgin polymers, (b) after 2 cycles of film deposition, and (c) after 3 cycles of film deposition.

PA showcases a porous structure reminiscent of seaweed, indicating a high degree of porosity. Consequently, it necessitates 3 cycles of film deposition to achieve the desired results. The substantial porosity on the surface of PA promotes strong adhesion and facilitates the growth of the copper sulfide film. In contrast, the surface of PP bears a resemblance to melted plastic and displays a porosity relatively lower than that of PA. For PP, the optimal outcome is achieved with 2 cycles of film deposition, as further cycles result in the agglomeration of film material.

These findings underscore the importance of customizing the number of film deposition cycles to align with the specific surface characteristics of different polymers. The choice of cycle count plays a pivotal role in shaping the resulting film morphology and its associated properties.

3.2. X-ray diffraction

The crystallinity and the preferred crystal orientation of the Cu_xS nanocomposite were analyzed by the XRD method. Figure 2 shows the diffraction pattern of the film. There is one high intensity diffraction peak around at $2\theta=28,46^\circ$ which is related to lattice planes of (101) (PDF 06-0464) the hexagonal phase of the Cu_xS covellite structure [4, 6, 22, 39]. The other peak that appeared with lower

intensities around at $2\theta=47^\circ$ is related to the lattice planes of (107) the Cu_xS covellite structure [39].

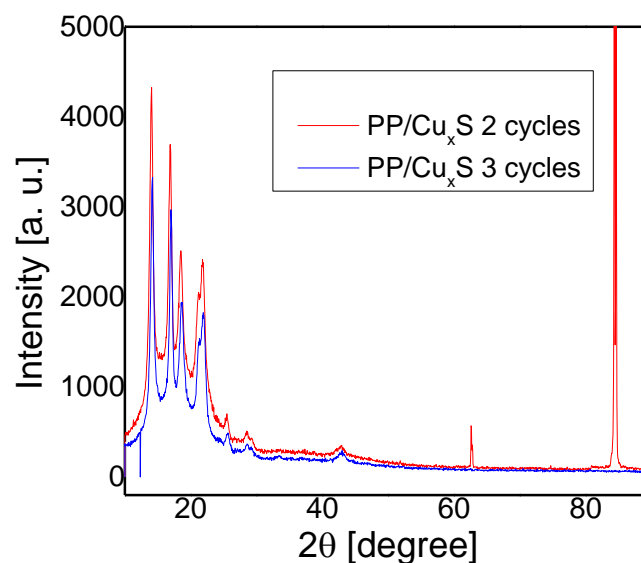
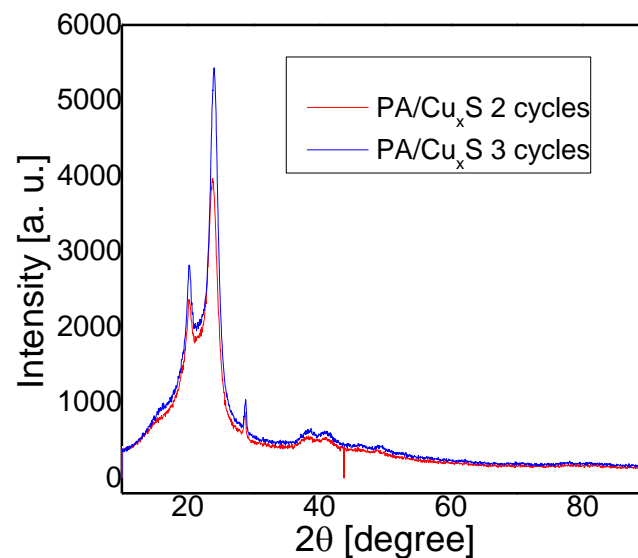


Figure 2. X-ray diffraction results of PA/Cu_xS and PP/Cu_xS after 2 or 3 cycles of deposition.

The peak of lower intensity in our case is visible only in the instance of Cu_xS on the flexible polymer PA. We also observe the appearance of an additional peak of very low intensity, noticeable only in the case of PP/Cu_xS after 3 cycles, corresponding to $2\theta=32.49$ degrees. This pertains to the Cu_{2-x}S ($0.6 \leq x \leq 1$) phase, present in the sample at a significantly lower concentration, as confirmed by the Raman spectrum [38].

3.3. UV-VIS Spectroscopy

UV/VIS analysis is able to describe the electrical properties of the materials. Bandgap (E_g), which indicated conductivity of the material: conductor, semiconductor or insulator, can be calculated from the data of this investigation. The optical absorption data have been analyzed to determine the optical bandgap values using the Tauc's relation [44]:

$$\alpha h = A(h\nu - E_g)^n \quad (1)$$

where α – the absorption coefficient, $h\nu$ – the photon energy, A – the proportionality constant, E_g – the optical bandgap, n – a constant associated with different types of electronic transitions.

The absorbance spectra of the film were measured in the range of 200–1000 nm, as shown in Figure 4. Films have max absorbance around 300 nm and then absorbance drops, one more hill in NIR region, around 900 nm, indicates a copper-deficient compound (Cu_xS or less).

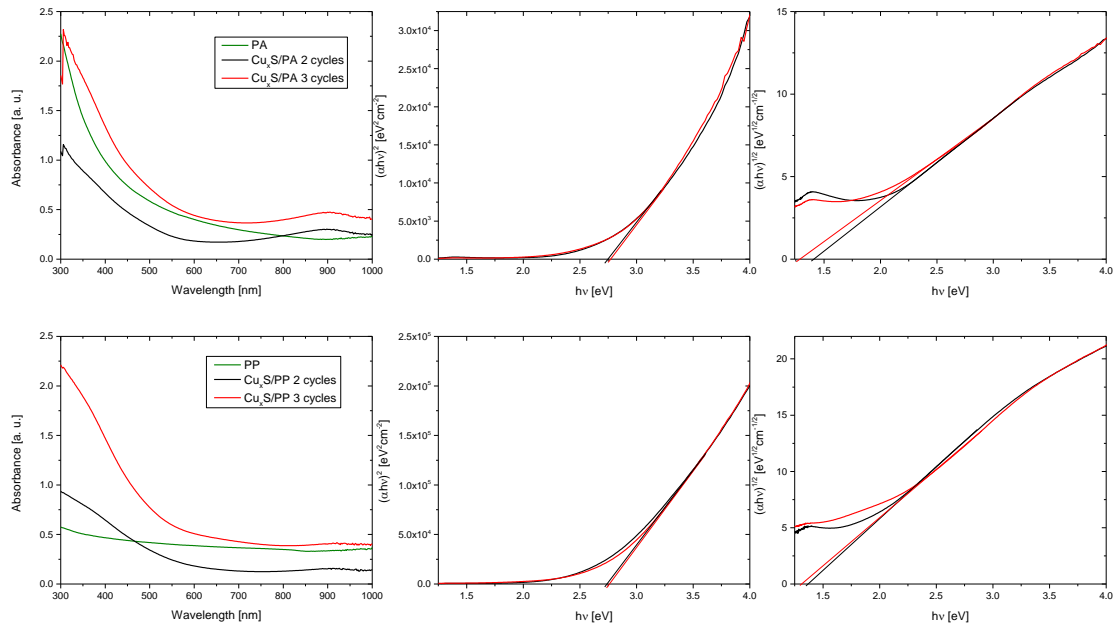


Figure 3. UV-VIS Absorbance spectra and spectra plot of $(\alpha hv)^2$ or $(\alpha hv)^{1/2}$ versus Photon energy ($h\nu$) for polymers with thin films.

The experimental values of $(\alpha hv)^2$ against $h\nu$ are plotted in Figure 3. The variation of $(\alpha hv)^2$ with $h\nu$ is linear, indicating that a direct transition is present. Extrapolating the straight-line portion of the plot of $(\alpha hv)^2$ against $h\nu$ to energy axis for the zero-absorption coefficient gives the optical band gap energy of the samples.

The energy band gap values for a thin film using PA polymer, which has a thickness of 0.05 cm, are as follows:

For the direct band gap:

- After 2 cycles: 2.75 eV
- After 3 cycles: 2.78 eV

For the indirect band gap:

- After 2 cycles: 1.41 eV
- After 3 cycles: 1.29 eV

These values represent the amount of energy required to transition an electron from the valence band to the conduction band. The direct band gap signifies the energy difference between the highest energy state in the valence band and the lowest energy state in the conduction band, whereas the indirect band gap considers transitions involving changes in momentum.

It is important to note that the number of film deposition cycles can have a discernible impact on the band gap values. In this particular case, subtle variations in the band gap values are observed between 2 and 3 cycles of film deposition for both direct and indirect transitions.

The energy band gap values for a thin film using PP (polypropylene) polymer, with a thickness of 0.02 cm, are as follows:

For the direct band gap:

- After 2 cycles: 2.76 eV
- After 3 cycles: 2.77 eV

For the indirect band gap:

- After 2 cycles: 1.37 eV
- After 3 cycles: 1.31 eV

It is noteworthy that the values of the direct band gap slightly exceed the typical range reported in the literature, which generally falls within 2.5 eV [45]. Although the film thickness did not differ significantly, the direct band gap values for all four samples were remarkably consistent. These results underscore that the PP/Cu_xS and PA/Cu_xS composites exhibit clear semiconductor properties, and their direct band gap values suggest their suitability as promising materials for the fabrication of solar cells.

3.4. Raman Spectroscopy PA and PP polymers with thin films

Raman spectroscopy provides valuable insights into the local structure of materials. Based on the XRD patterns, Cu_xS and Cu_{2-x}S can be expected in the Raman spectra. The knowledge of the vibrational properties of bulk material is deciding for the analysis of the vibration properties of nanoparticles; hence, we began the analysis of vibrational properties with a brief report of the data from the literature, which are related to the registered phases. Copper sulfide exists in five stable phases at room temperature. These phases have crystal structures that range from orthogonal to hexagonal. Hexagonal CuS crystals have a space group D_{6h}⁴ and a primitive unit cell that contains 12 atoms, namely, six of Cu and six S ones. Group theory analysis predicts eight Raman active modes of the zone-center for this crystal [46]:

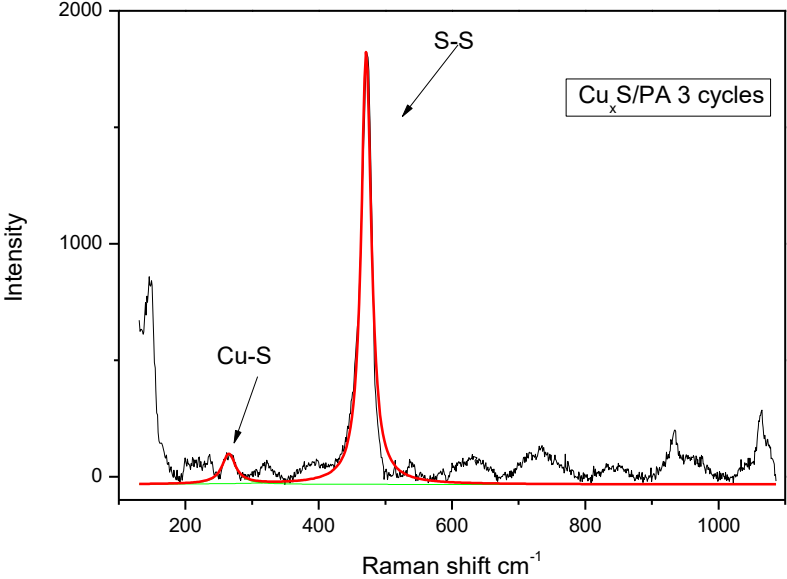
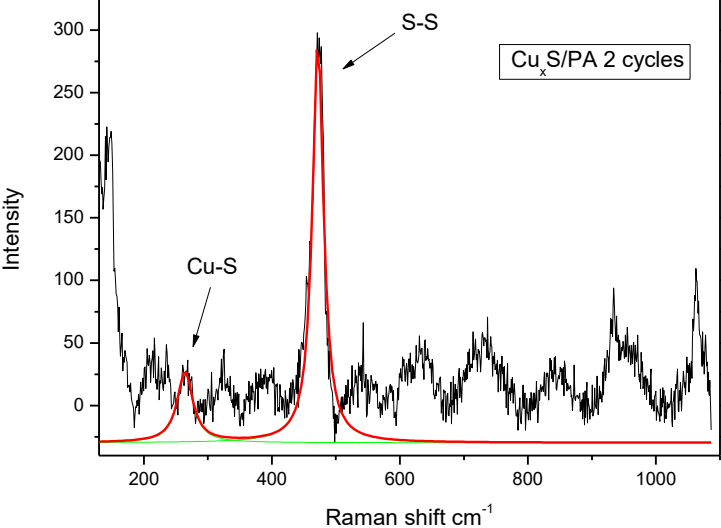
$$2A_{1g} + 2E_{1g} + 4E_{2g} \quad (2)$$

The Raman spectra are usually analyzed using the convolution of the Lorentzian functions, where each line has intensity (I), given with:

$$I(\omega) = \frac{2A}{\pi} \frac{W}{4(\omega - \omega_c)^2 + W^2} \quad (3)$$

where ω_c , W , and A are the position of the maximum, the half-width of the peak, and the peak intensity, respectively. In Figure 4, Raman spectra are depicted for PA and PP polymers with thin Cu_xS films following 2 or 3 cycles of film deposition, spanning the frequency range of 200-1100 cm⁻¹.

The data measured depicted with lines in Figure 4 resemble the calculated thick curve, which represents the sum of the components each one defined with Equation 3.



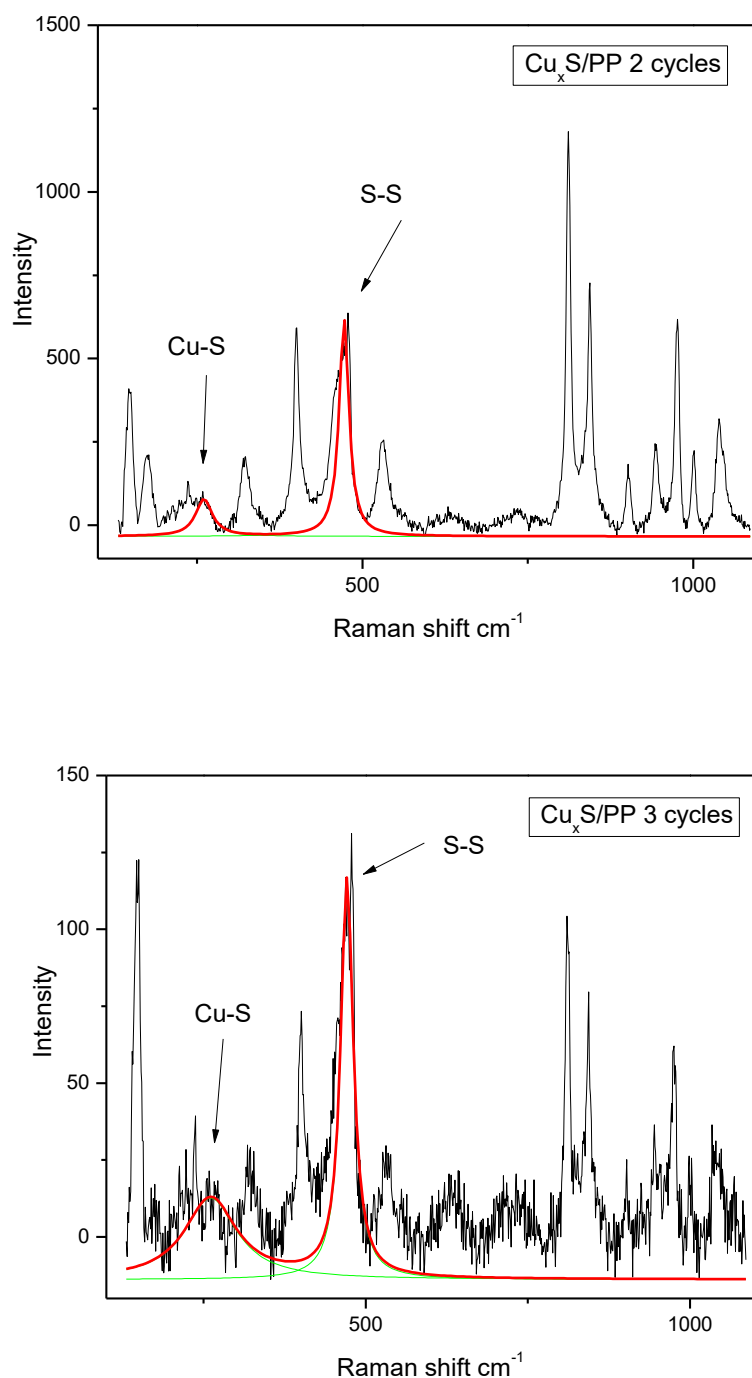


Figure 4. Raman spectra of the Cu_xS nanocomposite on PP and PA polymers.

A small peak at 265 cm⁻¹ corresponds to the Cu-S vibration in covellite (Cu_xS) [46]. Additionally, a highly sharp peak at 471 cm⁻¹ is attributed to the S-S stretching vibration of S₂ ions at the 4e sites [46]. The dominance of the S-S stretch band in the spectrum, particularly when the potential enters the region where Cu_{2-x}S is formed [47], suggests that lattice atoms are well-ordered in a periodic array. This result underscores the capability of Raman spectroscopy to distinguish between

copper sulfides with and without S-S bonding. Notably, the intensity of this peak increases after 3 cycles of film deposition. By increasing the number of deposition cycles, stable Cu_{2-x}S phases are obtained, opening up possibilities for new applications.

Raman spectroscopy is a technique that has enabled the determination of Cu_xS and Cu_{2-x}S phases composition in thin films nanocomposite. The presence of the Cu_xS phase is approximately 2,5%, while the Cu_{2-x}S phase is three times higher. In the case of PA polymer, after the third cycle of deposition, there is an increased agglomeration indicated by increased intensity of the mode. In the case of nanocomposite with PP, there is no pronounced agglomeration.

CONCLUSION

Copper sulfide thin films are deposited on a flexible polymer substrate using the chemical bath deposition method. Scanning electron microscopy was used to evaluate the changes in surface morphology of PA and PP after 2 or 3 cycles of film deposition Cu_xS . The thin copper sulfide films on surface of PP and PA are well dispersed, relatively uniform, and consist of randomly oriented particles. The XRD method was used to analyze the crystallinity and preferred crystal orientation of Cu_xS nanocomposite. There is one high intensity diffraction peak around at $2\theta=28,46^\circ$ which is related to lattice planes of (101) the hexagonal phase of the Cu_xS covellite structure. The other peak appeared with lower intensities around at $2\theta=47^\circ$ is related to the lattice planes of (107) the Cu_xS covellite structure. The peak of lower intensity in our case is visible only in the instance of Cu_xS on the flexible polymer PA. We also observe the appearance of an additional peak of very low intensity, noticeable only in the case of PP/ Cu_xS after 3 cycles, corresponding to $2\theta=32.49$ degrees. This pertains to the Cu_{2-x}S ($0.6 \leq x \leq 1$) phase, present in the sample at a significantly lower concentration, as confirmed by the Raman spectrum. Direct and indirect allowed transitions are exhibited for Cu_xS thin films with energy band gaps of 2.75–2.78 eV and 1.29–1.41 eV, respectively. Direct band gap values exceeding the conventional literature range indicate that these composites possess desirable semiconductor characteristics, rendering them potentially excellent candidates for utilization in photovoltaics applications. Raman spectroscopy has been utilized to analyze composition of Cu_xS and Cu_{2-x}S phases in thin film nanocomposition. In Raman spectra small peak at 265cm^{-1} corresponds to the Cu-S vibration in covellite (Cu_xS). Highly sharp peak at 471cm^{-1} is attributed to the S-S stretching vibration of S_2 ions at the $4e^-$ sites. The dominance of the S-S stretch band in the spectrum, particularly when the potential enters the region where Cu_{2-x}S is formed, suggests that lattice atoms are well-ordered in a periodic array.

Acknowledgement

This research was supported by the Science Fund of the Republic of Serbia, Grant No. 7504386, Nano Object in Own Matrix-Self Composite (NOOM-SeC).

References:

1. Rezig, B.; Duchemin, S.; Guastavino, F. Evaporated Layers of Cuprous Sulfides: Technology and Methods of Characterization. *Solar Energy Materials* **1979**, *2*, 53. [https://doi.org/10.1016/0165-1633\(79\)90030-3](https://doi.org/10.1016/0165-1633(79)90030-3)
2. Yepsen, O.; Yáñez, J.; Mansilla, H.D. Photocorrosion of Copper Sulfides: Toward a Solar Mining Industry. *Solar Energy* **2018**, *171*, 106. <https://doi.org/10.1016/j.solener.2018.06.049>
3. Lenggoro, I.W.; Kang, Y.C.; Komiyama, T.; Okuyama, K.; Tohge, N. Formation of Submicron Copper Sulfide Particles Using Spray Pyrolysis Method. *Japanese Journal of Applied Physics, Part 2: Letters* **1998**, *37*, L288. <https://iopscience.iop.org/article/10.1143/JJAP.37.L288/pdf>
4. Sabah, F.A.; Ahmed, N.M.; Hassan, Z.; Rasheed, H.S. High Performance CuS p-Type Thin Film as a Hydrogen Gas Sensor. *Sens Actuators A Phys* **2016**, *249*, 68. <http://dx.doi.org/10.1016/j.snb.2017.03.020>
5. Wu, C.; Zhang, Z.; Wu, Y.; Lv, P.; Nie, B.; Luo, L.; Wang, L.; Hu, J.; Jie, J. Flexible CuS Nanotubes–ITO Film Schottky Junction Solar Cells with Enhanced Light Harvesting by Using an Ag Mirror. *Nanotechnology* **2013**, *24*, 045402. <https://iopscience.iop.org/article/10.1088/0957-4484/24/4/045402>
6. Zhang, Y.; Tian, J.; Li, H.; Wang, L.; Qin, X.; Asiri, A.M.; Al-Youbi, A.O.; Sun, X. Biomolecule-Assisted, Environmentally Friendly, One-Pot Synthesis of CuS/Reduced Graphene Oxide Nanocomposites with Enhanced Photocatalytic Performance. *Langmuir* **2012**, *28*, 12893. <https://doi.org/10.1021/la303049w>
7. Peng, H.; Ma, G.; Sun, K.; Mu, J.; Wang, H.; Lei, Z. High-Performance Supercapacitor Based on Multi-Structural CuS@polypyrrole Composites Prepared by in Situ Oxidative Polymerization. *J. Mater. Chem. A* **2014**, *2*, 3303. <https://doi.org/10.1039/C3TA13859C>
8. Xu, J.; Zhang, J.; Yao, C.; Dong, H. Synthesis of Novel Highly Porous CuS Golf Balls by Hydrothermal Method and their Application in Ammonia Gas Sensing. *Journal of the Chilean Chemical Society* **2013**, *58*, 1722. <http://dx.doi.org/10.4067/S0717-97072013000200017>
9. Froment, M.; Cachet, H.; Essaaidi, H.; Maurin, G.; Cortes, R. Metal Chalcogenide Semiconductors Growth from Aqueous Solutions. *Pure and Applied Chemistry* **1997**, *69*, 77. <https://doi.org/10.1351/pac199769010077>
10. Patrick, R.A.D.; Mosselmans, J.F.W.; Charnock, J.M.; England, K.E.R.; Helz, G.R.; Garner, C.D.; Vaughan, D.J. The Structure of Amorphous Copper Sulfide Precipitates: An X-Ray Absorption Study. *Geochim Cosmochim Acta* **1997**, *61*, 2023. [https://doi.org/10.1016/S0016-7037\(97\)00061-6](https://doi.org/10.1016/S0016-7037(97)00061-6)

11. Flores-García, E.; González-García, P.; González-Hernández, J.; Ramírez-Bon, R. Non-Toxic Growth of Cu_xS Thin Films in Alkaline Medium by Ammonia Free Chemical Bath Deposition. *Optik (Stuttg)* **2017**, *145*, 589. <https://doi.org/10.1016/j.ijleo.2017.08.043>
12. Kozhevnikova, N.S.; Maskaeva, L.N.; Markov, V.P.; Lipina, O.A.; Chufarov, A.U.; Kuznetsov, M. V. One-Pot Green Synthesis of Copper Sulfide (I) Thin Films with p-Type Conductivity. *Mater Chem Phys* **2020**, *242*, 122447. <https://doi.org/10.1016/j.matchemphys.2019.122447>
13. Grozdanov, I.; Najdoski, M. Optical and Electrical Properties of Copper Sulfide Films of Variable Composition. *J Solid State Chem* **1995**, *114*, 469. <https://doi.org/10.1006/jssc.1995.1070>
14. Galdikas, A.; Mironas, A.; Strazdiene, V.; Setkus, A.; Ancutiene, I.; Janickis, V. Room-Temperature-Functioning Ammonia Sensor Based on Solid-State Cu_xS Films. *Sens Actuators B Chem* **2000**, *67*, 76. [https://doi.org/10.1016/S0925-4005\(00\)00408-1](https://doi.org/10.1016/S0925-4005(00)00408-1)
15. Pathan, H.M.; Desai, J.D.; Lokhande, C.D. Modified Chemical Deposition and Physico-Chemical Properties of Copper Sulphide (Cu_2S) Thin Films. *Appl Surf Sci* **2002**, *202*, 47. [https://doi.org/10.1016/S0169-4332\(02\)00843-7](https://doi.org/10.1016/S0169-4332(02)00843-7)
16. Arora, S.; Kabra, K.; Joshi, K.B.; Sharma, B.K.; Sharma, G. Structural, Elastic, Thermodynamic and Electronic Properties of Covellite, CuS . *Physica B Condens Matter* **2020**, *582*, 311142. <https://doi.org/10.1016/j.physb.2018.11.007>
17. Fjellvag, H.; Gronvold, F.; Stolen, S.; Andresen, A.F.; Muller-Kafer, R.; Simon, A. Low-Temperature Structural Distortion in CuS . *Zeitschrift fur Kristallographie - New Crystal Structures* **1988**, *184*, 111. <https://doi.org/10.1524/zkri.1988.184.1-2.111>
18. Raveau, B.; Sarkar, T. Superconducting-like Behaviour of the Layered Chalcogenides CuS and CuSe below 40 K. *Solid State Sci* **2011**, *13*, 1874. <https://doi.org/10.1016/j.solidstatesciences.2011.07.022>
19. Buckel, W.; Hilsch, R. Zur Supraleitung von Kupfersulfid. *Zeitschrift für Physik* **1950**, *128*, 324. <https://doi.org/10.1007/BF01333079>
20. Saito, S.-H.; Kishi, H.; Nié, K.; Nakamaru, H.; Wagatsuma, F.; Shinohara, T. Cu NMR Studies of Copper Sulfide. *Phys. Rev. B* **1997**, *55*, 14527. <https://journals.aps.org/prb/pdf/10.1103/PhysRevB.55.14527>
21. Hamed, M.S.G.; Mola, G.T. Copper Sulphide as a Mechanism to Improve Energy Harvesting in Thin Film Solar Cells. *J Alloys Compd* **2019**, *802*, 252. <https://doi.org/10.1016/j.jallcom.2019.06.108>
22. Marimuthu, T.; Anandhan, N.; Panneerselvam, R.; Ganesan, K.P.; Roselin, A.A. Synthesis and Characterization of Copper Sulfide Thin Films for Quantum Dot Sensitized Solar Cell and Supercapacitor Applications. *Nano-Structures & Nano-Objects* **2019**, *17*, 138. <https://doi.org/10.1016/j.nanoso.2018.12.004>
23. Sangamesha, M.A.; Pushpalatha, K.; Shekar, G.L.; Shamsundar, S. Preparation and Characterization of Nanocrystalline CuS Thin Films for Dye-Sensitized Solar Cells. *ISRN Nanomater* **2013**, *1*. <https://doi.org/10.1155/2013/829430>

24. Gainov, R.R.; Dooglav, A. V; Pen'kov, I.N.; Mukhamedshin, I.R.; Mozgova, N.N.; Evlampiev, I.A.; Bryzgalov, I.A. Phase Transition and Anomalous Electronic Behavior in the Layered Superconductor CuS Probed by NQR. *Phys. Rev. B* **2009**, *79*, 075115. <https://doi.org/10.1103/PhysRevB.79.075115>
25. Mazin, I.I. Structural and Electronic Properties of the Two-Dimensional Superconductor CuS with 113-Valent Copper. *Phys Rev B Condens Matter Mater Phys* **2012**, *85*, 115133. <https://doi.org/10.1103/PhysRevB.85.115133>
26. Wei Goh, S.; Buckley, A.N.; Lamb, R.N.; Rosenberg, R.A.; Moran, D. The Oxidation States of Copper and Iron in Mineral Sulfides, and the Oxides Formed on Initial Exposure of Chalcopyrite and Bornite to Air. *Geochimica et Cosmochimica Acta* **2006**, *70*, 2210. <https://doi.org/10.1016/j.gca.2006.02.007>
27. Van der Laan, G.; Pattrick, R.A.D.; Henderson, C.M.B.; Vaughan, D.J. Oxidation State Variations in Copper Minerals Studied with Cu 2p X-Ray Absorption Spectroscopy. *Journal of Physics and Chemistry of Solids* **1992**, *53*, 1185. [https://doi.org/10.1016/0022-3697\(92\)90037-E](https://doi.org/10.1016/0022-3697(92)90037-E)
28. Kumar, P.; Nagarajan, R.; Sarangi, R. Quantitative X-Ray Absorption and Emission Spectroscopies: Electronic Structure Elucidation of Cu₂S and CuS. *J Mater Chem C Mater* **2013**, *1*, 2448. <https://doi.org/10.1039/C3TC00639E>
29. Nakai, I.; Sugitani, Y.; Nagashima, K.; Niwa, Y. X-Ray Photoelectron Spectroscopic Study of Copper Minerals. *Journal of Inorganic and Nuclear Chemistry* **1978**, *40*, 789. [https://doi.org/10.1016/0022-1902\(78\)80152-3](https://doi.org/10.1016/0022-1902(78)80152-3)
30. Kurmaev, E.Z.; Van Ek, J.; Ederer, D.L.; Zhou, L.; Callcott, T.A.; Perera, R.C.C.; Cherkashenko, V.M.; Shamin, S.N.; Trofimova, V.A.; Bartkowski, S.; et al. Experimental and Theoretical Investigation of the Electronic Structure of Transition Metal Sulphides: CuS, And. *Journal of Physics: Condensed Matter* **1998**, *10*, 1687. <https://doi.org/10.1088/0953-8984/10/7/016>
31. Li, D.; Bancroft, G.M.; Kasrai, M.; Fleet, M.E.; Feng, X.H.; Yang, B.X.; Tan, K.H. S K- and L-Edge XANES and Electronic Structure of Some Copper Sulfide Minerals. *Phys Chem Miner* **1994**, *21*, 317. <https://doi.org/10.1007/BF00202096>
32. Fu, S.; Sun, Z.; Huang, P.; Li, Y.; Hu, N. Some Basic Aspects of Polymer Nanocomposites: A Critical Review. *NMS* **2019**, *1*, 2. <https://doi.org/10.1016/j.nanoms.2019.02.006>
33. Khan, I.; Khan, I.; Saeed, K.; Ali, N.; Zada, N.; Khan, A.; Ali, F.; Bilal, M.; Akhter, M.S. Polymer Nanocomposites: An Overview. *Smart Polymer Nanocomposites* **2023**, 167. <https://doi.org/10.1016/B978-0-323-91611-0.00017-7>
34. Chen, Y.-H.; Huang, C.-Y.; Lai, F.-D.; Roan, M.-L.; Chen, K.-N.; Yeh, J.-T. Electroless Deposition of the Copper Sulfide Coating on Polyacrylonitrile with a Chelating Agent of Triethanolamine and Its EMI Shielding Effectiveness. *Thin Solid Films* **2009**, *517*, 4984. <https://doi.org/10.1016/j.tsf.2009.03.137>
35. Pathan, H.M.; Desai, J.D.; Lokhande, C.D. Modified Chemical Deposition and Physico-Chemical Properties of Copper Sulphide (Cu₂S) Thin Films. *Appl Surf Sci* **2002**, *202*, 47. [https://doi.org/10.1016/S0169-4332\(02\)00843-7](https://doi.org/10.1016/S0169-4332(02)00843-7)

36. Balciunaite, E.; Petrasauskiene, N.; Alaburdaite, R.; Jakubauskas, G.; Paluckiene, E. Formation and Properties of Mixed Copper Sulfide (Cu_xS) Layers on Polypropylene. *Surfaces and Interfaces* **2020**, *21*, 100801. <https://doi.org/10.1016/j.surfin.2020.10080>
 37. Petrasauskiene, N.; Paluckiene, E.; Alaburdaite, R.; Gilić, M. Deposition of Copper Sulfide Films on Polyamide Surface. *Science of Sintering* **2022**, *54*, 139. <https://doi.org/10.2298/SOS2202139P>
 38. Janickis, V.; Petrašauskiene, N.; Žalėnkiene, S.; Morkvenaite-Vilkoñciene, I.; Ramanavicius, A. Morphology of CdSe-Based Coatings Formed on Polyamide Substrate. *J Nanosci Nanotechnol* **2018**, *18*, 604. <https://doi.org/10.1166/jnn.2018.13927>
 39. Alaburdaite, R.; Paluckiene, E. Investigation of Cu_xS Layers on Polypropylene Film Formed by Using Different Sulfuring Agents. *Chalcogenide Letters* **2018**, *15*, 139. https://www.chalcogen.ro/139_AlaburdaiteR.pdf
 40. Noeske, M.; Degenhardt, J.; Strudthoff, S.; Lommatzsch, U. Plasma Jet Treatment of Five Polymers at Atmospheric Pressure: Surface Modifications and the Relevance for Adhesion. *Int J Adhes Adhes* **2004**, *24*, 171. <https://doi.org/10.1016/j.ijadhadh.2003.09.006>
 41. Moloney, M.G. Functionalized Polymers by Chemical Surface Modification. *J. Phys. D: Appl. Phys* **2008**, *41*, 9. <http://dx.doi.org/10.1088/0022-3727/41/17/174006>
 42. Choi, Y.H.; Kim, J.H.; Paek, K.H.; Ju, W.T.; Hwang, Y.S. Characteristics of Atmospheric Pressure N_2 Cold Plasma Torch Using 60-Hz AC Power and Its Application to Polymer Surface Modification. *Surf Coat Technol* **2005**, *193*, 319. <https://doi.org/10.1016/j.surfcoat.2004.08.145>
 43. Alaburdaitė, R.; Krylova, V. Study of Thermo-Oxidative Chemical Pre-Treatment of Isotactic Polypropylene. *J Therm Anal Calorim* **2014**, *118*, 1331. <https://doi.org/10.1007/s10973-014-4226-0>
 44. Tauc, J.; Grigorovici, R.; Vancu, A. Optical Properties and Electronic Structure of Amorphous Germanium. *Physica status solidi (b)* **1966**, *15*, 627. <https://doi.org/10.1002/pssb.19660150224>
 45. Naşcu, C.; Pop, I.; Popescu, V.; Indrea, E.; Bratu, I. Spray Pyrolysis Deposition of CuS Thin Films. *Mater Lett* **1997**, *32*, 73. [https://doi.org/10.1016/S0167-577X\(97\)00015-3](https://doi.org/10.1016/S0167-577X(97)00015-3)
 46. Ishii, M.; Shibata, K.; Nozaki, H. Anion Distributions and Phase Transitions in $\text{CuS}_{1-x}\text{Se}_x$ ($x = 0-1$) Studied by Raman Spectroscopy. *J Solid State Chem* **1993**, *105*, 504. <https://doi.org/10.1006/jssc.1993.1242>
 47. Trajic, J.; Curcic, M.; Casas Luna, M.; Romcevic, M.; Remesova, M.; Matej Balaz, |; Ladislav Celko, |; Dvorak, K.; Romcevic, N. Vibrational Properties of the Mechanochemically Synthesized Cu_2SnS_3 : Raman Study. *J. Raman Spectrosc* **2022**, *53*, 977. <https://doi.org/10.1002/jrs.6318>
-

Апстракт

Флексибилни полимери модификовани бакар-сулфидима појавили су се као нова класа материјала, представљајући композитне структуре са изванредним особинама погодним за примену у флексибилној електроници. Ова студија се фокусира на депоновање слојева бакар-сулфида (Cu_xS) на површине полиамида и полипропилена путем методе хемијског таложења из купке, применом 2 или 3 циклуса таложења. Циљ је истражити утицај броја циклуса таложења и утврдити оптималне услове за процес таложења. Свеобухватна анализа танких филмова Cu_xS обухвата технике као што су скенирајућа електронска микроскопија (SEM), Раман спектроскопија, UV-VIS спектроскопија и рендгенска дифракција како би се расветлиле њихове структурне и оптичке карактеристике.

Кључне речи: Бакар-сулфид, Наноконтролит, Оптичка својства, SEM, Раман спектроскопија, UV-VIS спектроскопија, Рендгенска дифракција



Article

Tuning SERS Signal via Substrate Structuring: Valves of Different Diatom Species with Ultrathin Gold Coating

Martina Gilic ^{*}, Mohamed Ghobara  and Louisa Reissig

Institute of Experimental Physics, Freie Universität Berlin, Arnimallee 14, 14195 Berlin, Germany; mghobara@zedat.fu-berlin.de (M.G.); lreissig@zedat.fu-berlin.de (L.R.)

* Correspondence: martina.gilic@fu-berlin.de; Tel.: +49-17677405648

Abstract: The discovered light modulation capabilities of diatom silicious valves make them an excellent toolkit for photonic devices and applications. In this work, a reproducible surface-enhanced Raman scattering (SERS) enhancement was achieved with hybrid substrates employing diatom silica valves coated with an ultrathin uniform gold film. Three structurally different hybrid substrates, based on the valves of three dissimilar diatom species, have been compared to elucidate the structural contribution to SERS enhancement. The comparative analysis of obtained results showed that substrates containing cylindrical *Aulacoseira* sp. valves achieved the highest enhancement, up to 14-fold. Numerical analysis based on the frequency domain finite element method was carried out to supplement the experimental results. Our results demonstrate that diatom valves of different shapes can enhance the SERS signal, offering a toolbox for SERS-based sensors, where the magnitude of the enhancement depends on valve geometry and ultrastructure.

Keywords: diatom valve; SERS; surface-enhanced Raman scattering; guided-mode resonance; finite element method; hybrid SERS sensors



Citation: Gilic, M.; Ghobara, M.; Reissig, L. Tuning SERS Signal via Substrate Structuring: Valves of Different Diatom Species with Ultrathin Gold Coating.

Nanomaterials **2023**, *13*, 1594.

<https://doi.org/10.3390/nano13101594>

Received: 17 April 2023

Revised: 4 May 2023

Accepted: 6 May 2023

Published: 10 May 2023



Copyright: © 2023 by the authors. Licensee MDPI, Basel, Switzerland. This article is an open access article distributed under the terms and conditions of the Creative Commons Attribution (CC BY) license (<https://creativecommons.org/licenses/by/4.0/>).

1. Introduction

Since its discovery in 1974 as an outstanding technique for enhancing the Raman signal [1], surface-enhanced Raman scattering (SERS) is gaining increasing interest due to its sensitivity, which could enable single-molecule detection [2]. Despite the exponential growth of publications on SERS, the true mechanism of enhancement is not fully understood, although electromagnetic theory tends to cover all major SERS observations [3]. This technique is based on plasmonically active substrates, which couple laser photons and free electrons within these substrates to induce localized surface plasmon resonances (LSP) and surface plasmon polaritons (SPP) in metallic nanoparticles and the planar metallic surface with adjacent dielectric interfaces, respectively [2]. This leads to an enhancement of electromagnetic fields in close proximity to the surface, where the analyte molecules are adsorbed, consequently enhancing their Raman signal.

In recent years, the sensitivity of the SERS technique has been further improved by employing hybrid substrates, which additionally incorporate dielectric photonic crystals (PCs) or resonant gratings [4]. Such structures have a characteristic interaction with light that can, in a certain wavelength range, obtain a high evanescent field at the surface where the plasmonic structures are often located and thus additionally enhance the SERS signal. For instance, in Hu et al. [5], the presence of a resonant 2D dielectric grating led to the coupling of a guided-mode resonance (GMR) with the LSP, resulting in an improved SERS signal. Nevertheless, the fabrication of such structures often requires clean-room techniques that come with high environmental and financial costs.

As an alternative green solution, some biomaterials have been suggested to replace such artificial dielectric structures in the fabrication of hybrid SERS substrates [6–10]. Among these, diatoms have been proposed as an outstanding source of biosilica with

periodic porosity, mainly in the range of visible light wavelengths [11]. Diatoms are unicellular aquatic microalgae enclosed in an intricate porous exoskeleton [12], representing one of the exquisite examples of natural 2D photonic crystals [13,14]. Unlike artificial PCs fabricated with expensive techniques such as lithography, thus being a limiting factor for disposable sensors, diatoms are abundant and versatile [11,14,15]. Diatoms can be cultivated under a wide range of conditions if nutrients and light are provided, and their biosilica can be retrieved [16], modified [15,17], and utilized as building blocks in photonic applications [14,18]. Each of the thousands of species discovered so far has a unique morphology, valve geometry, and pore pattern [12]. Other examples of biomaterials used in fabrication of hybrid SERS substrates include peacock feathers and opal [19], as well as butterfly wings [20].

Diatom biosilica, i.e., mainly their valves, have been successfully employed in the fabrication of various hybrid SERS sensors. These efforts have recently been reviewed in [11]. It has been suggested that diatom valves contribute to SERS enhancement primarily through GMR [11,21] but also by concentrating analyte molecules as well as nanoparticles on their surface and pore rims. In previous work, valves of several diatom species, mainly *Pinnularia* spp., have been utilized to fabricate hybrid substrates for SERS coated with either silver or gold nanoparticles or, less often, thin films [11]. The creation of “hot spots” between nanoparticles (NPs) leads to SERS enhancement factors of up to 10^{16} . Nevertheless, homogeneous distribution of NPs remains a big challenge, leaving the hot spots to be placed randomly and thus hampering the reproducibility of the SERS signal. One of the possible strategies to overcome the consequence of the inhomogeneous distribution of NPs could be to create “hot volumes” by placing arrays of weakly coupled metal nanohelices, as in [22]. On the other hand, a continuous metallic thin film may enable homogeneity of the SERS signal across a hybrid substrate. It could also reveal the contribution of structural features of the valve of a given species to SERS and the photonic properties, such as GMR. In the literature, attempts to coat diatoms with homogeneous metallic thin films are scarce [11]. For instance, in Managò et al. [23], *Pseudo-nitzschia multistriata* valves were coated with 20–50 nm thick gold films, where films of 20 nm thickness showed cracks and discontinuities. With increasing film thickness, the uniformity improved, with SERS signal reproducibility reaching 80%. However, the 50 nm film exhibited a roughness of up to 10 nm. Kwon et al. [24] coated *Coscinodiscus* sp. with thin films of 15 nm but without disclosing any data on roughness. Moreover, by using thin plasmonic films, one eliminates the influence of incoming light polarization, because in the case of metallic NPs, the strongest signal is obtained when laser light is polarized parallel to the central axis of the NPs [25], and in the case of rippled surfaces, there is a complex correspondence between patterns of nanogaps, localized hot spots, and polarization [26].

In this work, we experimentally evaluate SERS enhancement, homogeneity, and reproducibility obtained with hybrid substrates consisting of biosilica valves of three diatom species—small pennate *Gomphonema parvulum*, medium-sized centric *Aulacoseira* sp., and large centric *Coscinodiscus radiatus*—of very different structural features, coated with an ultrathin uniform gold film of 10 nm thickness. We deliberately chose three extremely distinct species to investigate the contribution of their structural features and the associated optical properties. A numerical analysis using the frequency domain method supplements the experimental results.

2. Materials and Methods

2.1. Hybrid Substrate Preparation

Three morphologically distinct diatom valves belonging to three different species were scrutinized in this study. Fresh cultures of centric diatom *Coscinodiscus radiatus* (Cosc) and of pennate diatom *Gomphonema parvulum* (Gomp) were kindly provided by Dr. Cathleen Oschatz (Max Planck Institute of Colloids and Interfaces, Potsdam, Germany), while a diatomite (DE) sample was purchased from EP minerals (Reno, NV, USA) with abundant *Aulacoseira* sp. (Aula). The siliceous valves were extracted from the fresh cultures via

oxidation using the hot hydrogen peroxide method to remove organic matter, followed by washing several times with deionized water. Fossil valves of *Aulacoseira* sp. (Aula) were purified from the DE sample using the cold HCl method. After purification, the clean valves were kept in deionized water for further use.

To obtain a monolayer of clean valves, about 60 μL of the valve suspension was spread over clean glass substrates via the drop-casting method and left to dry under ambient conditions. The concentration of the valves was optimized for each sample to avoid agglomeration while forming the monolayer. To obtain a homogenous and well-adhered ultrathin gold film across the valves, a self-assembled monolayer (SAM) was applied to the substrates before the thermal evaporation process. For this, the silica surface of the obtained monolayer was firstly activated using a plasma cleaner (Harrick PDC-32G, Ithaca, NY, USA) in a low-pressure air atmosphere at mid-power, employing RF ≈ 10 MHz for generating the plasma for 10 min. Then, the samples were transferred directly into a vacuum desiccator with an open Eppendorf containing about 80 μL of (3-Mercaptopropyl)trimethoxysilane (MPTMS). Thereafter, the desiccator was evacuated immediately, using a rough vacuum pump for 40 min. After three days in the evacuated desiccator, the substrates were transferred directly to a physical vapor deposition chamber (KJLC Nano 36, Dresden Germany), where a high vacuum (10^{-6} Torr) was applied. The deposition was carried out with an initial rate of 0.1 $\text{\AA}/\text{s}$ and a final thickness of 100 \AA (10 nm). The thickness was estimated using an integrated quartz crystal microbalance. After deposition, the hybrid substrates were stored in a clean box for further use.

In order to compare the hybrid devices with the performance of a bare ultrathin gold film, a reference substrate was fabricated without diatom valves. This created a transparent electrode with a resistance of $(45 \pm 3) \Omega$ over the whole film. Our previous work showed that this film has a maximum UV–VIS transmittance at 532 nm and a maximum absorbance at 890 nm, where plasmonic resonance reaches the maximum (Figure S1).

2.2. Characterization

Structural characterization of diatom valves as well as of the ultrathin gold layer was performed with a Hitachi SU8030 scanning electron microscope, supported with a secondary electron detector.

For SERS measurements, about 7 μL of 1 mM Rhodamine 6G (R6G) in ethanol was dropped on top of the gold and left to dry at ambient conditions. SERS measurements and mapping were carried out with a backscattering configuration on a Horiba XploRA confocal Raman instrument equipped with a charge-coupled device (CCD) detector. The spectra acquisition was carried out using an excitation laser wavelength of 638 nm of ca. 40 mW power, in a spectral range of 500–2100 cm^{-1} , with an integration time of 15 s per spectrum and averaged over 5 accumulations. Raman mapping was performed with a 1 μm step in the case of Aula and a 0.5 μm step in the cases of Cosc and Gomp, with an integration time of 1 s per step. For focusing the light, the 100x objective (NA = 0.9) was used, giving a beam size of approximately 0.5 μm . Grating was set to 1200 grooves/mm.

2.3. Numerical Analysis

The numerical calculations were based on the finite element frequency domain method (FEFD) implemented in COMSOL Multiphysics 5.5. Two-dimensional models representing 2D cross-sections (CSs) across the valves were built based on the structural parameters extracted from SEM analysis. A layer of 10 nm thickness, representing the thin gold film, was added to the CSs. The CSs were analyzed in a large rectangular simulation box, illuminating from the left-hand-side boundary with a transverse electric field of 1 V/m strength. Perfectly matched layers were applied to the other three boundaries. The refractive indices of air and silica were set to 1.00 and 1.46, respectively.

3. Results

3.1. Morphology and Ultrastructure of the Hybrid Substrates

Scanning electron microscopy (SEM) was performed to reveal the fine structural parameters of diatom valves as well as the homogeneity of the ultrathin gold layer. Our previous AFM measurements confirmed the homogeneity and smoothness of the evaporated gold film on glass activated with the SAM layer, with an average roughness value (R_a) of 0.42 nm (Figure S2). The fine structure of the thin gold film on a valve of *Gomphonema parvulum* is presented in Figure 1c, where the smooth continuous nature of the film without the presence of cracks and voids can be observed. The structure of the gold film on a reference glass substrate without diatom valves as well as over the other two diatom valves (*Coscinodiscus radiatus* and *Aulacoseira* sp.) is presented in Figure S2, with similar observations regarding the quality of the gold film.

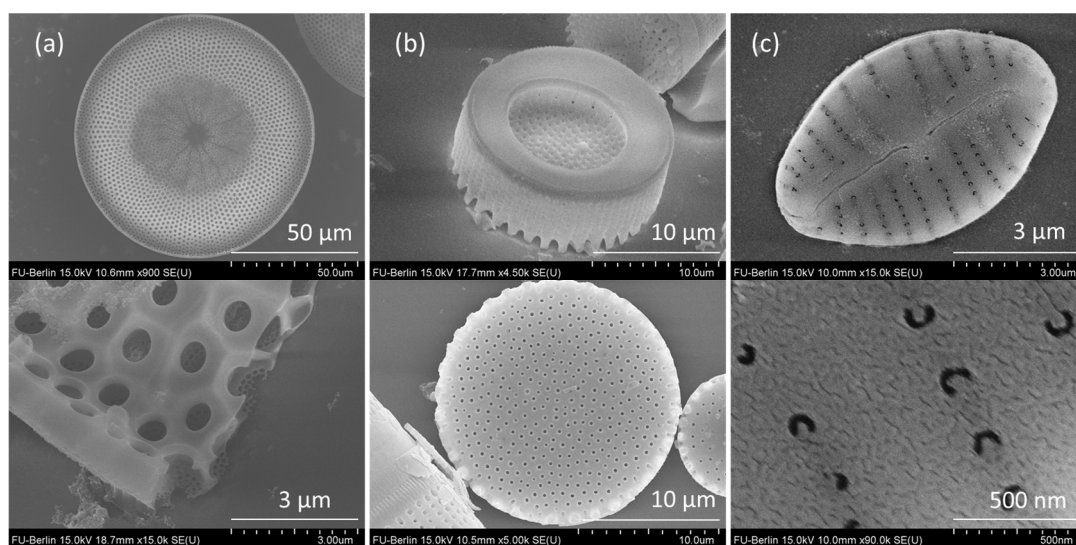


Figure 1. SEM images of (a) *Coscinodiscus radiatus*, (b) *Aulacoseira* sp., and (c) *Gomphonema parvulum* diatom valves with corresponding details.

SEM micrographs of the three diatom valves chosen are presented in Figure 1. Gomp valves have an elliptic shape with an approximate length of 7 μm , an average width of 4.6 μm , punctate areolae of 100 nm diameter and 214 nm spacing, and striae spacing of 490–570 nm (Figure 1c). The complete description of Gomp valves is provided in Ghobara et al. [27]. Cosc valves have a circular shape about 100 μm in diameter, with inner pores of 1.2 μm and outer pores of 100 nm diameter, both regularly arranged in hexagonal symmetry (Figure 1a). Unlike Gomp and Cosc, whose valves are of about equal size within the studied samples, cylindrical Aula valves come in a variety of sizes, ranging from 6 to 20 μm valve diameter, and generally follow the rule that the smaller the valve face size, the longer the height. For SERS analysis, we chose the valves with bigger diameters (15–20 μm) that come with a hexagonal arrangement of pores of 250–300 nm in diameter and 0.6–1 μm spacing. In Figure 1b, the top and bottom sides of Aula valves are depicted. While the top side is shaped like a disk with spines at the ridges, the bottom side has a ring-like shape.

3.2. SERS Enhancement over Different Substrates

The cationic dye Rhodamine 6G (R6G) was used as a typical probe for SERS measurements. R6G dissolved in ethanol has a strong absorption in the VIS region, with absorption maximum at 554 nm and a vibronic shoulder at 518 nm (Figure S3), which is due to a solvent effect that is slightly red-shifted compared to data from the literature (530 nm) [28]. According to the Franck–Condon rule, the luminescence spectrum was inverted as well as red-shifted [29]. Due to strong luminescence in the VIS region, it is not possible to

obtain normal Raman spectra with the typically used green or red laser excitation lines. However, coating the surface with metal should quench the photoluminescence due to non-radiative interaction with the metal surface, allowing the strong SERS signal of R6G to be observed [30]. In our case, the luminescence was still not quenched when using the green laser excitation line at 532 nm on the reference sample R6G on glass coated with gold, limiting the observation of a strong, unhampered SERS signal. In contrast, using the red excitation line at 638 nm on the same sample yields a strong SERS signal with the characteristic modes of R6G [31] at around 610, 770, 1187, 1312, 1360, 1508, 1600, and 1648 cm^{-1} . Detailed analysis of the origin of each mode of R6G can be found in [32].

Figure 2a demonstrates the comparison among the SERS spectra of R6G on different hybrid substrates comprising different biosilica valves as well as the reference Au film on glass. Different spectra for each hybrid substrate are shown in the same color, and they stand for the signal reproducibility between different valves. Compared to the reference sample, each of the three substrates dramatically enhances the SERS signal. The averaged signal intensity of each characteristic mode of R6G on the four samples is depicted in Figure 2b, while the relative enhancement of the SERS signal is presented in Figure 2c. Depending on the mode observed, the signal of the spectrum obtained on Cosc was enhanced 6–8 times compared to the SERS signal obtained on the reference sample, while the hybrid substrates based on Gomp showed a 5–7-time enhancement. Finally, the signal of the spectrum obtained on Aula underwent an 8–14-time enhancement, with noticeable variation in the enhancement of different modes. The strongest relative enhancement was observed for the mode at 1312 cm^{-1} (Figure 2c). It must be emphasized that those values do not stand for the absolute enhancement factor of the SERS signal, but instead the relative enhancements compared to the thin gold layer on glass, containing no diatom valves.

Raman mapping was carried out to test the homogeneity on each hybrid substrate, as well as the SERS improvement with respect to the flat unpatterned gold film surrounding the valves. In Figure 3, Raman maps of the intense mode at 1360 cm^{-1} on different hybrid substrates are presented. In the case of the substrate based on Aula valves coated with a thin gold layer (Figure 3a), the mapping is performed with steps of 1 μm . The mapping image corresponds to the optical image, and without a doubt, the signal is homogeneously stronger on the valve than outside of it. As the Cosc valve is much bigger, only a small part of it is mapped with fine steps of 0.5 μm (Figure 3b). Here, in the mapping image, the pore structure is preserved, i.e., the enhancement is stronger inside the pores, suggesting that more light is trapped within. In the case of the small Gomp valve, a mapping with a fine step of 0.5 μm was carried out to image the whole valve as well as the surrounding gold-coated glass substrate (Figure 3c). In this case, the mapping image corresponds to the optical image as well. Nevertheless, the quality of the result is hampered due to a strong luminescence arising from the valve edges.

3.3. Numerical Analysis

Numerical calculations were carried out on representative 2D cross-sections of different hybrid substrates to investigate the possible contribution of the valves' light modulation capabilities, specifically GMR, to the obtained SERS enhancement. The structural parameters necessary to build the 2D CSs, such as pore size and spacing, were extracted from the SEM measurements (see Figure 1).

The Gomp valve has a distinct 1D grid-like structure, consisting of alternating striae and costae, as demonstrated previously when its GMR was investigated [27]. In Ghobara et al., the longitudinal CSs with grid-like structure were able to couple the light at a specific range of wavelengths inside the grid, leading to the formation of an intense standing wave, with simultaneous enhancement in reflectance and a drop in transmission [27]. By coating the CSs with a 10 nm gold layer, the resonance wavelength maximum λ_{GMR} is slightly shifted, with a reduction in the normalized electric field strength $E_{\text{Norm,GMR}}$ within the grid structure. For example, the CS close to the valve edges with maximum striae spacing showed a zero-mode GMR at 610 nm (Figure 4c) instead of 613 nm for the same CS without

a gold layer. For all Gomp CSs, no GMR maximum is obtained at the excitation wavelength $\lambda_{exc} = 638$ nm. Nevertheless, the field strength of the CS close to the edge is still high in the near field, where the probe R6G molecules are adsorbed in the real measurements (Figure 4c, bottom).

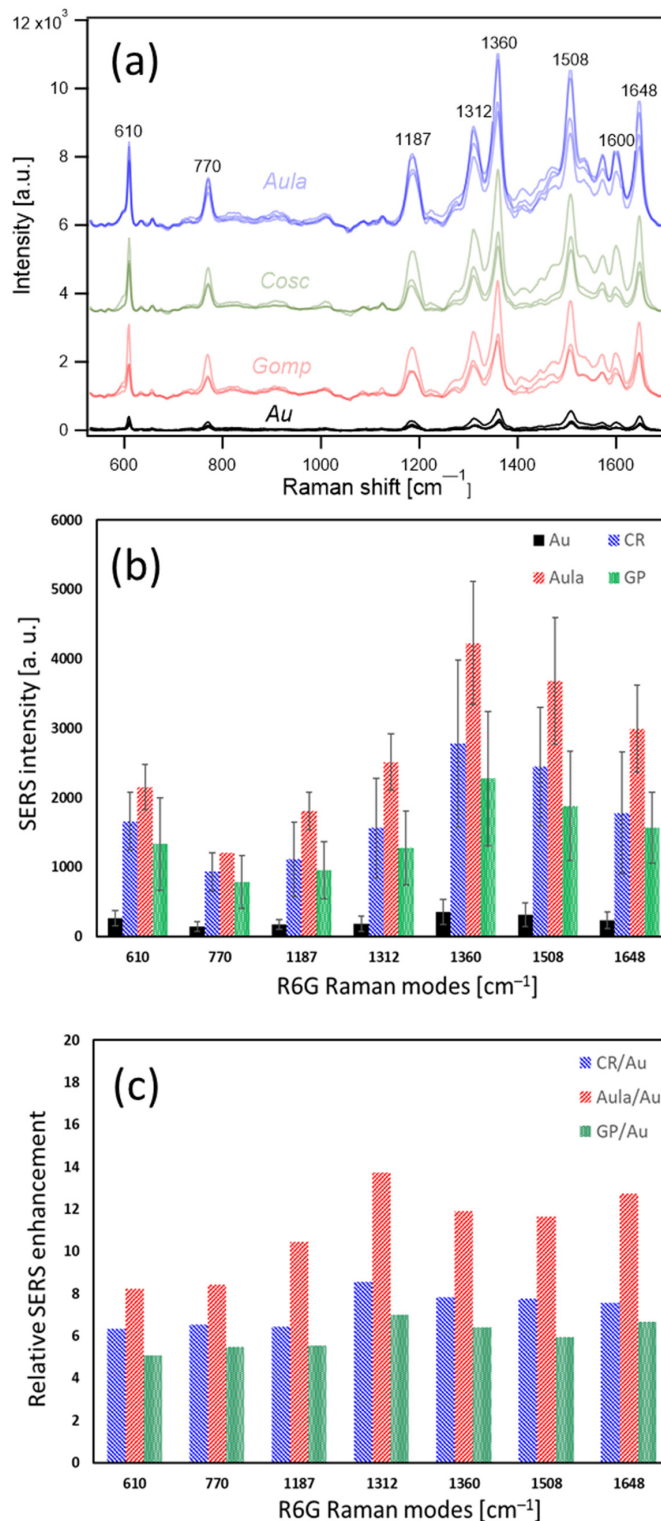


Figure 2. SERS spectra of Rhodamine 6G molecules on different hybrid substrates (a), SERS intensity of Rhodamine 6G modes on different hybrid substrates (b), and relative SERS enhancement of each mode (c).

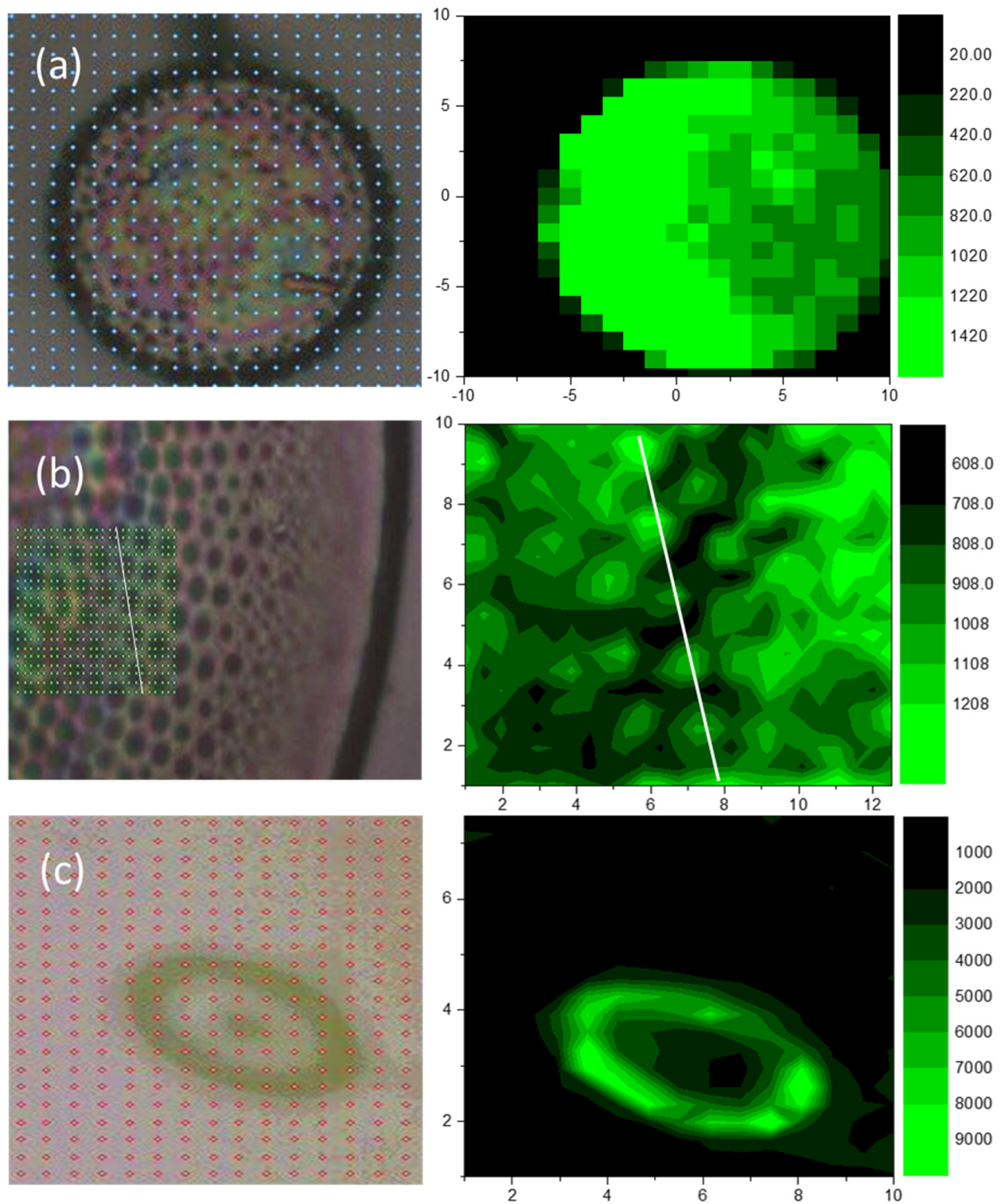


Figure 3. Raman mapping of the intense mode of Rhodamine 6G at 1360 cm^{-1} over Aula (a), Cosc (b), and Gomp (c) single valves covered with thin gold film (right) with corresponding light microscope images (left).

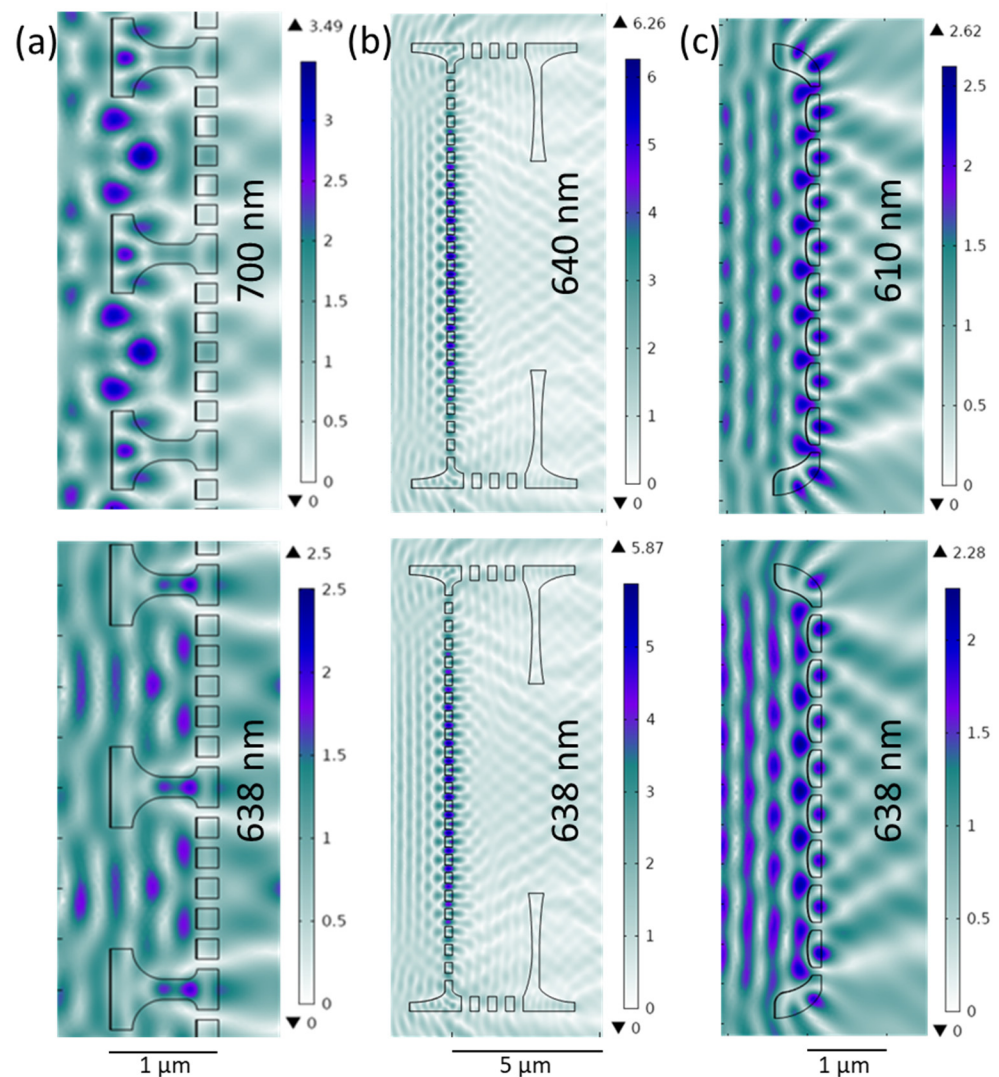


Figure 4. Electromagnetic field enhancement in 2D cross-sections of valve models coated with 10 nm thick gold film at λ_{GMR} (top) and λ_{exc} (bottom)—detail of the model of Cosc valve (a), Aula valve (b), and Gomp valve (c). The electromagnetic field impinges from the left with an input strength of 1 V/m.

The created 2D CS of the Cosc valve represents a cross-section through a whole valve, including its mantle (curved edges). After coating the CS with a 10 nm gold layer, a GMR maximum was observed at 700 nm. In Figure 4a, a small part of this CS, showing only two areolae, is presented. At λ_{exc} , away from the maximum, the E_{Norm} drops from 3.49 to 2.5 V/m; however, the electric field is still confined inside the areolae (Figure 4a, bottom). This likely matches SERS mapping results, suggesting that light is trapped within the valves regardless of the GMR.

In the case of the Aula valve, as already described, the structural parameters showed a relatively large variation: pore spacing ranges between 0.6 and 1 μm and pore size between 250 and 300 nm. For the Aula 2D CS with a 10 nm gold layer (Figure 4b), a GMR maximum is obtained at 640 nm (λ_{GMR}) for the pore spacing of 0.61 μm , slightly off λ_{exc} (638 nm). At λ_{exc} , E_{Norm} drops from 6.27 to 5.88 V/m (Figure 4b, bottom). With increased pore spacing, λ_{GMR} exhibits a strong red shift (Figure 5a), and for the pore spacing of 900 nm, the resonance wavelength appears at 910 nm. It is worth mentioning that at higher λ_{GMR} , in the red and infrared part of the spectrum, E_{Norm} drops and consequently spreads more evenly towards the valve edge. In Figure 5a, the pore spacing dependence of λ_{GMR} is demonstrated. Pore size and valve thickness dependence were also simulated (Figure 5b,c)

and in both cases, λ_{GMR} as well as E_{Norm} show negligible changes with the simulated parameter.

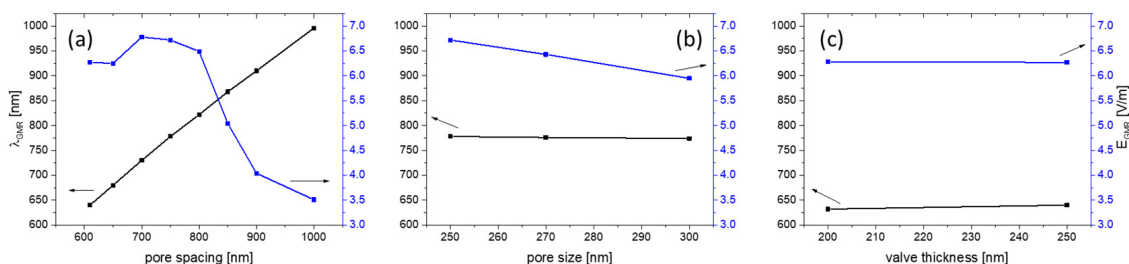


Figure 5. GMR wavelength and E_{Norm} GMR dependence on pore spacing (valve thickness 250 nm, pore size 250 nm) (a); on pore size (valve thickness 250 nm, pore spacing 750 nm) (b); and on valve thickness (pore size 250 nm, pore spacing 610 nm) (c).

4. Discussion

The exceptional smoothness, adhesion, and conductivity of the ultrathin gold film—in addition to optical transparency—is attributed to the as-used fabrication method involving a molecular adhesive monolayer of MPTMS [33]. Such properties cannot be obtained by evaporating gold directly on a glass substrate [34]. Reducing film roughness on diatom valves helps elucidate the enhancement contribution of the valves with respect to the obtained SERS enhancement. Introducing diatom valves to the substrate adds micro- to nano-scale structuring to the film. On structured metal films, unlike the flat film of the reference substrate, the plasmonic excitations could be localized within nano-scale features, resulting in a combination of propagating and confined plasmon excitations [24].

The pore size and pore spacing in diatoms are usually addressed as the key parameters in considering the valves' photonic crystal features. In many diatom valves, the pore diameter spans four orders of magnitude, from 3 to 2000 nm [12,14,17,35], and the pore spacing is in the same range, in many cases overlapping with the wavelength of visible light. The pore size and spacing of our three structurally distinct valves are comparable with λ_{exc} . Pore size and pore spacings of Gomp are smaller than λ_{exc} . For Aula, pore sizes are approx. $\lambda_{\text{exc}}/2$, while the spacing matches or exceeds λ_{exc} . Finally, for Cosc, the pore size is $2\lambda_{\text{exc}}$ and the spacing approx. $3\lambda_{\text{exc}}$. Therefore, the periodic porosity of the valves is similar to PC slabs and could have features such as GMR for off-axis light propagation. Nevertheless, unlike artificial PC slabs, diatom valves are of finite size, with curved edges, and often with more complex symmetries [35].

In resonant gratings and PC slabs, with a spacing comparable to the incident wavelength, the GMR can be supported depending on different parameters, including pore spacing, fill factor, thickness, light incident angle, and light polarization [36–38]. The supported GMR can couple to plasmonic resonances that can strongly enhance the electromagnetic field at the interface (by evanescence), where the probe molecules are located. This increases the absorption cross-section of the probe molecules, which eventually leads to the enhancement of scattering, including Raman, obtaining a greatly surface-enhanced Raman signal. For this, λ_{exc} should match or be close to λ_{GMR} [21,39,40].

The simulation results show that Gomp valves can partially support GMR close to λ_{exc} , while the GMR supported by Cosc valves are probably off λ_{exc} . In the case of Aula valves, GMR are only supported close to λ_{exc} if the lower value of the pore spacing is considered. However, the single Aula valve has a variation in pore spacing, defects, and imperfections. In the case of defects and imperfections, the porous valve face still supports GMR, but with shifted values, as demonstrated in Figure S4 where the central pore is blocked (left) and the cross-section reduced just on the analytical grid (right). The Cosc valves might support a different mechanism by trapping light inside the areolae, acting like a microcavity. Unlike planar PC slabs, the presence of the mantle can couple the light into the valve, as has been suggested through near-field scanning optical microscopy [41]. This can also add up to

the observed enhancement in SERS. Finally, it should be noted that the two-dimensional simulations have limitations, especially when considering resonance phenomena, as the valves have three-dimensional structure. The simulations also did not include the influence of the substrate.

5. Conclusions

In this work, we fabricated hybrid SERS substrates based on different naturally designed diatom valves coated with a thin smooth gold film. The SERS signal obtained on such hybrid substrates was reproducible and, compared to a reference substrate consisting of a gold layer on glass without diatoms, increased on average by a factor of 6, 7, and 11 in the case of Gomp, Cosc, and Aula, respectively. Our findings suggest that probably all diatom valves can be employed successfully as substrates in SERS-based sensors. Nevertheless, under equal conditions, the magnitude of enhancement varies depending on their geometry and ultrastructure. GMR seems to not be the exclusive mechanism for enhancing the SERS signal in diatom-based SERS hybrid sensors. More efforts are required in the future to understand the real mechanisms for the obtained enhancement.

Supplementary Materials: The following supporting information can be downloaded at: <https://www.mdpi.com/article/10.3390/nano13101594/s1>, Figure S1: UV–VIS Absorbance spectrum of a 10 nm gold film on a glass slide activated with MPTMS; Figure S2: AFM image of the 10 nm gold film on a glass slide (left); and SEM micrographs of the gold film on a glass slide (top right), Aula valve (middle right) and Cosc valve (bottom right). A glass slide was activated with MPTMS before the gold layer was evaporated; Figure S3: UV–VIS Absorbance spectrum of 10^{-3} M Rhodamine 6G dissolved in ethanol; Figure S4: The influence of defects (left) and the absence of curved edges (right) on GMR in Aula valve.

Author Contributions: Conceptualization, L.R. and M.G. (Martina Gilic); methodology—hybrid substrate preparation, M.G. (Mohamed Ghobara); methodology—SEM characterization, M.G. (Martina Gilic); methodology—SERS measurements and mapping, M.G. (Martina Gilic) and M.G. (Mohamed Ghobara); numerical analysis, M.G. (Martina Gilic); formal analysis, M.G. (Martina Gilic) and M.G. (Mohamed Ghobara); writing—original draft preparation, M.G. (Martina Gilic); writing—review and editing, L.R., M.G. (Martina Gilic) and M.G. (Mohamed Ghobara); visualization, M.G. (Martina Gilic) and M.G. (Mohamed Ghobara); project administration, L.R.; funding acquisition, L.R. All authors have read and agreed to the published version of the manuscript.

Funding: This work was funded by Deutsche Forschungsgemeinschaft, grant number [RE-3109\2-1], project number [422038271].

Data Availability Statement: All data needed to evaluate the conclusions in the paper are present in the paper and the Supplementary Materials.

Conflicts of Interest: The authors declare no conflict of interest.

References

1. Fleischmann, M.; Hendra, P.J.; McQuillan, A.J. Raman Spectra of Pyridine Adsorbed at a Silver Electrode. *Chem. Phys. Lett.* **1974**, *26*, 163–166. [[CrossRef](#)]
2. Langer, J.; Jimenez de Aberasturi, D.; Aizpurua, J.; Alvarez-Puebla, R.A.; Auguie, B.; Baumberg, J.J.; Bazan, G.C.; Bell, S.E.J.; Boisen, A.; Brolo, A.G.; et al. Present and Future of Surface-Enhanced Raman Scattering. *ACS Nano* **2020**, *14*, 28–117. [[CrossRef](#)]
3. Moskovits, M. Surface-Enhanced Raman Spectroscopy: A Brief Retrospective. *J. Raman Spectrosc.* **2005**, *36*, 485–496. [[CrossRef](#)]
4. Wang, A.; Kong, X. Review of Recent Progress of Plasmonic Materials and Nano-Structures for Surface-Enhanced Raman Scattering. *Materials* **2015**, *8*, 3024–3052. [[CrossRef](#)]
5. Hu, M.; Fattal, D.; Li, J.; Li, X.; Li, Z.; Williams, R.S. Optical Properties of Sub-Wavelength Dielectric Gratings and Their Application for Surface-Enhanced Raman Scattering. *Appl. Phys. A* **2011**, *105*, 261–266. [[CrossRef](#)]
6. Chen, Y.-M.; Pekdemir, S.; Bilican, I.; Koc-Bilican, B.; Cakmak, B.; Ali, A.; Zang, L.-S.; Onses, M.S.; Kaya, M. Production of Natural Chitin Film from Pupal Shell of Moth: Fabrication of Plasmonic Surfaces for SERS-Based Sensing Applications. *Carbohydr. Polym.* **2021**, *262*, 117909. [[CrossRef](#)]
7. Wang, Y.; Wang, M.; Sun, X.; Shi, G.; Zhang, J.; Ma, W.; Ren, L. Grating-like SERS Substrate with Tunable Gaps Based on Nanorough Ag Nanoislands/Moth Wing Scale Arrays for Quantitative Detection of Cypermethrin. *Opt. Express* **2018**, *26*, 22168. [[CrossRef](#)]

8. Zang, L.-S.; Chen, Y.-M.; Koc-Bilican, B.; Bilican, I.; Sakir, M.; Wait, J.; Çolak, A.; Karaduman, T.; Ceylan, A.; Ali, A.; et al. From Bio-Waste to Biomaterials: The Eggshells of Chinese Oak Silkworm as Templates for SERS-Active Surfaces. *Chem. Eng. J.* **2021**, *426*, 131874. [[CrossRef](#)]
9. Shi, G.C.; Wang, M.L.; Zhu, Y.Y.; Shen, L.; Ma, W.L.; Wang, Y.H.; Li, R.F. Dragonfly Wing Decorated by Gold Nanoislands as Flexible and Stable Substrates for Surface-Enhanced Raman Scattering (SERS). *Sci. Rep.* **2018**, *8*, 6916. [[CrossRef](#)]
10. Tian, L.; Jiang, Q.; Liu, K.-K.; Luan, J.; Naik, R.R.; Singamaneni, S. Bacterial Nanocellulose-Based Flexible Surface Enhanced Raman Scattering Substrate. *Adv. Mater. Interfaces* **2016**, *3*, 1600214. [[CrossRef](#)]
11. de Tommasi, E.; de Luca, A.C. Diatom Biosilica in Plasmonics: Applications in Sensing, Diagnostics and Therapeutics [Invited]. *Biomed. Opt. Express* **2022**, *13*, 3080. [[CrossRef](#)] [[PubMed](#)]
12. Round, F.E.; Crawford, R.M.; Mann, D.G. *Diatoms: Biology and Morphology of the Genera*; Cambridge University Press: Cambridge, UK, 1990; ISBN 0521363187.
13. Fuhrmann, T.; Landwehr, S.; el Rharbi-Kucki, M.; Sumper, M. Diatoms as Living Photonic Crystals. *Appl. Phys. B* **2004**, *78*, 257–260. [[CrossRef](#)]
14. Ghobara, M.M.; Ghobara, M.M.; Mazumder, N.; Vinayak, V.; Reissig, L.; Gebeshuber, I.C.; Tiffany, M.A.; Gordon, R.; Gordon, R. On Light and Diatoms: A Photonics and Photobiology Review. In *Diatoms: Fundamentals and Applications*; Wiley: Hoboken, NJ, USA, 2019; pp. 129–189.
15. Ghobara, M.M.; Ghobara, M.M.; Ghobara, M.M.; Mohamed, A. Diatomite in Use: Nature, Modifications, Commercial Applications and Prospective Trends. In *Diatoms: Fundamentals and Applications*; Wiley: Hoboken, NJ, USA, 2019; pp. 471–509.
16. Wang, Y.; Cai, J.; Jiang, Y.; Jiang, X.; Zhang, D. Preparation of Biosilica Structures from Frustules of Diatoms and Their Applications: Current State and Perspectives. *Appl. Microbiol. Biotechnol.* **2013**, *97*, 453–460. [[CrossRef](#)]
17. Ghobara, M.M.; Gordon, R.; Reissig, L. The Mesopores of Raphid Pennate Diatoms: Toward Natural Controllable Anisotropic Mesoporous Silica Microparticles. In *Diatom Morphogenesis*; Wiley: Hoboken, NJ, USA, 2021; pp. 10–11.
18. De Tommasi, E. Light Manipulation by Single Cells: The Case of Diatoms. *J. Spectrosc.* **2016**, *2016*, 1–13. [[CrossRef](#)]
19. Perozziello, G.; Candeloro, P.; Coluccio, M.; Das, G.; Rocca, L.; Pullano, S.; Fiorillo, A.; De Stefano, M.; Di Fabrizio, E. Nature Inspired Plasmonic Structures: Influence of Structural Characteristics on Sensing Capability. *Appl. Sci.* **2018**, *8*, 668. [[CrossRef](#)]
20. Zhang, M.; Meng, J.; Wang, D.; Tang, Q.; Chen, T.; Rong, S.; Liu, J.; Wu, Y. Biomimetic Synthesis of Hierarchical 3D Ag Butterfly Wing Scale Arrays/Graphene Composites as Ultrasensitive SERS Substrates for Efficient Trace Chemical Detection. *J. Mater. Chem. C* **2018**, *6*, 1933–1943. [[CrossRef](#)]
21. Ren, F.; Campbell, J.; Wang, X.; Rorrer, G.L.; Wang, A.X. Enhancing Surface Plasmon Resonances of Metallic Nanoparticles by Diatom Biosilica. *Opt. Express* **2013**, *21*, 15308. [[CrossRef](#)]
22. Caridad, H.; Winters, S.; McCloskey, D.; Duesberg, G.; Donegan, J.; Krstić, V. Hot-Volumes as Uniform and Reproducible SERS-Detection Enhancers in Weakly-Coupled Metallic Nanohelices. *Sci. Rep.* **2017**, *7*, 45548. [[CrossRef](#)]
23. Managò, S.; Zito, G.; Rogato, A.; Casalino, M.; Esposito, E.; de Luca, A.C.; de Tommasi, E. Bioderived Three-Dimensional Hierarchical Nanostructures as Efficient Surface-Enhanced Raman Scattering Substrates for Cell Membrane Probing. *ACS Appl. Mater. Interfaces* **2018**, *10*, 12406–12416. [[CrossRef](#)]
24. Kwon, S.Y.; Park, S.; Nichols, W.T. Self-Assembled Diatom Substrates with Plasmonic Functionality. *J. Korean Phys. Soc.* **2014**, *64*, 1179–1184. [[CrossRef](#)]
25. Kim, K.; Shin, D.; Kim, K.L.; Shin, K.S. Electromagnetic Field Enhancement in the Gap between Two Au Nanoparticles: The Size of Hot Site Probed by Surface-Enhanced Raman Scattering. *Phys. Chem. Chem. Phys.* **2010**, *12*, 3747. [[CrossRef](#)] [[PubMed](#)]
26. D’Acunto, M.; Fuso, F.; Micheletto, R.; Naruse, M.; Tantussi, F.; Allegrini, M. Near-field surface plasmon field enhancement induced by rippled surfaces. *Beilstein J. Nanotechnol.* **2017**, *8*, 956–967. [[CrossRef](#)] [[PubMed](#)]
27. Ghobara, M.; Oschatz, C.; Fratzl, P.; Reissig, L. Numerical Analysis of the Light Modulation by the Frustule of Gomphonema Parvulum: The Role of Integrated Optical Components. *Nanomaterials* **2022**, *13*, 113. [[CrossRef](#)] [[PubMed](#)]
28. Jensen, L.; Schatz, G.C. Resonance Raman Scattering of Rhodamine 6G as Calculated Using Time-Dependent Density Functional Theory. *J. Phys. Chem. A* **2006**, *110*, 5973–5977. [[CrossRef](#)] [[PubMed](#)]
29. Sakai, M.; Ohmori, T.; Fujii, M. Two-Color Picosecond Time-Resolved Infrared Super-Resolution Microscopy. In *Handai Nanophotonics*; Elsevier: Amsterdam, The Netherlands, 2007; Volume 3, pp. 189–195.
30. Lindon, J.; Tranter, G.; Koppenaal, D. *Encyclopedia of Spectroscopy and Spectrometry*, 2nd ed.; Academic Press: Cambridge, MA, USA, 2010.
31. He, X.N.; Gao, Y.; Mahjour-Samani, M.; Black, P.N.; Allen, J.; Mitchell, M.; Xiong, W.; Zhou, Y.S.; Jiang, L.; Lu, Y.F. Surface-Enhanced Raman Spectroscopy Using Gold-Coated Horizontally Aligned Carbon Nanotubes. *Nanotechnology* **2012**, *23*, 205702. [[CrossRef](#)]
32. Sil, S.; Kuhar, N.; Acharya, S.; Umapathy, S. Is Chemically Synthesized Graphene ‘Really’ a Unique Substrate for SERS and Fluorescence Quenching? *Sci. Rep.* **2013**, *3*, 3336. [[CrossRef](#)]
33. Stec, H.M.; Williams, R.J.; Jones, T.S.; Hatton, R.A. Ultrathin Transparent Au Electrodes for Organic Photovoltaics Fabricated Using a Mixed Mono-Molecular Nucleation Layer. *Adv. Funct. Mater.* **2011**, *21*, 1709–1716. [[CrossRef](#)]
34. Kossov, A.; Merk, V.; Simakov, D.; Leosson, K.; Kéna-Cohen, S.; Maier, S.A. Optical and Structural Properties of Ultra-Thin Gold Films. *Adv. Opt. Mater.* **2015**, *3*, 71–77. [[CrossRef](#)]

35. Ghobara, M.M.; Tiffany, M.A.; Gordon, R.; Reissig, L. Diatom Pore Arrays' Periodicities and Symmetries in the Euclidean Plane: Nature Between Perfection and Imperfection. In *Diatom Morphogenesis*; Wiley: Hoboken, NJ, USA, 2021; pp. 117–158.
36. Wang, S.S.; Magnusson, R. Theory and Applications of Guided-Mode Resonance Filters. *Appl. Opt.* **1993**, *32*, 2606. [[CrossRef](#)]
37. Wang, S.S.; Magnusson, R.; Bagby, J.S.; Moharam, M.G. Guided-Mode Resonances in Planar Dielectric-Layer Diffraction Gratings. *J. Opt. Soc. Am. A* **1990**, *7*, 1470. [[CrossRef](#)]
38. Collin, S. Nanostructure Arrays in Free-Space: Optical Properties and Applications. *Rep. Prog. Phys.* **2014**, *77*, 126402. [[CrossRef](#)] [[PubMed](#)]
39. Yang, J.; Ren, F.; Chong, X.; Fan, D.; Chakravarty, S.; Wang, Z.; Chen, R.; Wang, A. Guided-Mode Resonance Grating with Self-Assembled Silver Nanoparticles for Surface-Enhanced Raman Scattering Spectroscopy. *Photonics* **2014**, *1*, 380–389. [[CrossRef](#)] [[PubMed](#)]
40. Kraai, J.A.; Wang, A.X.; Rorrer, G.L. Photonic Crystal Enhanced SERS Detection of Analytes Separated by Ultrathin Layer Chromatography Using a Diatom Frustule Monolayer. *Adv. Mater. Interfaces* **2020**, *7*, 2000191. [[CrossRef](#)]
41. D'Mello, Y.; Bernal, S.; Petrescu, D.; Skoric, J.; Andrews, M.; Plant, D.V. Solar Energy Harvesting Mechanisms of the Frustules of *Nitzschia Filiformis* Diatoms. *Opt. Mater. Express* **2022**, *12*, 4665. [[CrossRef](#)]

Disclaimer/Publisher's Note: The statements, opinions and data contained in all publications are solely those of the individual author(s) and contributor(s) and not of MDPI and/or the editor(s). MDPI and/or the editor(s) disclaim responsibility for any injury to people or property resulting from any ideas, methods, instructions or products referred to in the content.

UDK: 519.718; 620.181.4; 666.3.019; 661.112.3

Synthesis and Characterization of Monophase $\text{CaO-TiO}_2\text{-SiO}_2$ (Sphene) Based Glass-Ceramics

Jelena Maletaškić^{1,5*}, Bratislav Todorović², Martina Gilić³, Milena Marinović Cincović⁴, Katsumi Yoshida⁵, Anna Gubarevich⁵, Branko Matović¹

¹Institute of Nuclear Sciences Vinča, Department of Material Science, Center of Excellence, CEXTREME LAB University of Belgrade, P. O. Box 522, 11000 Belgrade, Serbia

²Faculty of Technology, University of Niš, P.O. Box 79, 16000 Leskovac, Serbia

³Institute of Physics, University of Belgrade, Pregrevica 118, 11080 Belgrade, Serbia

⁴Institute of Nuclear Sciences Vinča, Laboratory for Radiation Chemistry and Physics, University of Belgrade, Mike Petrovića Alasa 12-14, P.O. Box 522, 11001 Belgrade, Serbia

⁵Laboratory for Advanced Nuclear Energy, Institute of Inovative Research, Tokyo Institute of Technology, 2-12-1, Ookayama, Meguro-ku, Tokyo, 152-8550 Japan

Abstract:

Sphene based glass-ceramics (CaTiSiO_5), an excellent candidate for a host lattice of ceramic materials and for nuclear waste immobilization, has been prepared from a powder mixture of CaCO_3 , TiO_2 and SiO_2 using vibro-milling for homogenization. Starting powders were melted at 1400 °C for 2 h, cooled to room temperature, grounded again, then crystallized by thermal treatment yielding a sphene glass-ceramic. The evolution of the phase composition during thermal treatment was investigated by X-ray powder diffraction (XRPD), FT-IR, Raman and thermal analyses (TG-DTA). Pure synthetic single phase sphene was formed at 800 °C for 4 h, even it is very hard to obtain monophase powder at such low temperature. Powder morphology was analyzed by scanning electron microscopy (SEM).

Keywords: *Sphene; Glass-ceramics; Mechanochemistry; XRPD, TG-DTA.*

1. Introduction

Glass-ceramics can be used for various applications, such as thermal, chemical, biological and dielectric ones. These kinds of materials offer great possibilities as we can control their properties, including strength, resistance to abrasion and coefficient of thermal expansion [1]. Another advantage is the simple fabrication process in combination with a lower production cost [2-5]. The synthesis of the parent glass is an important step in preparing the final glass-ceramic material because the precursors and their percentage in the glass composition manage the precipitation of the crystalline phases. The results of this process can provide glass-ceramic with the desired properties.

Beside the biomaterials field, the glass-ceramics can be used as nuclear waste storage. They are significantly more durable than borosilicate glasses in a wide variety of leachates at

*) Corresponding author: jelena.pantic@vinca.rs

neutral or alkaline pH values [6]. In previous research, the Canadian Nuclear Fuel Waste Management program has considered the possibility of waste storage with glass-ceramics containing crystalline titanite embedded in an aluminosilicate glass [7, 8]. It can also be used for the stabilization of waste sludge [9, 10] and other waste material [11, 12].

Sphene or titanite (CaTiSiO_5 or $\text{CaTiO}(\text{SiO}_4)$) belongs to the nesosilicate family of minerals. It crystallizes in monoclinic symmetry in two space groups: $A2/a$ and $P2_1/a$ [13]. Sphene is a phase well known for its excellent containment capacity and long-term behavior (high chemical durability and self-radiation resistance). It has good thermal stability and it is an excellent candidate as a host material [14], as well as biomedical engineering (coatings on Ti-6Al-4V) [15]. Furthermore, it can be used for nuclear waste disposal [16], luminescent materials [17] and pigments [18-21] because of the ability to incorporate many elements into its crystal lattice.

In our work, we report the synthesis of sphene without additional phases. It is very difficult to obtain pure synthetic monophase titanite, especially below 1200°C . Several different methods like sol-gel, coprecipitation, combustion, spray pyrolysis, freeze-drying and hydrothermal methods have been used. In most cases, pure sphene was not obtained [22-27]. There are always some traces of crystobalite (SiO_2), perovskite (CaTiO_3), wollastonite (CaSiO_3) and other phases, besides sphene.

When preparing the glass-ceramics at the laboratory, the crystallization of the parent glass is carried in two-phase via thermal treatment: nucleation and growth. In this paper we present the evolution of the crystallization, followed by scanning electron microscopy (SEM), Fourier transforms infrared spectroscopy (FTIR), Raman spectroscopy and X-ray powder diffraction (XRPD), with the temperature of the crystal growth thermal treatment, in the range 650 - 1250°C . The formation process from glass to the final glass-ceramic product is discussed for different temperature treatments.

2. Materials and Experimental Procedures

2.1. Powder preparation and synthesis

Reactants used in the synthesis were commercial powders: TiO_2 (Lab. Art. 808 E. Merck), SiO_2 (ASP-K-amorphous, Prahovo) and CaCO_3 (pro analysi, 11490, Kemika, Zagreb). Sample was prepared from stoichiometric amounts of powders and weighed 5 grams. The powder mixtures were homogenized in the vibratory mill (Fritsch Pulverisette Analysette Laborette, type 09 003, no. 155, 380 volt). Detailed description of the synthesis procedures for sample can be found in the original paper [28]. Samples were ground for 30 min in air atmosphere prior to melting at 1400°C in a platinum crucible for 2 h. After melting, sample was poured in water and grinded for glass homogenization before further thermal treatment. The glass was transformed into glass-ceramics by annealing in an open-air atmosphere in furnace. Calcination of powders was carried out at different temperatures from 600 to 1250°C in at a heating rate of $10^\circ\text{C}/\text{min}$ and a soaking period of 4 h in alumina crucibles.

2.2. Characterization

The thermal stability of samples was investigated by non-isothermal thermogravimetric analysis (TG) and DTA analysis using a SETARAM SETSYS Evolution-1750 instrument. The measurements were conducted at a heating rate of $10^\circ\text{C}/\text{min}$ in a dynamic air atmosphere (flow rate $16\text{ cm}^3/\text{min}$) in the temperature range from 30 to 1250°C

Fourier transform infrared spectroscopy (FTIR) was performed in the absorbance mode using a BOMEM Michelson Series MB FTIR spectrometer set to give undeformed spectra. The resolution was 4 cm^{-1} in the 400 - 2000 cm^{-1} analyzed range. The spectra were

obtained at room temperature from KBr pressed pellets prepared by mixing 1.5 mg of a sample with 150 mg of KBr.

All of the samples were characterized at room temperature by X-ray powder diffraction (XRPD) using Ultima IV Rigaku diffractometer equipped with Cu $K_{\alpha 1,2}$ radiation using a generator voltage (40.0 kV) and a generator current (40.0 mA). The range of $10 - 90^\circ 2\theta$ was used for all powders in a continuous scan mode with a scanning step size of 0.02° and at a scan rate of $2^\circ/\text{min}$. Phase analysis was done by using the PDXL2 software (version 2.0.3.0) [23], with reference to the patterns of the International Centre for Diffraction Data database (ICDD) [29], version 2012.

The average crystallite size (D) was calculated on the basis of the full-width at half-maximum intensity (FWHM) of the main reflections by applying Scherrer's formula:

$$D_{hkl} = K\lambda / (\beta \cdot \cos\theta) \quad (2)$$

where K is a Scherrer's constant (~ 0.9), λ is the wavelengths of the X-ray used, θ is diffraction angle and β is corrected half-width for instrumental broadening given as $\beta = (\beta_m - \beta_s)$ where β_m and β_s are observed half-width and half-width of the standard monoclinic sphe sample, respectively.

Internal lattice strain ($\Delta d/d$) of calcined samples was estimated from the Williamson-Hall plots, using following equation [30]:

$$\beta_{total} \cos\theta = (K\lambda)/D + (4\Delta d/d) \cdot \quad (3)$$

where β_{total} represents full-width half-maximum of the characteristic XRPD peak and Δd is the difference of the d spacing corresponding to a typical peak. The strain of nanocrystals, $\Delta d/d$, can be estimated from the slope of function $\beta \cdot \cos\theta$ vs. $\sin\theta$ whereas crystallite size, D , can be estimated from the y-intercept.

Micro-Raman scattering measurements were performed at room temperature using a Jobin-Yvon T64000 triple spectrometer system equipped with a liquid-nitrogen cooled CCD detector. The $\lambda=514.5$ nm line of an Ar^+/Kr^+ mixed laser was used as an excitation source.

Microstructure and grain size were investigated using Field Emission Scanning Electron Microscopy (FESEM), performed on a JEOL-5200F Scanning electron microanalyzer.

3. Results and Discussion

The results of thermal analysis of sample (as-prepared glass) after melting at 1400°C are presented in Figure 1. As TG curve indicates, there is no obvious mass loss. At low temperature (below 300°C), small exothermic peaks corresponding to volatiles appear larger, presumable due to the use of coarse powder [31]. As shown in DTA curves, there is a small endothermic peak attributed to the glass transition temperature range. Its minimum that starts at 760°C refers to the glass transition temperature (T_g). The temperature at 886°C belongs to sharp exothermic peak, due to the amorphous-crystalline transformation. The maximum temperature belongs to the crystallization peak temperature (T_p).

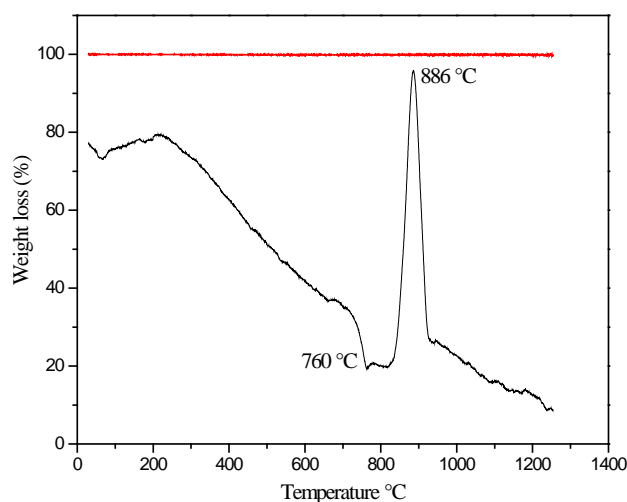


Fig. 1. DTA/TG diagram for as-synthesized amorphous glass up to a heat treatment temperature of 1250 °C. Black line – DTA; red line – TG.

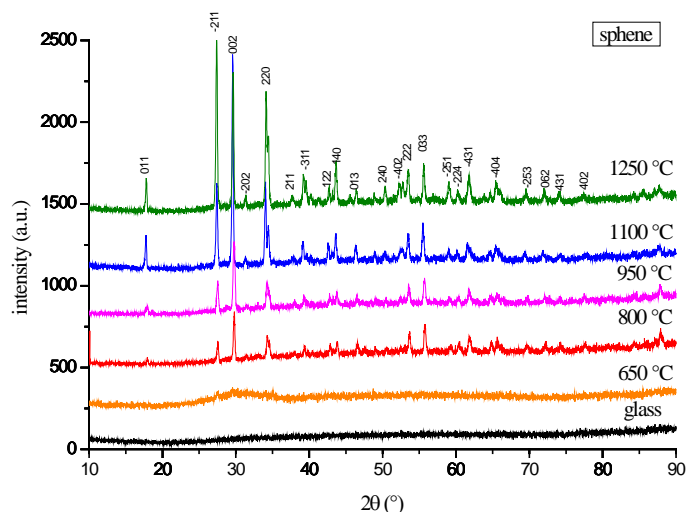


Fig. 2. X-ray powder diffraction patterns of sphene glass-ceramics (30 min grinding) after melting at 1400 °C and calcination at different temperatures (650-1250 °C). All the peaks belong to sphene.

The changes in the X-ray pattern due to annealing are presented in Figure 2. The pattern of glass sample and sample obtained at 650 °C corresponds to amorphous materials; no crystalline phases were detected. According to the results of TG/DTA, the glass starts to crystallize around 760 °C. At 800 °C X-ray powder diffraction results indicated that there was a significant change in the sample, and glass recrystallized to form sphene (CaTiSiO_5). All of the diffraction peaks belonging to sphene were observed. On further increasing the temperature up to 1250 °C, the intensity of sphene reflections increased, due to better crystallization. In addition, the peaks moved to slightly higher scattering angles on annealing, while the lattice volume decreases [32, 33]. The height of the strongest peak, the (200) reflection, is plotted against the annealing temperature in Figure 3, and the changes in lattice volume are similarly plotted in Figure 4. Sphene is a principle crystalline phase above 800 °C.

The main reflections in these patterns are observed at 2θ of 17, 27, 29, and 34 °, which are typical for the sphene structure. All the structure information was taken from American Mineralogist Crystal Data Structure Base (AMCDSB) [34]. Pure synthetic single phase sphene was formed at 800 °C for 4 h, even it is very hard to obtain monophasic powder at such low temperature.

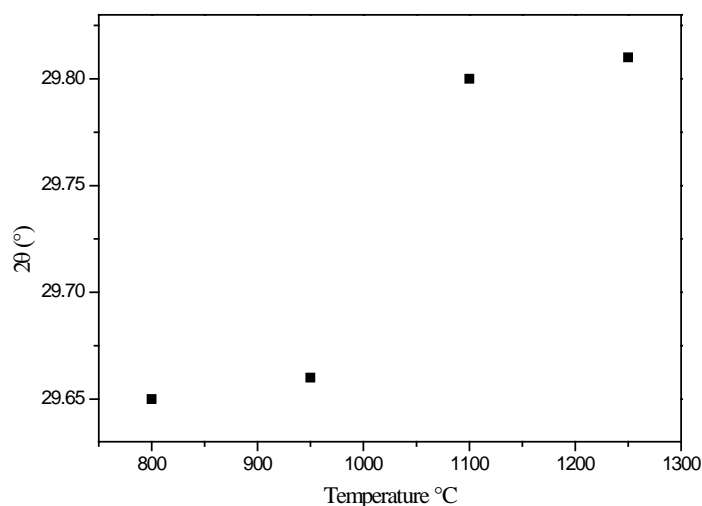


Fig. 3. Position of (200) X-ray powder diffraction peak, measured from samples calcinated at different temperatures (800-1250 °C).

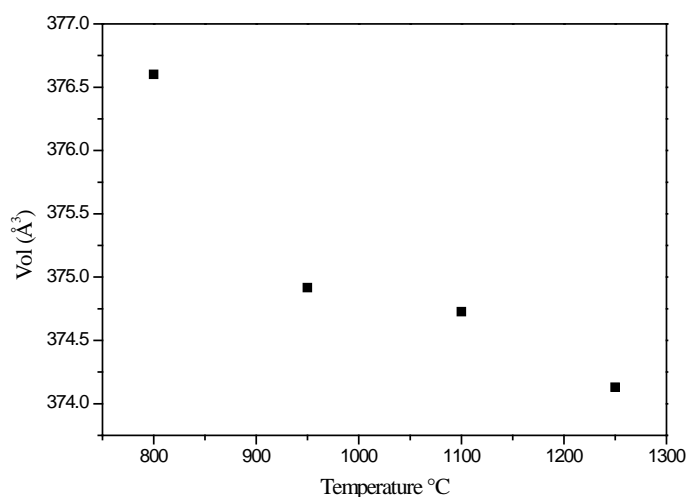


Fig. 4. Decrease in lattice volume as a function of annealing temperature. Measurements were made with samples calcinated at different temperatures (800-1250 °C).

The values of crystallite size and internal strain of samples after melting at 1400 °C and calcined at different temperatures for 4 h are presented in Table I. The average crystallite size increases with an increase in calcination temperature (up to 1100 °C) because of accelerated diffusion at higher temperatures, with decreasing the lattice parameters. At 1250 °C, due to close temperature range of melting point, crystallite size starts to decrease. Furthermore, the internal strain of samples calcined at different temperature which was

estimated from the slope of Williamson – Hall plots is presented in Figure 5. Just after the crystallization, there is no evident strain.

Tab. I Lattice parameter and crystallite size of sphene glass-ceramics (30 min grinding) after melting at 1400 °C and calcination at different temperatures (650-1250 °C).

Temperatures (°C)	Lattice parameter (Å)	β (°)	D (nm)
650	amorphous	/	/
800	a = 7.0859 b = 8.8062 c = 6.5478	112.8200	23
950	a = 7.0808 b = 8.7882 c = 6.5413	112.9181	25
1100	a = 7.0911 b = 8.7893 c = 6.5316	112.9995	28
1250	a = 7.0946 b = 8.7716 c = 6.5328	113.0340	16

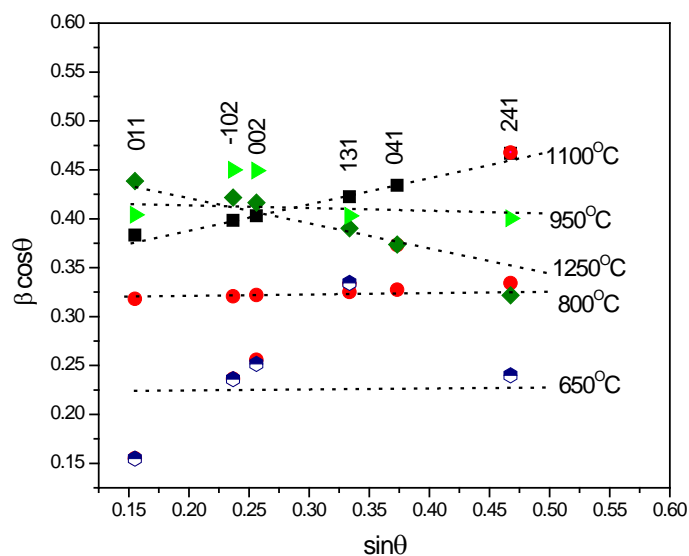


Fig. 5. Williamson-Hall plot of sphene glass-ceramics (30 min grinding) after melting at 1400 °C and calcination at different temperatures (650-1250 °C). The dotted lines are visual guides.

To confirm X-ray powder diffraction results, FT-IR measurements were done. FT-IR spectra of samples sintered at different temperatures are shown in Figure 6. From 800 °C up to 1250 °C, vibrations centered at about: 895 cm^{-1} , 870 cm^{-1} , 694 cm^{-1} , 561 cm^{-1} , 468 cm^{-1} and 424 cm^{-1} correspond to vibration of sphene and they are in good agreement with published data [35-38]. The spectra are dominated by the IR band near 870 cm^{-1} which is attributed mainly to SiO_4 stretching modes. The broad band near 694 cm^{-1} is associated with TiO_6 octahedral stretching modes, polarized along the crystallographic a -axis and it is related to the crystal quality [39]. Vibration band around 1636 cm^{-1} due to the asymmetric stretching mode of CO_3^{2-} were also detected [40].

The effect of temperature increase is seen as a decrease in band width, an increase in band intensity associated with Si-O bending at 561 cm^{-1} and the Si-O stretching band at about 870 cm^{-1} [41, 42]. All peaks shift to higher wavenumbers with increasing temperature.

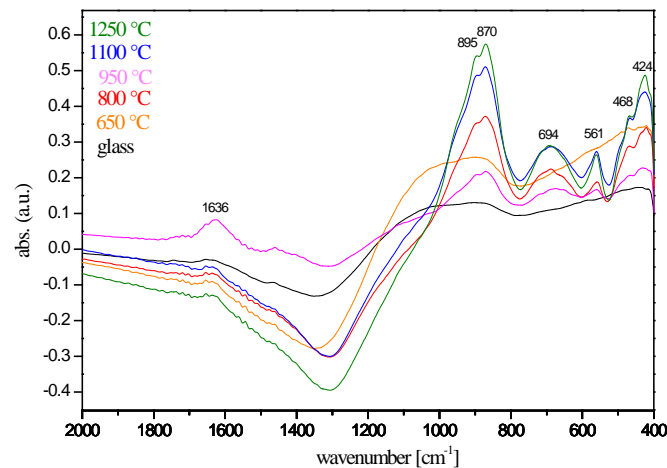


Fig. 6. FTIR absorption spectra of sphene glass-ceramics after (30 min grinding) after melting at $1400\text{ }^{\circ}\text{C}$ and calcination at different temperatures ($650\text{--}1250\text{ }^{\circ}\text{C}$).

The Raman spectra collected from samples are shown in Figure 7. The characteristic bands of sphene that occur in Raman spectra are centered around 167, 258, 473, 548 and 608 cm^{-1} [38, 43]. All peaks shift to higher wavenumbers with increasing temperature.

The position of the peak near 608 cm^{-1} belongs to a symmetrical mode from Ti–O bond stretching and Ti–O–Ti bond bending [44–46]. As peak intensity increases with increasing temperature, band width of this peak decreases [47].

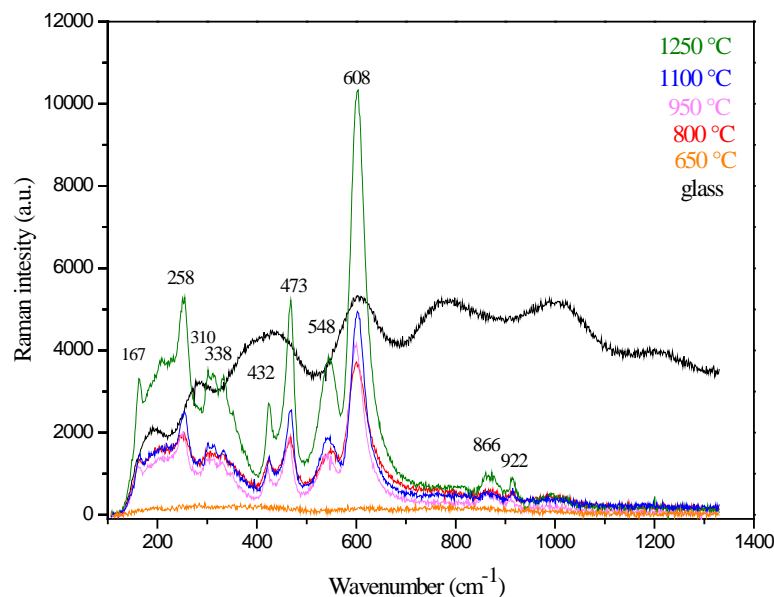


Fig. 7. The Raman spectra of sphene glass-ceramics (30 min grinding) after melting at $1400\text{ }^{\circ}\text{C}$ and calcination at different temperatures ($650\text{--}1250\text{ }^{\circ}\text{C}$).

On increasing temperature, the peaks near 432 and 473 cm^{-1} related to SiO_4 bending modes as well as the external SiO_4 mode near 258 cm^{-1} have the same dependence, an increasing wavenumber and a decreasing band width. Peak near 473 cm^{-1} belongs to the SiO_4 bending mode [43]. The Raman peaks near 866 cm^{-1} correspond to Si-O stretching modes in orthosilicates [47].

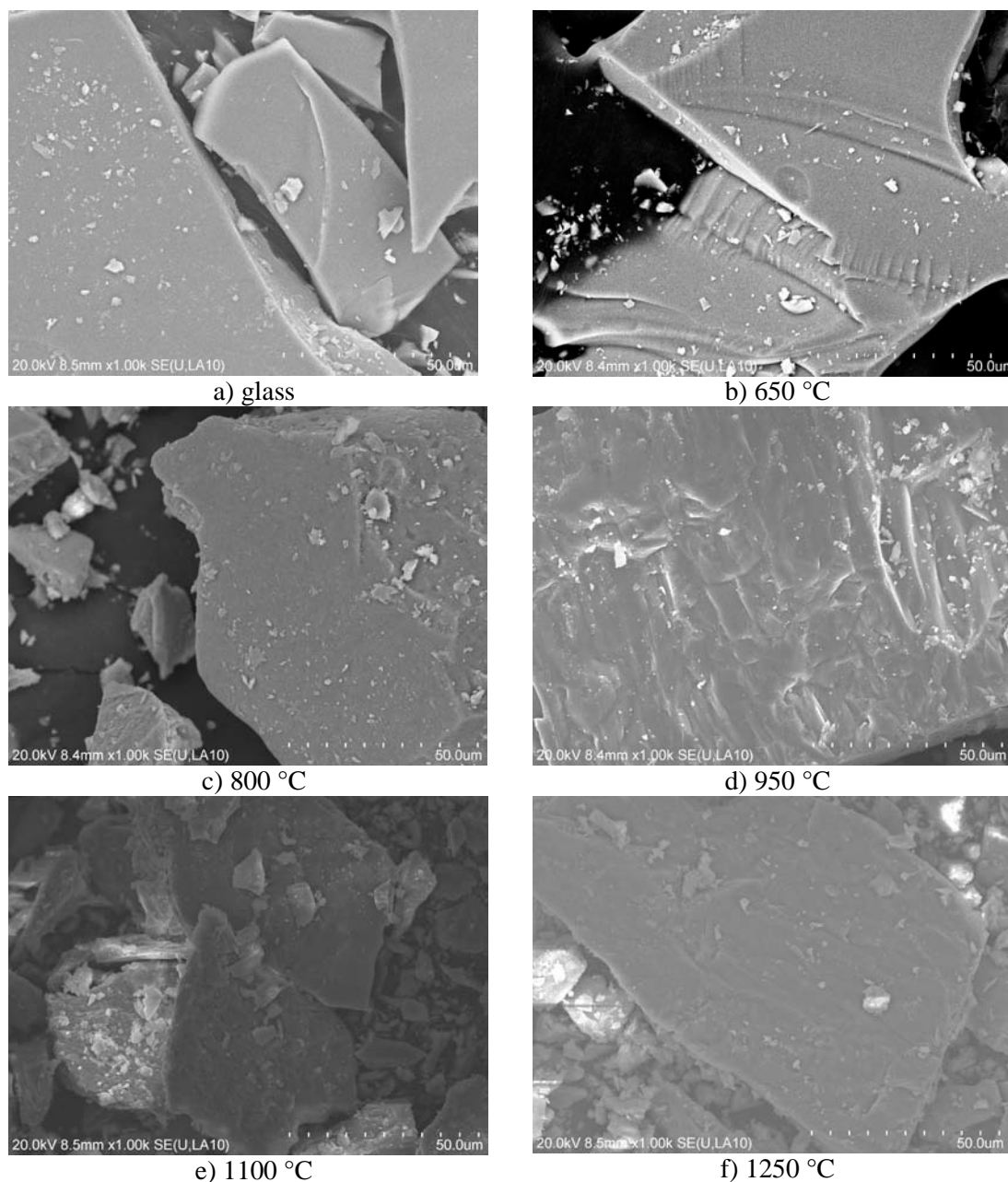


Fig. 8. SEM micrographs (a-f) of spene glass-ceramics (30 min grinding) after melting at 1400 °C and calcination at different temperatures (650 - 1250 °C).

Due to the increasing degree of cristalization all peaks shift to higher wavenumbers. Ti-O bond stretching band shifts from $601 \pm 0.5\text{ cm}^{-1}$ to $608 \pm 0.5\text{ cm}^{-1}$. O-Si-O bending modes at $466 \pm 0.5\text{ cm}^{-1}$ shifts to $473 \pm 0.5\text{ cm}^{-1}$, $422 \pm 0.5\text{ cm}^{-1}$ shifts to $432 \pm 0.5\text{ cm}^{-1}$ and $253 \pm 0.5\text{ cm}^{-1}$ shifts to $258 \pm 0.5\text{ cm}^{-1}$. Si-O stretching modes at $862 \pm 0.8\text{ cm}^{-1}$ shifts to a

position at $866 \pm 0.8 \text{ cm}^{-1}$ (Figure 7). The lowest-energy mode occurring near 167 cm^{-1} also shows a slight shift to higher wavenumbers, from $161 \pm 0.5 \text{ cm}^{-1}$ shift to $167 \pm 0.5 \text{ cm}^{-1}$.

Regarding amorphous systems, in Ti–Si–O frameworks the Ti^{4+} cations can occur as 6-, 5- and 4- coordinated [48, 49], and penta- and tetra-coordinated Ti^{4+} can be found in heavily metamict sphene [50-52]. When decreasing Ti coordination, the Ti–O bond strength increases. As a result, in a disordered framework, the Ti–O bond stretching mode would move to higher wavenumbers as compared to the Ti–O bond stretching mode having only TiO_6 octahedra.

The SEM micrographs of glass-ceramics obtained at various temperatures are shown in Figure 8. Samples were crushed in mortar prior the measurements. For glass obtained at $650 \text{ }^\circ\text{C}$, particles with irregular shapes were observed, as shown in Figure 6(b). After being calcined at higher temperatures ($800\text{-}1250 \text{ }^\circ\text{C}$), similar anhedral shape is seen (Figure 8 (c–f)). Particles have a smooth fracture surface with no obvious cracks or faults on the surface.

4. Conclusion

Glass and glass-ceramics in the $\text{CaO-TiO}_2\text{-SiO}_2$ system have been successfully synthesized. From DTA curves, glass transition temperature (T_g) starts at $760 \text{ }^\circ\text{C}$ and temperature at $886 \text{ }^\circ\text{C}$ belongs to the crystallization peak temperature (T_p). X-ray powder diffraction results indicated that at $800 \text{ }^\circ\text{C}$ glass recrystallize to form sphene (CaTiSiO_5), and the peaks moved to slightly higher scattering angles on annealing, while the lattice volume decreases. Pure synthetic single phase sphene was formed at $800 \text{ }^\circ\text{C}$ for 4 h, despite being difficult to obtain monophase powder at such low temperature. The effect of temperature increase in FT-IR and Raman measurements is seen as a decrease in band width and an increase in band intensity. All peaks shift to higher wavenumbers with increasing temperature, according to the Raman. SEM images showed anhedral shaped particles.

For crystal growth temperature (T_c) ranging from 800 to $1250 \text{ }^\circ\text{C}$, sphene is the only crystalline phase. Thus there is a wide range of temperature for the preparation of monophase sphene-based glass-ceramics that can be designed as durable waste forms for immobilization.

Acknowledgments

Financial support from the Serbian Education and Science Ministry in the Framework of project No. 45012 is gratefully acknowledged. One of the authors Jelena Maletaskic, as well as Branko Matovic, gratefully acknowledge the financial support from the Tokyo Institute of Technology, Laboratory for Advanced Nuclear Energy, Institute of Innovative Research, 2-12-1, O-okayama, Meguro-ku, Tokyo 152-8550, as visiting professors.

5. References

1. D.U. Tulyaganov, S. Agathopoulos, J.M. Ventura, M.A. Karakassides, O. Fabrichnaya, J.M.F. Ferreira, Synthesis of glass–ceramics in the CaO-MgO-SiO_2 system with B_2O_3 , P_2O_5 , Na_2O and CaF_2 additives, *J. Eur. Ceram. Soc.* 26 (2006) 1463-1471.
2. W. Holand, G. Beall, *Glass–Ceramic Technology*, 2nd ed. Wiley-American Ceramic Society, Westerville, OH, 2012.
3. N.M. Pavlushkin, *Principals of Glass Ceramics Technology*, 2nd ed. Stroiizdat, Moscow, 1979 (in Russian).
4. P.W. McMillan, *Glass-Ceramics*. Academic Press, London, 1964.
5. Z. Strnad, *Glass-Ceramic Materials*. Elsevier, Amsterdam, 1986.

6. P.J. Hayward, D.C. Doern, I.M. George, Dissolution of a sphene glass- ceramic, and of its component sphene and glass phases in Ca-Na-Cl brines, *J. Am. Ceram. Soc.* 73 (1990) 544-511.
7. P.J. Hayward, Glass ceramics. In W. Lutze and R. Ewing, Eds., *Radioactive waste forms for the future*, Elsevier, New York (1988) 427-492.
8. P. Hayward, E. Cechetto, Development of sphene-based glass ceramics tailored for Canadian waste disposal conditions, In Topp, S., Ed., *Scientific Basis for Nuclear Waste Management* 3 (1982) 91-98.
9. I. Krstić, S. Zec, V. Lazarević, M. Stanisavljević, T. Golubović, Use of Sintering to Immobilize Toxic Metals Present in Galvanic Sludge into a Stable Glass-Ceramic Structure, *Sci. Sinter.* 50 (2018) 139-147.
10. A. P. Parra, M. Vlasova, P. A. Márquez Aguilar, T. Tomila, Peculiarities of a Glass-Sludge Mixture Subjected to Low-Temperature Treatment *Sci. Sinter.* 49 (2017) 207-224.
11. M. Cocic, B. Matovic, M. Posarac, T. Volkov-Husovic, J. Majstorovic, V. Tasic, S. Devic, N. Vusovic, Thermal Shock Properties of Glass-ceramics Synthesized From a Glass Frit, *Sci. Sinter.* 49 (2017) 139-147.
12. M. Cocić, M. Logar, S. Erić, V. Tasić, S. Dević, S. Cocić, B. Matović, Application of the Final Flotation Waste for Obtaining the Glass-ceramic Materials, *Sci. Sinter.* 49 (2017) 431-443.
13. E.S. Dana, *Manual of mineralogy*. 17th ed. John Wiley & Sons Inc. (1959) 412-413.
14. M. Gascoune, Evidence for the stability of the potential nuclear waste host, sphene, over geological time, from uranium-lead ages and uranium series measurement. *App. Geolchem.* 1 (1986) 199-210.
15. C. Wu, Y. Ramaswamy, X. Liu, G. Wang, H. Zreiqat, Plasma-sprayed CaTiSiO₅ ceramic coating on Ti-6Al-4V with excellent bonding strength, stability and cellular bioactivity, *J. R. Soc. Interface* 6 (2009) 159-168.
16. A.E. Ringwood, S.E. Kesson, K.D. Reeve, D.M. Levins, E.J. Ramm, SYNROC. In: Lutze W, Ewing RC, editors. *Radioactive waste forms for the future*, North-Holland, Amsterdam (1988) 233-334.
17. M. Gaft, L. Nagli, R. Reisfeld, G. Panczer, Laser-induced time-resolved luminescence of natural titanite CaTiOSiO₄, *Opt. Mater.* 24 (2003) 231-241.
18. P. Escribano, C. Guillem, J. Alarcon, Cr-SnO₂-CaO-SiO₂ based ceramic pigments, *Am. Ceram. Soc. Bull.* 63 (1984) 1492-1494.
19. J. Carda, P. Escribano, G. Monros, M.D. Rodrigo, J. Alarcon, Co-SnO₂-CaO-SiO₂ based ceramic pigments, *Interceram.* 39 (1990) 22-24.
20. L. Ferrer, M. Sales, J. Alarcon, Sphene structure based ceramic pigments, *Third Euro-ceram.* 2 (1993) 935-939.
21. J. Pantić, M. Prekajski, M. Dramićanin, N. Abazović, N. Vuković, A. Kremenović, B. Matović, Preparation and characterization of chrome doped sphene pigments prepared via precursor mechanochemical activation, *J. Alloy. Comp.* 579 (2013) 290-294.
22. T.S. Lyubenova, F. Matteucci, A. Costa, M. Dondi, J. Carda. Ceramic pigments with sphene structure obtained by both spray- and freeze drying techniques, *Powder Technol.* 193 (2009) 1-5.
23. T.S. Lyubenova, F. Matteucci, A.L. Costa, M. Dondi, M. Ocaña, J. Carda, Synthesis of Cr-doped CaTiSiO₅ ceramic pigments by spray drying, *Mater. Res. Bull.* 44 (2009) 918-924.
24. T. Malcherek, C.M. Domeneghetti, V. Tazzoli, E.K.H. Salje, U. Bismayer, A high temperature diffraction study of synthetic titanite CaTiOSiO₄, *Phase Transitions* 69 (1999) 119-131.
25. M. Muthuraman, N.A. Dhas, K.C. Patil, Combustion synthesis of oxide materials for nuclear waste immobilization, *Bull. Mater. Sci.* 17 (1994) 977-987.

26. M. Muthuraman, K.C. Patil, Synthesis, properties, sintering and microstructure of sphene, CaTiO_5 : A comparative study of coprecipitation, sol-gel and combustion processes, *Mater. Res. Bull.* 33 (1998) 655-661.
27. R. Ellemann-Olesen, A high-temperature diffraction study of the solid solution CaTiOSiO_4 - CaTiOGeO_4 , *Am. Miner.* 90 (2005) 1325-1334
28. J. Pantić, A. Kremenović, A. Došen, M. Prekajski, N. Stanković, Z. Bašcarević, B. Matović, Influence of mechanical activation on sphene based ceramic material synthesis, *Ceram. Inter.* 39 (2013) 483-488.
29. PDXL Version 2.0.3.0 Integrated X-ray Powder Diffraction Software. Tokyo, Japan: Rigaku Corporation (2011) 196-8666.
30. Powder Diffraction File, PDF-2 Database and announcement of new database release 2012, International Centre for Diffraction Data (ICDD).
31. J. Rodriguez-Carvajal, Collected Abstract of Powder Diffraction Meeting, Toulouse (1990) 127.
32. J.B. Higgins, P.H. Ribbe, The crystal chemistry and space groups of natural and synthetic titanites, *Am. Mineral.* 61 (1976) 878-888.
33. E.R. Vance and J.B. Metson, Radiation damage in natural titanite, *Phys. Chem. Minerals* 12 (1985) 255-260
34. R.T. Downs, M. Hall-Wallace, The American Mineralogist Crystal Structure Database, *Am. Min.* 88 (2003) 247-250.
35. J.A. Gadsden, Infrared Spectra of minerals and related inorganic compounds, Butterworth, Group addresses, England, Australia, Canada, New Zealand, South Africa, U.S.A., 1975.
36. H. Moenke, *Mineralspectren*. Deutsche Akademie der Wissenschaften zu Berlin, Akademie – Verlag – Berlin, 1962.
37. J. Pantić, V. Kahlenberg, V. Poharc-Logar, A. Kremenović, Natural $\text{CaO-TiO}_2\text{-SiO}_2$ based ceramics, *Process. Appl. Ceram.* 5 [2] (2011) 79-84.
38. J. Pantic, V. Urbanovich, V. Poharc-Logar, B. Jokić, M. Stojmenović, A.Kremenović, B. Matović, Synthesis and characterization of high-pressure and high-temperature sphene (CaTiSiO_5), *Phys. Chem. Miner.* 41 (2014) 775-782.
39. H.W. Meyer, M. Zhang, U. Bismayer, E.K.H. Salje, C. Schmidt, S. Kek, W. Morgenroth, T. Bleser, Phase transformation of natural titanite: An infrared, Raman spectroscopic, optical birefringence and X-ray diffraction study. *Phase Trans.* 59 (1996) 39-60.
40. P.J. Hayward, E.R. Vance, C.D. Cann, S.L. Mitchell Crystallization of sphene-based glass-ceramics for immobilization of high-level nuclear fuel reprocessing wastes. In: Wicks GG, Ross WA (eds) *Advances in Ceramics*. Am Ceramic Society, (1984c) 291-301.
41. E.K.H. Salje, U. Bismayer, Hard Mode Spectroscopy: The Concept and Applications, *Phase Trans.* 63 (1997) 1-75
42. M. Zhang, E.K.H. Salje, U. Bismayer, Structural phase transition near 825 K in titanite: Evidence from infrared spectroscopic observations, *Am. Mineral.* 82 (1997) 30-35.
43. A.M. Heyns, P.M. Harden, L.C. Prinsloo, Resonance Raman study of the high-pressure phase transition in chromium-doped titanite, CaTiOSiO_4 , *J. Raman Spectrosc.* 31 (2000) 837-841.
44. V. Kostov-Kytin, B. Mihailova, Y. Kalvachev, M. Tarassov, Atomic arrangements in amorphous sodium titanosilicate precursor powders, *Micropor. Mesopor. Mater.* 86 (2005) 223-230.
45. Y. Su, M.L. Balmer, B.C. Bunker, Raman Spectroscopic Studies of Silicotitanates, *J. Phys. Chem. B.* 104 (2000) 8160-8169
46. T. Beirau, B. Mihailova, G. Matveeva, U. Kolb, T. Malcherek, L.A. Groat, U. Bismayer Structural anisotropy and annealing-induced nanoscale atomic rearrangements in metamict titanite, *Am. Mineral.* 97 (2012) 1354-1365.

47. E. Dowty, Vibrational interactions of tetrahedra in silicate glasses and crystals: I. Calculations on ideal silicate-aluminate-germanate structural units, *Phys. Chem. Mineral.* 14 (1987) 80-93.
48. H.V. Alberto, N.A. de Campos, B.O. Mysen, The structural role of titanium in silicate glasses - a Raman-study of the system CaO-SiO₂-TiO₂. *Phys. Chem. Glasses* 36 (1995) 114-122.
49. H. Nasu, K. Kurachi, A. Mito, J. Matsuoka, K. Kamiya, Second harmonic generation and structure of mixed alkali titanosilicate glasses. *J. Non-Cryst. Solids* 217 (1997) 182-188.
50. F.C. Hawthorne, L.A. Groat, M. Raudsepp, N.A. Ball, M. Kimata, F.D. Spike, R. Gaba, N.M. Halden, G.R. Lumpkin, R.C. Ewing, R.B. Gregor, F.W. Lytle, T.S. Ercit, G.R. Rossman, F.J. Wicks, R.A. Ramik, B.L. Sherriff, M.E. Fleet, C. McCammon, Alpha-decay damage in titanite, *Am. Mineral.* 76 (1991) 370-396.
51. F. Farges, Fivefold-coordinated Ti⁴⁺ in metamict zirconolite and titanite: A new occurrence shown by Ti K-edge XANES spectroscopy, *Am. Mineral.* 82 (1997) 44-50.
52. M. Zhang, E.K.H. Salje, U. Bismayer, L.A. Groat, T. Malcherek, Metamictization and recrystallization of titanite: An infrared spectroscopic study. *Am. Mineral.* 87 (2002) 882-890.

Сажетак: *Стакло-керамика на бази сфена (CaTiSiO₅), као одличан кандидат за имобилизацију нуклеарног отпада, припремљена је из мешаве реактаната TiO₂, SiO₂ и CaCO₃ користећи вибро-млин за хомогенизацију. Почетни прахови су стопљени на 1400 °C током 2h, охлађени до собне температуре, поново самлевени, затим калцинисани на одређеним температурама дајући стакло-керамику. Еволуција фазног састава током калцинације испитивана је рендгенском дифрактометријом праха, ИЦ спектроскопијом, Раманском и термалном анализом (ТГ-ДТА). Сфен, без додатних фаза, формиран је на 800 °C током 4h, иако га је веома тешко добити у монофаном облику на тако ниској температури. Морфологија прахова је анализирана скенирајућом електронском микроскопијом (СЕМ).*

Кључне речи: *сфен стакло-керамика, механохемија, рендгенска дифрактометрија праха, ТГ-ДТА.*

© 2020 Authors. Published by association for ETRAN Society. This article is an open access article distributed under the terms and conditions of the Creative Commons — Attribution 4.0 International license (<https://creativecommons.org/licenses/by/4.0/>).





Surface optical phonon (SOP) mode in ZnS/Poly (methylmethacrylate) nanocomposites

Milica Curcic^a, Branka Hadzic^a, Martina Gilic^{a,*}, V. Radojevic^b, Andjelika Bjelajac^c, Ivana Radovic^d, Dejan Timotijevic^a, Maja Romcevic^a, Jelena Trajic^a, Nebojsa Romcevic^a

^a Institute of Physics Belgrade, University of Belgrade, 11080, Belgrade, Serbia

^b Faculty of Technology and Metallurgy, University of Belgrade, 11000, Belgrade, Serbia

^c Innovation Center of Faculty of Technology and Metallurgy, 11000, Belgrade, Serbia

^d Vinča Institute of Nuclear Sciences, University of Belgrade, 11000, Belgrade, Serbia

ARTICLE INFO

Keywords:

Nanostructured materials

Optical properties

Phonons

Light absorption and reflection

ABSTRACT

The polymer nanocomposite ZnS/Poly (methylmethacrylate) was prepared by the solution casting method and its structural and optical properties were investigated using XRD, SEM, TEM, HRTEM, and Raman spectroscopy. The basic material, ZnS, has the cubic structure and its crystallite size was estimated to be 2.3 nm, which implies that a strong confinement regime is in effect. Analysis of Raman spectra was performed using the fitting procedure based on effective medium theory. As a result, the surface optical phonon (SOP) mode was detected. It was found that the shape and position of the SOP mode depend on the type of the composite.

1. Introduction

As a semiconductor, the zinc sulfide (ZnS) has gained considerable attention and is found to be applicable in optoelectronic, electroluminescent, and blue light emitting diode devices [1–8]. ZnS has two available allotropic forms – the wurtzite and zinc blende. The crystallographic form of wurtzite is hexagonal, whereas the zinc blende has the cubic crystallographic structure, is more stable and as such, is more common of the two. The ZnS in the form of the bulk material has a direct band gap positioned primarily in the UV region [9,10]. The wurtzite and the zinc blende forms have the band gaps of 3.77 and 3.72 eV, respectively. The band gap increases with a decrease in size from the bulk to the nanoscale [11,12]. Since ZnS easily absorbs moisture and oxidizes in air [13], it is not very stable as a pure compound in the atmosphere. Therefore, surfactants or capping agents are added to the ZnS nanoparticles to prevent structural transformation and surface reactions.

A nanocomposite consists of two or more different materials in which at least one of the components has a dimension smaller than 100 nm [14]. In polymer nanocomposites, the composing elements are an organic polymer matrix and inorganic components (semiconductors). Nanocomposites can include three dimensional metal matrix composites, lamellar composites, colloids, porous materials, gels, as well as copolymers in which nanosized material is dispersed within the bulk

matrix. The properties of the nanocomposites depend on their components, morphology, and interface characteristic. In order to extend the area of their potential applications, mechanical, thermal, and electronic properties of conventional polymer materials had to be improved [15, 16]. As a thermoplastic polymer, Poly (methylmethacrylate) i.e. PMMA has many excellent properties. Its favorable properties include excellent transparency and ultraviolet resistance, as well as good abrasion resistance, hardness, and stiffness. Consequently, it is widely used in many applications, for example in lenses, light pipes, bathroom fittings, skylights, toys, etc. In addition, PMMA is non-degradable and biocompatible, which qualifies it for use in tissue engineering where typical applications are fracture fixations, intraocular lenses, and dentures [17].

For nanocrystals of relatively small dimensions, surface modes and the effects of dimension are expected to appear, along with the normal modes of an infinite lattice. Namely, in the frequency range between longitudinal optical phonon frequency (ω_{LO}) and transversal optical phonon frequency (ω_{TO}), a new mode known as a surface optical phonon (SOP) mode appears.

In our previous papers [18–22] we worked on investigating surface optical phonons (SOP) in semiconducting nanoparticles or thin films. In all those cases, SOP appeared because the nano-objects of investigated materials were well separated in the air.

In this paper we report the synthesis and structural and optical

* Corresponding author.

E-mail address: martina@ipb.ac.rs (M. Gilic).

<https://doi.org/10.1016/j.physe.2019.113708>

Received 10 May 2019; Received in revised form 20 August 2019; Accepted 6 September 2019

Available online 9 September 2019

1386-9477/© 2019 Elsevier B.V. All rights reserved.

studies of polymer nanocomposites prepared by the incorporation of ZnS nanoparticles (pure and functionalized with silane) into the matrices of polymer PMMA. The studies of the metal sulfides/polymer nanocomposites were carried out by XRD, SEM, TEM, HRTEM and Raman spectroscopy. By extending our research to nanoparticles embedded in polymer matrix we would like to complete the knowledge about the SOP properties in A_2B_6 semiconducting materials.

2. Materials and methods

2.1. Initial components

Commercially available PMMA pellets (Acryrex® CM205, Chi Mei Corp. Korea, $M_w \approx 90400$ g/mol, $n = 1.49$, $\lambda = 633$ nm) were used as a matrix in sample preparation. Dimethylformamide (DMF, anhydrous, 99.8%, Sigma-Aldrich) was used as a solvent. For surface modification with QD3-Mercaptopropyltrimethoxysilane (MPTMS) – Dynasylane, Evonik Industries and toluene, hexane (Sigma Aldrich) were used.

Mechanochemical synthesis of ZnS nanoparticles was performed in a Pulverisette 6 planetary mill. The milling parameters were: the weight charge of total powder mixture in the mill of 14.2 g, 50 balls with the diameter of 10 mm and ball charge in the mill of 360 g, milling chamber and balls made of tungsten carbide, and rotation speed of the planet carrier of 500 rpm. The milling time was 10 min and the argon atmosphere was used as a protective medium in the mill.

The X-ray diffraction measurements of the ZnS powders obtained after 10 min milling times were performed using Philips 1050 X-ray powder diffractometer with Ni-filtered $Cu\ K\alpha$ radiation and Bragg-Bretano focusing geometry. XRD pattern is presented in Fig. 1a and shows mainly the reflection of cubic phases (JCPDS 03-0524). The space group of the cubic unit cell is $F\bar{4}3m$ (T_d^2) and the cell contains four formula weights of ZnS [23]. The refracting planes denoted with (hkl) indices are (111), (220), and (311). Using the X-ray Line Profile Fitting

Program (XFIT) with a Fundamental Parameters convolution approach to generating line profiles the coherent domain size of the synthesized powder was determined to be 2.3 nm.

In Fig. 1b, the TEM analysis was employed to identify regions with pure zinc, pure sulfur, or homogeneous ZnS distribution. In the bright field image the morphology looks like an aggregate produced by smaller clusters compacted during milling.

The high resolution TEM (HRTEM-Phillips Tecnai 200 operated at 200 kV), is an excellent method to study metal sulfide semiconductor nanostructures, where core-shell or stoichiometric system can be distinguished [24,25]. In Fig. 1c an area of $16\text{ nm} \times 16\text{ nm}$ is observed. Several clusters are clearly identifiable, in particular, three of them of sizes of 2.6, 3.7, and 3.4 nm.

2.2. Modification of ZnS QDs

ZnS nanoparticles were dispersed in 150 ml of toluene round-bottom flask equipped with a reflux condenser under the flow of nitrogen. When the boiling point of toluene was achieved, 1 g of 3-Mercaptopropyltrimethoxysilane (MPTMS), which is further on referred to as silane, was added and the resulting white suspension was stirred and refluxed for 22 h. After the completion of the reaction, the particles were filtrated and washed with hexane to remove the excess of silane. The particles were dried at 40°C in the oven for 12 h and then used in the preparation of nanocomposites.

2.3. Preparation of PMMA and ZnS/PMMA nanocomposites

In the preparation of precursor solutions, DMF was used as the solvent for the PMMA. In a typical process, homogenous solution of polymer with respect to the amount of composite films was prepared by dissolving the polymeric granules (PMMA, $m = 10.65$ g) in 40 ml of DMF under magnet stirring for 48 h at room temperature on the mixture. The concentration of PMMA in DMF solution was 22 % wt. Therefore, PMMA was produced in the form of a film by solvent casting method. Namely, the resulting PMMA solution was casted in a horizontally positioned Petri dish. The solution was air dried for 24 h at room temperature and the obtained film was kept in a dryer for additional 24 h at 60°C in order to eliminate the residual solvent.

In the synthesis of quantum dots/polymer (ZnS/PMMA) composite films the solutions were obtained in a similar manner. The concentration of PMMA in the DMF solution was 22 % wt. The concentration of ZnS particles in the films was 0.06 % wt. The mixture was stirred for 24 h. The ZnS/PMMA films were produced using the identical procedure as was the case with the PMMA. Namely, the solution was casted by placing it on a Petri dish and drying it for 24 h at room temperature, which was followed by drying in a dryer oven for additional 24 h at 60°C .

The morphology of samples was investigated by SEM using the high resolution electron microscope MIRA3 TESCAN with accelerating voltage of 5, 12, and 20 kV. The SEM micrographs of ZnS nanoparticles and ZnS/PMMA nanocomposite are presented in Fig. 2. The micrographs of ZnS nanoparticles and nanoparticles in silane are given in Fig. 2a and b. The micrographs show that the powder is composed of well-defined and separated nanoparticles as well as of nanoparticle clusters that have spherical shape and approximate size of 17–30 nm. There are no macroscopic defects like a pinhole, peeling, or cracks. The clusters of about 60 nm, are visible in Fig. 2c and d.

3. Results and discussion

The Raman spectra of the PMMA, ZnS nanoparticles, ZnS nanoparticles in silane, ZnS/PMMA nanocomposite, and ZnS in silane/PMMA nanocomposite, measured in the spectral range of $200\text{--}650\text{ cm}^{-1}$ at room temperature, are presented in Fig. 3. The micro-Raman spectra were taken in the backscattering configuration and analyzed by the TriVista 557 system equipped with a nitrogen cooled charge-coupled-

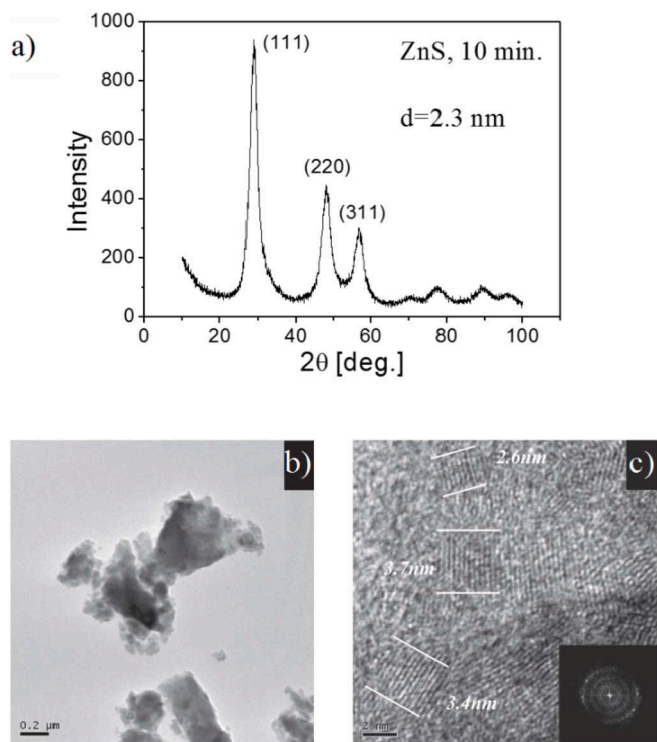


Fig. 1. (a) The XRD spectra of the ZnS powder after 10 min milling time, (b) the TEM analysis of mechanochemically synthesized ZnS nanoparticles – bright field, and (c) the HRTEM analysis of ZnS nanoparticles. The size of nanoparticles is determined to be approximately 3 nm.

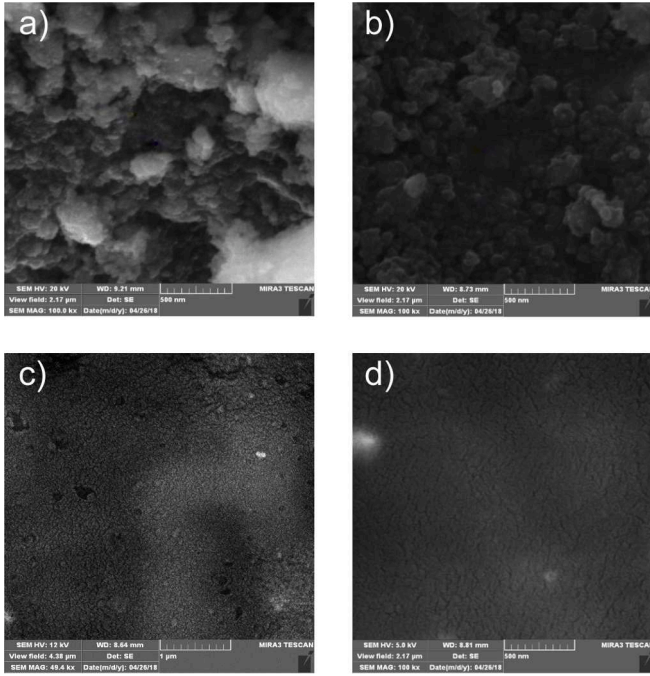


Fig. 2. SEM images. (a) ZnS nanoparticles, (b) ZnS nanoparticles in silane, (c) ZnS/PMMA nanocomposite, and (d) ZnS in silane/PMMA nanocomposite.

device detector. As an excitation source, the 532 nm line of Ti:Sapphire laser was used. This excitation energy is in the off-resonance regime for all the considered materials; consequently, for the ZnS nanoparticles as well. Since Raman spectra are usually analyzed by decomposing them into Lorentzian or Gaussian shape elements, we chose to assume that all phonon lines are of the Lorentzian type.

The Raman spectrum of PMMA is presented in Fig. 3a. Intense modes at 236, 299, 362, 402, 481, 555, and 599 cm^{-1} , as well as 4 modes of lesser intensity at about 278, 318, 382, and 505 cm^{-1} were detected. The theoretically fitted curve, which is obtained by convolving 11 Lorentz profiles and the line that describes Rayleigh scattering is also given in Fig. 3a. The obtained result is in a good agreement with the values given in the literature [26,27].

Fig. 3b shows the Raman spectrum of cubic ZnS nanoparticles. In the experimentally obtained spectrum the dominant wide structures are detected at 218, 264, 347, and 483 cm^{-1} .

As determined in Refs. [23,28–30], the Raman frequency of 347 cm^{-1} is associated to the A_1 and E_1 symmetry LO modes. At a lower frequency, a resolvable doublet with the peak at 264 cm^{-1} is observed. These peaks are assigned to the A_1 and E_1 TO modes. The mode at 218 cm^{-1} can be assigned to the LA symmetry. The appearance of this mode in the spectrum is a consequence of the violation of the selection rules due to the nanodimension. The Raman active mode at 347 cm^{-1} is asymmetrical, and the asymmetric peak broadening occurs toward the low-frequency side of the Raman spectrum. The dashed curve in Fig. 3b is obtained as the convolution of the Lorentz shapes of the known phonons of ZnS. Due to the discussed asymmetry of LO phonon at 347 cm^{-1} , this theoretically obtained curve differs from the experimental results.

Similar effect is registered in the Raman spectra of other samples. In the spectrum corresponding to the ZnS in silane, the modes at 259, 345, 489, 520, and 576 cm^{-1} are registered and are depicted in Fig. 3c. Fig. 3d shows that the modes of ZnS nanoparticles in PMMA are located at 262, 353, 364, 408, 488, 559, and 601 cm^{-1} . The intense modes at 260, 301, 354, 362, 406, 488, 559, and 601 cm^{-1} in Fig. 3e correspond to the ZnS nanoparticles in silane/PMMA. In all these cases the registered phonons can be attributed to either the pure ZnS or the pure PMMA. The difference between the experimentally measured spectrum

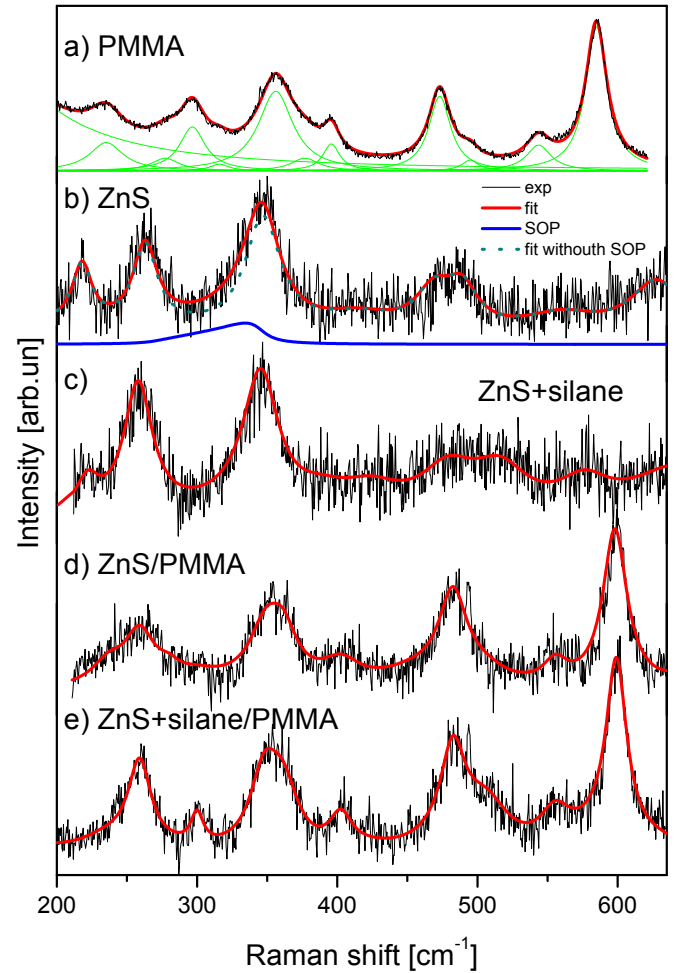


Fig. 3. Fitted and experimental Raman spectra. (a) The PMMA, (b) ZnS nanoparticles, (c) ZnS in silane, (d) ZnS/PMMA, and (e) ZnS in silane/PMMA.

and the curve obtained by convolving the Lorentz shapes located at the determined frequencies is the most noticeable for the pure ZnS.

The asymmetry and broadening around the Raman peak at 347 cm^{-1} , which is in the symmetric stretching vibration region, undoubtedly correspond to the variation of a secondary-structure. In a nanocrystal, this is usually considered to be a surface effect, and a “surface optical” phonon (SOP) mode is assigned to it. In order to analyze the surface optical phonon we have to take into account that nanoparticles are surrounded by silane and PMMA.

The part of spectra in Fig. 3 where the discrepancy between the experimental and theoretical spectra is located, is adjusted using the effective medium theory. Namely, the surface phonon modes are observed for particle sizes smaller than the wavelength of the exciting laser light. Usually these modes of small particles appear in polar crystals [31]. The dielectric function for the polar semi-insulating semiconductor:

$$\epsilon_1(\omega) = \epsilon_\infty \prod_{i=1}^n \frac{\omega_{LO_i}^2 - \omega^2 - i\omega\gamma_{iLO}}{\omega_{TO_i}^2 - \omega^2 - i\omega\gamma_{iTO}}, \quad (1)$$

describes its optical properties in the IR region. Here, ω_{TO} and ω_{LO} are the frequencies of the transverse and longitudinal optical bulk phonons, respectively; ϵ_∞ is the dielectric constant at high frequencies, and γ is the damping constant. The bulk phonons in small particles have properties similar to those of the corresponding phonons in an infinite nanocomposite; however, their wave functions are adapted to the geometry of a small particle.

There are many mixing models for the effective dielectric permittivity of such a mixture. The Bruggeman model is preferred for high concentration of the inclusions since there are no restrictions for volume fraction (f) [32,33]. The effective dielectric function of the Bruggeman nanocomposite is given by:

$$(1-f) \frac{\epsilon_1 - \epsilon_{eff}}{\epsilon_{eff} + g(\epsilon_1 - \epsilon_{eff})} + f \frac{\epsilon_2 - \epsilon_{eff}}{\epsilon_{eff} + g(\epsilon_2 - \epsilon_{eff})} = 0, \quad (2)$$

where g is a geometric factor depending on the shape of the inclusions. For three dimensional spherical particles $g=1/3$ and for two-dimensional circles $g=1/2$. Our nanoparticles of ZnS are clustered and not well separated in silane/PMMA, namely, they occupy a significant volume. Consequently, the condition for Bruggeman formula with $g=1/3$ is satisfied. Due to a narrow range of the spectra, the effective medium theory is applicable and ϵ_2 is taken to be constant. In our case, spherical nanoparticles of ZnS with dielectric function given by Eq. (1), are characterized with $\epsilon_2 = 1, 1.5,$ and 2.1 if they are homogeneously distributed in air (for ZnS nanoparticles obtained by mechanochemical synthesis); in air and silane; and in air, silane, and PMMA; respectively. The intensity of Raman spectrum related to SOP is described with

$$I_{SOP}(\omega) \sim I_m \left(-\frac{1}{\epsilon_{eff}} \right) \quad (3)$$

In Fig. 3 SOP mode is shown with the blue line. The solid line in Fig. 3b–e is obtained by joining the contributions of SOPs and the phonons described with Lorentz curves. The agreement of the theoretical model obtained in this manner with the experimental results is excellent.

The parameters adjustment was carried out automatically, by means of the least-square fitting of theoretical (I_t) and experimental (I_e) intensity at q arbitrarily taken points:

$$\delta = \sqrt{\frac{1}{q} \sum_{j=1}^q (I_{ej} - I_{tj})^2} \quad (4)$$

The value of δ was minimized until it became with the usual experimental error (less than 2%). For all samples the determination errors of the frequencies and damping coefficients were about 3–6 and 10–15% respectively.

The significant change in the intensity and line shape of simulated SOP mode, described with Eq. (3), is caused predominantly by the variation of the main volume fraction (f) and damping rate γ_{LO} , as illustrated in Fig. 4 ($\epsilon_2 = 1$). In our case, the position of the SOP mode's maximum directly follows the change in the filling factor (Fig. 4a), whereas its dependence on the dumping (Fig. 4b) is noticeably weaker.

From Fig. 4 it can be seen that SOP mode moves toward higher wavenumbers when filling factor increases. The position of surface optical phonon (SOP) mode frequencies is obtained from Ref. [18] to be

$$\omega_{SOP} = \max \left(I_m \left(-\frac{1}{\epsilon_{eff}} \right) \right)$$

The SOP mode dependences on the type of environment and filing factor are shown in Fig. 5a and b, respectively. The four lines in Fig. 5a are the best fit lines for SOP mode in Fig. 3. Fig. 5a illustrates the change in the SOP mode for different environments. The peak positions for ZnS, ZnS in silane, ZnS/PMMA, and ZnS in silane/PMMA move consecutively toward higher wavenumbers. The dependence of the SOP mode position on the filing factor f is obtained to be practically linear, as can be seen in Fig. 5b. Having in mind the linearity of this dependence, one can further conclude that the filling factor and dumping g_2 increase when ZnS is embedded in silane, and are even bigger when ZnS in silane is embedded in PMMA.

The obtained results lead to the conclusion that the studied nanocomposites obtained from nanodimensional ZnS and PMMA exhibit significant surface effects.

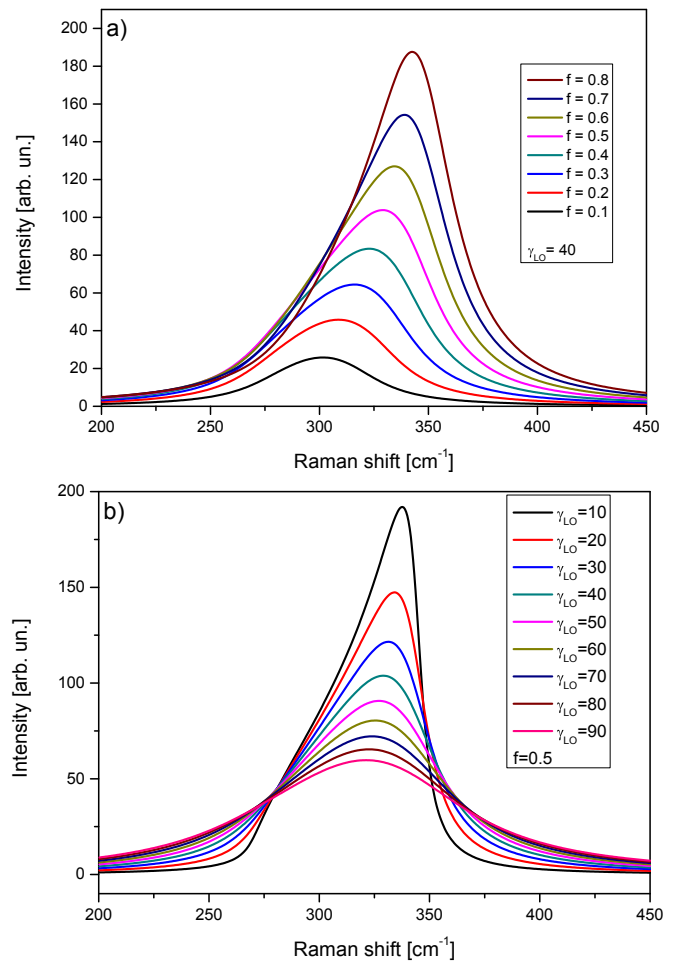


Fig. 4. Surface optical phonon (SOP) mode position. (a) The dependence on the filing factor and (b) the dependence on the phonon damping.

In comparison with SOP registered at similar nano-objects embedded in air there is a significant difference, i.e. in case of nanoparticles embedded in polymer matrix, the clusters of nanoparticles are created, and consequently, the cluster dimensions are larger than the dimensions of nanoparticles in air. However, those clusters are well separated one from others, so there is no interaction between them. Effectively, the value of filling factor is increased, and the surface phonon is weakened.

Moreover, by choosing the right polymer matrix and synthesis parameters, one can adjust the position and intensity of SOP, which is an advantage in application of these materials in electronic and sensor industry [34].

4. Conclusion

The results of studying optical and structural properties of ZnS nanoparticles and polymer nanocomposites ZnS in silane/PMMA and ZnS/PMMA are presented. The X-ray diffraction (XRD) analysis of the synthesized nanocrystal identified its structure to be cubic. The size of initial ZnS crystallite of the cubic structure was estimated to be 2.3 nm, and it was determined that it is randomly distributed in the PMMA matrix. The optical properties were studied by the Raman spectroscopy at room temperature. The analysis of the Raman spectra was conducted using the fitting procedure. Since, nanoparticles were surrounded by the silane and PMMA, the Bruggeman model of effective medium was applied. The Raman measurements revealed the asymmetry and broadening around the peak at 347 cm^{-1} that is located in the symmetric stretching vibration region, and led to the conclusion that this peak

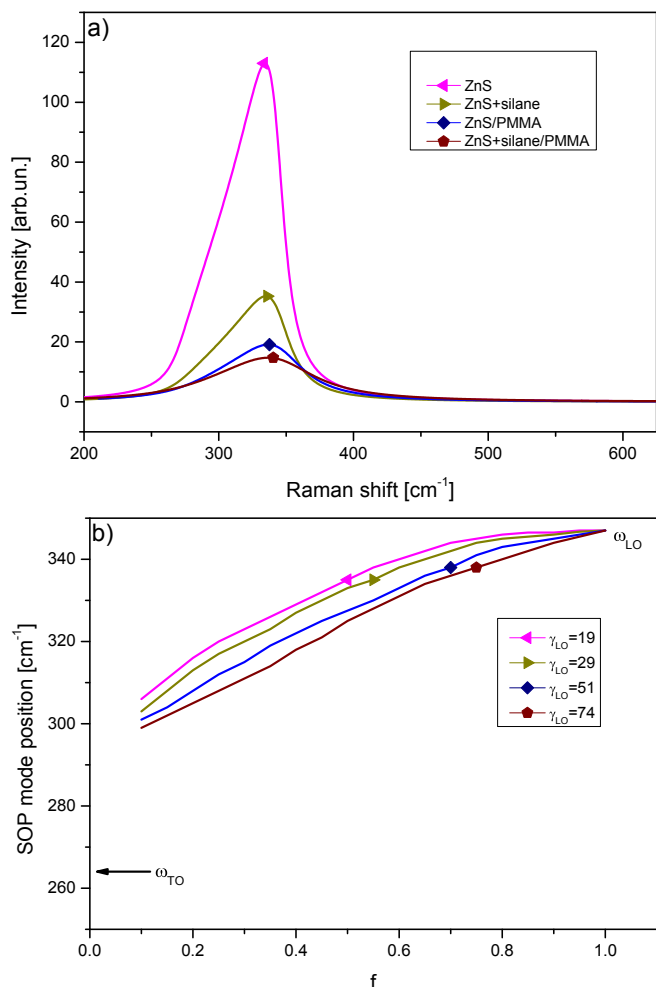


Fig. 5. (a) The Raman spectra of SOP modes for different environments and (b) the surface optical phonon (SOP) mode position dependence on the filling factor.

undoubtedly corresponds to the surface optical phonon (SOP) mode. The dependence of the SOP mode position on the filling factor (f) was analyzed for different composite materials, and it was determined that the SOP mode is moving towards higher wavenumbers when the filling factor increases.

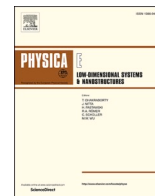
Acknowledgements

This work was supported by Serbian Ministry of Education, Science and Technological Development under Projects III 45003, TR 34011 and III 45019.

References

- J.-M. Hwang, M.-O. Oh, I. Kim, J.-K. Lee, C.-S. Ha, Preparation and characterization of ZnS based nano-crystalline particles for polymer light-emitting diodes, *Curr. Appl. Phys.* 5 (2005) 31–34. <https://doi.org/10.1016/j.cap.2003.11.075>.
- H. Naz, R. Nauman Ali, X. Zhu, B. Xiang, Effect of Mo and Ti doping concentration on the structural and optical properties of ZnS nanoparticles, *Physica E* 100 (2018) 1–6.
- Y.W. Jun, J.W. Seo, J.O. Sang, J. Cheon, Recent advances in the shape control of inorganic nano-building blocks, *Coord. Chem. Rev.* 249 (2005) 1766–1775. <https://doi.org/10.1016/j.ccr.2004.12.008>.
- S. Bhattacharyya, I. Perelshtein, O. Moshe, D.H. Rich, A. Gedanken, One-step solvent-free synthesis and characterization of Zn1-xMnxSe@C nanorods and nanowires, *Adv. Funct. Mater.* 18 (2008) 1641–1653. <https://doi.org/10.1002/adfm.200700653>.
- A. Dev, S. Chaudhuri, B.N. Dev, ZnO 1-D nanostructures: low temperature synthesis and characterizations, *Bull. Mater. Sci.* 31 (2008) 551–559.
- G. Murugadoss, B. Rajamannan, U. Madhusudhanan, Synthesis and characterization of water-soluble ZnS: Mn²⁺ nanocrystals, *Chalcogenide Lett.* 6 (2009) 197–201.
- P. Vinotha Boorana Lakshmi, K. Sakthi Raj, K. Ramachandran, Synthesis and characterization of nano ZnS doped with Mn, *Cryst. Res. Technol.* 44 (2009) 153–158. <https://doi.org/10.1002/crat.200800271>.
- H. Yang, S. Santra, P.H. Holloway, Syntheses and applications of Mn-doped II-VI semiconductor nanocrystals, *J. Nanosci. Nanotechnol.* 5 (2005) 1364–1375.
- N. Ūzar, M.Ç. Arikian, Synthesis and investigation of optical properties of ZnS nanostructures, *Bull. Mater. Sci.* 34 (2011) 287–292. <https://doi.org/10.1007/s12034-011-0085-5>.
- R. John, S.S. Florence, Structural and optical properties of ZnS nanoparticles synthesized by solid state reaction method, *Chalcogenide Lett.* 6 (2009) 535–539.
- R. Seoudi, S.H.A. Allehyani, D.A. Said, A.R. Lashin, A. Abouelsayed, Preparation, characterization, and size control of chemically synthesized CdS nanoparticles capped with poly(ethylene glycol), *J. Electron. Mater.* 44 (2015) 3367–3374. <https://doi.org/10.1007/s11664-015-3838-x>.
- T.T.Q. Hoa, L.V. Vu, T.D. Canh, N.N. Long, Preparation of ZnS nanoparticles by hydrothermal method, *J. Phys. Conf. Ser.* 187 (2009) 012081–012086. <https://doi.org/10.1088/1742-6596/187/1/012081>.
- W. Hertl, Surface chemical properties of zinc sulfide, *Langmuir* 4 (1988) 594–598.
- T.E. Twardowski, Introduction to Nanocomposites Material Properties, Processing, Characterization, Destech Publications, Lancaster, Pa, USA, 2007.
- M. Tamborra, M. Striccoli, R. Comparelli, M.L. Curri, A. Petrella, A. Agostiano, Optical properties of hybrid composites based on highly luminescent CdS nanocrystals in polymer, *Nanotechnology* 15 (2004) S240–S244.
- F. Hussain, M. Hojjati, M. Okamoto, R.E. Gorga, Review article: polymer-matrix nanocomposites, processing, manufacturing, and application: an overview, *J. Compos. Mater.* 40 (2006). <https://doi.org/10.1177/0021998306067321>, 1511–1175.
- N.A. Peppas, R. Langer, New challenges in biomaterials, *Science* 263 (1994) 1715–1720.
- B. Hadžić, N. Romčević, M. Romčević, I. Kuryliszyn-Kudelska, W. Dobrowolski, J. Trajić, D. Timotijević, U. Narkiewicz, D. Sibera, Surface optical phonons in ZnO (Co) nanoparticles: Raman study, *J. Alloy. Comp.* 540 (2012) 49–56. <https://doi.org/10.1016/j.jallcom.2012.06.076>.
- M. Gilić, J. Trajić, N. Romčević, M. Romčević, D.V. Timotijević, G. Stanišić, I. S. Yahia, Optical properties of CdS thin films, *Opt. Mater.* 35 (2013) 1112–1117. <https://doi.org/10.1016/j.optmat.2012.12.028>.
- B. Hadžić, N. Romčević, M. Romčević, I. Kuryliszyn-Kudelska, W. Dobrowolski, R. Wróbel, U. Narkiewicz, D. Sibera, Raman study of surface optical phonons in ZnO(Mn) nanoparticles, *J. Alloy. Comp.* 585 (2014) 214–219. <https://doi.org/10.1016/j.jallcom.2013.09.132>.
- B. Hadžić, N. Romčević, M. Romčević, I. Kuryliszyn-Kudelska, W. Dobrowolski, U. Narkiewicz, D. Sibera, Influence of SOP modes on Raman spectra of ZnO(Fe) nanoparticles, *Opt. Mater.* 42 (2015) 118–123. <https://doi.org/10.1016/j.optmat.2014.12.029>.
- J. Mitrić, N. Paunović, M. Mitrić, B. Vasić, U. Ralević, J. Trajić, M. Romčević, W. Dobrowolski, I.S. Yahia, N. Romčević, Surface optical phonon – plasmon interaction in nanodimensional CdTe thin films, *Physica E* 104 (2018) 64–70. <https://doi.org/10.1016/j.physe.2018.07.021>.
- J. Trajić, R. Kostić, N. Romčević, M. Romčević, M. Mitrić, V. Lazović, P. Balaz, D. Stojanović, Raman spectroscopy of ZnS quantum dots, *J. Alloy. Comp.* 637 (2015) 401–406. <https://doi.org/10.1016/j.jallcom.2015.03.027>.
- F. Paraguay-Delgado, W. Antunez-Flores, M. Miki-Yoshida, A. Aguilar-Elgueyabal, P. Santiago, J.R. Diaz, J.A. Ascencio, Structural analysis and growing mechanisms for long SnO₂ nanorods synthesized by spray pyrolysis, *Nanotechnology* 16 (2005) 688–694. <https://doi.org/10.1088/0957-4484/16/6/011>.
- O. Solcova, Ch D. Uecker, U. Steinike, K. Jiratova, Effect of the support on the reducibility of high-loaded nickel catalysts, *Appl. Catal., A* 94 (1994) 153–160. [https://doi.org/10.1016/0926-860X\(93\)85004-9](https://doi.org/10.1016/0926-860X(93)85004-9).
- R.M. Dukali, I. Radović, D.B. Stojanović, P.S. Uskoković, N. Romčević, V. Radojević, R. Aleksić, Preparation, characterization and mechanical properties of Bi₁₂SiO₂₀/PMMA composite films, *J. Alloy. Comp.* 583 (2014) 376–381. <https://doi.org/10.1016/j.jallcom.2013.08.206>.
- K.J. Thomas, M. Sheeba, V.P.N. Nampoory, C.P.G. Vallabhan, P. Radhakrishnan, Raman spectra of polymethyl methacrylate optical fibres excited by a 532 nm diode pumped solid state laser, *J. Opt. A Pure Appl. Opt.* 10 (2008) 055303–055305. <https://doi.org/10.1088/1464-4258/10/5/055303>.
- J. Trajić, M. Romčević, N. Romčević, B. Babić, B. Matović, P. Balaz, Far-infrared spectra of mesoporous ZnS nanoparticles, *Opt. Mater.* 57 (2016) 225–230. <https://doi.org/10.1016/j.optmat.2016.05.004>.
- J. Serrano, A. Cantarero, M. Cardona, N. Garro, R. Luck, R.E. Tallman, T.M. Ritter, B.A. Weinstein, Raman scattering in β -ZnS, *Phys. Rev. B* 69 (2004), 014301.
- Y.C. Cheng, C.Q. Jin, F. Gao, X.L. Wu, W. Zhong, S.H. Li, P.K. Chu, *J. Appl. Phys.* 106 (2009) 123505. <https://doi.org/10.1103/PhysRevB.69.014301>.
- G. Irmer, Raman scattering of nanoporous semiconductors, *J. Raman Spectrosc.* 38 (2007) 634–646. <https://doi.org/10.1002/jrs.1703>.

- [32] J. Saarinen, E.M. Vartiainen, K. Peiponen, On tailoring of nonlinear spectral properties of nanocomposites having Maxwell Garnett or Bruggeman structure, *Opt. Rev.* 10 (2003) 111–115.
- [33] X.C. Zeng, D.J. Bergman, P.M. Hui, D. Stroud, Effective-medium theory for weakly nonlinear composites, *Phys. Rev. B* 38 (1988) 10970–10973. <https://doi.org/10.1103/PhysRevB.38.10970>.
- [34] I. Kuryliszyn-Kudelska, W. Dobrowolski, M. Arciszewska, N. Romcevic, M. Romcevic, B. Hadzic, D. Sibera, U. Narkiewicz, Superparamagnetic and ferrimagnetic behavior of nanocrystalline ZnO(MnO), *Physica E* 98 (2018) 10–16. <https://doi.org/10.1016/j.physe.2017.12.008>.



Surface optical phonon and multi – phonon transitions in YVO₄:Eu³⁺ nanopowders

J. Mitrić^{a,*}, N. Paunović^a, M. Mitrić^c, J. Ćirković^b, M. Gilić^a, M. Romčević^a, N. Romčević^a

^a Institute of Physics, University of Belgrade, Pregrevica 118, 11080, Belgrade, Serbia

^b Institute for Multidisciplinary Research, University of Belgrade, Kneza Višeslava 1a, 11030, Belgrade, Serbia

^c Institute Vinča, University of Belgrade, P.O. Box 522, 11001, Belgrade, Serbia

ARTICLE INFO

Keywords:

Surface optical phonon

Multi

Phonon

Yttrium orthovanadate

Europium

Infrared spectroscopy

uv

Vis spectroscopy

ABSTRACT

In this paper two methods of preparation of yttrium orthovanadate nanopowders were presented: Solid State Reaction (top – down approach) and Solution Combustion Synthesis (bottom – up approach). For starting structural characterization, X – Ray Powder Diffraction (XPRD) and Field Emission Scanning Electron Microscopy (FESEM) were used. We report the change in reflection spectra in europium doped YVO₄ nanopowders with comparison to its bulk analog. In UV–Vis reflection spectra we consider the change in values of band gap in these structures, after resizing it from bulk to nanomaterial. In Far – Infrared (FIR) reflection spectra, we registered the existence of Surface Optical Phonon (SOP) and different multi – phonon processes which alter the reflection spectra of bulk YVO₄. The influence of Eu ions is reflected through multi – phonon processes that occur and are connected with energy transfer from YVO₄ lattice to Eu ions. All IR spectra were modeled using classical oscillator model with Drude part added which takes into account the free carrier contribution. Since our samples are distinctively inhomogeneous materials, we use Effective Medium theory in Maxwell Garnett approximation to model its effective dielectric function.

1. Introduction

Semiconducting nanomaterials, especially nanophosphors have attracted great attention of researchers, due to their wide spectrum of applications in industry, technology as well as in fundamental science. When made in nanorange, phosphor materials exhibit enhanced optical properties as against their bulk counterparts, due to quantum size effects and increased surface – to – volume ratio. Yttrium orthovanadate is a widely used red phosphor with many applications in just recent years – in solar cells [1], cancer treatment [2], biotechnology [3], optical imaging [4] etc.

For nanopowders, a valuable tool in the investigation of the structural and optical changes in a material made due to resizing the bulk crystal on nanoscale is the optical spectroscopy – in this case specifically far – infrared and UV – VIS spectroscopy. When excited by UV light, photoluminescence quantum yield of the europium emission in yttrium orthovanadate crystal, goes up to 70% [5]. In YVO₄:Eu³⁺ structure UV radiation excites the vanadate group, which has the ability of efficient excitation transfer to the europium ions (Fig. 1).

When irradiated with UV radiation, three major steps occur in the

excitation and emission process in YVO₄:Eu³⁺ structure. First step is the absorption of UV light by (VO₄)³⁻ groups. Then, thermal activated energy, which comes from the UV excitation source, migrates through the vanadate sub – lattice, inducing the transfer of excited energy to europium ions. In the end, strong red (⁵D₀ – ⁷F₂) and orange (⁵D₀ – ⁷F₁) emission due to de – excitation process of excited europium ions occur [6].

One of the important properties of semiconductors is their band gap. Studying the band gap of semiconductors is important for interpreting their structural and optical properties and it is of a great importance examining its expansion in order to understand their properties. Application of semiconductors is in large level determined by their band gap width. Bulk semiconductors are usually very limited in their application due to their small and indirect band gap. Bulk crystal is set up of a large number of atoms and molecules, with a number of adjacent energy levels, which form bulk electronic bands. With the reduction of particle size to a nano level, where every particle is made up out of a small number of atoms or molecules, the number of overlapping orbitals decreases, and the eventually width of the band gap of a nanomaterial gets narrower when compared to bulk crystal (this means that there will be

* Corresponding author.

E-mail address: jmitric@ipb.ac.rs (J. Mitrić).

<https://doi.org/10.1016/j.physe.2021.114923>

Received 7 May 2021; Received in revised form 3 August 2021; Accepted 4 August 2021

Available online 14 August 2021

1386-9477/© 2021 Elsevier B.V. All rights reserved.

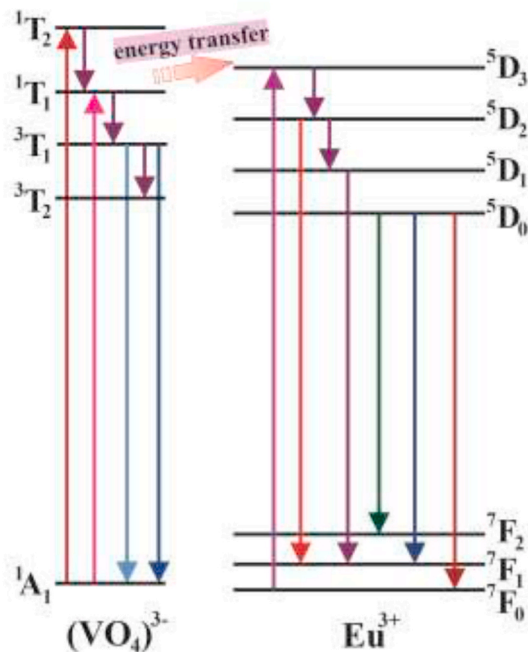


Fig. 1. Energy levels and energy transfer model of Eu^{3+} ion and $(\text{VO}_4)^{3-}$ tetrahedron in YVO_4 .

an increase of energy between valence and conduction band). This is the reason why nanomaterials have wider band gap compared to their bulk counterparts. The larger the band gap (i.e. forbidden region), the greater the restriction of the electron movement will be. This is well known as the *quantum size effect*. As a consequence of size reduction, there is a shift of absorption spectrum of nanomaterials towards the lower wavelengths, known as a *blue shift*.

In bulk crystals, bulk longitudinal (ω_{LO}) and transversal (ω_{TO}) optical phonon frequency occur. In crystals with relatively small dimensions, a new frequency appears – Surface Optical Phonon (SOP) frequency (ω_{SOP}) which is located between the ω_{LO} and ω_{TO} frequency. That means that due to effects of dimension, in addition to the modes of infinity lattice, surface modes will be manifested. And in the case of crystals with extremely low dimensions, only the surface mode perseveres.

Different types of interactions with electromagnetic radiation takes an important place in semiconductors. On one side, we have investigated electron – phonon interaction in ceramic nanopowders [7]; surface optical phonon – plasmon in thin films [8]. Besides that, we have studied damping influence on interaction appearance [9], plasmon – impurity local phonons [10], as well as plasmon – different phonons interactions [11].

A special attention should be given to the choice of method for nanopowder preparation, because nanostructured samples with good crystallization and homogenous particle size exhibit extraordinary properties different from their bulk analogs. At the same time, a very important thing for their application in industry and technology is finding a fast, cheap and reproducible technique for obtaining fine nanophosphors.

In this paper two types of methods were presented. One, the top – down approach, *Solid State Reaction Method* (SSR), (which implies extensive milling), which is a classical ceramic method and the other, bottom – up approach, *Solution Combustion Synthesis* (SCS). Top down approaches have advantages like large scale production and deposition over a large substrate; also, with these techniques, chemical purifications are not required. Disadvantages of top – down methods are varied particles shapes or geometry, different impurities (stresses, defects and imperfections); also, one must be very careful not to have broad size distribution of particles. Bottom – up approaches, on the other hand,

offer ultra – fine nanoparticles, with controlled deposition and narrow size distribution. Unlike the previous techniques, bottom – up approaches do not offer large scale production so easily, and require chemical purification. Therefore, we have chosen one technique from both approaches so they can be compared. In this paper we offer two simple, fast, cheap and yet reproducible techniques for yttrium orthovanadate nanopowder preparation.

1.1. Bulk crystal of YVO_4

Yttrium orthovanadate crystal has a zircon – type of structure, and crystallizes in 141. Space group, $I4_1/amd$ shown in Fig. 2. In this structural type, Y ions occupy **4a** crystallographic (Wyckoff) site with coordinates $[[0, 3/4, 1/8]]$.

V ions occupy **4b** crystallographic site, and coordinates $[[0, 1/4, 3/8]]$; while O ions occupy **16h** crystallographic site, with coordinates $[[0, y, z]]$.

This structure belongs to $4/mmm$ Laue class, where fourfold axis is a unique symmetry operation and has an expressed anisotropy of physical properties. V ions are in tetrahedral surrounding of O ions, while the surrounding of Y ions is made of oxygen coordination sphere with eight O ions which form a highly distorted cube.

From a group – theory analysis [12] it is known for this type of symmetry with two chemical formulas in the primitive cell ($I4_1/amd - D_{4h}^{19}$) to have following modes in the center of the Brillouin zone at the Γ point: $\Gamma(k=0) = 2A_{1g} + 5E_g + 4B_{1g} + 1B_{2g} + 4A_{2u} + 5E_u + 1A_{2g} + 1A_{1u} + 1B_{1u} + 2B_{2u}$. E_u and A_{2u} modes show dipole moments oriented perpendicular and along the c directions, respectively; and four out of five E_u modes are infrared active.

Infrared reflection spectrum of bulk YVO_4 can be found in the literature [13]. In the measured reflectivity spectra, two sharp features at the lowest frequency can be found, and they correspond to the unscreened infrared – active optical phonon modes. This spectrum is characterized with four peaks of which three are easily seen, while the fourth is a shoulder of the second reflectivity band, and it is more evident at lower temperatures. Since bulk YVO_4 has no metallic contribution (i.e. free carrier contribution), the Lyddane – Sachs Teller (LST) relation (Lorentz oscillator model) can be an optimal model to analyze reflection spectra and to model an appropriate dielectric function of a material.

In this paper we report the change in reflection spectra of europium

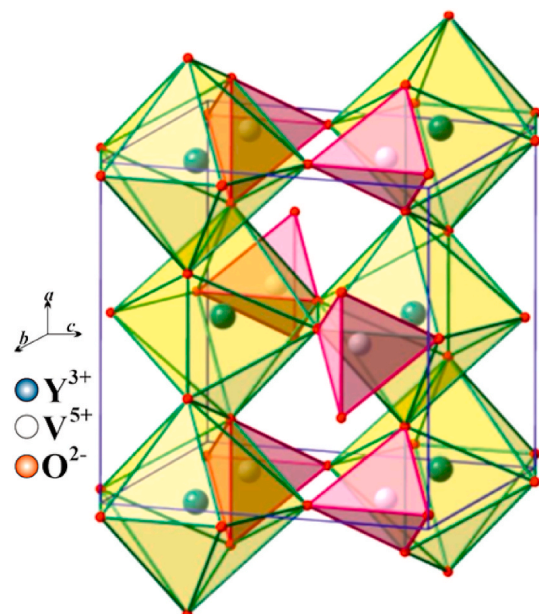


Fig. 2. Crystal structure of YVO_4 .

doped YVO_4 nanopowders with comparison to its bulk analog. In UV – VIS reflection spectra we consider the change in values of a band gap of europium doped YVO_4 when it is resized from bulk to nanomaterial. In IR reflection spectra we carry out phonon investigation in order to explain the change in optical properties of investigated nanopowders. We show the existence of surface optical phonon (SOP) and different phonon processes which alter the reflection spectra of bulk YVO_4 . Full characterization of materials is made with X – Ray Powder Diffraction (XRPD) and Field Emission Scanning Electron Microscopy (FESEM).

2. Sample preparation and characterization methods

Nanopowders prepared by SCS were obtained using stoichiometric quantities of starting chemicals $\text{Y}(\text{NO}_3)_3 \cdot 6\text{H}_2\text{O}$, NH_4VO_3 , NH_4NO_3 and $\text{Y}(\text{NO}_3)_3 \cdot 6\text{H}_2\text{O}$, purchased from ABCR with the purity of 99.99%. Urea was purchased from Sigma – Aldrich. Eu^{3+} concentration was 1%. 4.8 g of NH_4NO_3 and 3.003 g of urea, $(\text{NH}_2)_2\text{CO}$ which were used as an organic fuels were added to a dry mixture of 0.357 g $\text{Eu}(\text{NO}_3)_3 \cdot 6\text{H}_2\text{O}$, 4.676 g of NH_4VO_3 and 15.32 g of $\text{Y}(\text{NO}_3)_3 \cdot 6\text{H}_2\text{O}$. Then, mixture was combusted with the flame burner at $\sim 500^\circ\text{C}$. Then, the solid solution starts to act like cloud – shape mixture which then was annealed in air atmosphere at 1200°C for 2 h. The annealing of material offers full crystallinity. This sample was labeled as YVS.

Solid state reaction procedure was performed using stoichiometric quantities of starting chemicals, then powdered and baked on 900°C for 5 h. Starting chemicals, Y_2O_5 , Y_2O_3 and Eu_2O_3 with purity of 99.99% were purchased from ABCR. Concentration of Eu ions was 1%. This sample was labeled as YVC. Both samples, YVS and YVC, were made in a series of 5 samples, and every measurement is an average of these 5 samples.

These two simple, but yet reproducible and efficient methods provide two morphologically different samples. In this way methods can be compared and analyzed.

Structural characteristics of yttrium orthovanadate nanopowders were obtained using Philips PW 1050 diffractometer equipped with a PW 1703 generator, 40 kV \times 20 mA, using Ni filtered $\text{Co K}\alpha$ radiation of 0.1778897 nm, at room temperature. $15\text{--}85^\circ$ range was used during 2 h, with a scanning step of 0.05° and 10s scanning time per step.

Morphologies of prepared samples were examined by Field Emission Scanning Electron Microscopy using FEI Scios 2 with an acceleration voltage between cathode and anode 15 kV.

All UV–Vis reflectance spectra were recorded in the wavelength range of 200–1200 nm on the Shimadzu UV – 2600 spectrophotometer equipped with an integrated sphere. The reflectance spectra were measured relative to a reference sample of BaSO_4 .

The infrared reflectivity measurements were performed at room temperature. BOMEM DA – 8 Fourier – transform infrared spectrometer was used. A Hyper beamsplitter and DTGS (deuterated triglycine sulfate) pyroelectric detector were used to cover the wave number region $80\text{--}650\text{ cm}^{-1}$. Spectra were collected with 2 cm^{-1} resolution with 500 interferometer scans added for each spectrum.

2.1. X – ray powder diffraction

Results for YVC and YVS are shown in Fig. 3. The diffractograms confirm that both samples are monophased and that they crystallized in zircon – type of structure. All reflections are in good agreement with JCPDS card 17–0341. Also, all samples show no other reflections other than ones who originate from YVO_4 structure. Since Eu^{3+} concentration in these samples is 2%, one cannot be identified by XRD. Crystallite sizes are 53 nm and 58 nm for YVC and YVS, respectively. Crystallite sizes were determined using Debye Scherrer formula. This formula gives value of average crystallite size, and from our calculations the deviation is around 5 nm. To reduce this error, series of every sample were made (5 from each) to reduce the influence of chemical modification and other

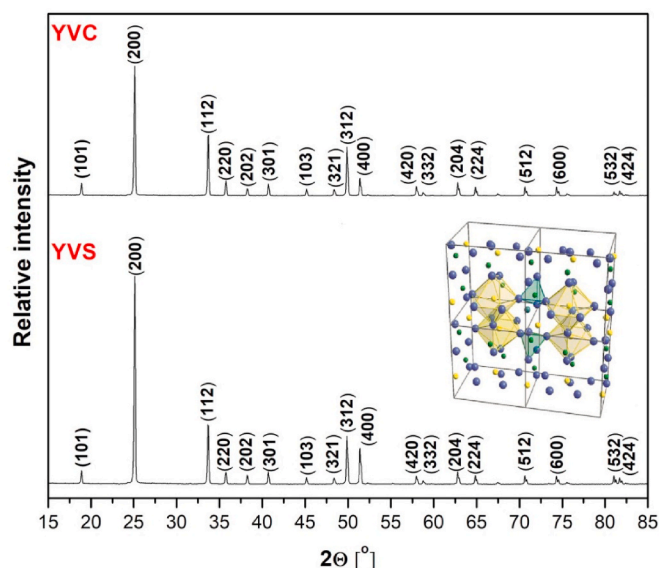


Fig. 3. XRD patterns of europium doped yttrium – orthovanadate nanopowder prepared by Solid State Reaction Method (YVC) and Solution Combustion Synthesis (YVS).

processing conditions). Even though Debye Scherrer is a rough method for determining crystallite size and one could use other methods for determining this value, like Williamson – Hall analysis which could in some way reduce this problem, this would suggest to rely on some other assumptions which could add up to an error. Crystallite size for sample YVC is smaller than one obtained in YVS. This was expected because of method of preparation. YVC was prepared using Solid State Reaction Method, which includes rather aggressive milling, and therefore results in smaller crystallite size than sample YVS, which was obtained with Solution Combustion Synthesis.

2.2. Field emission scanning electron microscopy

FESEM photographs are shown in Figs. 4 and 5, for YVS and YVC respectively; with $10\,000\times$ and $35\,000\times$ magnification. Particle sizes are 2 μm and 3 μm , for YVC and YVS, respectively. These values are much larger than the ones obtained with XRD. Reason for this is crystallite agglomeration. Regardless of agglomeration, trend in crystallite size between two methods of preparation remains the same as in crystallite sizes determined by XRD. One more thing must be noticed, and that is difference in crystallinity between samples. As can be seen from Figs. 4 and 5, sample YVC is more crystalline than YVS, which has more of a cloud – shape structure. This was marked with yellow rectangles in Figs. 4 and 5. On a larger scale, both samples consist of clearly defined and separated grains which can be seen on right hand side of Figs. 4 and 5.

3. Results and discussion

3.1. UV – VIS spectroscopy

In this section we investigated optical UV–Vis reflection spectra of europium – doped yttrium orthovanadate nanopowders. Special attention was given to obtaining band gap values. Band gap values were obtained using Tauc plot [14]. It is important to have information about band gap values, because band structure is responsible for the wide range of electrical characteristics. Tauc, Davis and Mott [15] have proposed an expression:

$$ah\nu = A(h\nu - E_g)^{1/n} \quad (1)$$

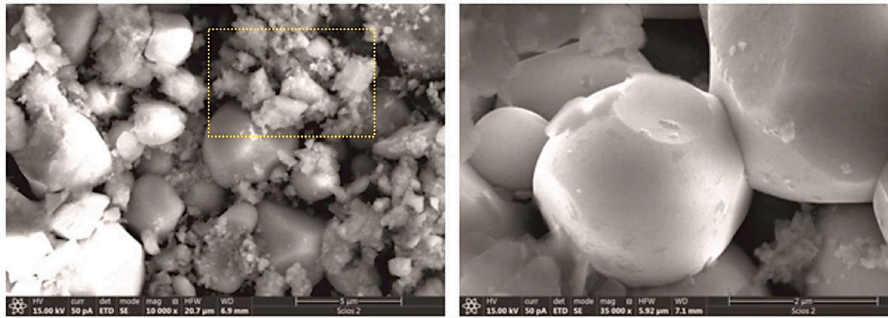


Fig. 4. FESEM photographs of europium doped yttrium – orthovanadate nanopowder prepared by Solid State Reaction Method (YVS).

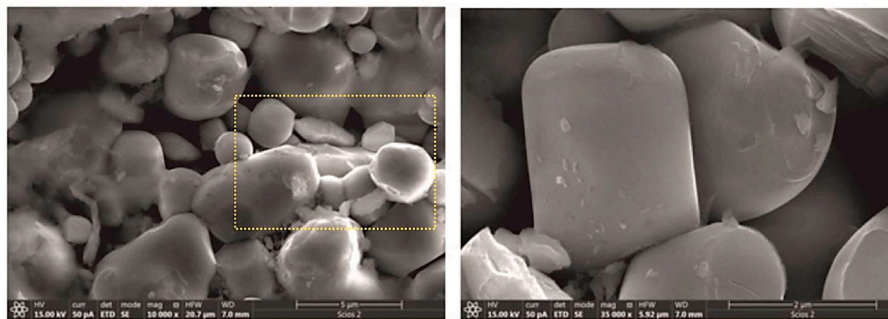


Fig. 5. (a) FESEM photographs of europium doped yttrium – orthovanadate nanopowder prepared by Solid State Reaction Method (YVC).

where α is the absorption coefficient (which is a property of a material; it defines the amount of light absorbed by it); h is the Planck's constant and $h\nu$ is the photon energy. A represents transition probability constant (which depends on the effective mass of the charge carriers in the material) and E_g is the band gap. Number n defines the nature of transition. If transition is direct, n equals $1/2$ and $3/2$, for the allowed and forbidden transitions, respectively. In the case of indirect transitions, n is 2 for allowed and 3 for forbidden transitions. In our case n is $3/2$.

Then, the obtained diffuse reflectance spectra are converted to Kubelka – Munk function [16]:

$$\alpha = \frac{(1 - R)^2}{2R} \quad (2)$$

where R is a reflectance value. Using Eqs. (1) and (2), we obtain $(\alpha h\nu)^{1/n}$ vs. $h\nu$ plot. By extrapolating the linear portion of mentioned dependence to the energy axes at the $(\alpha h\nu)^{1/n} = 0$ value, the band gap value is obtained – the intercept of the plot with x – axis gives the value of band gap. The results obtained with UV – VIS spectroscopy, UV – VIS reflectance and diffuse reflectance Kubelka – Munk spectra for YVS and YVC are presented in Figs. 6 and 7 respectively.

From Table 1 values of calculated band gap for europium doped yttrium orthovanadate nanopowders prepared by two methods, as well as literature data for bulk YVO_4 were presented. With regard to section 2 where it was explained how band gap values increases with decreasing grain size, we got matching results. Namely, we got two values of band gap for samples made with two methods, YVC and YVS: 3, 55 eV and 3,17 eV, respectively. Since crystallite size of YVC (53 nm) is smaller than in YVS (58 nm), it is expected that the band gap value will be greater for YVC, due to quantum size effect described earlier. Both E_g values for nanophosphors are greater than the E_g value for bulk crystal YVO_4 , which is expected. With this we conclude that Solid State Reaction Method provides samples with higher band gap values than samples prepared by Solution Combustion Synthesis.

When under the UV–Vis radiation, three major steps occur in YVO_4 :

Eu^{3+} : 1. absorbance of radiation by $(VO_4)^{3-}$ groups; 2. transfer of the excited energy to Eu^{3+} ions which migrated through vanadate sublattice; and 3. red emission induced by de – excitation process of excited Eu^{3+} ions. This was represented in Fig. 1.

Peak at around 272 nm originates from absorption of $(VO_4)^{3-}$ groups [17]. According to the literature, this peak is an attribution to charge transfer from oxygen ligands to the central vanadium atom in $(VO_4)^{3-}$ group. In that way, UV–Vis spectra from Figs. 6a and 7a prove there is an energy transfer between $(VO_4)^{3-}$ and Eu^{3+} ions. Peak at 343 nm originates from $(VO_4)^{3-}$ in the lattice [18]. Peak at 272 nm in YVS is clearly seen. On the other hand, in YVC sample, splitting of 272 nm mode is obvious. The mode split because reflectance values cannot go below zero values; and increase in intensity of reflectance compared to YVS is caused by multi – phonon processes which seem to be more dominant in YVC rather than in YVS.

In one of our previous papers [19] it is shown how Eu ions exchange with Y ions, and without any significant disturbance of symmetry take place in YVO_4 structure. Clearly, Eu ions have more influence in YVC sample, which has more crystallinity and smaller crystallite size, and are more efficiently distributed throughout the YVC sample. More evidence on multi – phonon processes which are present in YVC will be shown more clearly using Infrared Spectroscopy.

Results like this also confirm that these materials are suitable for many optical devices. Following our previous research [20] these phosphors represent an excellent hosts for optical excitation and emission of europium. Also, since the samples were made using two different techniques on different temperatures (500 and 900 °C), a certain evidence of thermal stability on emission quantum yield and lifetime was shown which is in good agreement with the literature [21].

3.2. Infrared spectroscopy

Subject of this paper are distinctively inhomogeneous materials. They are built out of embedded components in a matrix, and every one of them has its own macroscopic properties. A macroscopic property can

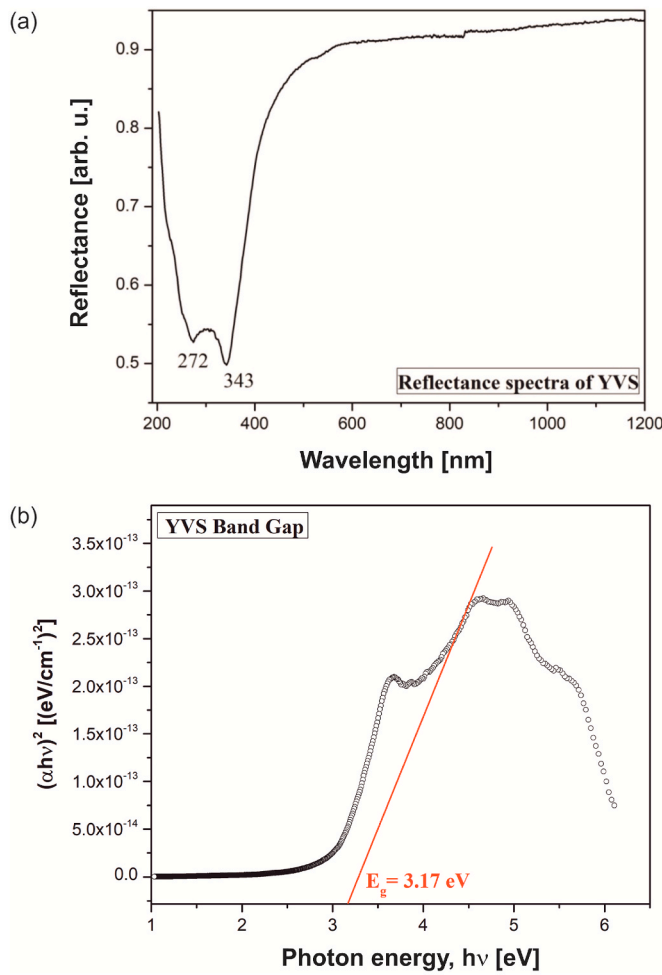


Fig. 6. (a) UV – VIS reflectance spectra of europium doped yttrium – orthovanadate nanopowder prepared by Solid State Reaction (YVS). (b) Kubelka – Munk plot for europium – doped yttrium – orthovanadate nanopowder prepared by Solid State Reaction (YVS).

be attributed to every component of this material, as well as to a matrix. For example, this can be a dielectric permittivity. A medium where dielectric permittivity of every component and its surrounding (matrix) can be substituted with one value of dielectric permittivity, an *effective dielectric permittivity*, is called an effective medium, and theory which describes this is known as Effective Medium Theory. In other words, within this model, a heterogeneous system can be seen, from a bigger scale, as a homogeneous system, with its own properties which are often called effective properties, with one important fact: on a scale comparable with the dimensions of the system constituents, the system cannot be regarded as a homogeneous medium. Theory of effective medium has several approximations [22], of which two are most common: Maxwell Garnet and Bruggemann approximation. The first one implies that constitutive parts of one medium are very well separated out of matrix they've been embedded in, and that there is no electrostatic interactions between them. On the other hand, Bruggemann approximation describes systems where constitutive parts cannot be separated out of their surroundings.

When visible light, λ , interacts with a material described above, where its nanoparticles have characteristic size d , and dielectric function ϵ_2 , which are randomly distributed in a matrix with a dielectric constant ϵ_1 , in the limit $\lambda \gg d$, the heterogeneous composite can be treated as a homogenous, and this system can be described with Effective Medium Theory. Since the samples we investigate are well defined, spherical and separated nano grains (as seen in Figs. 4 and 5), we use Maxwell Garnet

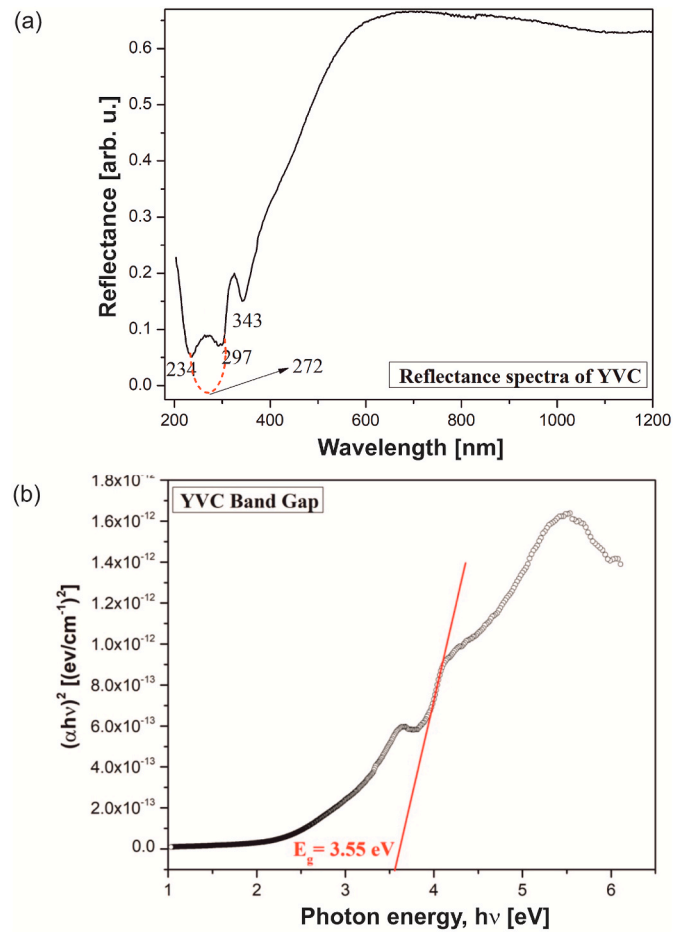


Fig. 7. (a) UV – VIS reflectance spectra of europium doped yttrium – orthovanadate nanopowder prepared by Solution Combustion Synthesis (YVC). (b) Kubelka – Munk plot for europium – doped yttrium – orthovanadate nanopowder prepared by Solution Combustion Synthesis.

Table 1

Band gap values for YVC, YVS and literature data for bulk YVO_4 bulk crystal.

YVC	YVS	YVO_4 bulk (literature) [22]
3.56 eV	3.16 eV	2.85 eV

model for the present case. Following postulates of this approximation, for the effective permittivity of so called homogeneous medium we get [23]:

$$\epsilon_{eff} = \epsilon_1 + 3f_1 \frac{\epsilon_1(\epsilon_2 - \epsilon_1)}{\epsilon_2 + 2\epsilon_1} \quad (3)$$

where ϵ_2 is a dielectric permittivity of nanoparticles located randomly in a homogeneous environment with dielectric permittivity ϵ_1 , which is, in our case, air; and occupy a volume fraction f (so called filling factor).

For modeling dielectric permittivity of above described nanoparticles, we have used a classical oscillator model with Drude part added (second addition in Eq. (3)) which takes into account the free carrier contribution [24]:

$$\epsilon_2(\omega) = \epsilon_\infty \left(\prod_{k=1}^n \frac{\omega_{LO}^2 - \omega^2 + i\gamma_{LO}\omega}{\omega_{TO}^2 - \omega^2 + i\gamma_{TO}\omega} - \frac{\omega_p^2}{\omega(\omega - i\tau^{-1})} \right) \quad (4)$$

where ϵ_∞ is a bound charge contribution (assumed to be constant), transverse and longitudinal frequencies are noted with ω_{TO} and ω_{LO} , γ_{TO} and γ_{LO} are their damping coefficients, ω_p is plasma frequency and free

carrier relaxation time is marked by τ .

Calculated spectra were obtained by a fitting procedure using a previously described model which is represented with solid lines in Figs. 8 and 9. Using the least – square fitting procedure of the experimental (R_{exp}) and theoretical (R_{th}) reflectivity, at q arbitrarily taken points, the parameter adjustment was carried out, automatically.

$$\delta = \sqrt{\frac{1}{q} \sum_{j=1}^q (R_{exp} - R_{th})^2} \quad (5)$$

Minimalization of δ was carried out until it met the conditions of commonly accepted experimental error of less than 3%.

Theoretical model in Figs. 8c and 9, show excellent match with the experimental results, for YVS and YVC samples, respectively. In Table 2, best fitting parameters are presented. In Eq. (4), transversal optical

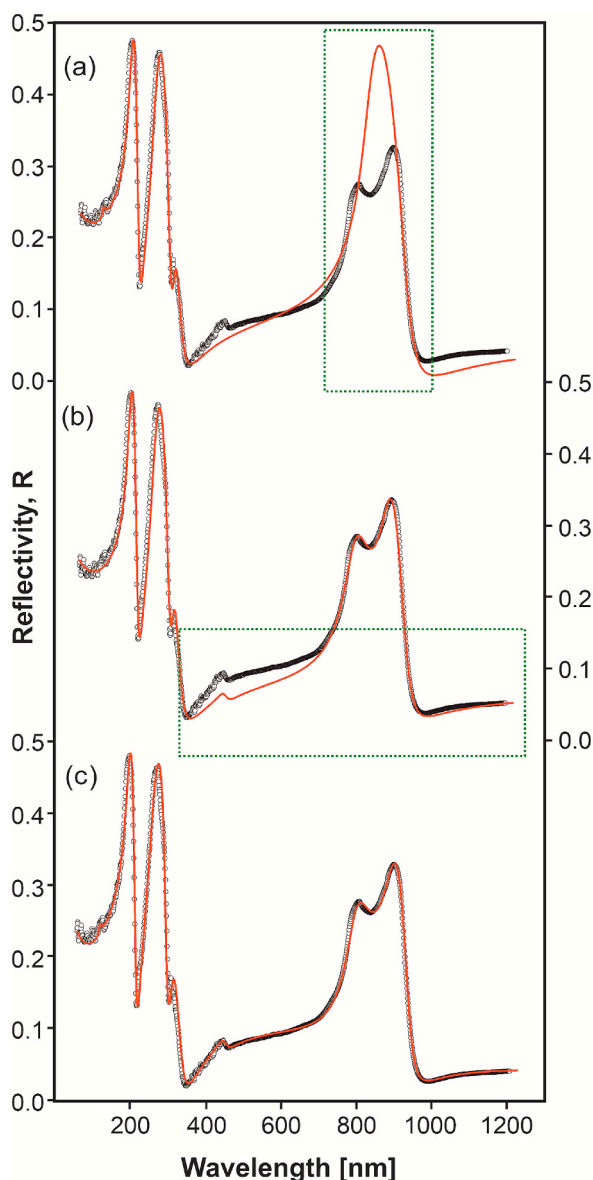


Fig. 8. Infrared reflection spectra of YVO₄ nanopowders prepared by Solution Combustion Synthesis (sample YVS). Experimental spectra are presented by open circles, while solid red lines are calculated spectra obtained by a fitting procedure based on the model given by Eqs. (3) and (4). Spectrum (a) shows fitting procedure without taking into account SOP phonons, (b) spectrum without taking into account multiphonon processes and (c) IR reflection spectrum of YVS when SOP phonons and multiphonon process were considered.

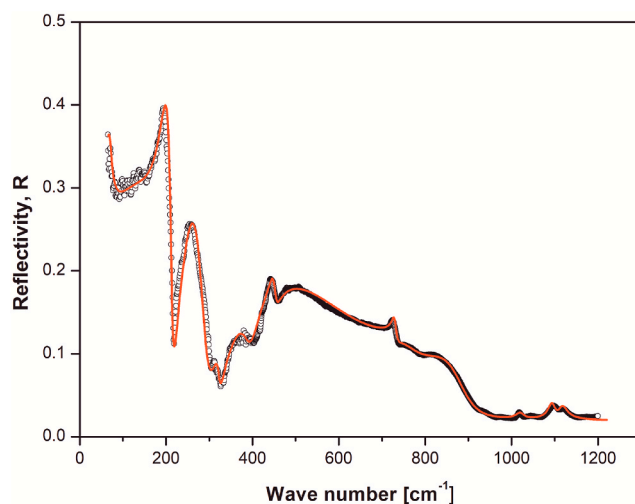


Fig. 9. Infrared reflection spectra of YVO₄ nanopowders prepared by Solid State Reaction (sample YVC). Experimental spectra are presented by open circles, while solid red lines are calculated spectra obtained by a fitting procedure based on the model given by Eqs. (3) and (4).

Table 2
Best fitted parameters of IR reflection spectra for YV, YVC and YVC; bulk literature data and their assignments.

	YVC [cm ⁻¹]	YVS [cm ⁻¹]	Bulk YVO ₄ (Literature data) [cm ⁻¹] [13]	Assignment
ϵ_{∞}	1.8	2.25	4.0	
F	0.79	0.93	1	
Γ_p	85	200		
ω_p	100	89		Plasmon frequency which plays role of ω .
ω_{TO3}	212	198	195	E_u mode, IR active
ω_{LO3}	214	219	220	
ω_{TO4}	234	259	263	E_u mod, IR active
ω_{LO4}	292	300	309	
ω_{TO5}	321	311	309	E_u mod, IR active
ω_{LO5}	323	337	311	
ω_{TO6}	397	–	–	Multiphonon processes
ω_{LO6}	393	–	–	
ω_{TO7}	400	470	–	
ω_{LO7}	645	650	–	
ω_{TO8}	450.5	452	–	
ω_{LO8}	452	454	–	
ω_{TO9}	730.2	–	–	
ω_{LO9}	731	–	–	
ω_{TO10}	759	794	780	SOP formation. E_u mod, IR active
ω_{LO10}	863	890	–	SOP phonon
ω_{LO11}	887	935	930	
ω_{TO11}	1020	–	–	Multiphonon processes
ω_{LO11}	1021	–	–	
ω_{TO12}	1093.5	–	–	
ω_{LO12}	1096	–	–	
ω_{TO13}	1116	–	–	
ω_{LO13}	1117.5	–	–	

frequency, ω_{TO} , was perceived as the characteristic frequency for a given material. As regards to spectra from Fig. 8a and 8b, they show the procedure, step by step, in order to get the best fit presented in Fig. 8c. Model used in Fig. 8a did not take into account the existence of SOP. Actually, this model suits the bulk structure of YVO₄ the best, when there's no SOP [25]. After we took this into account, we notice that, when bulk YVO₄ was resized to nanoscale, wide mode on the highest frequencies in bulk spectrum of YVO₄ [13] split into two modes. Since this was modeled with dielectric function which takes into account the existence of SOP, we conclude that the reason for splitting this wide

mode is occurrence of SOP mode in these structures. After including SOP modes into reflection spectra of nanostructures, we still have slight differences between experimental and theoretical results (Fig. 8b) at frequency between two sharp modes at lowest, and one wide mode at highest frequencies.

Reasons for this slight difference presented in Fig. 8b are different multi-phonon processes, with frequencies obtained in Table 2. After we took this into account, we got excellent match of theoretical and experimental results, shown in Fig. 8c.

From this we conclude that influence in reflection IR spectra in majority comes from SOP mode and not from multi-phonons. Still, when we compare two spectra from 8c and 9, we do see differences, which originate from different contributors to reflection IR spectra. In sample made with Solution Combustion Synthesis (YVS), the contribution of SOP is greater than in samples made with Solid State Reaction (YVC). Yet, in sample YVC, influence of multi-phonon contributors is greater than in YVS which is also shown in UV-Vis measurements. We see that from Table 2, for the wavenumbers greater than 1020 cm^{-1} , where we modeled multi-phonon modes for YVC and not for YVS, because of the greater influence of SOP in this sample which completely covered possible multi-phonon processes in YVS. From all of this, we can say that, when we compare to nanopowders prepared with two different methods, one can say that for YVS, influence of SOP mode dominates, and for sample YVC, multi-phonon modes dominate over SOP modes.

Now, let us discuss the results obtained in Table 2. In Eq. (3) we have defined the parameter called filling factor. It is a parameter which describes the volume fraction occupied by the nanoparticle (or nanoparticle aggregates) in the surrounding medium. In Table 2, filling factors of prepared nanopowders, YVC and YVS, together with value for bulk crystal YVO_4 are presented. Intensity and shape change of SOP modes presented in Figs. 8 and 9 (described with Eq. (4)) are notably affected by variation of filling factor, f .

In our case, position of SOP modes maxima directly follows the change in filling factor. Position of SOP modes frequencies are obtained from Eq. (6) [26], and the results are presented in Fig. 10.

$$\omega_{\text{SOP}} = \max \left(I_m \left(-\frac{1}{\epsilon_{\text{eff}}} \right) \right) \quad (6)$$

In bulk crystal YVO_4 [13], at room temperature, four modes in infrared reflection spectra have been detected at 195, 263, 311 and 780 cm^{-1} . These modes are separated into internal (motions of the tetrahedral VO_4) and external (translations and rotations of the VO_4 tetrahedron). All of these modes, as expected, are shifted after resizing bulk

to nanomaterial to 212, 234, 323 and 759 cm^{-1} for YVC, and to 198, 259, 337 and 794 cm^{-1} for YVS, respectively. Appearance of new phonons is due to break-down of the selection rules, as a consequence of resizing of the bulk crystal to nanostructure. Some modes occur due to appearance of surface optical phonon mode and some due to multi-phonon processes (one is, as we said, more dominant in YVS and other in YVC) in addition to modes which occur owing to Eu ion and its interaction with YVO_4 lattice. All of the modes are represented and assigned in Table 2.

Based on these results, it is clear that filling factor of prepared nanopowders depends on method of preparation, but yet it has a linear dependence of occurred surface optical phonon frequency. Also, SOP mode has the role of the LO phonon which we have also showed in our earlier works in different nanostructures [8].

Vibrational spectroscopy of nanostructures for discovering surface optical phonons represents an extremely active and exciting field with many possibilities for scientific and technological development. This arising new phenomena offer not only new perspective for material characterization, but also a fundamental understanding of processes at nanoscale. Better understanding of phonon properties of phosphors shown in this paper leads to wide application of these nanostructured materials for nanophosphor coatings [27], biomedical application [28], luminescence efficiency [29] etc. Also, discovery of surface phonons in these materials offer great use in heteronanostructures [30] to enhance the photoluminescence properties.

On the other side, multiphonon processes have been investigated for the first time in this nanostructured orthovanadate. Understanding multiphonon processes and charge transfers within a phosphor structure leads to its better application in self-assembled quantum dots [31] and different luminescent materials [32].

4. Conclusion

In this paper we showed two methods of preparation of yttrium orthovanadate nanopowders, Solution Combustion Synthesis and Solid State Reaction Method. Samples prepared by Solution Combustion Synthesis offer slightly bigger crystallite size, and therefore smaller width of band gap compared to samples prepared by Solid State Reaction Method, which provides samples with band gap up to 3.56 eV which was obtained using UV-Vis spectroscopy. Splitting of 272 nm mode from UV-Vis spectra for sample made by Solid State Reaction Method gives an indication of more dominant multi-phonon modes in this sample rather than in one made by Solid Combustion Synthesis. This was caused by doping and transfer of excited energy which migrates through vanadate sublattice to Eu ions; and after causes red emission induced by de-excitation process of excited Eu ions. For modeling Infrared Reflection spectra of both samples, Effective Medium Theory in Maxwell Garnett approximation was used and classical oscillator model, with Drude part added which takes into account concentration of free carriers. We showed that in both samples characteristic frequency of Surface Optical Phonon occurs as a consequence of resizing bulk crystal to nano scale. Also, that SOP has greater influence in sample prepared by Solution Combustion Synthesis, while in sample prepared by Solid State Reaction Method multi-phonon modes are more dominant and cover SOP modes. This was a confirmation of previous UV-Vis results. Since change in intensity and shape of SOP modes depends on variation of filling factor, we have considered the values of filling factor and its dependence on SOP mode position and came to a conclusion that SOP frequency has a linear dependence on filling factor, where SOP mode plays a role of LO phonon. All results obtained, show not only occurrence of nanoscale phenomena – surface optical phonon and multiphonon processes in $\text{YVO}_4:\text{Eu}^{3+}$ nanostructures, but its potential use in wide fields of science and technology.

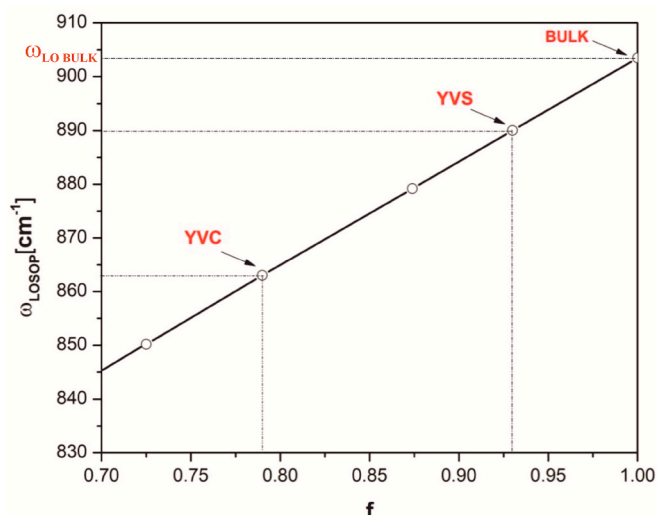


Fig. 10. Surface Optical Phonon mode position vs. filling factor.

Declaration of competing interest

The authors declare that they have no known competing financial interests or personal relationships that could have appeared to influence the work reported in this paper.

Acknowledgments

The authors acknowledge funding provided by the Institute of Physics Belgrade through the grant by the Ministry of Education, Science, and Technological Development of the Republic of Serbia.

References

- [1] T. Voitenko, S.A. Nedilko, K. Savva, M. Androulidaki, S.G. Nedilko, E. Stratakis, O. Chukova, A. Papadopoulos, Deposition of luminescent vanadate nanoparticles on silicon solar cells, in: IEE 40th International Conference on Electronics and Nanotechnology (ELNANO), Kyiv, Ukraine 251–254, 2020.
- [2] D. Hu, D. Li, X. Liu, Z. Zhou, J. Tang, Y. Shen, Vanadium-based nanomaterials for cancer diagnosis and treatment, *Biomed. Mater.* (2020) in press.
- [3] D. Dosev, M. Nichkova, I.M. Kennedy, Inorganic lanthanide nanophosphors in biotechnology, *J. Nanosci. Nanotechnol.* 8 (3) (2008) 1052–1067 (16).
- [4] L.P. Singh, N.V. Jadhav, S. Sharma, B.N. Pandey, S.K. Srivastava, R. S. Ningthoujam, Hybrid nanomaterials YVO₄:Eu/Fe₃O₄ for optical imaging and hyperthermia in cancer cells, *J. Mater. Chem. C* 3 (2015) 1965–1975.
- [5] W.L. Wanmaker, A. Bril, J.W. Vrugt, J. Broos, Luminescent properties of Eu-activated phosphors of the type AIII₂BnOn, *Philips Res. Rep.* 21 (1966) 270.
- [6] J. Su, X. Mi, J. Sun, L. Yang, C. Hui, L. Lu, Z. Bai, X. Zhang, Tunable luminescence and energy transfer properties in YVO₄:Bi³⁺, Eu³⁺ phosphors, *J. Mater. Sci.* 52 (2) (2017) 1–11.
- [7] J. Mitrić, J. Krizan, J. Trajić, G. Krizan, M. Romčević, N. Paunović, B. Vasić, N. Romčević, Structural properties of Eu³⁺ doped Gd₂Zr₂O₇ nanopowders: far-infrared spectroscopy, *Opt. Mater.* 75 (2018) 662–665.
- [8] J. Mitrić, N. Paunović, M. Mitrić, B. Vasić, U. Ralević, J. Trajić, M. Romčević, W. D. Dobrowolski, I.S. Yahia, N. Romčević, Surface optical phonon – plasmon interaction in nanodimensional CdTe thin films, *Physica: Low Dimens. Syst. Nanostruct.* 104 (2018) 64–70.
- [9] N. Romčević, M. Romčević, W.D. Dobrowolski, L. Kilanski, M. Petrović, J. Trajić, B. Hadžić, Z. Lazarević, M. Gilić, J.L. Ristić – Đurović, N. Paunović, A. Reszka, B. J. Kowalski, I.V. Fedorchenko, S.F. Marenkin, Far – infrared spectroscopy of Zn_{1-x}Mn_xGeAs₂ single crystals: plasma damping influence on plasmon – phonon interaction, *J. Alloys Compd.* 649 (2015) 375–379.
- [10] N. Romčević, J. Trajić, T.A. Kuznetsova, M. Romčević, B. Hadžić, D.R. Khokhlov, Far – infrared study of impurity local modes in Ni – doped PbTe, *J. Alloys Compd.* 442 (2007) 324–327.
- [11] J. Trajić, M. Romčević, M. Romčević, V.N. Nikiforov, *Mater. Res. Bull.* 42 (2007), 2201–2192.
- [12] C. Pecharroman, M. Ocana, P. Tartaj, C.J. Serna, Optical constants of tetragonal and cubic zirconias in the infrared, *Mater. Res. Bull.* 29 (1994) 417.
- [13] C.Z. Bi, J.Y. Ma, J. Yan, X. Fang, D.Z. Yao, B.R. Zhao, X.G. Qiu, Far – infrared optical properties of YVO₄ single crystal, *Eur. Phys. J. B* 51 (2006) 167–171.
- [14] P. Makula, M. Pacia, W. Macyk, How to correctly determine the band gap energy of modified semiconductor photocatalysts based on UV – Vis spectra, *J. Phys. Chem. Lett.* 9 (23) (2018) 6814–6817.
- [15] X. Li, H. Zhu, J. Wei, K. Wang, E. Xu, Zh Li, D. Wu, Determination of band gaps of self – assembled carbon nanotube films using Tauc/Davis – Mott model, *Appl. Phys. A* 97 (2009) 341–344.
- [16] P. Kubelka, F. Munk, Ein Beitrag zur Optik der Farbanstriche, *Zeits F. Teck. Physik.* 12 (1931) 593–601.
- [17] H. Wang, O. Odawara, H. Wada, Facile and chemically pure preparation of YVO₄:Eu³⁺ colloid with novel nanostructures via laser ablation in water, *Sci. Rep.* 6 (2016) 20507.
- [18] J. Su, X. Mi, J. Sun, L. Yang, C. Hui, L. Lu, Z. Bai, X. Zhang, Tunable luminescence and energy transfer properties in YVO₄:Bi³⁺, Eu³⁺ phosphors, *J. Mater. Sci.* 52 (2) (2017).
- [19] J. Mitrić, U. Ralević, M. Mitrić, J. Ćirković, G. Krizan, M. Romčević, M. Gilić, N. Romčević, Isotope – like effect in YVO₄:Eu³⁺ nanopowders: Raman spectroscopy, *J. Raman Spectrosc.* 50 (2019) 802–808.
- [20] D. Šević, M.S. Rabasović, J. Krizan, S. Savić – Šević, M. Mitrić, M. Gilić, B. Hadžić, N. Romčević, Characterization and luminescence kinetics of Eu³⁺ doped YVO₄ nanopowders, *Mater. Res. Bull.* 88 (2017) 121–126.
- [21] A. Huignard, V. Buissette, A.-C. Franville, T. Gacoin, J.-P. Boilot, Emission processes in YVO₄:Eu nanoparticles, *J. Phys. Chem. B* 107 (2003) 6754–6759.
- [22] J. Trajić, M.S. Rabasović, S. Savić – Šević, D. Šević, B. Babić, M. Romčević, J. L. Ristić – Đurović, N. Paunović, J. Krizan, N. Romčević, Far – infrared spectra of dysprosium doped yttrium aluminum garnet nanopowder, *Infrared Phys. Technol.* 77 (2016) 226–229.
- [23] J.C.M. Garnett, Colours in meta glasses and in metallic films, *Philos. Trans. Royal Soc. A* 203 (1904) 385–420.
- [24] I.J. Uhanov, *Opt. Svojtva Poluprovodnikov*, Nauka, Moskva, 1977.
- [25] C.Z. Bi, J.Y. Ma, J. Yan, X. Fang, D.Z. Yao, B.R. Zhao, X.G. Qiu, Far – infrared optical properties of YVO₄ single crystal, *Eur. Phys. J. B* 51 (2006) 167–171.
- [26] B. Hadžić, N. Romčević, M. Romčević, I. Kuryliszyn – Kudelska, W. Dobrowolski, J. Trajić, D.V. Timotijević, U. Narkiewicz, D. Sibera, Surface optical phonons in ZnO(Co) nanoparticles: Raman study, *J. Alloys Compd.* 540 (2012) 49–56.
- [27] R. Kubrin, Nanophosphor coatings: technology and applications, opportunities and challenges, *KONA Powder and Particle Journal* 31 (22 – 52) (2014).
- [28] T. Thu Huong, H. Thi Phuong, L. Thi Vinh, H. Thi Khuyen, T. Kim Anh, L. Quoc Minh, Functionalized YVO₄:Eu³⁺ nanophosphors with desirable properties for biomedical applications, *J. Sci – Adv. Mater. Dev.* 1 (3) (2016) 295–300.
- [29] T. Minakova, S. Mjakin, V. Bakhmetyev, M. Sychov, I. Zyatikov, I. Ekimova, V. Kozik, Y.-W. Chen, I. Kurzina, High efficient YVO₄ luminescent materials activated by europium, *Crystals* 9 (2019) 658.
- [30] H. Zhu, H. Hu, Z. Wang, D. Zuo, Synthesis of YVO₄:Eu³⁺/YBO₃ heteronanostructures with enhanced photoluminescence properties, *Nanoscale Res. Lett.* 4 (2009) 1009–1014.
- [31] L. Magnusdottir, A. Uskov, S. Bischoff, J. Mork, Multiphonon capture processes in self-assembled quantum dots, in: *Technical Digest. Summaries of Papers Presented at the Quantum Electronics and Laser Science Conference. Postconference Technical Digest (IEEE Cat. No.01CH37172)*, 2001, pp. 206–207.
- [32] R. Liu, L. Liu, Y. Liang, Energy transfer and color – tunable luminescence properties of YVO₄:Re (Re = Eu³⁺, Sm³⁺, Dy³⁺, Tm³⁺) phosphors via molten salt synthesis, *Opt. Mater. Express* 8 (6) (2018) 1686.



Structural and optical characterization of titanium–carbide and polymethyl methacrylate based nanocomposite

Jelena Pešić¹ · Andrijana Šolajić¹ · Jelena Mitrić¹ · Martina Gilić¹ · Ivan Pešić² · Novica Paunović¹ · Nebojša Romčević¹

Received: 11 October 2021 / Accepted: 10 March 2022 / Published online: 12 May 2022

© The Author(s), under exclusive licence to Springer Science+Business Media, LLC, part of Springer Nature 2022

Abstract

The rich chemistries and unique morphologies of titanium carbide MXenes, made them strong candidates for many applications like sensors and electronic device materials. During the synthesis procedure, chemical etching, oxidation occurs and residual materials, like titanium-dioxide nanocrystals and nanosheets are often present in resulting material. As titanium-carbide MXenes are suggested to be used as additive in organic polymer matrices for production of nanocomposites, it is essential to consider the presence of the oxides and other residuals together with MXene flakes in synthesis results, and consequently in produced nanocomposite. In this study we present structural and optical characterization of such polymer nanocomposite titanium carbide/PMMA (Polymethyl methacrylate) consisting of Ti_3C_2 , TiC_2 MXenes and TiC , and TiO_2 residues of synthesis in PMMA matrix, as a multicomponent nanocomposite. Using XRD, infra-red and Raman spectroscopy, followed by comparative study on the vibrational properties using density functional theory calculations, we characterize this nanocomposite. Further, the SEM measurements are performed, demonstrating the produced titanium-carbide-based flakes in nanocomposite are well defined and separated to nanosized grains, allowing us to use Maxwell–Garnet model to analyse infrared spectrum. This enables us to determine the presence of the optical modification of polymer matrices corresponding to a volume fraction of 0.25.

Keywords Titanium-carbide nanoparticles · PMMA composite · Multicomponent nanocomposite

This article is part of the Topical Collection on Photonics:Current Challenges and Emerging Applications.

Guest edited by Jelena Radovanovic, Dragan Indjin, Maja Nestic, Nikola Vukovic and Milena Milosevic.

✉ Jelena Pešić
yelena@ipb.ac.rs

¹ Institute of Physics Belgrade, University of Belgrade, Pregrevice 118, Belgrade 11080, Serbia

² Faculty of Technology and Metallurgy, University of Belgrade, Belgrade 11000, Serbia

1 Introduction

Nanocomposites are the combination of two or more different materials where a minimum of one of the components has dimension less than 100 nm Twardowski (2007). The polymer nanocomposites are made of organic polymer matrix (in this research, polymethyl methacrylate—PMMA) and inorganic components (titanium carbide nanoparticles). The properties of the obtained nanocomposites depend on the individual properties of each component, morphology and the interface characteristics. In an attempt to improve the properties of conventional polymer materials and extend the fields of their applications, functionalization has emerged as important method in improvement of their not satisfactory electronic, thermal and mechanical properties Tamborra et al. (2004); Hussain et al. (2006). In addition to typical advantages of polymers (such are light-weight, low cost, and good processability), the improvement of electrical properties (e.g., electrical conductivity) with the addition of a small amount of conductive fillers into polymer matrices have promoted polymer nanocomposites into versatile multifunctional materials. Many applications like household electronics, memory and microwave devices are potentially available with addition of metal oxide nanoparticles to polymer. This enables the modification of the polymer's physical properties as well as the implementation of new features in the polymer matrix creating new type of materials known as the polymer nanocomposites. PMMA as a thermoplastic polymer, has many extraordinary properties, like great transparency and ultraviolet resistance, high abrasion resistance, hardness and stiffness and making it widely used in many applications ranging from everyday items to high tech devices. Further, PMMA is nondegradable and biocompatible which makes it an excellent candidate in medical applications like tissue engineering with typical applications such as fracture fixation, intraocular lenses and dentures Peppas and Langer (1994).

Multicomponent nanocomposites based of layered and 2D materials have drawn significant attention in past decade with promises of various applications. Reduction of dimensionality of the system to the truly atomic-scale 2D is related to the occurrence of all new amazing properties in low-dimensional material, since the reduction of available phase space and decreased screening lead to enhancement of quantum effects and increased correlations. Low-dimensional materials have been studied intensively both for their fundamental properties and insight in basic principles of matter but as well for their colossal potential for applications. A discovery of true two-dimensional material graphene Novoselov et al. (2004) and its remarkable properties like and experimental observation of Klein tunnelling, quantum Hall effect and superconductivity Novoselov et al. (2004); Katsnelson et al. (2006); Zhang et al. (2005); Durajski et al. (2019); Pešić et al. (2014); Margine et al. (2016); Durajski et al. (2020) paved the way for investigation of a new family of materials in low-dimensional physics. The new field of two-dimensional materials research has arose and investigated not only graphene but many more crystal structures where, just like in graphene, cells are connected in at least one direction by the van der Waals' forces Novoselov et al. (2016).

Transition metal carbides are important group of materials for applications since they possess some desired characteristics such as thermal stability, wear and corrosion resistance, electronic, magnetic as well as catalytic properties. Titanium-carbide powders are generally used for manufacturing cutting tools, used in treatment of metals and as abrasive-resistant materials. In 2011 Naguib et al. (2011), the group of early transition metal carbides and/or carbo-nitrides labeled as MXenes. MXenes are produced by the etching out of the A layers from MAX phases Naguib et al. (2011, 2012, 2013). Name MAX phase

comes from its chemical composition: $M_{n+1}AX_n$, where M is an early transition metal, A is mainly a group IIIA or IVA (i.e., groups 13 or 14) element, X is carbon and/or nitrogen, and $n = 1, 2, \text{ or } 3$.

During the synthesis of titanium-carbide MXenes by chemical etching, oxidation can occur which results in presence of TiO_2 consisted of nanosheets and numerous TiO_2 nanocrystals Naguib et al. (2014). There are several studies Zhu et al. (2016); Gao et al. (2015) whose researched is focused in possible applications of TiO_2 -MXene structures. It is demonstrated the joint effects of Ti_3C_2 and TiO_2 endowed TiO_2 - Ti_3C_2 nanocomposites with excellent properties and improved functionalities Zhu et al. (2016). In this work we investigate the structural and optical properties of polymer nanocomposites prepared by the incorporation of titanium-carbide nanoparticles consisting of Ti_3C_2 , TiC_2 TiC and TiO_2 into the matrices of polymer PMMA. The sample of nanocomposite material was prepared, the PMMA matrix with titanium-carbide particles, PMMA/ TiC . As for similar materials Shan et al. (2021, 2020, 2021); Tan et al. (2021); Jafari et al. (2020); Tan et al. (2021) proper understanding of composition of materials used in composite is crucial and XRD analysis for the titanium-carbide flakes. The structural and morphology studies of the nanocomposites were carried out by SEM and Raman spectroscopy. Infrared spectroscopy is a very powerful technique in analysis of various nanoparticle and nanocomposite materials prepared in various techniques Dastan (2015); Dastan and Chaure (2014); Dastan et al. (2014); Dastan and Chaure (2017). To further understand properties of our inhomogeneous nanocomposite we used infrared spectroscopy with Maxwell–Garnet model. To further support optical characterization, calculations based on density functional theory were performed.

2 Samples preparation and structural characterization

2.1 Titan-carbide/PMMA composite synthesis

In this work, titanium-carbide/PMMA nanocomposite sample was made from mixture of MXene based titanium-carbide nanoflakes in PMMA matrix. Production of layered titanium-carbide flakes is based on MXene synthesis by selective etching of Al atomic layers from Ti_3AlC_2 MAX phase, we used the so-called 'mild' method with lithium fluoride (LiF) and hydrochloric acid (HCl) Tu et al. (2018). This method was described in Naguib et al. (2011). Procedure of composite preparation is described in Fig. 1.

Commercially available PMMA Acryrex CM205 (Chi Mei Corp. Korea, ($M_w \approx 90400$ g/mol, $n = 1.49$, $\lambda = 633$ nm) pellets were used as a matrix for sample preparation. Ti_3AlC_2 MAX phase was processed and kindly donated from Layered Solids Group, Drexel University. Titanium-carbide flakes were obtained by sonification in the water and drying the supernatant in a Petri dish in the oven for 30 minutes on 90°C .

Composite was prepared with 10 wt% PMMA solution in acetone (Carlo Erbe Reagents, Spain) and added dried titanium-carbide flakes. After stirring the solution was poured in Petri dish Cao et al. (2017) and dried in oven 24h on 40°C . Content of titanium-carbide flakes in the sample was 1.7 wt%.

The morphology of the produced composite has been investigated by FESEM using high resolution electron microscope MIRA3 TESCAN. Samples display separated nano-sized grains. Fig. 2a presents FESEM image of MXene flakes delaminated in water showing morphology of obtained flakes, b FESEM image of the PMMA/titanium-carbide

Fig. 1 Schematic describing the synthesis process of MXenes from MAX phases and preparation of composite

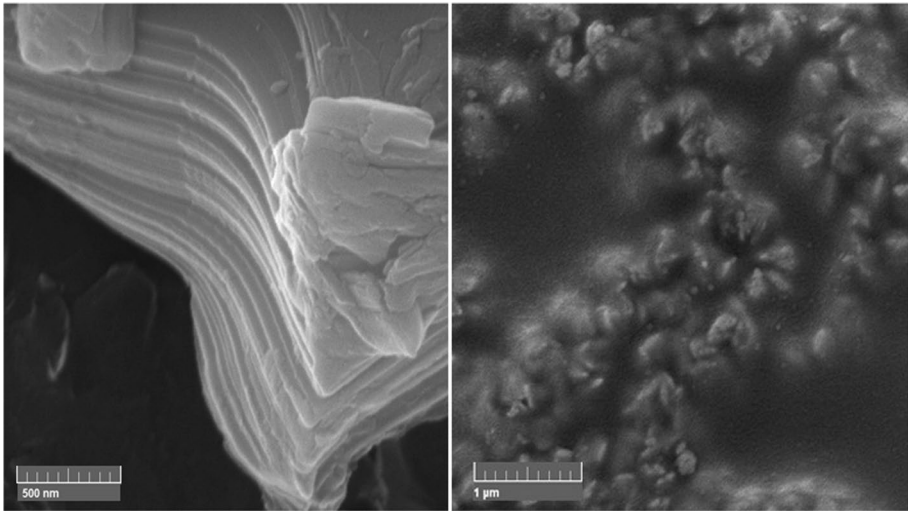
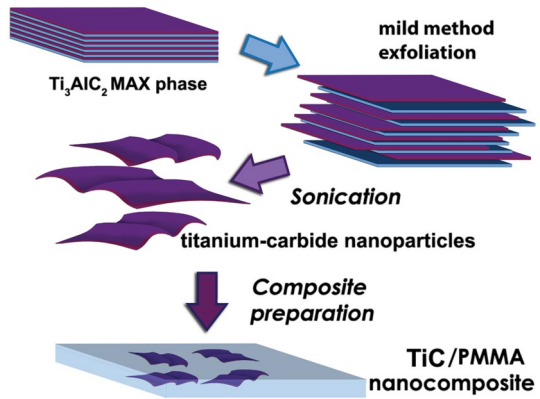


Fig. 2 FESEM photos of **a** Flakes delaminated in water; **b** PMMA composite prepared with titanium-carbide flakes

nanocomposite. Characteristic layered structure of MXenes is visible on FESEM image and confirming success of delamination and exfoliation procedures. Obtained flakes demonstrate multilayered structure with few μm in diameter. In Fig. 2b typical accordion like structure can be indicated in nanosize grain-like structures, clustered in PMMA matrix.

2.2 XRD

X-ray diffraction powder (XRD) technique was used to determine structural characteristics of titanium-carbide based flakes to be used in composites. Philips PW 1050 diffractometer equipped with a PW 1730 generator was used. The same conditions were used for all samples, 40 kV \times 20 mA, using Ni filtered Co $K\alpha$ radiation of 0.1778897 nm at room temperature. Measurements were carried out in the 2θ range of 20–80° with a scanning step

Fig. 3 XRD pattern for titanium-carbide flakes, starting material for PMMA/TiC composite

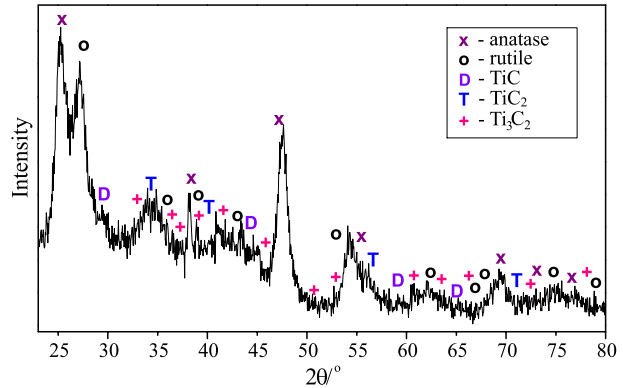
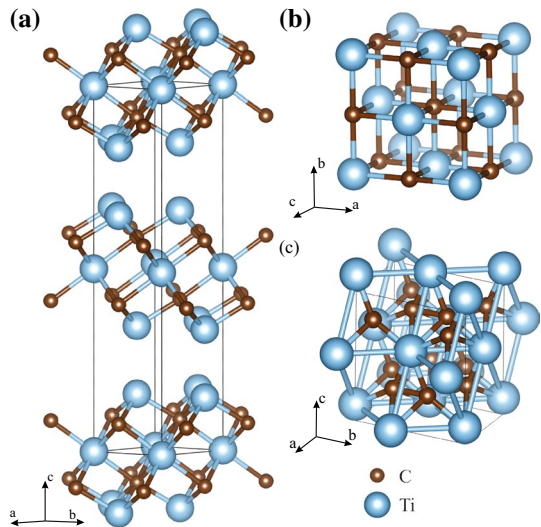


Fig. 4 Schematic representation of Titanium-carbide structures present at composite **a** Ti_3C_2 , **b** TiC and **c** TiC_2



of 0.05° and 10 s scanning time per step. In Fig. 3 is presented XRD pattern for titanium-carbide flakes, starting material for composite. The different phases of titanium carbide can be noticed from diffractogram— Ti_3C_2 , TiC and TiC_2 together with TiO_2 . TiO_2 is widely present as anatase and rutile and it is confirmed that they belong to space groups $P6_3/mmc$ (194), $Fm\bar{3}m$ (225) $Fm2m$ (42), $I4_1/amd$ (141), $P4_2/mnm$ (136), respectively. The unit cells of MXene structures Ti_3C_2 , TiC and TiC_2 are presented in Fig. 4. These structures were further used in DFT analysis of optical spectroscopy results in Sect. 3.3.

3 Results and discussion

3.1 Raman spectroscopy

The micro-Raman spectra were taken in the backscattering configuration and analyzed by the TriVista 557 system equipped with a nitrogen cooled charge-coupled-device

detector. As an excitation source, we used the 532 nm line of Ti:Sapphire laser. Excitation energy is in the off-resonance regime for all the considered materials. The Raman spectra of the PMMA, PMMA/TiC, and titanium-carbide flakes, measured in the spectral range of 100–1100 cm^{-1} at room temperature, are presented in Fig. 5.

The Raman spectrum of PMMA is presented in Fig. 5a. Intense modes at 235, 300, 362, 400, 484, 560, 603, 660, 733, 815, 839, 864, 911, 967, 985, 1063 and 1091 cm^{-1} were detected. The obtained results are in a good agreement with the values given in the literature Willis et al. (1969); Thomas et al. (2008); Čurčić et al. (2020).

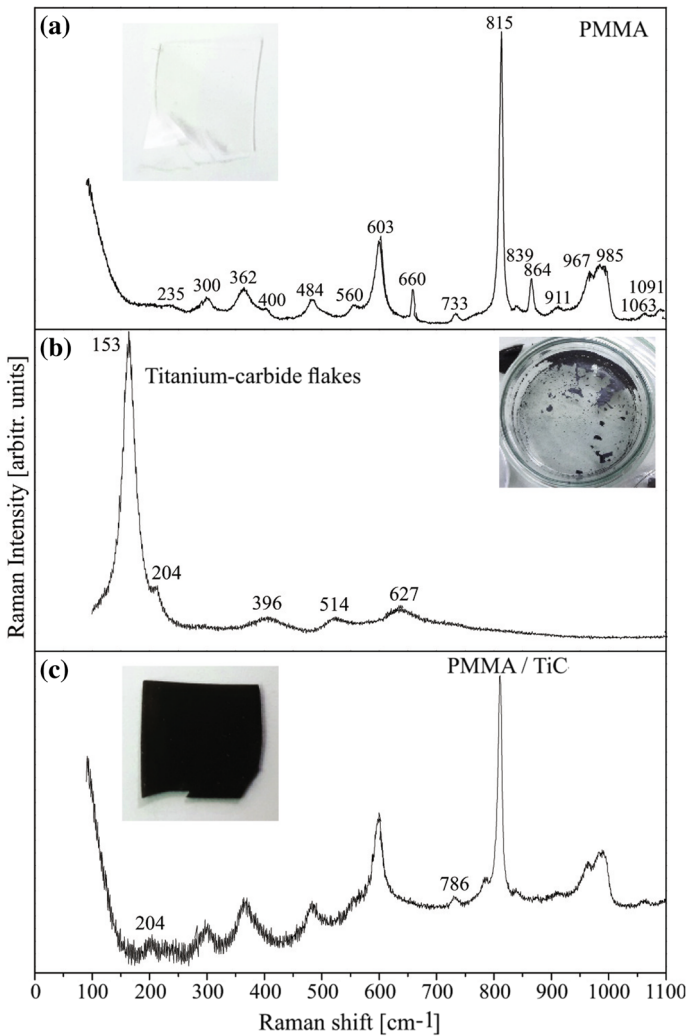


Fig. 5 Raman spectra with photo of the sample of **a** PMMA, **b** Titanium-carbide flakes, **c** PMMA/TiC composite. Only titanium-carbide related peaks are marked in this spectrum. Unassigned peaks correspond to PMMA from **a** spectrum

In Fig. 5b spectrum of titanium-carbide flakes after etching procedure is presented. Several characteristic peaks can be distinguished on 153 cm^{-1} , 204 cm^{-1} , 396 cm^{-1} , 514 cm^{-1} and 627 cm^{-1} . Peaks at 153 cm^{-1} and 627 cm^{-1} correspond to doubly degenerated E_{2g} modes of Ti_3C_2 . The frequency associated with E_{2g} modes is calculated to be at 161 cm^{-1} for the bare Ti_3C_2 . Since their main contribution is from in-plane vibrations of Ti and C atoms, it can be influenced by the vibrations of the terminal atoms (as a residue of synthesis procedure) weaken the in-plane motion of the Ti and C atoms, hence there is shift to lower frequency. The terminal groups play significant roles for the vibrational modes: the terminal atoms weakening the motions in which the surface Ti atoms are involved while strengthening the out-of-plane vibration of the C atoms; the corresponding vibrational frequencies dramatically change with the various terminal atoms Zhao et al. (2016). This is consistent with XRD results suggesting significant amount of TiO_2 as a residue of synthesis procedure as described in introduction. This can be also visible in Raman spectrum of titanium-carbide flakes on 204 cm^{-1} and 514 cm^{-1} . The doubly degenerated modes at 621 cm^{-1} correspond to the in-plane vibration of the C atoms Hu et al. (2015). In Fig. 5c spectrum of PMMA/TiC is presented, only titanium-carbide related peaks at 204 and 786 cm^{-1} are marked in this spectrum. Unassigned peaks correspond to PMMA peaks marked on a) panel.

As XRD analysis demonstrated, obtained flakes contain both MXene flakes and titanium-dioxide as the residue of synthesis procedure. To further understand and assign this spectra we performed theoretical analysis of all materials identified in XRD pattern using density functional theory calculations. Calculations provided us a guide for identification of peaks and all results are summarized in Table 1.

3.2 Far-infrared spectroscopy

Far-infrared reflection spectra were measured at room temperature in the spectral range from 40 to 600 cm^{-1} , carried out with a BOMEM DA 8 spectrometer. The experimental data are represented at Fig. 6a and by circles at Fig. 6b–d. As expected, the reflection spectra of nanocomposites are by intensity placed between the starting composites. In order to analyse far-infrared spectra we have used the classical oscillator model with free carrier contribution, as a base for Maxwell–Garnet effective medium approximation Abstreiter (1984); Carter and Bate (1971). The low-frequency dielectric properties of single crystals are described by classical oscillators corresponding to the TO modes, to which the Drude part is superimposed to take into account the free carrier contribution:

$$\epsilon_s(\omega) = \epsilon_\infty + \sum_{k=1}^l \frac{\epsilon_\infty S_k}{\omega_{TOk}^2 - \omega^2 - i\gamma_{TOk}\omega} - \frac{\epsilon_\infty \omega_p^2}{\omega(\omega + i\Gamma_p)}, \quad (1)$$

where ϵ_∞ is the bound charge contribution and it is assumed to be a constant, ω_{TOk}^2 is the transverse optical-phonon frequency, ω_p^2 the plasma frequency, γ_{TOk} is damping, Γ_p is the plasmon mode damping coefficient, and S_k is the oscillator strength.

In general, the optical properties of an inhomogeneous material are described by the complex dielectric function that depends on 3D distribution of constituents. The investigated mixture consists of two materials with two different dielectric components. One is treated as a host, and the other as the inclusions. The characterization of the inhomogeneous material by the two dielectric functions is not useful, since one need to know the exact geometrical arrangement of the constituents of the material. However, if the wavelength of

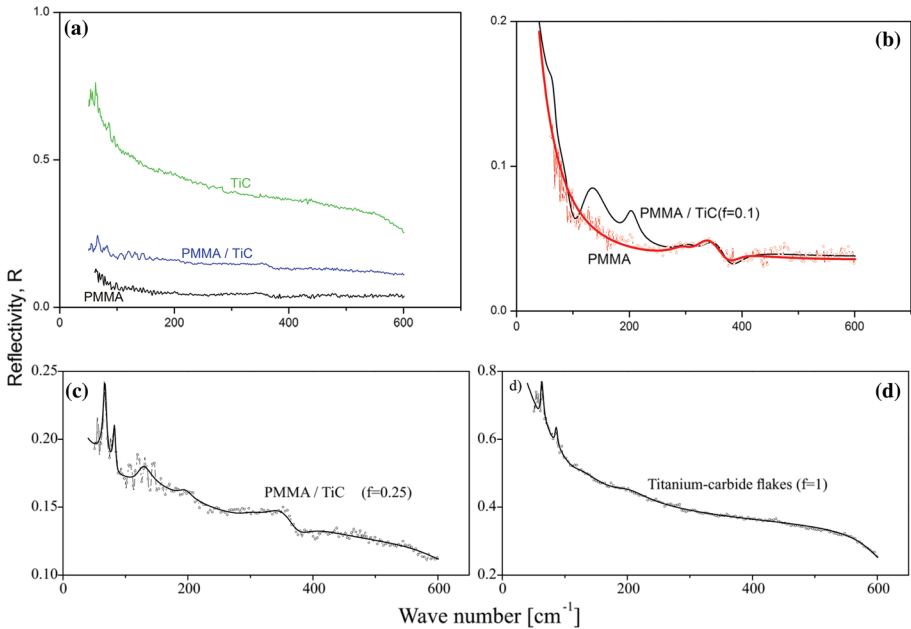


Fig. 6 Infrared analysis: **a** Infrared spectra of Titanium-carbide flakes (green) and composites PMMA/TiC (blue) and pure PMMA (black), **b**, **c**, and **d** circles represent experimental data and solid lines are fit obtained by Maxwell–Garnet model as described in Sect. 3.2

Table 1 Raman and infrared spectrum analysis and modes assignation for synthesized titanium-carbide flakes and PMMA/TiC composite

	Titanium-carbide flakes		PMMA/TiC		Description
	Raman	IR	Raman	IR	
ω_1		62.4	66		E_u, Ti_3C_2
ω_2		85.8	81		B_1, TiO_2 rutile
ω_3		119	127		A_{2u}, Ti_3C_2 and $B_1 TiC_2$
ω_4	153				E_g, Ti_3C_2
ω_5	204	200	204	195	E, TiO_2 anatase
ω_6	396				$A_2, TiC_2; E, TiO_2$ anatase
ω_7	514				A_1, TiO_2 anatase
ω_8		620		615	E_u, Ti_3C_2
ω_9	627				E_g, Ti_3C_2
ω_{10}			786		A_g, TiO_2 rutile
ω_p		80		150	
f		1		0.25	

Infrared modes fit is obtained by Maxwell–Garnet model. Modes assignation is performed using values obtained using DFT calculations

the electromagnetic radiation is much larger than the size of inclusions, classical theories of inhomogeneous material presume that the material can be treated as a homogeneous substance with an effective dielectric function. In the literature, many mixing models can

be found for the effective permittivity of such mixture. Some are present in ref Sihvola (1999). Optical properties of such materials depend upon the properties of constituents, as well as their volume fraction. Since our samples are well defined and separated nanosized grains (as demonstrated on FESEM images, Fig. 2), we used Maxwell–Garnet model for present case. For the spherical inclusions case, the prediction of the effective permittivity of mixture, ϵ_{eff} , according to the Maxwell–Garnet mixing rule is Garnett (1904):

$$\epsilon_{eff} = \epsilon_1 + 3f\epsilon_1 \frac{\epsilon_2 - \epsilon_1}{\epsilon_2 + 2\epsilon_1 - f(\epsilon_2 - \epsilon_1)} \quad (2)$$

Here, spheres of permittivity ϵ_2 (Titanium-carbide) are located randomly in homogeneous environment ϵ_1 (PMMA) and occupy a volume fraction f .

Solid lines in Fig. 6 are calculated spectra obtained by a fitting procedure based on the previously presented model. The agreement of the theoretical model obtained in this manner with the experimental results is excellent.

To demonstrate the model, together with the infrared spectrum of PMMA, Fig. 6b is given the theoretical spectrum of PMMA/TiC nanocomposites for $f = 0.1$. The properties of TiC structures are clearly visible. A larger share of TiC structures leads to the spectrum in Fig 6c, which was obtained for $f = 0.25$. In Fig. 6d, for $f=1$ of course there is no effect from PMMA.

3.3 Discussion

In Table 1 are summarized results from spectroscopic measurements of obtained nanocomposites. As stated above, for infrared measurements the agreement of the theoretical model with obtained spectra is excellent and best fit parameters are presented in this table.

To further support our results we performed DFT based calculations and calculated vibrational frequencies in Γ point for all materials present after titanium-carbide flakes exfoliation, which we determined are present using XRD, Fig. 3. Obtained values are compared to experimental Raman and infrared spectrum and modes have been assigned. Results are summarized in Table 1. We presented only modes that can be assigned to peaks from the spectra. In infrared spectra we can notice good agreement with theoretical calculations, specially for low-energy E_u and A_{2u} mode of Ti_3C_2 which is present the composite spectrum (Fig. 6b, c) as in starting titanium-carbide material (Fig. 6d). As shown in XRD we notice peaks originating from TiO_2 and TiC_2 in mid-energy region. High-energy mode E_u on 620 cm^{-1} is present in spectrum of PMMA/TiC. In Table 2 are summarized calculated optical modes for Ti_3C_2 with symmetry 194 group used in analysis.

DFT calculations were performed using the Quantum Espresso software package Gianozzi (2009), based on the plane waves and pseudopotentials. The PBE (Perdew, Burke and Ernzerhof) Perdew et al. (1996) exchange-correlation functional was employed and PAW (Projector augmented waves) pseudopotentials were used. Energy cutoff for wavefunctions and charge density were set to 52 Ry and 575 Ry to ensure the convergence. The Brillouin zone was sampled using the Monkhorst-Pack scheme, with $8 \times 8 \times 8$ k-points mesh for TiC_2 , $8 \times 8 \times 4$ for Ti_3C_2 , $12 \times 12 \times 12$ for TiC, and $8 \times 8 \times 8$ for TiO_2 (Rutile and Anatase structures). Phonon frequencies are calculated within the DPFT (Density Functional Perturbation Theory) implemented in Quantum Espresso Baroni et al. (2001). In order to obtain the lattice parameters more accurately, van der Waals forces were treated using the Grimme-D2 correction Grimme (2006)

Table 2 Vibrational modes for Ti_3C_2 with symmetry group 194, calculated from the measured data

Ti_3C_2 (P6 ₃ /mmc)		
cm ⁻¹	Symmetry	Raman or IR active
65.0	E _u	I
135.2	A _{2u}	I
160.6	E _g	R
161.4	E _g	R
229.9	A _{1g}	R
269.3	A _{1g}	R
271.1	E _u	I
271.7	E _u	I
371.4	A _{2u}	I
382.4	A _{2u}	I
549.1	A _{2u}	I
554.4	A _{2u}	I
611.2	E _g	R
620.4	E _g	R
624.1	E _u	I
626.4	E _u	I
653.2	A _{1g}	R
658.3	A _{1g}	R

Optical spectroscopy results supported with the DFT numerical calculation confirm that produced composites PMMA/TiC show optical modification comparing to pure PMMA. Our X-ray diffraction investigation of synthesized nanomaterials identified presence of Ti_3C_2 and TiC_2 MXenes and residual TiO_2 and TiC from the synthesis procedure, which can be also supported from the optical spectroscopy results.

4 Conclusion

In this paper, we present results of optical and structural investigation of composite based on titanium-carbide nanoflakes (Ti_3C_2 , TiC_2 , TiC and TiO_2) in PMMA matrix. X-ray diffraction (XRD) investigation of synthesized nanomaterials identified presence of Ti_3C_2 and TiC_2 MXenes and residual TiO_2 and TiC from the synthesis procedure. The optical properties were studied by Raman and infrared spectroscopy at room temperature. The analysis of the Raman spectra was made by the fitting procedure. For analysis of infrared spectra we used Maxwell–Garnet model. In order to identify and assign vibrational modes, vibrational frequencies of all identified materials were calculated using density functional theory, and compared with experimental results. We confirmed optical modification in composite structure compared to pure PMMA. Further analysis that goes beyond the scope of this publication studies mechanical properties of composite materials, confirming improvements compared to pure PMMA. The obtained composite showed enhanced hardness, elastic modulus and tensile strength compared with pure PMMA Pestic et al. (2019).

Acknowledgements The authors acknowledge funding provided by the Institute of Physics Belgrade and Faculty of Technology and Metallurgy, through the grant by the Ministry of Education, Science and Technological Development of the Republic of Serbia. All calculations were performed using computational resources at Johannes Kepler University, Linz, Austria.

Author Contributions Conceptualization, JP and NR; investigation JP, AŠ, JM, MG, IP, NP; validation, JP, NP, NR; formal analysis, JP, AŠ, JM, MG, NP, NR; writing JP and AŠ; writing–review and editing, JP, AŠ, NP, NR; visualization, AŠ; supervision, NR; project administration, NR; funding acquisition, NR. All authors have read and agreed to the published version of the manuscript.

Funding The authors acknowledge funding provided by the Institute of Physics Belgrade and Faculty of Technology and Metallurgy, through the grant by the Ministry of Education, Science and Technological Development of the Republic of Serbia.

Data availability All additional material is available at authors on request.

Code availability Not applicable.

Declarations

Conflict of interest The Authors declare no conflict of interest.

Ethical approval Not applicable.

Informed consent Not applicable.

Consent for publication All authors consent to publication results presented in manuscript.

References

- Abstreiter, G.: Light Scattering in Solids IV. Springer, New York (1984)
- Baroni, S., de Gironcoli, S., Dal Corso, A., Giannozzi, P.: Phonons and related crystal properties from density-functional perturbation theory. *Rev. Mod. Phys.* **73**, 515–562 (2001)
- Cao, Y., Deng, Q., Liu, Z., Shen, D., Wang, T., Huang, Q., Du, S., Jiang, N., Lin, C.-T., Yu, J.: Enhanced thermal properties of poly (vinylidene fluoride) composites with ultrathin nanosheets of mxene. *RSC Adv.* **7**(33), 20494–20501 (2017)
- Carter, D.L., Bate, R.T.: *The Physics of Semimetals and Narrow-gap Semiconductors: Proceedings*, vol. 32. Pergamon, Texas, USA (1971)
- Ćurčić, M., Hadžić, B., Gilić, M., Radojević, V., Bjelajac, A., Radović, I., Timotjević, D., Romčević, M., Trajić, J., Romcevic, N.: Surface optical phonon (sop) mode in ZnS/poly (methylmethacrylate) nanocomposites. *Physica E* **115**, 113708 (2020)
- Dastan, D.: Nanostructured anatase titania thin films prepared by sol-gel dip coating technique. *J. Atom. Mol. Condens. Matter Nano Phys.* **2**, 109–114 (2015)
- Dastan, D., Chauré, N.B.: Influence of surfactants on TiO₂ nanoparticles grown by sol-gel technique. *Int. J. Mater. Mech. Manuf.* **2**, 21 (2014)
- Dastan, D., Chauré, N.: Kartha: Surfactants assisted solvothermal derived titania nanoparticles: synthesis and simulation. *J. Mater. Sci.* **28**, 7784–7796 (2017)
- Dastan, D., Londhe, P.U., Chauré, N.B.: Characterization of TiO₂ nanoparticles prepared using different surfactants by sol-gel method. *J. Mater. Sci.* **25**, 3473–3479 (2014)
- Durajski, A.P., Skoczylas, K.M., Szczaeniak, R.: Superconductivity in bilayer graphene intercalated with alkali and alkaline earth metals. *Phys. Chem. Chem. Phys.* **21**, 5925–5931 (2019). <https://doi.org/10.1039/C9CP00176J>
- Durajski, A.P., Auguscik, A.E., Szczaeniak, R.: Tunable electronic and magnetic properties of substitutionally doped graphene. *Physica E* **119**, 113985 (2020). <https://doi.org/10.1016/j.physe.2020.113985>
- Gao, Y., Wang, L., Zhou, A., Li, Z., Chen, J., Bala, H., Hu, Q., Cao, X.: Hydrothermal synthesis of TiO₂/Ti₃C₂ nanocomposites with enhanced photocatalytic activity. *Mater. Lett.* **150**, 62–64 (2015)

- Garnett, J.M.: XII. Colours in metal glasses and in metallic films. *Philosoph. Trans. R. Soc. Lond. Ser. A* **203**, 385–420 (1904)
- Giannozzi, P., et al.: QUANTUM ESPRESSO: a modular and open-source software project for quantum simulations of materials. *J. Phys. Condens. Matter* **21**(39), 395502 (2009)
- Grimme, S.: Semiempirical GGA-type density functional constructed with a long-range dispersion correction. *J. Comput. Chem.* **27**(15), 1787–1799 (2006)
- Hu, T., Wang, J., Zhang, H., Li, Z., Hu, M., Wang, X.: Vibrational properties of t_3c_2 and $\text{t}_3\text{c}_2\text{t}_2$ ($t = \text{o}, \text{f}, \text{oh}$) monosheets by first-principles calculations: a comparative study. *Phys. Chem. Chem. Phys.* **17**(15), 9997–10003 (2015)
- Hussain, F., Hojjati, M., Okamoto, M., Gorga, R.E.: Review article: polymer-matrix nanocomposites, processing, manufacturing, and application: an overview. *J. Compos. Mater.* **40**(17), 1511–1575 (2006). <https://doi.org/10.1177/0021998306067321>
- Jafari, A., Tahani, K., Dastan, D., Asgary, S., Shi, Z., Yin, X.-T., Zhou, W.-D., Garmestani, H.: Ştefan Ţălu: Ion implantation of copper oxide thin films; statistical and experimental results. *Surf. Interfaces* **18**, 100463 (2020)
- Katsnelson, M.I., Novoselov, K.S., Geim, A.K.: Chiral tunnelling and the Klein paradox in graphene. *Nat. Phys.* **2**, 620–625 (2006)
- Margine, E.R., Lambert, H., Giustino, F.: Electron-phonon interaction and pairing mechanism in superconducting ca-intercalated bilayer graphene. *Sci. Rep.* **6**, 21414 (2016)
- Naguib, M., Kurtoglu, M., Presser, V., Lu, J., Niu, J., Heon, M., Hultman, L., Gogotsi, Y., Barsoum, M.W.: Two-dimensional nanocrystals produced by exfoliation of t_3alc_2 . *Adv. Mater.* **23**(37), 4248–4253 (2011). <https://doi.org/10.1002/adma.201102306>
- Naguib, M., Mashtalir, O., Carle, J., Presser, V., Lu, J., Hultman, L., Gogotsi, Y., Barsoum, M.W.: Two-dimensional transition metal carbides. *ACS Nano* **6**(2), 1322–1331 (2012). <https://doi.org/10.1021/nn204153h>
- Naguib, M., Halim, J., Lu, J., Cook, K.M., Hultman, L., Gogotsi, Y., Barsoum, M.W.: New two-dimensional niobium and vanadium carbides as promising materials for li-ion batteries. *J. Am. Chem. Soc.* **135**(43), 15966–15969 (2013). <https://doi.org/10.1021/ja405735d>
- Naguib, M., Mashtalir, O., Lukatskaya, M.R., Dyatkin, B., Zhang, C., Presser, V., Gogotsi, Y., Barsoum, M.W.: One-step synthesis of nanocrystalline transition metal oxides on thin sheets of disordered graphitic carbon by oxidation of mxenes. *Chem. Commun.* **50**, 7420–7423 (2014)
- Novoselov, K.S., Geim, A.K., Morozov, S.V., Jiang, D., Zhang, Y., Dubonos, S.V., Grigorieva, I.V., Firsov, A.A.: Electric field effect in atomically thin carbon films. *Science* **306**(5696), 666–669 (2004). <https://doi.org/10.1126/science.1102896>
- Novoselov, K.S., Mishchenko, A., Carvalho, A., Castro Neto, A.H.: 2d materials and van der Waals heterostructures. *Science* **353**, 6298 (2016). <https://doi.org/10.1126/science.aac9439>
- Peppas, N., Langer, R.: New challenges in biomaterials. *Science* **263**(5154), 1715–1720 (1994). <https://doi.org/10.1126/science.8134835>
- Perdew, J.P., Burke, K., Ernzerhof, M.: Generalized gradient approximation made simple. *Phys. Rev. Lett.* **77**, 3865–3868 (1996)
- Pesic, I., Radojevic, V., Barsoum, N. M. Tomic, Romcevic, N.: Preparation, characterization and mechanical properties of mxene/pmma composite. TechConnect World Innovation Conference and Expo, Boston, MA, USA. <https://www.techconnectworld.com/World2019/wednesday.htmlW6.26> (2019)
- Pešić, J., Gajić, R., Hingerl, K., Belić, M.: Strain-enhanced superconductivity in li-doped graphene. *EPL (Europhys. Lett.)* **108**(6), 67005 (2014). <https://doi.org/10.1209/0295-5075/108/67005>
- Shan, K., Yi, Z.-Z., Yin, X.-T., Dastan, D., Dadkhah, S., Coates, B.T., Garmestani, H.: Mixed conductivities of a-site deficient Y, Cr-doubly doped srTiO_3 as novel dense diffusion barrier and temperature-independent limiting current oxygen sensors. *Adv. Powder Technol.* **31**(12), 4657–4664 (2020)
- Shan, K., Yi, Z.-Z., Yin, X.-T., Cui, L., Dastan, D., Garmestani, H., Alamgir, F.M.: Diffusion kinetics mechanism of oxygen ion in dense diffusion barrier limiting current oxygen sensors. *J. Alloy. Compd.* **855**, 157465 (2021)
- Shan, K., Zhai, F., Yi, Z.-Z., Yin, X.-T., Dastan, D., Tajabadi, F., Jafari, A., Abbasi, S.: Mixed conductivity and the conduction mechanism of the orthorhombic CAZRO3 based materials. *Surf. Interfaces* **23**, 100905 (2021)
- Sihvola, A.H.: *Electromagnetic Mixing Formulas and Applications*, vol. 47. IET, UK (1999)
- Tamborra, M., Striccoli, M., Comparelli, R., Curri, M., Petrella, A., Agostiano, A.: Optical properties of hybrid composites based on highly luminescent CDS nanocrystals in polymer. *Nanotechnology* **15**(4), 240 (2004)

- Tan, G.-L., Tang, D., Dastan, D., Jafari, A., Shi, Z., Chu, Q.-Q., Silva, J.P.B., Yin, X.-T.: Structures, morphological control, and antibacterial performance of tungsten oxide thin films. *Ceram. Int.* **47**(12), 17153–17160 (2021)
- Tan, G.-L., Tang, D., Dastan, D., Jafari, A., Silva, J.P.B., Yin, X.-T.: Effect of heat treatment on electrical and surface properties of tungsten oxide thin films grown by HFCVD technique. *Mater. Sci. Semicond. Process.* **122**, 105506 (2021)
- Thomas, K., Sheeba, M., Nampoory, V., Vallabhan, C., Radhakrishnan, P.: Raman spectra of polymethyl methacrylate optical fibres excited by a 532 nm diode pumped solid state laser. *J. Opt. A Pure Appl. Opt.* **10**(5), 055303 (2008)
- Tu, S., Jiang, Q., Zhang, X., Alshareef, H.N.: Large dielectric constant enhancement in mxene percolative polymer composites. *ACS Nano* **12**(4), 3369–3377 (2018)
- Twardowski, T.E.: *Introduction to Nanocomposite Materials: Properties, Processing, Characterization*, DEStech Publications Inc, Lancaster, USA (2007)
- Willis, H., Zichy, V., Hendra, P.: The laser-Raman and infra-red spectra of poly (methyl methacrylate). *Polymer* **10**, 737–746 (1969)
- Zhang, Y., Tan, Y.-W., Stormer, H.L., Kim, P.: Experimental observation of the quantum hall effect and Berry's phase in graphene. *Nature* **438**, 201–204 (2005)
- Zhao, T., Zhang, S., Guo, Y., Wang, Q.: TiC_2 : a new two-dimensional sheet beyond mxenes. *Nanoscale* **8**(1), 233–242 (2016)
- Zhu, J., Tang, Y., Yang, C., Wang, F., Cao, M.: Composites of TiO_2 nanoparticles deposited on Ti_3C_2 mxene nanosheets with enhanced electrochemical performance. *J. Electrochem. Soc.* **163**(5), 785–791 (2016)

Publisher's Note Springer Nature remains neutral with regard to jurisdictional claims in published maps and institutional affiliations.

Advanced Ceramics and Applications

Edited by
Rainer Gadow and Vojislav V. Mitic

DE GRUYTER

Editors

Prof. Dr. Rainer Gadow

University of Stuttgart

Institute for Manufacturing Technologies of Ceramic Components and Composites

Allmandring 7b

70569 Stuttgart

Germany

rainer.gadow@ifkb.uni-stuttgart.de

Prof. Dr. Vojislav V. Mitic

University of Niš

Department of Microelectronics

Knez Mihajlova 35

11000 Belgrad

Serbia

vmitic.d2480@gmail.com

ISBN 978-3-11-062513-4

e-ISBN (PDF) 978-3-11-062799-2

e-ISBN (EPUB) 978-3-11-062516-5

Library of Congress Control Number: 2021932222

Bibliographic information published by the Deutsche Nationalbibliothek

The Deutsche Nationalbibliothek lists this publication in the Deutsche Nationalbibliografie; detailed bibliographic data are available on the Internet at <http://dnb.dnb.de>.

© 2021 Walter de Gruyter GmbH, Berlin/Boston

Cover image: Gettyimages / undefined undefined

Typesetting: Integra Software Services Pvt. Ltd.

Printing and binding: CPI books GmbH, Leck

www.degruyter.com



Foreword: Pro "Advanced Ce

It is a pleasure to no
tions" organized und
bian Academy of Scie

Advanced ceram
of the future industr
spectrum of applicat
communication, heal

This conference i
ogy and industrial d
research centers and
eign countries espec

After a decade-lor
and experienced scie
all over the globe an
seek for joint resear
like China, South Ko
Balkan Ceramics and

The Conference r
ramic Federation (ICF
cludes all Western an
to strengthen the con
prestigious American
support.

The conference it
covering fundamenta
hospitals. New develo
sectors, but also inn
dics, as well as nice c

A very positive po
students and research

Finally, the efforts
Society and the Serbi
be given the courage t
Balkan region.

As one of the four
the conference has no
but also penetrated W
the conference worldv

<https://doi.org/10.1515/9783>

Zorica Ž. Lazarević, Martina Gilić, Aleksandra Milutinović,
Nebojša Romčević, Hana Ibrahim Elswie, Vesna Radojević,
Dalibor L. Sekulić

15 Growth and characterization of calcium fluoride single crystals

Abstract: The calcium fluoride (CaF_2) single crystals were grown using the Bridgman technique. By optimizing growth conditions, $\langle 111 \rangle$ -oriented CaF_2 crystals up to 20 mm in diameter were grown. Number of dislocations in CaF_2 crystals was $5 \times 10^4 - 2 \times 10^5$ per cm^2 . Selected CaF_2 single crystals is cut into several tile diamond saw. The plates were polished, first with the silicon carbide, then with the paraffin oil and finally with a diamond paste. The obtained crystals were studied by X-ray diffraction, Raman spectroscopy, far-IR reflectivity and by the measurement of transmission in the mid-IR range. The crystal structure is confirmed by XRD. One Raman and two IR optical modes predicted by group theory are observed. In the transmission spectra, except modes originated from vibration of $-\text{CH}_2$ groups, hydroxyl groups $-\text{OH}$ and KBr , is visible a peak at 671 cm^{-1} assigned to the Ca-F stretching vibrations. A low photoluminescence testifies that the concentration of oxygen defects within the host of CaF_2 is small. The electrical and dielectric properties of CaF_2 single crystal were studied.

Keywords: optical materials, CaF_2 , Raman spectroscopy, IR spectroscopy, photoluminescence

15.1 Introduction

Crystals are the unacknowledged pillars of modern technology. Without crystals, there would be no electronic industry, no photonic industry, no fiber optic communications, which depend on materials/crystals such as semiconductors, superconductors,

Acknowledgments: This research was financially supported by the Ministry of Education, Science and Technological Development of the Republic of Serbia through Projects No. III45003 and TR34011. The results presented in this chapter are mainly from the doctoral thesis of Hana Ibrahim Elswie which was under the supervision of Prof. Vesna Radojević and Zorica Lazarević.

Zorica Ž. Lazarević, Martina Gilić, Aleksandra Milutinović, Nebojša Romčević, Institute of Physics, University of Belgrade, Belgrade, Serbia, lzorica@yahoo.com

Hana Ibrahim Elswie, Vesna Radojević, Faculty of Technology and Metallurgy, University of Belgrade, Belgrade, Serbia, hanaibrahim52@yahoo.com

Dalibor L. Sekulić, Faculty of Technical Sciences, University of Novi Sad, Novi Sad, Serbia, dalsek@yahoo.com

polarizers, transducers, radiation detectors, ultrasonic amplifiers, ferrites, magnetic garnets, solid state lasers, non-linear optics, piezo-electric, electro-optic, acousto-optic, photosensitive, refractory of different grades, crystalline films for microelectronics and computer industries [1]. Crystal growth is an interdisciplinary subject covering physics, chemistry, material science, chemical engineering, metallurgy, crystallography, mineralogy and others. In the past few decades, there has been a growing interest on crystal growth processes, particularly in view of the increasing demand of materials for technological applications. The materials can be grown in single crystal form from the melt provided they melt congruently without decomposition at the melting point and do not undergo any phase transformation between the melting point and room temperature. Depending on the thermal characteristics, the following techniques are employed: Bridgman, Czochralski, Kyropoulos, zone melting and Verneuil techniques. Schematics of the two Bridgman configurations and other crystal growth techniques are shown in Figures 15.1–15.6 [1, 2]. Czochralski method for obtain different optical materials and solid state lasers has been reviewed by several authors [3–7]. For most compound semiconductor materials, melt growth methods are the main methods of industrial manufacture as they provide a rapid growth of large single crystals.

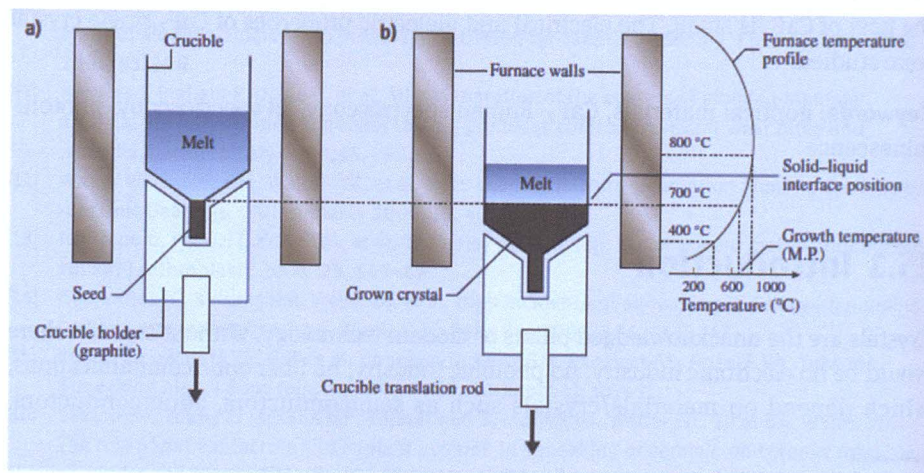


Figure 15.1: Schematic diagram of a vertical Bridgman (VB) crystal growth process in a single-zone furnace: (a) at the beginning of the experiment and (b) with partially grown crystal.

Fluorides have attracted considerable research interest because they exhibit many unique properties that may increase their applications in optics and electronics. Among them, alkaline-earth fluorides are dielectric and have a wide transmission range, and therefore they are widely used in optical components, microelectronic and optoelectronic devices [8–10]. CaF_2 is a kind of typical alkaline-earth fluorides.

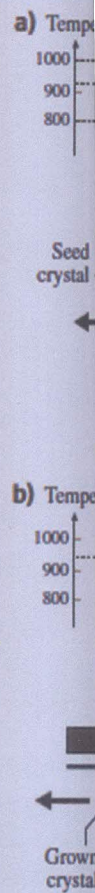


Figure 15.2: Schematic diagram of a vertical Bridgman (VB) crystal growth process in a single-zone furnace:

It has a well-centered laser with an optical phosphor host laser range of wavelengths some interesting attention has been paid to laser [13, 14]. Also, the importance in the and high laser

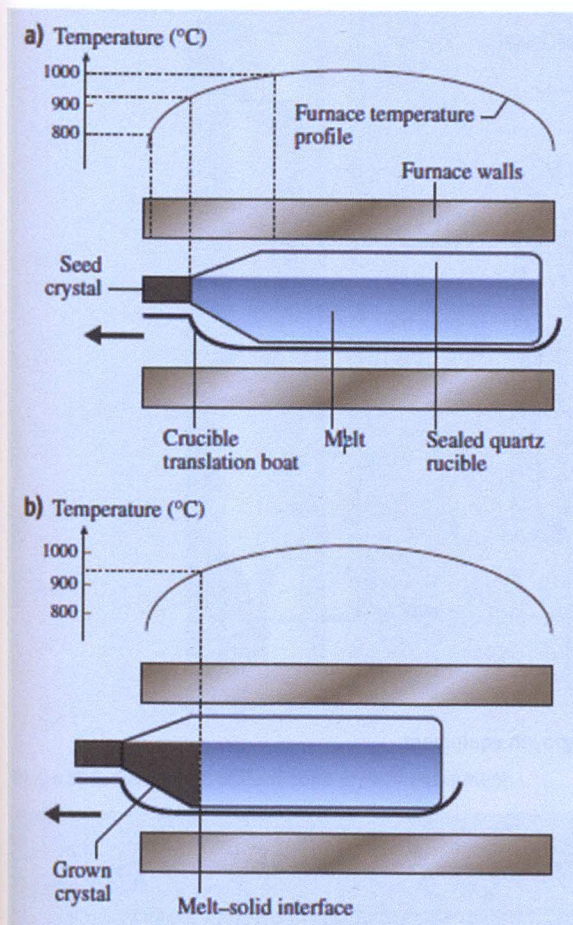


Figure 15.2: Schematic diagram of a horizontal Bridgman (HB) crystal growth process in a single-zone furnace: (a) at the beginning of the experiment and (b) with partially grown crystal.

It has a well-known fluorite structure, in which Ca^{2+} ions lie at the nodes in a face-centered lattice, while F^- ions lie at the centers of the octants [11]. Furthermore, with an optically isotropic fluorite structure, the CaF_2 crystal is suitable as a phosphor host because it exhibits outstanding transmission characteristics for a wide range of wavelength (0.3–8 mm) [12]. When CaF_2 is doped with rare-earth (RE), some interesting luminescence properties can be expected. As a result, general attention has been drawn on this field recently. CaF_2 doped with RE could be used as laser [13, 14] and fluorescent labeling material in biological applications [15–17].

Also, CaF_2 crystals exhibit some excellent properties such as high transmittance in the far UV to mid IR range, low refractive index, high chemical resistance and high laser damage threshold. Such properties make this crystal very important

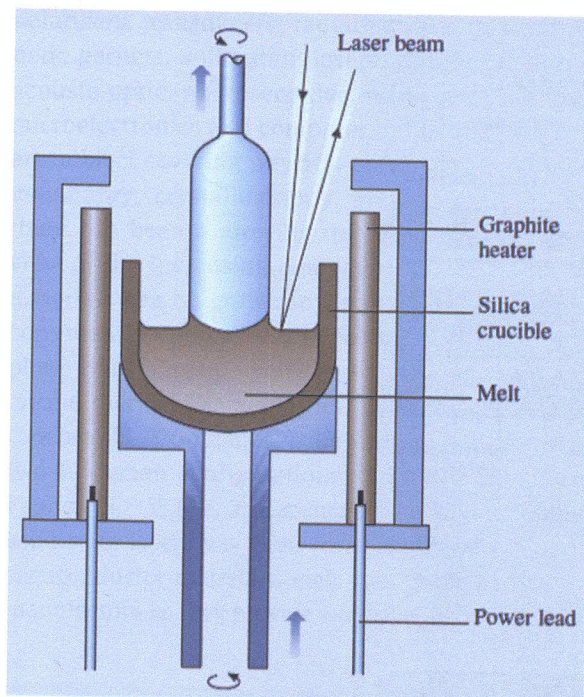


Figure 15.3: Schematic of Czochralski growth equipment.

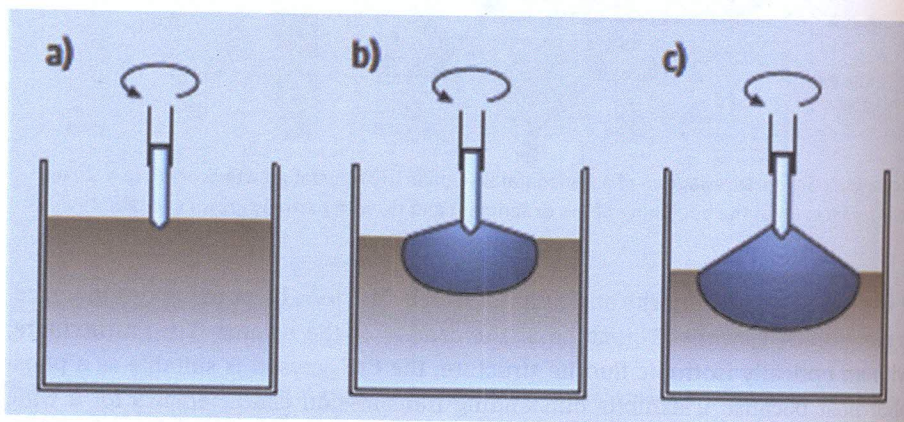


Figure 15.4: Schematic of Kyropoulos growth equipment. (a) The seed crystal contacts the melt, a small amount melts and then cooling is commenced to produce (b) and (c).

Figure 15.5: Schem

for use in the ma
raphy [18, 19].

Generally Ca
cations require
single crystals
growth and the
nology is found
and in particular
homogeneous dop
CaF₂ has been s
Recently, therm
vestigated and c
mechanical prop
boundaries are
ceramics of CaF₂

Calcium flu
The fluorite stru
CaF₂ is consider

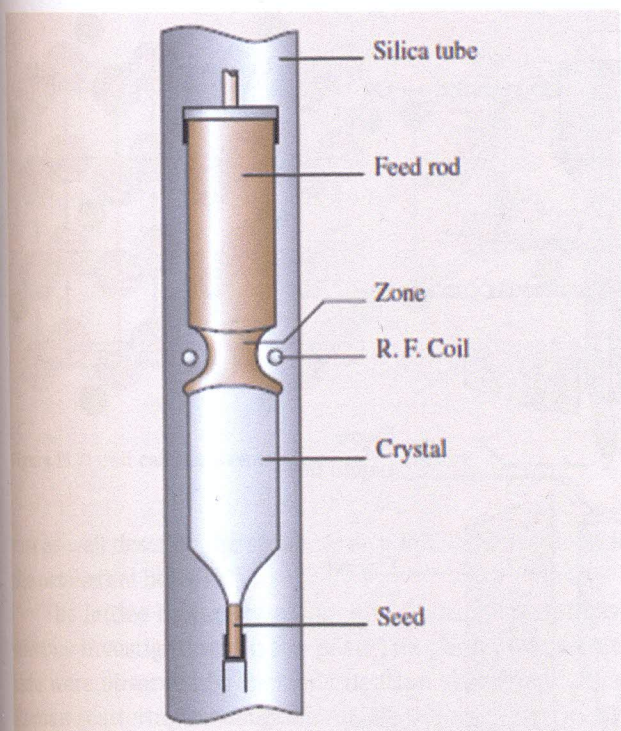


Figure 15.5: Schematic of float-zone growth equipment.

for use in the manufacture of special lenses, and especially for use in the photolithography [18, 19].

Generally CaF_2 single crystals are grown by the Bridgman method and the applications require large diameter CaF_2 single crystals [20, 21]. But growing large-size single crystals has been very tough because of the grain boundaries during the growth and the cracks during the cooling process [22]. Recently ceramic laser technology is found to exhibit more advantages over the single crystal growth processes and in particular, the ceramics can be produced in large volumes and with the homogeneous doping of laser active ions in the host materials [23]. Polycrystalline CaF_2 has been synthesized for the first time with dysprosium as an active ion [24]. Recently, thermal conductivity of the natural calcium fluoride ceramics has been investigated and compared with single crystals of CaF_2 and are found to exhibit better mechanical properties over single crystals [25]. Also, it was confirmed that the grain boundaries are transparent to phonons as well as to photons in synthetic optical ceramics of CaF_2 .

Calcium fluoride, fluorite, is a well-known face-centered cubic mineral [26]. The fluorite structure is shared with a wide variety of other compounds, for which CaF_2 is considered the type compound. The structure of fluorite has eight fluorine

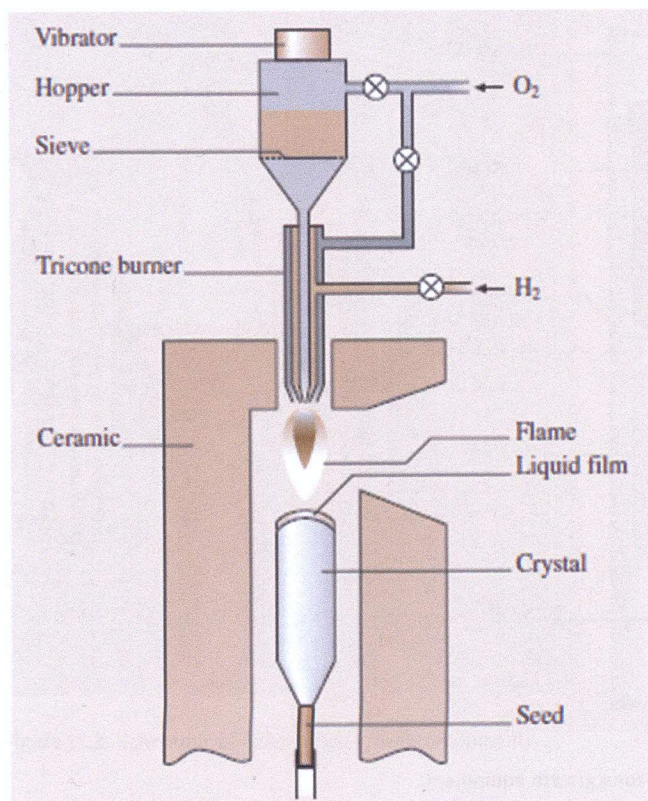


Figure 15.6: Schematic of Verneuil growth equipment.

atoms arranged in a cube around the calcium atom, with the cubes of fluorine edge-connected in a face-centered cubic array. Conversely, the fluorine atom is surrounded by four calcium atoms arranged in an ideal tetrahedron, with the tetrahedra also edge-connected. Fluorite has a very simple structure (Figure 15.7). Calcium (green) atoms in a face-centered pattern contain a cube of fluorine atoms (purple). Darker shades are used to portray calcium atoms toward the rear of the unit cell. We can also view the structure as a simple cubic array of fluorine atoms with a calcium atom in the center of alternate cubes. Considered that way, there are obviously diagonal planes of cubes containing no cations. These planes will evidently be planes of weakness, accounting for fluorite's excellent octahedral cleavage.

Since each fluoride ion has four nearest-neighbor calcium ions, the coordination in this structure is described as (8:4). Although the radii of the two ions ($F^- = 117$ pm, $Ca^{2+} = 126$ pm) do not allow true close packing, they are similar enough that one could

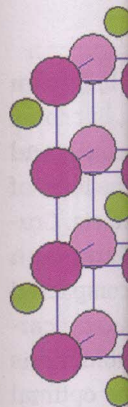


Figure 15.7: Crystal structure of fluorite.

just as well as the octahedron.

The lattice parameters of fluorite were determined by Raman scattering. The data have indicated that the structure must be a simple cubic lattice.

It may be noted that the structure of fluorite is very similar to that of calcium fluoride. The structure of fluorite is a face-centered cubic lattice of calcium atoms with a cube of fluorine atoms in the center of each cube. The structure of calcium fluoride is a simple cubic lattice of fluorine atoms with a calcium atom in the center of each cube.

The atomic structure of fluorite is very simple. The structure is a face-centered cubic lattice of calcium atoms with a cube of fluorine atoms in the center of each cube. The structure of calcium fluoride is a simple cubic lattice of fluorine atoms with a calcium atom in the center of each cube.

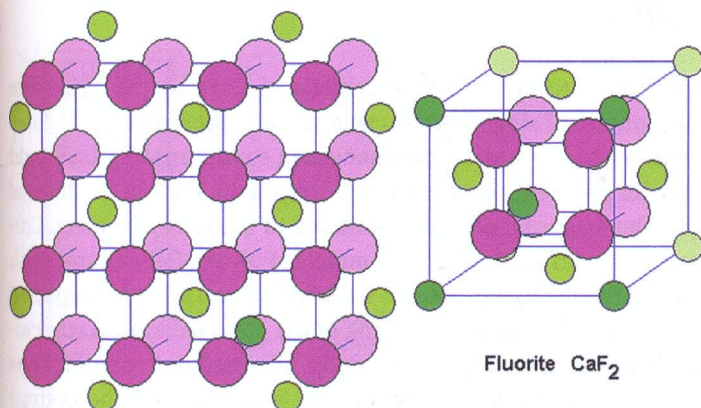


Figure 15.7: Unit cell representation of CaF_2 structure.

just as well describe the structure as a FCC lattice of fluoride ions with calcium ions in the octahedral holes [27].

The lattice dynamics of calcium fluoride crystal have been the subject of numerous investigations in the past. The phonon dispersion curves of calcium fluoride were observed by inelastic neutron scattering [28] and optical investigations. Raman scattering measurements [29, 30] and IR reflectivity measurements [31–33] have indicated pronounced phonon anharmonicity and defect induced scattering what must be included in oscillator model in order to estimate the lattice dynamical quantities properly.

It may be noted that the Bridgman method is one of the most popular methods of crystal growth because it is very easy to perform in a vacuum and in an inert atmosphere [34, 35]. The entire melted batch of CaF_2 in the crucible (which is of cylindrical shape with a conical bottom) is slowly lowered into the colder part of the furnace, so that the crystallization process begins at the bottom of the crucible at the top of the cone. Reviewing the literature it can be noted that the crucible can be made from spectroscopically pure graphite [22, 36–39] or platinum [40].

The aim of our work was to produce CaF_2 single crystal. The structural and optical properties obtained crystals were characterized using XRD, Raman and IR spectroscopy and measurement of transmission. The photoluminescence (PL) emission spectrum of CaF_2 has a broad band in the range of 320 nm to 475 nm. We have carried out a detailed study about electrical and dielectric properties of CaF_2 single crystal over a relatively wide range of frequencies as a function of temperature.

15.2 Experimental

The BCG365 device was used to obtain single crystals of CaF_2 by the Bridgman method [41, 42]. Initial samples of single crystals were mostly transparent, but some were cracked. Therefore, we had to make some changes in conditions of growth and construction of crucible. Experiments have been performed with CaF_2 in the form of a powder. The CaF_2 powder was compacted and sintered in the form of tablets. Crucible could easily be filled with such obtained tablets. Powder CaF_2 (Rare Earth Products Limited) purity of 99.99% was used in the experiment. It was compacted under a pressure of $3,500 \text{ kg cm}^{-2}$, and the sintering of the obtained tablets was carried out at $900 \text{ }^\circ\text{C}$ under an inert atmosphere of argon. We tried out combinations of various growth rates and generator powers with the aim to define the optimal growth conditions. Power generator was initially $P_{\text{gen}} = 3.8 \text{ kW}$, and was later increased to $P_{\text{gen}} = 3.94 \text{ kW}$. We tested different crystal growth rates.

Crucible with the charge placed on the holder in the upper chamber furnace. Then the apparatus is sealed, and then put into operation a vacuum apparatus and cooling water. After establishing a vacuum, the generator gradually increases the heating power all the mass has melted. The maximum used power was 3.94 kW . Since the charge melted, the crucible slowly descends to the lower (cold) chamber of the furnace. At the top of the cone, which arrives first in a colder area, a germ of future crystallization is formed. Continued further lowering the crucible, and the power supply generators have been gradually decreasing.

When lowered muffle up to 30 mm in length, the descent rate was $R = 6.8 \text{ mm h}^{-1}$. In a further descent we increased the speed at $R = 12.7 \text{ mm h}^{-1}$. In subsequent experiments, we used only the rate of descent crucible of $R = 6.8 \text{ mm h}^{-1}$ over the entire length of the chamber. During the growth of single crystals, a modified holder was used. His cooling fins at the upper end are slightly higher, while conventional brackets have all cooling fins of the same size. In Figure 15.8 shows a schematic representation of the apparatus, and Figure 15.9 gives the look and dimensions of the crucible that was used during the experiment.

The observations relating to the dislocation were recorded by observing an etched surface of CaF_2 crystal, using a Metaval of Carl Zeiss Java metallographic microscope with magnification of $270\times$. A selected CaF_2 single crystal was cut into several tiles with the diamond saw. The plates were polished, first with the silicon carbide, then with the paraffin oil, and finally with a diamond paste. The obtained finely polished samples were used for the characterization by Raman, IR and luminescence spectroscopy.

The crystal plane of cleavage of calcium fluoride crystal is $\langle 111 \rangle$. Thin panels for testing dislocations were obtained by splitting of individual pieces of crystal. Conc. H_2SO_4 was used as an etching solution. The samples were etched for 15 min .

The crystal structure of CaF_2 single crystal was approved using the X-ray diffractometer (XRD, Model Philips PW 1050 diffractometer) equipped with a PW 1730 generator, $40 \text{ kV} \times 20 \text{ mA}$, and using CuK_α radiation of 1.540598 \AA at the room temperature.

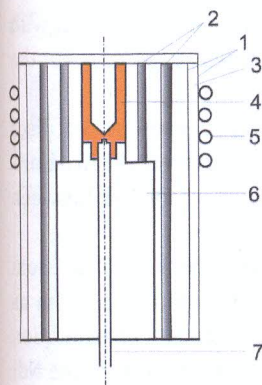


Figure 15.8: A schematic view of an apparatus for Bridgman-grown CaF_2 single crystals: 1) quartz tube; 2) ceramics; 3) line for cooling; 4) graphite crucible; 5) spiral for heating; 6) graphite crucible carrier and 7) spindle.

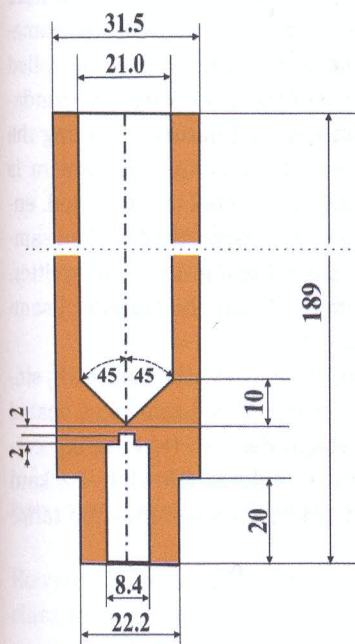


Figure 15.9: Schematic view – layout and dimensions of the crucibles used in the experiment for Bridgman-grown CaF_2 single crystals.

Measurements were done in 2θ range of $10\text{--}90^\circ$ with scanning step width of 0.05° and 10 s scanning time per step.

The Raman scattering measurements of CaF_2 crystal were performed in the back-scattering geometry at room temperature in the air using a Jobin-Yvon T64000 triple spectrometer, equipped with a confocal microscope (100x) and a nitrogen-cooled charge coupled device detector (CCD). The spectra had been excited by a 514.5 nm line of Coherent Innova 99 Ar^+ – ion laser with an output power of less than 20 mW to avoid local heating due to laser irradiation. Spectra were recorded in the range from 100 to 800 cm^{-1} .

The room temperature far-infrared reflectivity measurement was carried out with a BOMEM DA-8 FIR spectrometer. A DTGS pyroelectric detector was used to cover the wave number range from 50 to 600 cm^{-1} .

The transmission spectra of CaF_2 samples (powdered and pressed in the discs with KBr) were obtained by transmission Fourier-transform infrared (FTIR) Hartmann&Braun spectrometer, MB-series. The FTIR spectra were recorded between 4,000 and 400 cm^{-1} with a resolution of 4 cm^{-1} .

Photoluminescence (PL) studies reported in this work were performed at room temperature using Optical Parametric Oscillator (Vibrant OPO) tuned at 350 nm as excitation source. The experimental setup used in this study consists of excitation and detection part (Figure 15.10). Pulsed excitation was provided by a tunable Nd:YAG laser system with pulse duration of about 5 ns and repetition rate of 10 Hz. Time resolved streak images of the emission spectrum excited by OPO system were collected by using a spectrograph (SpectraPro 2300i) and recorded with a Hamamatsu streak camera (model C4334). All streak camera operations were controlled by the HPD-TA (High Performance Digital Temporal Analyzer) software. The fundamental advantage of the streak camera is its two-dimensional nature, enabling the acquiring of the temporal evolution of laser-induced phenomena. The camera is equipped with image intensifier so single photons can be detected and counted, enabling the detection of even very small photoluminescence response of excited sample. The excitation and detection optical axes were aligned using the beam splitter, so it was possible to tune the angle of excitation beam regarding the surface of sample and to maintain the high sensitivity of detection.

In order to study the electrical and dielectric properties of synthesized CaF_2 single crystal, the plan-parallel plate with dimensions of $11 \times 11 \times 2 \text{ mm}^3$ was coated with high-purity silver paste on adjacent faces as electrodes. AC (alternating current) parameters were measured using an impedance analyzer (Hewlett-Packard 4194A) at various temperatures between 25 °C and 175 °C in the frequency range 100 Hz to 1 MHz. For more details see Ref [43].

15.3 Results and discussion

CaF_2 single crystals are obtained by the vertical Bridgman method in vacuum. The best results were obtained with a crystal growth rate of 6.8 mm h^{-1} . The obtained single crystal of CaF_2 was 90 mm in length and 20 mm in diameter (Figure 15.11).

Because of the low temperature gradient came to a sudden crystallization process with appearance of dendrites in the bottom of the crucible. This was the reason why change was made in the construction of crucible. The cone on the bottom of the crucible was extended into a narrow tube. This form avoid the appearance of dendrites. The crystals which were obtained from the thus-constructed crucible were of better quality.

STREAKSCOPE HEAD
Spectrograph

Figure 15

Howeve
clung th
The
(rangin
stresses
tions or
sided p
Bridgma
Afte
conc. H
output c
even aft
schedul

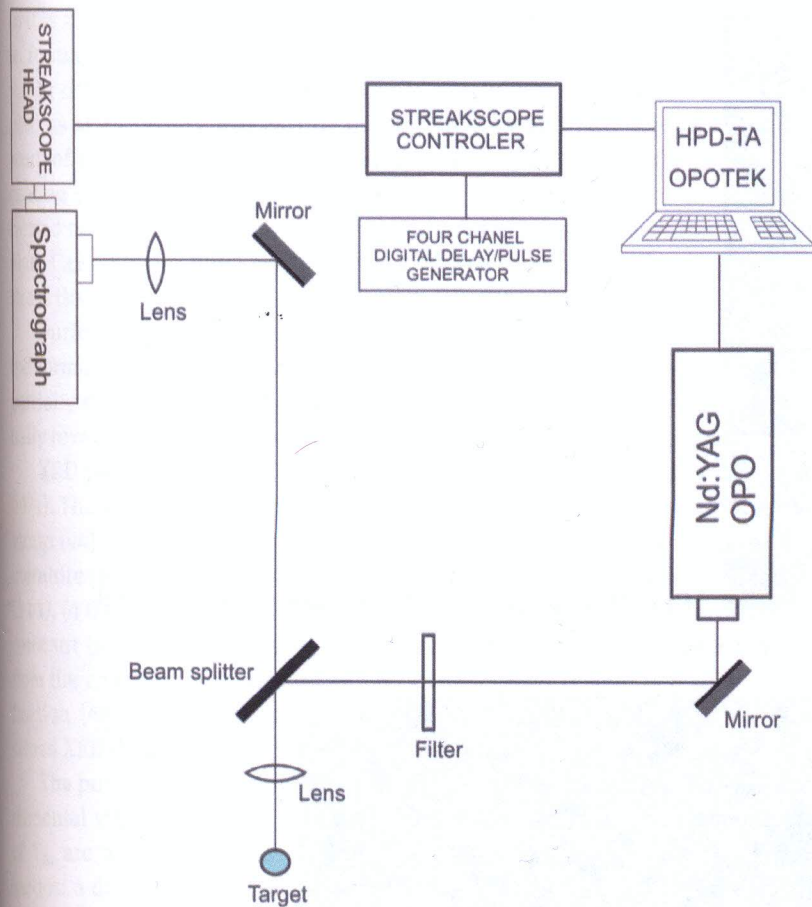


Figure 15.10: Experimental setup for photoluminescence measurements.

However, when grinding the upper surface of the crystal, due to impurities that have clung there, there have been cracks in crystals per plane cleavage $\langle 111 \rangle$.

The general conclusion is that in all samples relatively high dislocation density (ranging from 60,000 to 140,000) was observed as a consequence of greater internal stresses, which have emerged in the process of cooling. From Figure 15.12 dislocations on CaF_2 single crystal can be observed. Etch pits have the shape of a three-sided pyramid. Number of dislocations in CaF_2 crystals which were made by the Bridgman method was $5 \times 10^4 - 2 \times 10^5$ per cm^2 (Figure 15.6).

After heating to 400 °C and gradual cooling, crystal etching was done with conc. H_2SO_4 and observation under a microscope. In places where there were the output of dislocations were not observed any major changes. The same was the case even after heating at a temperature of 600 °C. By observation under a microscope schedule dislocations remained unchanged. However, heating the crystals at 860 °C,

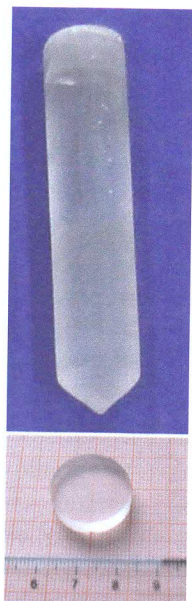


Figure 15.11: Photographs of Bridgman-grown CaF_2 single crystal.

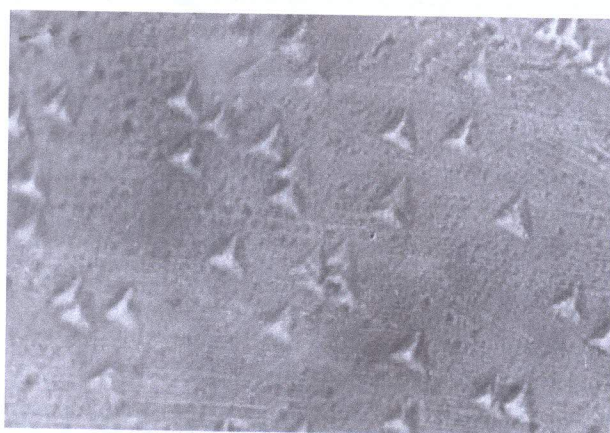


Figure 15.12: The microscopic image of the surface CaF_2 crystal plate in the direction $\langle 111 \rangle$. Magnification of 270x.

after a gradual cooling, etching with conc. H_2SO_4 and observation under a microscope showed a different schedule point of exit of dislocations in the crystal surface. There was a movement of dislocations. It was seen that internal stress partially disappeared as a result of dislocation, with their stress fields partially reversed. In so doing, the concentration of the dislocations is not changed practically. After heating, it was noticed that the crystal on the surface was milky white. This layer was very thin,

so it is assumed that the formation of a thin layer of CaF_2 is due to the formation of a thin layer of CaF_2 .

In order to eliminate the process of annealing at a temperature of annealing, the annealing of the bulk was carried out under a vacuum. The plate CaF_2 did not show any stress than non-annealed.

During the annealing process, the formation of a thin layer of CaF_2 partially disappeared, but it was partially reversed, but it was not completely reversed.

XRD pattern (JCPDS 0971). The sample was in the $\langle 111 \rangle$ group [44]. The XRD pattern is in the literature [45–47]. The XRD pattern shows the $(3\ 1\ 1)$, $(4\ 0\ 0)$, $(3\ 1\ 1)$ constant (a) of the $\langle 111 \rangle$ from the equation of the lattice constant fraction [48]. The XRD pattern obtained XRD diagram.

The primitive lattice constant of T_{1u} are acoustic modes: a doubly degenerate LO T_{1u} and a triply degenerate T_{2g} .

The room-temperature Raman spectra of CaF_2 crystal.

T_{2g} mode originates from a single triply degenerate T_{2g} mode, which remains stationary in the $\langle 111 \rangle$ direction [52–60].

The far-infrared Raman spectra of CaF_2 crystal. The experimental Raman spectra were obtained using a Raman spectrometer [61, 62]:

so it is assumed that there was a diffusion of oxygen and partial oxidation of CaF_2 , i.e. formation of CaO .

In order to eliminate stresses in the crystal, we made a crystal annealing. The process of annealing was carried out on the plate and bulk crystal CaF_2 . The temperature of annealing of the plate was at 1,000 °C for 3 h, and the temperature of annealing of the bulk crystal was at 1,000 °C and 1,080 °C for 1–3 h. Annealing was carried out under an inert atmosphere of argon. It was noticed that after annealing, plate CaF_2 did not have enough stress. Annealing bulk single crystal CaF_2 had less stress than non-annealing.

During the annealing process there is a movement of dislocations. This leads to the formation of sub-boundaries, and, as a result, the internal stress in the crystal partially disappears. During the movement of dislocations their stress fields are partially reversed, but the dislocation density is practically not changed.

XRD pattern (Figure 15.13) was indexed by using JCPDS database (card no. 87-0971). The sample of CaF_2 single crystal was of cubic structure with the $Fm\bar{3}m$ space group [44]. The XRD pattern was found to match exactly with those reported in the literature [45–47]. The displayed peaks correspond to $(h k l)$ values of (1 1 1), (2 2 0), (3 1 1), (4 0 0), (3 3 1) and (4 2 2). Using the $(h k l)$ values of different peaks, the lattice constant (a) of the sample was calculated. Their lattice parameter was calculated from the equation of plane spacing for cubic crystal system and Bragg's law for diffraction [48]. The lattice parameter was 5.460 ± 0.011 Å, calculated from the obtained XRD diagram, which was in good agreement with the literature [49].

The primitive cell of a fluorite structure contains three atoms that give nine fundamental vibrations in the center of Brillouin zone $6T_{1u}(\text{IR}) + 3T_{2g}(\text{R})$. The first three of T_{1u} are acoustic modes. At the Γ point, there are three distinct optic phonon modes: a doubly degenerate infrared-active TO T_{1u} , an infrared-active nondegenerate LO T_{1u} and a triply degenerate Raman-active mode T_{2g} between them [50, 51].

The room-temperature first order T_{2g} one-band spontaneous Raman scattering spectra of CaF_2 crystal is shown in Figure 15.14.

T_{2g} mode originates from the stretching vibrations of F atoms around Ca. In this single triply degenerate Raman mode with frequency $\omega = 319.7 \text{ cm}^{-1}$ Ca^{2+} cation remains stationary and the neighboring fluoride F^{-1} ions vibrate against each other [52–60].

The far-infrared reflectivity spectrum of the CaF_2 substrate is shown in Figure 15.15a. The experimental data are presented with circles. The solid line in Figure 15.15a was obtained using the dielectric function in the factorized form given by eq. (15.1) [61, 62]:

$$\varepsilon(\omega) = \varepsilon_{\infty} \prod_{j=1}^n \frac{\omega_{j\text{LO}}^2 - \omega^2 + i\omega\gamma_{j\text{LO}}}{\omega_{j\text{TO}}^2 - \omega^2 + i\omega\gamma_{j\text{TO}}} \quad (15.1)$$

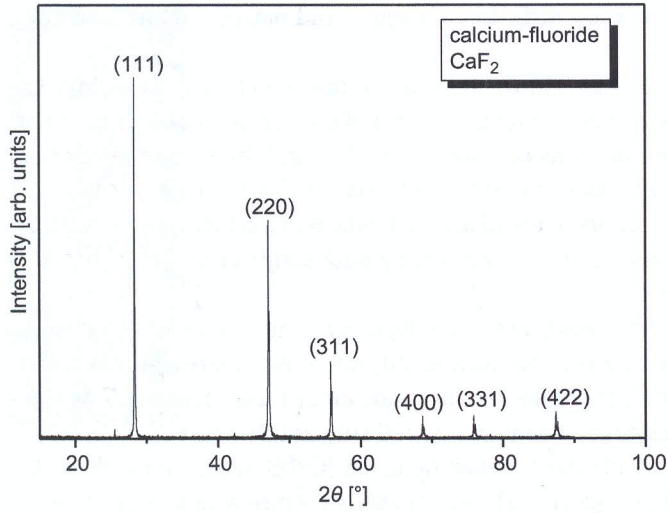


Figure 15.13: X-ray diffraction pattern of the CaF₂ powdered sample.

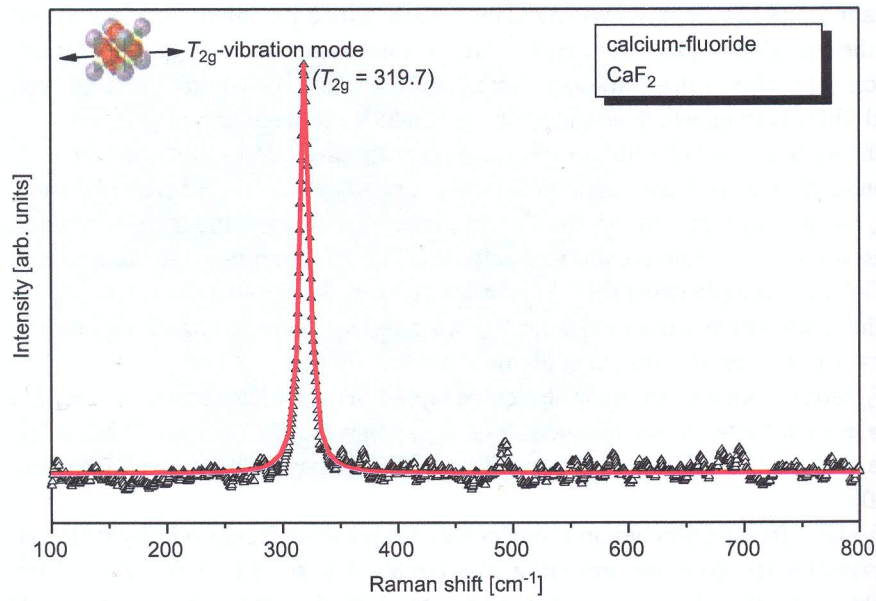


Figure 15.14: Raman spectrum of CaF₂ single crystals, recorded at room temperature.

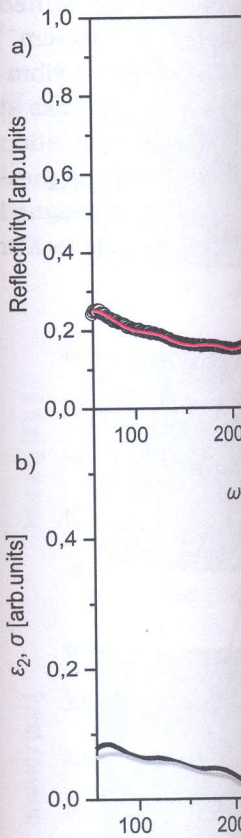


Figure 15.15: IR spectrum of CaF₂.

The number of mechanical frequencies, ν_{ILO} and ν_{ILO} , respectively, and ϵ_{∞} is

As a result of the somewhat higher than active modes are allowed that the main reflectivity result of a two-phonon metric fluorite-structure, actively high damping 130 cm⁻¹ could be caused by point <100>. Kramers and $\omega_{\text{LO}} = 475$ cm⁻¹, in

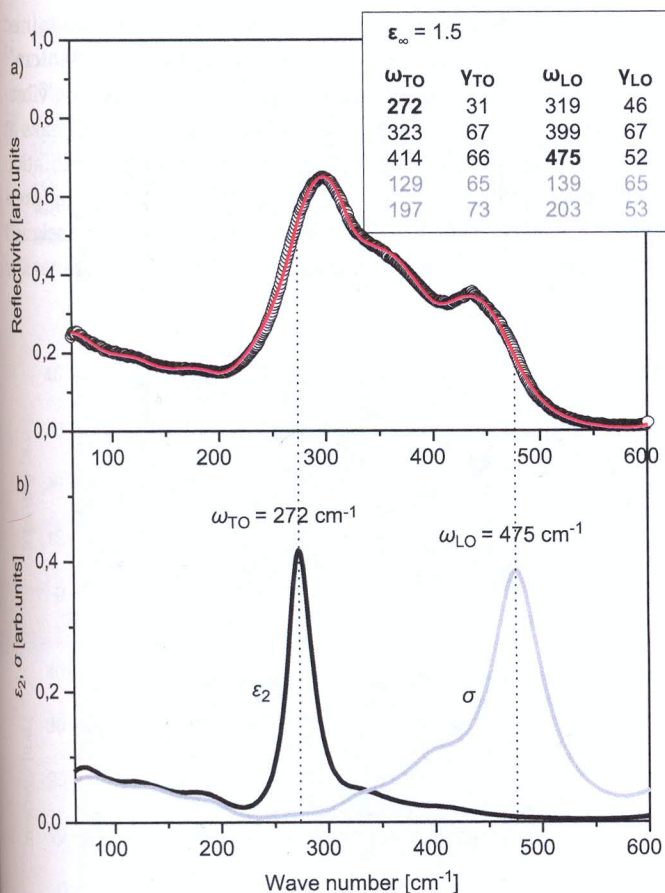


Figure 15.15: IR spectrum of CaF₂ single crystals, recorded at room temperature.

The number of modes is n , ω_{jLO} and ω_{jTO} are the longitudinal and transverse optical frequencies, γ_{jLO} and γ_{jTO} denote longitudinal and transverse damping constants, respectively, and ϵ_∞ is the dielectric constant (permittivity) at high frequency.

As a result of the best fit we obtained the $\omega_{TO} = 272 \text{ cm}^{-1}$ and $\omega_{LO} = 475 \text{ cm}^{-1}$, somewhat higher than in Ref [63]. (TO/LO = 257/463). In pure CaF₂, only two infrared active modes are allowed by the crystal symmetry (split TO-LO mode), but we see that the main reflectivity band of CaF₂ exhibits a feature centered about 360 cm^{-1} as a result of a two-phonon combination. This feature has been observed in all stoichiometric fluorite-structured crystals [64]. There are two additional weak modes with relatively high dampings in the range of low energies. We suppose that mode about 130 cm^{-1} could be caused by impurities and about 200 cm^{-1} is a TO-mode from the X point $\langle 100 \rangle$. Kramers-Krönig analysis of far-IR reflectance data gives $\omega_{TO} = 272 \text{ cm}^{-1}$ and $\omega_{LO} = 475 \text{ cm}^{-1}$, in accordance with fitting procedure (Figure 15.15b).

FTIR transmission was measured in order to check the purity of the obtained CaF_2 . As shown in Figure 15.16, the sharp peaks of the absorption at $2,854\text{ cm}^{-1}$ and $2,936\text{ cm}^{-1}$ are assigned to the symmetric and antisymmetric stretching vibration of $-\text{CH}_2$ groups [65]. Also, the spectrum shows two broad IR absorption peaks at $\sim 3,432\text{ cm}^{-1}$ and $1,628\text{ cm}^{-1}$ are assigned to the symmetrically stretching vibration and antisymmetric stretching vibration of hydroxyl groups $-\text{OH}$, implying the presence of H_2O molecules [66]. The peak at 671 cm^{-1} in the FTIR spectrum was assigned to the Ca-F stretching vibration of CaF_2 [67]. The band at $\sim 2,357\text{ cm}^{-1}$ is due to KBr pellets used for recording FTIR spectrum [68].

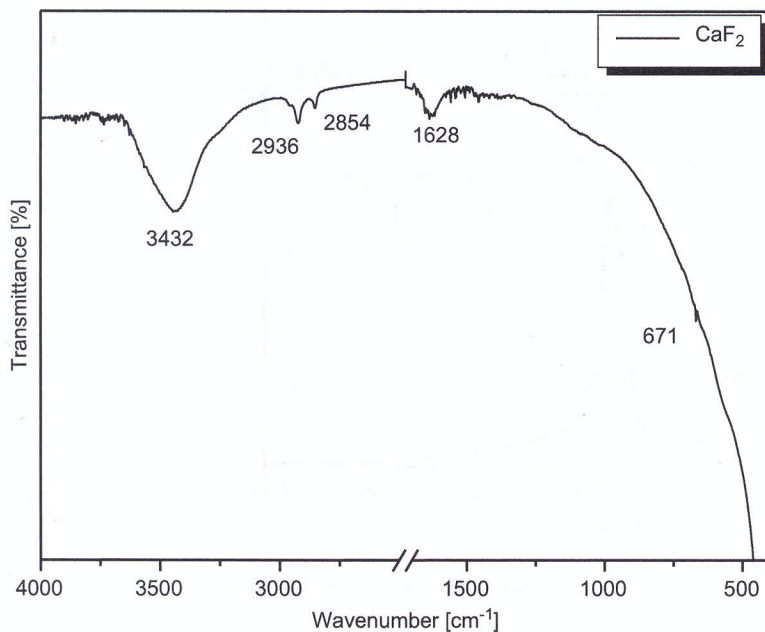


Figure 15.16: FTIR spectrum of CaF_2 .

We have measured the photoluminescence response of the CaF_2 crystal sample for various excitation wavelengths and different angles of excitation beam. The streak image of the fluorescence emission spectrum of CaF_2 is presented in Figure 15.17a. The photoluminescence response was very small; see Figure 15.17a where a typical optical response of sample is presented. Although the streak images were acquired in photon counting mode using a very large number of expositions (20,000), very small number of photons were counted. The vertical axis in Figure 15.17a corresponds to the fluorescence development in time domain of 200 ns. The beginning of the vertical axis is cut off in order to avoid undesirable part of the spectra (excitation at 320 nm and second harmonic of Nd:YAG laser at 532 nm).

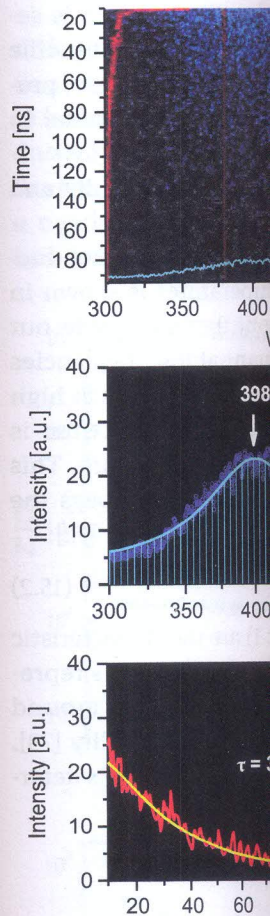


Figure 15.17: (a) Streak image of CaF_2 crystal as a function of time.

Enlarged integrated... Our pure sample of CaF_2 out in [69] this band might perhaps could be characterized by the occurrence of defects in crystal structure [69], so the luminescence structure described in [69] are doped with Ag, Eu, Tb, applications where high purity is not welcomed character.

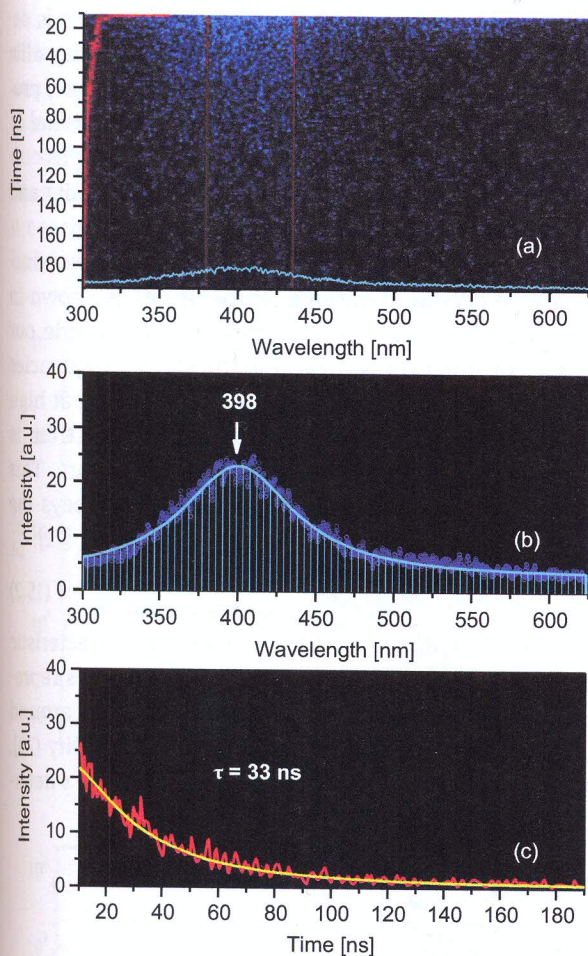


Figure 15.17: (a) Streak image of the fluorescence spectra of CaF_2 crystal. (b) Fluorescence spectra of CaF_2 crystal as a function of wavelength (integrated profile). (c) Fluorescence spectra of CaF_2 crystal as a function of time (integrated profile) and fitted curve.

Enlarged integrated profile of the fluorescence of CaF_2 is presented in Figure 15.17b. Our pure sample of CaF_2 crystal shows a broad band in 300–500 nm range. As pointed out in [69] this band might be induced due to the formation of color centers. These centers perhaps could be created by oxygen defects within the host of CaF_2 . However, the occurrence of defects in crystal is very rare compared to the nanostructures described in [69], so the luminescence of our sample is very weak compared to the luminescence of structure described in [69]. To obtain good luminescence response, the samples of CaF_2 are doped with Ag, Eu, Tb, Cu or Dy [69, 70]. However, CaF_2 crystal is usually used in applications where high optical transmission is needed and photoluminescence is not welcomed characteristics [71].

Fluorescence line profile (fluorescence decay) from image Figure 15.17a is selected using the integration process in region from 340 nm to 460 nm. That profile is fitted using High Performance Digital Temporal Analyzer (HPD-TA) software, provided by Hamamatsu. Fluorescence decay and fitted curve are shown together in Figure 15.17c. The obtained lifetime is 33 ns ($\chi^2 = 1.07$).

The properties of the crystal, such as density of dislocations, crystallinity and impurities concentrations, determine the optical quality.

The frequency dependence of the AC electrical conductivity, that is, conductivity spectra for studied CaF₂ single crystal at various temperatures is shown in Figure 15.18. These plots indicate the existence of two contributions inside our sample. Namely, DC conductivity contribution is predominant at low frequencies and high temperatures, whereas the frequency-dependent term dominates at high frequencies. Moreover, the observed dispersion in the conductivity spectrum is shifted toward the higher frequency side with the increase of temperature. This variation of AC conductivity with frequency at different temperatures obeys the power law given by the empirical formula (eq. (15.2)) proposed by Jonscher [72]:

$$\sigma_{AC}(\omega) = A\omega^s \tag{15.2}$$

where ω is the angular frequency of AC field. A and s ($0 \leq s \leq 1$) are the characteristic parameters which are temperature dependent. The Jonscher's coefficient s represents the degree of interaction between mobile ions with the lattices around them, and the prefactor parameter A determines the strength of polarizability [73]. In general, the nature of the temperature dependence of frequency exponent s determines the AC conduction mechanism in the material [43].

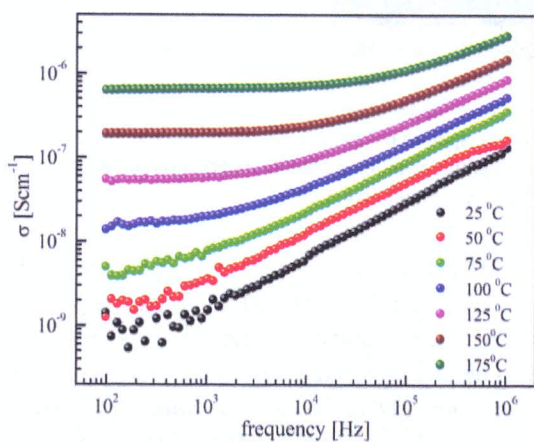


Figure 15.18: Frequency dependence of AC conductivity for CaF₂ single crystal at different temperatures.

Changes in the real different temperatures f... ticed that the magnitude in both applied frequen... ductivity of the CaF₂ sa... the temperature-depend... a nearly negative slop... low-frequency relaxati...

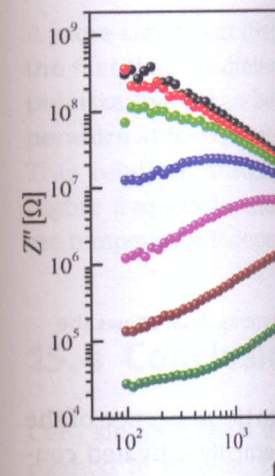
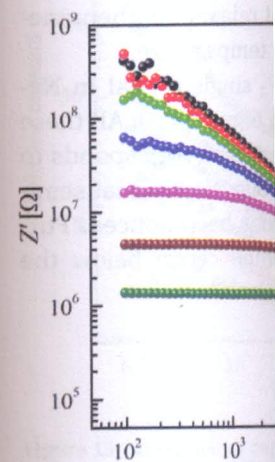


Figure 15.19: The variation of impedance with frequency a...

Changes in the real and imaginary part of complex impedance with frequency at different temperatures for CaF_2 single crystal are shown in Figure 15.19. It can be noticed that the magnitude of part of complex impedance (Z') decreases with an increase in both applied frequency and temperature, indicating an increase in AC electrical conductivity of the CaF_2 sample with increasing frequency and temperature. In addition, the temperature-dependent Z' shows a plateau on the low frequency side followed by a nearly negative slope on the high-frequency side, indicating a crossover from low-frequency relaxation behavior to high-frequency dispersion phenomenon.

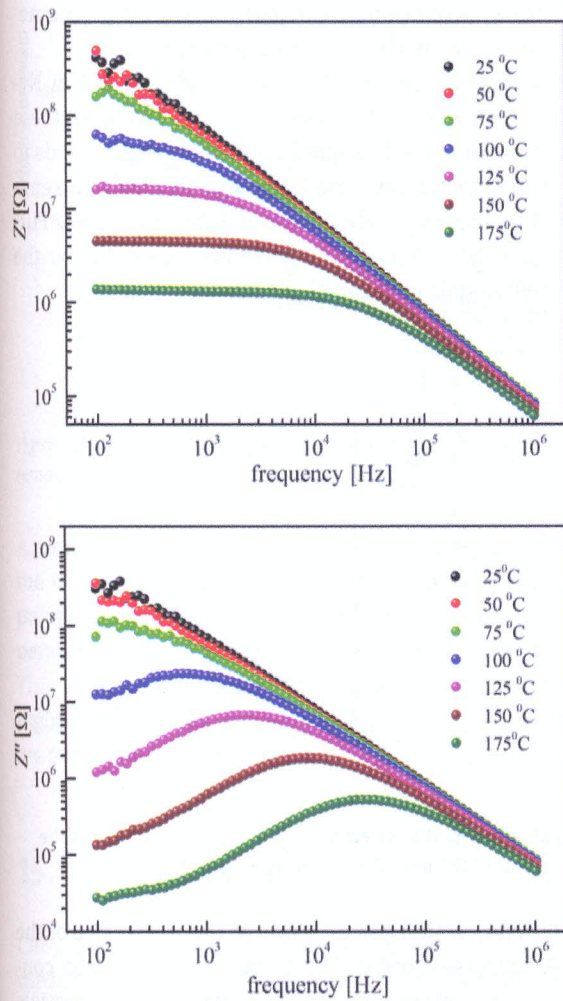


Figure 15.19: The variation of real part (above) and imaginary part (below) of the complex impedance with frequency at measured temperatures for CaF_2 single crystal.

This segment of nearly constant real impedance becomes dominant with increasing temperature, suggesting strengthened relaxation behavior [74].

The imaginary part of complex impedance (Z'') initially increases, reaches a peak and then decreases continuously with increasing frequency at all temperatures. It is evident that the Z'' spectrum of CaF_2 is characterized by the appearance of only one peak at a certain frequency that is called relaxation frequency. This suggests that a single relaxation process dominates over the conduction mechanism in synthesized CaF_2 . As the temperature rises the magnitude of observed peak in Z'' spectrum decreases considerably with the peak shift towards higher-frequency side. Such behavior indicates the presence of temperature-dependent electrical relaxation phenomenon and that the relaxation time decreases with increasing temperature.

The representation of complex impedance data for CaF_2 single crystal in Nyquist/Cole-Cole plot at different temperatures is illustrated in Figure 15.20. All these plots are characterized by the presence of a single semicircle, which corresponds to the bulk effects and indicates that the material is homogeneous. No residual semicircle at low frequencies attributed to the electrode effects has been noticed. Further, impedance spectra show depressed semicircles with their center below the real axis, which points to the non-Debye type of relaxation [75].

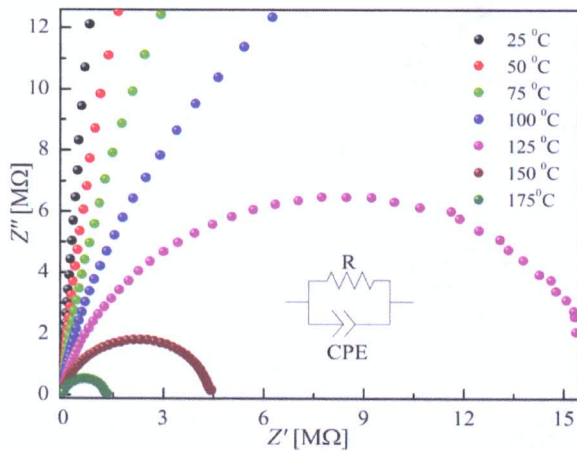


Figure 15.20: Impedance spectra of CaF_2 single crystal at selected temperatures. *Inset* shows the proposed equivalent circuit model for analysis of the impedance data.

In addition, the radius of the semicircles, which corresponds to the resistance of the material, decreases as temperature increases, indicating a thermally activated conduction mechanism in studied CaF_2 . It is well known that in single crystal materials this kind of impedance response can be interpreted by means of an equivalent electrical circuit model consisting of one parallel RC element [76]. But taking into account the observed non-ideal Debye type behavior of sample, it is usual that the

constant phase element insert of Figure 15.20.

The effect of applied single crystal at different temperatures. The analysis of the graph shows that with increasing frequency, exhib

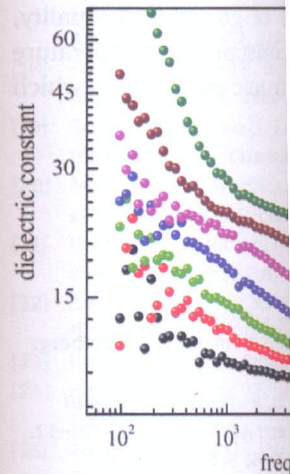


Figure 15.21: Frequency dependence of dielectric constant at different temperatures.

A more significant dispersion is observed at low frequencies. This relatively insignificant dispersion at higher frequencies can be attributed to the fact that the dielectric constant is temperature independent.

15.4 Conclusions

CaF_2 single crystals in dielectric method in vacuum. The crystals were annealed and bulk crystal CaF_2 . The annealing time was 3 h, and the temperature of annealing was for 1–3 h. Number of disloc

constant phase element (CPE) is used instead of ordinary capacitor as shown in the insert of Figure 15.20.

The effect of applied electric field frequency on the dielectric constant of CaF_2 single crystal at different temperatures is represented in Figure 15.21. It is clear from the analysis of the graph that dielectric constant decreases continuously with increasing frequency, exhibiting a normal dielectric behavior [77].

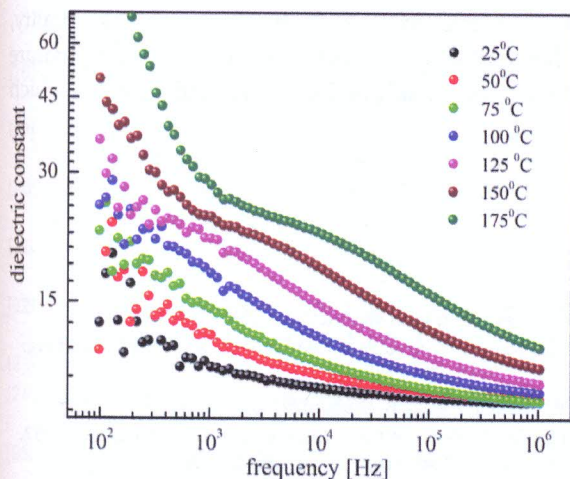


Figure 15.21: Frequency dependence of dielectric constant for CaF_2 single crystal at different temperatures.

A more significant dispersion in a low-frequency region can be explained based on the fact that the dielectric constant, in general, is directly related to the dielectric polarization. It can be observed that the variation of dielectric constant with temperature at low frequencies is much more pronounced than at higher frequencies. This relatively insignificant variation of dielectric constant with temperature at higher frequencies can be ascribed to the atomic and electronic polarizations which are temperature independent.

15.4 Conclusions

CaF_2 single crystals in diameter of 20 mm are obtained by the vertical Bridgman method in vacuum. The crystal growth rate was 6.0 mm h^{-1} . In order to eliminate stresses, crystals were annealed. The process of annealing was carried out on the plate and bulk crystal CaF_2 . The temperature of annealing of the plate was at $1,000 \text{ }^\circ\text{C}$ for 3 h, and the temperature of annealing of the bulk crystal was at $1,000 \text{ }^\circ\text{C}$ and $1,080 \text{ }^\circ\text{C}$ for 1–3 h. Number of dislocations is of the order of 5×10^4 – 2×10^5 per cm^2 . The Raman

T_{2g} optical mode at 319.7 cm^{-1} was observed. Kramers-Krönig analysis of the far-IR reflectance data for fluorite structure, as well as the fitting procedure, gave the same values for IR modes: $\omega_{TO} = 272\text{ cm}^{-1}$ and $\omega_{LO} = 475\text{ cm}^{-1}$. The FTIR transmission spectra indicate that there are some amounts of $-\text{CH}_2$, $-\text{OH}$ or water molecules and organic groups adhering to the surfaces. Photoluminescence intensity of the obtained crystal is very low, which is an advantage for applications where high optical transmission is needed. Based on our work and observations during the experiment, it could be concluded that the obtained transparent single crystal CaF_2 is of good optical quality, which was the goal of our work. The variation of dielectric constant with temperature at higher frequencies can be ascribed to the atomic and electronic polarizations which are temperature independent.

References

- [1] Brice JC. *Crystal Growth Processes*. New York: John Wiley&Sons, 1986.
- [2] Dhanaraj G, Byrappa K, Prasad V, Dudley M. *Handbook of Crystal Growth*. Berlin Heidelberg: Springer-Verlag, 2010.
- [3] Lazarević ZŽ, Kostić S, Romčević MJ, Trajić J, Hadžić B, Stojanović D, Romčević NŽ. Study of $\text{Bi}_{12}\text{SiO}_{20}$ single crystals obtained by Czochralski method. *Optoelectr Adv Mat* 2011, 5, 150–52.
- [4] Lazarević ZŽ, Mihailović P, Kostić S, Romčević MJ, Mitrić M, Petričević S, Radunović J, Petrović-Damjanović M, Gilić M, Romčević NŽ. Determination of magneto-optical quality and refractive index of bismuth germanium oxide single crystals grown by Czochralski technique. *Opt Mater* 2012, 34, 1849–59.
- [5] Petrović M, Romčević N, Romčević M, Stanišić G, Vasiljević-Radović D, Trajić J, Lazarević Z, Kostić S. Spectroscopy characterization of MnDe nanoclusters randomly distributed in HgMnTe single crystal. *J Cryst Growth* 2012, 338, 75–79.
- [6] Lazarević ZŽ, Kostić S, Radojević V, Romčević M, Hadžić B, Trajić J, Romčević NŽ. Spectroscopy study of $\text{Bi}_{12}\text{GeO}_{20}$ single crystals. *Optoelectr Adv Mat* 2013, 7, 58–61.
- [7] Kostić S, Lazarević ZŽ, Radojević V, Milutinović A, Romčević M, Romčević NŽ, Valčić A. Study of structural and optical properties of YAG and Nd: YAG single crystals. *Mater Res Bull* 2015, 63, 80–87.
- [8] Tsai RY, Shiau SC, Lin D, Ho FC, Hua MY. Ion-assisted codeposition of CaF_2 -rich CaF_2 - TiO_2 composites as infrared-transmitting films. *Appl Opt* 1999, 38, 5452–57.
- [9] Wang H, Liu R, Chen K, Shi X, Xu Z. Electrodeposition and characterization of CaF_2 and rare earth doped CaF_2 films. *Thin Solid Films* 2011, 519, 6438–42.
- [10] Fujihara S, Kadota Y, Kimura TJ. Role of organic additives in the sol-gel synthesis of porous CaF_2 anti-reflective coatings. *Sol-Gel Sci Technol* 2002, 24, 147–51.
- [11] Hull AW. The crystal structure of calcium. *Phys Rev* 1921, 17, 42.
- [12] Sharonov MY, Zhmurova ZI, Krivandina EA, Bystrova AA, Buchinskaya II, Sobolev BP. Spectroscopic properties of nonstoichiometric multicomponent fluoride crystals with fluorite structure doped with Pr^{3+} ions. *Opt Commun* 1996, 124, 558–67.
- [13] Petit V, Doualan JL, Camy P, Menard V, Moncorge R. CW and tunable laser operation of Yb^{3+} doped CaF_2 . *Appl Phys B* 2004, 78, 681–84.
- [14] Lucca A, Debourg G, Moncorge R. High-power laser operation of CaF_2 crystals. *Opt Commun* 1999, 161, 2767–69.
- [15] Stouwdam JW, Rauwerdink JA, van der Stoep J, van der Vliet A. Energy transfer to visible light emission from CaF_2 crystals. *Opt Commun* 2007, 180, 100–104.
- [16] Michalet X, Pinaud B, Dubois V, S. Quantum dots for single-photon emission. *Opt Commun* 2007, 180, 105–109.
- [17] Sivakumar S, Frank CW. Single-photon source from a CaF_2 crystal. *Am Chem Soc* 2007, 129, 1234–1235.
- [18] Xu X, Ling L, Wang L. CaF_2 crystal for dental composite. *J Appl Phys* 2007, 101, 043501.
- [19] Samuel P, Ishizawa T. Growth of transparent CaF_2 crystals. *J Cryst Growth* 2007, 301, 1–10.
- [20] Molchanova A, Friebohn H. Growth of large CaF_2 crystals. *J Cryst Growth* 2007, 301, 11–16.
- [21] Paraschiva M, Nicolae M. Growth of CaF_2 crystals. *Acta Phys* 2007, 101, 043501.
- [22] Senguttuvan N, Aoshima T. Growth of fluoride single crystals. *J Cryst Growth* 2007, 301, 17–22.
- [23] Ikesue A, Aung YL. Growth of fluoride single crystals. *J Cryst Growth* 2007, 301, 23–28.
- [24] Hatch SE, Parsons V. Growth of fluoride single crystals. *J Cryst Growth* 1964, 5, 153–54.
- [25] Popov PA, Dykel'skiy V, Basiev TT. Thermal stability of CaF_2 crystals. *J Cryst Growth* 2007, 301, 29–34.
- [26] Kotz J, Treichel P, T. Growth of fluoride single crystals. *J Cryst Growth* 1970, 3, 492–99.
- [27] Tilley RJD. *Crystals*. New York: Kluwer Academic, 1996.
- [28] Elcombe MM, Pryor W. Growth of fluoride single crystals. *J Cryst Growth* 1970, 3, 492–99.
- [29] Elliott RJ, Hayes W. Studies of effects of fluoride crystals. *J Cryst Growth* 1970, 3, 492–99.
- [30] Mead DG, Wilkinson J. Growth of fluoride single crystals. *J Cryst Growth* 1970, 3, 492–99.
- [31] Kaiser W, Spitzer W. Growth of fluoride single crystals. *J Cryst Growth* 1970, 3, 492–99.
- [32] Lowndes RP. Anharmonic vibrations in CaF_2 . *J Cryst Growth* 1970, 3, 492–99.
- [33] Hisano K. Thermal stability of CaF_2 crystals. *J Cryst Growth* 1970, 3, 492–99.
- [34] Luković D, Nikolić P. Growth of fluoride single crystals. *J Cryst Growth* 1970, 3, 492–99.
- [35] Nikolić PM, Vujatović G, Nikolić N. Thermal stability of CaF_2 crystals. *J Cryst Growth* 1970, 3, 492–99.
- [36] Xu J, Shi M, Lu B, Li. Growth of fluoride single crystals. *J Cryst Growth* 1970, 3, 492–99.
- [37] Stepanov IV, Feofilov SI. Growth of fluoride single crystals. *J Cryst Growth* 1970, 3, 492–99.
- [38] Molev GV, Bozhevolna. Growth of fluoride single crystals. *J Cryst Growth* 1970, 3, 492–99.

- [14] Lucca A, Debourg G, Jacquemet M, Druon F, Balembos F, Georges P, Camy P, Doualn JL, Moncorge R. High-power diode-pumped Yb^{3+} : CaF_2 femtosecond laser. *Opt Lett* 2004, 29, 2767–69.
- [15] Stouwdam JW, Raudsepp M, van Veggel FCJM. Colloidal nanoparticles of LaVO_4 : Energy transfer to visible and near-infrared emitting lanthanide ions. *Langmuir* 2005, 21, 7003–08.
- [16] Michalet X, Pinaud F, Bentolila L, Tsay J, Doose S, Li J, Sundaresan G, Wu A, Gambhir S, Weiss S. Quantum dots for live cells, in vivo imaging, and diagnostics. *Science* 2005, 307, 538–44.
- [17] Sivakumar S, Frank C, van Veggel JM, May PS. Bright white light through up-conversion of a single NIR source from sol-gel-derived thin film made with Ln^{3+} -doped LaF_3 nanoparticles. *J Am Chem Soc* 2007, 129, 620–25.
- [18] Xu X, Ling L, Wang R, Burgess JO. Formation and characterization of a novel fluoride-releasing dental composite. *Dent Mater* 2006, 22, 1014–23.
- [19] Samuel P, Ishizawa H, Ezura Y, Ueda KI, Moorthy Babu S. Spectroscopic analysis of Eu doped transparent CaF_2 ceramics at different concentration. *Opt Mater* 2011, 33, 735–37.
- [20] Molchanova A, Friedricha J, Wehrhan G, Müller G. Study of the oxygen incorporation during growth of large CaF_2 -crystals. *J Cryst Growth* 2005, 273, 629–37.
- [21] Paraschiva M, Nicoara I, Stef M, Bunoiu OM. Distribution of Pb^{2+} ions in PbF_2 -doped CaF_2 crystals. *Acta Phys Pol A* 2010, 117, 466–70.
- [22] Senguttuvan N, Aoshima M, Sumiya K, Ishibashi H. Oriented growth of large size calcium fluoride single crystals for optical lithography. *J Cryst Growth* 2005, 280, 462–66.
- [23] Ikesue A, Aung YL. Ceramic laser materials. *Nat Photonics* 2008, 2, 721–27.
- [24] Hatch SE, Parsons WF, Weagley RJ. Hot-pressed polycrystalline CaF_2 : Dy^{2+} laser. *Appl Phys Lett* 1964, 5, 153–54.
- [25] Popov PA, Dykel'skii KV, Mironov IA, Smirnov AN, Smolyanskii PL, Fedorov PP, Osiko VV, Basiev TT. Thermal conductivity of CaF_2 optical ceramic. *Doklady Physics* 2007, 52, 7–9.
- [26] Kotz J, Treichel P, Townsend J. *Chemistry and Chemical Reactivity, Enhanced Edition*. New York: Kluwer Academic/Plenum Publishers, Vol. 3, 2002.
- [27] Tilley RJD. *Crystals and crystal Structures*. England: John Wiley&Sons Ltd., 2006.
- [28] Elcombe MM, Pryor AW. The lattice dynamics of calcium fluoride. *J Phys C: Solid State Phys* 1970, 3, 492–99.
- [29] Elliott RJ, Hayes W W, Kleppmann WG, Rushworth AJ, Ryan JF. Experimental and theoretical studies of effects of anharmonicity and high-temperature disorder on Raman scattering in fluorite crystals. *Proc R Soc A* 1978, 360, 317–45.
- [30] Mead DG, Wilkinson GR. The temperature dependence of the Raman spectra of some alkaline earth crystals with the fluorite structure. *J Phys C: Solid State Phys* 1977, 10, 1063–70.
- [31] Kaiser W, Spitzer WG, Kaiser RH, Howarth LE. Infrared Properties of CaF_2 , SrF_2 , and BaF_2 . *Phys Rev* 1962, 127, 1950.
- [32] Lowndes RP. Anharmonicity in the alkaline earth fluorides. *J Phys C* 1971, 4, 3083.
- [33] Hisano K. Thermal emission spectra of CaF_2 thin films. *Infrared Phys* 1985, 25, 415–21.
- [34] Luković D, Nikolić PM, Vujatović S, Savić S, Urošević D. Photoacoustic properties of single crystal $\text{PbTe}(\text{Ni})$. *Sci Sinter* 2007, 39, 161–67.
- [35] Nikolić PM, Vujatović SS, Ivetić T, Nikolić MV, Cvetković O, Aleksić OS, Blagojević V, Branković G, Nikolić N. Thermal diffusivity of single crystal $\text{Bi}_{0.9}\text{Sb}_{0.1}$. *Sci Sinter* 2010, 42, 45–50.
- [36] Xu J, Shi M, Lu B, Li X, Wu A. Bridgman growth and characterization of calcium fluoride crystals. *J Cryst Growth* 2006, 292, 391–94.
- [37] Stepanov IV, Feofilov PP. Artificial fluorite. In: *Rost Kristalov*. Vol. I, Moscow, Russia: Akademia Nauk SSSR, 1957, 229. in Russian.
- [38] Molev GV, Bozhevolnov VE, Korobkov VI, Karelin VV. On the distribution of Sc^{3+} impurity in directed crystallization of fluorite from the melt. *J Cryst Growth* 1973, 19, 117–21.

- [39] Recker K, Leckebusch R. Zur züchtung von CaF_2 -UND $\text{CaF}_2(\text{U})$ -einkristallen aus der dampfphase. *J Crys Growth* 1971, 9, 274–80.
- [40] Guggenheim H. Growth of highly perfect fluoride single crystals for optical masers. *J Appl Phys* 1963, 34, 2482–85.
- [41] Elswie HI, Kostić S, Radojević V, Romčević NŽ, Hadžić B, Trajić J, Lazarević ZŽ. Growth, characterization and optical quality of calcium fluoride single crystals grown by the Bridgman method. *Optoelectr Adv Mat* 2016, 10, 522–25.
- [42] Elswie HI, Lazarević ZŽ, Radojević V, Gilić M, Rabasović M, Šević D, Romčević NŽ. The Bridgman method growth and spectroscopic characterization of calcium fluoride single crystals. *Sci Sinter* 2016, 48, 333–41.
- [43] Čajko KO, Sekulić DL, Lukić-Petrović S, Šiljegović MV, Petrović DM. Temperature-dependent electrical properties and impedance response of amorphous $\text{Ag}_x(\text{As}_{40}\text{S}_{30}\text{Se}_{30})_{100-x}$ chalcogenide glasses. *J Mater Sci – Mater El* 2017, 28, 120–28.
- [44] Gerward L, Olsen JS, Steenstrup S, Malinowski M, Åsbrink S, Waskowska A. X-ray diffraction investigations of CaF_2 at high pressure. *J Appl Crystallogr* 1992, 25, 578–81.
- [45] Hong B-C, Kawano K. Luminescence studies of the rare earth ions-doped CaF_2 and MgF_2 films for wavelength conversion. *J Alloys Compd* 2006, 408-412, 838–41.
- [46] Alharbi ND. Size controlled CaF_2 nanocubes and their dosimetric properties using photoluminescence technique. *J Nanomaterials* 2015, 16, 302–10.
- [47] Fujihara S, Kadota Y, Kimura T. Role of organic additives in the sol-gel synthesis of porous CaF_2 anti-reflective coatings. *J Sol-Gel Sci Technol* 2002, 24, 147–54.
- [48] Biswas S, Kar S, Chaudhuri S. Growth of different morphological features of micro and nanocrystalline manganese sulfide via solvothermal process. *J Cryst Growth* 2007, 299, 94–102.
- [49] Scholz G, Dörfel I, Heidemann D, Feist M, Stösser R. Nanocrystalline CaF_2 particles obtained by high-energy ball milling. *J Solid State Chem* 2006, 179, 1119–28.
- [50] Wang Y, Zhang LA, Shang S, Kui Z, Liu, Chen LQ. Accurate calculations of phonon dispersion in CaF_2 and CeO_2 . *Phys Rev B* 2013, 88, 024304.
- [51] Schmalzl K, Strauch D, Schober H. Lattice-dynamical and ground-state properties of CaF_2 studied by inelastic neutron scattering and density-functional methods. *Phys Rev B* 2003, 68, 144301.
- [52] Chang RK, Lacina B, Pershan PS. Raman scattering from mixed crystals $(\text{Ca}_x\text{Sr}_{1-x})\text{F}_2$ and $(\text{Sr}_x\text{Ba}_{1-x})\text{F}_2$. *Phys Rev Lett* 1966, 17, 755–58.
- [53] Ferraro JR, Horan H, Quattrochi A. Pressure dependence of the infrared-active optical phonon modes in alkaline-earth fluorides. *J Chem Phys* 1971, 55, 664–66.
- [54] Oostra DJ, den Hartog HW. Raman spectroscopy of superionic solid solutions of alkaline-earth and rare-earth halides. *Phys Rev B* 1984, 29, 2423–32.
- [55] Ricci PC, Casu A, de Giudici G, Scardi P, Anedda A. Phonon confinement effect in calcium fluoride nanoparticles. *Chem Phys Lett* 2007, 444, 145–48.
- [56] Kaminskii AA, Bagayev SN, Eichler HJ, Rhee H, Ueda K, Takaichi K, Oka K, Shibata H, Hatanaka Y, Matsumoto Y. Steady-state picosecond stimulated Raman scattering in two host-crystals for Ln^{3+} and Ln^{2+} lasants. *Laser Phys Lett* 2006, 8, 385–91.
- [57] Tu J, FitzGerald SA, Campbell JA, Sievers AJ. Glass-like properties observed in low-frequency Raman scattering of mixed fluoride crystals. *J Non-Cryst Solids* 1996, 203, 153–58.
- [58] Su L, Xu J, Yang W, Jiang X, Dong Y. Raman spectra of undoped and uranium doped CaF_2 single crystals. *Chinese Optics Letters* 2005, 3, 219–21.
- [59] Russell JP, The Raman spectrum of calcium fluoride, *Proceedings of the Physical Society*, vol. 85, pp. 194–96, 1965.
- [60] Russell JP. Raman spectroscopy using a gas laser. *J Phys France* 1965, 26, 620–26.
- [61] Gervais F. *Infrared and Millimeter Waves*. Vol. 8, New York: Academic, 1983, 279–339.
- [62] Kadlec F, Simon P, Raimbou J. *J Phy Chem Solids* 1999, 60.
- [63] Ganesan S, Burstein E. Sele Fluorite structure and the in CaF_2 . *Journal de Physique* 1962, 127, 1950–54.
- [64] Kaiser W, Spitzer WG, Kaise *Rev* 1962, 127, 1950–54.
- [65] Song J, Zhi G, Zhang Y, Mei different doping concentrat
- [66] Zhou L, Chen D, Luo W, War CaF_2 nano-crystals prepared
- [67] Tahvildari K, Esmaeilpour M characterization. *Int J Nano*
- [68] Pandurangappa C, Lakshmi characterization of CaF_2 na
- [69] Singh VS, Joshi CP, Moharil of $\text{CaF}_2:\text{Eu}^{2+}$. Luminescence
- [70] Salah N, Alharbi ND, Habib activated by different eleme 10.1155/2015/136402.
- [71] Fairfield Crystal Technology
- [72] Jonscher AK. The “universal
- [73] Ben Said R, Louati B, Guida diphosphate. *Ionics* 2017, 2
- [74] Chen W, Zhu W, Tan OK, Ch spectroscopy of cobalt ferrit
- [75] Jlassi I, Sdiri N, Elhouichet $\text{P}_2\text{O}_5\text{-Li}_2\text{O-Al}_2\text{O}_3$ glass sys
- [76] Mirsaneh M, Furman E, Rya measurements of amorphou 112907.
- [77] Wanga J, Wanga CC, Li QJ, Y High-temperature relaxatio

- [62] Kadlec F, Simon P, Raimboux N. Vibrational spectra of superionic crystals $(\text{BaF}_2)_{1-x}(\text{LaF}_3)_x$. *J Phy Chem Solids* 1999, 60, 861–66.
- [63] Ganesan S, Burstein E. Selection rules for second order infrared and raman processes. II. Fluorite structure and the interpretation of the second order infrared and Raman spectra of CaF_2 . *Journal de Physique* 1965, 26, 645–48.
- [64] Kaiser W, Spitzer WG, Kaiser RH, Howarth LE. Infrared Properties of CaF_2 , SrF_2 , and BaF_2 . *Phys Rev* 1962, 127, 1950–54.
- [65] Song J, Zhi G, Zhang Y, Mei B. Synthesis and characterization of CaF_2 nanoparticles with different doping concentrations of Er^{3+} . *Nano-Micro Lett* 2011, 3, 73–78.
- [66] Zhou L, Chen D, Luo W, Wang Y, Yu Y, Liu F. Transparent glass ceramic containing Er^{3+} : CaF_2 nano-crystals prepared by sol-gel method. *Mater Lett* 2007, 61, 3988–90.
- [67] Tahvildari K, Esmaeilipour M, Ghamamy S, Nabipour H. CaF_2 nanoparticles: synthesis and characterization. *Int J Nano Dim* 2012, 2, 269–73.
- [68] Pandurangappa C, Lakshminarasappa BN, Nagabhusana BM. Synthesis and characterization of CaF_2 nanocrystals. *J Alloys Compd* 2010, 489, 592–95.
- [69] Singh VS, Joshi CP, Moharil SV, Muthalci PL, Dhopte SM. Modification of luminescence spectra of $\text{CaF}_2:\text{Eu}^{2+}$. *Luminescence* 2015, 30, 1101–05.
- [70] Salah N, Alharbi ND, Habib SS, Lochab SP. Luminescence properties of CaF_2 nanostructure activated by different elements. *J Nanomaterials* 2015, 16, 136402. DOI: <http://dx.doi.org/10.1155/2015/136402>.
- [71] Fairfield Crystal Technology, <http://www.fairfieldcrystal.com>.
- [72] Jonscher AK. The “universal” dielectric response. *Nature* 1977, 267, 673–79.
- [73] Ben Saïd R, Louati B, Guidara K. AC conduction mechanism of the zinc potassium diphosphate. *Ionics* 2017, 23, 2397–404.
- [74] Chen W, Zhu W, Tan OK, Chen XF. Frequency and temperature dependent impedance spectroscopy of cobalt ferrite composite thick films. *J Appl Phys* 2010, 108, 034101-034101-7.
- [75] Jlassi I, Sdiri N, Elhouichet H, Ferid M. Raman and impedance spectroscopy methods of $\text{P}_2\text{O}_5\text{-Li}_2\text{O-Al}_2\text{O}_3$ glass system doped with MgO . *J Alloys Compd* 2015, 645, 125–30.
- [76] Mirsaneh M, Furman E, Ryan JV, Lanagan MT, Pantano CG. Frequency dependent electrical measurements of amorphous GeSbSe chalcogenide thin films. *Appl Phys Lett* 2010, 96, 112907.
- [77] Wanga J, Wanga CC, Li QJ, Yu Y, Zhang J, Zheng J, Cheng C, Li YD, Wang H, Huang SG. High-temperature relaxations in CaF_2 single crystals. *Mater Sci Eng B* 2014, 188, 31–34.

Република Србија
МИНИСТАРСТВО ПРОСВЕТЕ,
НАУКЕ И ТЕХНОЛОШКОГ РАЗВОЈА
Комисија за стицање научних звања

Број: 660-01-00001/1398
08.07.2020. године
Београд

ИНСТИТУТ ЗА ФИЗИКУ			
ПРИМЉЕНО: 22. 07. 2020			
Рад.јед.	б р о ј	Арх.шифра	Прилог
0701	625/1		

На основу члана 22. став 2. члана 70. став 5. Закона о научноистраживачкој делатности ("Службени гласник Републике Србије", број 110/05, 50/06 – исправка, 18/10 и 112/15), члана 3. ст. 1. и 3. и члана 40. Правилника о поступку, начину вредновања и квантитативном исказивању научноистраживачких резултата истраживача ("Службени гласник Републике Србије", број 24/16, 21/17 и 38/17) и захтева који је поднео

Инстџитут за физику у Београду

Комисија за стицање научних звања на седници одржаној 08.07.2020. године, донела је

**ОДЛУКУ
О СТИЦАЊУ НАУЧНОГ ЗВАЊА**

Др Марџина Гилић

стиче научно звање
Виши научни сарадник

у области природно-математичких наука - физика

О Б Р А З Л О Ж Е Њ Е

Инстџитут за физику у Београду

утврдио је предлог број 1677/1 од 05.11.2019. године на седници Научног већа Института и поднео захтев Комисији за стицање научних звања број 1691/1 од 07.11.2019. године за доношење одлуке о испуњености услова за стицање научног звања *Виши научни сарадник*.

Комисија за стицање научних звања је по претходно прибављеном позитивном мишљењу Матичног научног одбора за физику на седници одржаној 08.07.2020. године разматрала захтев и утврдила да именована испуњава услове из члана 70. став 5. Закона о научноистраживачкој делатности ("Службени гласник Републике Србије", број 110/05, 50/06 – исправка, 18/10 и 112/15), члана 3. ст. 1. и 3. и члана 40. Правилника о поступку, начину вредновања и квантитативном исказивању научноистраживачких резултата истраживача ("Службени гласник Републике Србије", број 24/16, 21/17 и 38/17) за стицање научног звања *Виши научни сарадник*, па је одлучила као у изреци ове одлуке.

Доношењем ове одлуке именована стиче сва права која јој на основу ње по закону припадају.

Одлуку доставити подносиоцу захтева, именованој и архиви Министарства просвете, науке и технолошког развоја у Београду.

ПРЕДСЕДНИК КОМИСИЈЕ

Ђ. Јововић
Др Ђурђица Јововић,
научни саветник





**CHEMISTRY &
CHEMICAL
TECHNOLOGY**

CONFERENCE 2023 VILNIUS

CONFERENCE BOOK

**March 10, 2023
VILNIUS**

**THE CONFERENCE IS DEDICATED TO PROF. EDVARDAS
RAMANAUSKAS 100TH ANNIVERSARY**



Conference Book
International Conference
Chemistry and Chemical technology

CCT-2023

The conference is dedicated to prof. Edvardas Ramanauskas
100th anniversary

Copyright © 2023. Published by Vilnius University Press This is an Open Access article distributed under the terms of the Creative Commons Attribution Licence, which permits unrestricted use, distribution, and reproduction in any medium, provided the original author and source are credited.

<https://doi.org/10.15388/CCT.2023>

ISBN 978-609-07-0833-0 (Leidinio forma: Elektroninis - PDF)

Vilnius, Lithuania 2023

Effect of Deposition Cycles on the Properties of Copper Sulfide Thin Films Deposited by CBD

M. Gilić^{1,2}, R. Alaburdaitė³, E. Paluckienė³, N. Petrašauskienė^{3*}

¹Institute of Experimental Physics, Freie Universität Berlin, 14195 Berlin, Germany

²Institute of Physics Belgrade, 11080 Belgrade, Serbia

³Department of Physical and Inorganic Chemistry, Kaunas University of Technology, Radvilenu 19, LT-50254 Kaunas, Lithuania

*Corresponding author, e-mail: neringa.petrasauskiene@ktu.lt

The deposition of copper sulfide as a thin layer onto the surface of the polymer is a promising approach to obtain electrically conductive films. Flexible, transparent polymer substrate coated with copper sulfide is expected to be useful in many fields, for example, as reflectors for concentrating collectors, heat mirrors, and solar control coatings [1], as conductive substrates for deposition of metal and semiconductors [1, 2], as gas sensors functioning at temperatures close to room temperature [3].

The chemical bath deposition (CBD) technique has been used for the deposition of copper sulfide thin films on polypropylene (PP) substrates. The Cu_xS thin film deposition was carried out at room temperature using a mixture of 0.05 M CuCl_2 and 0.05 M $\text{Na}_2\text{S}_2\text{O}_3$ solutions for 16 h. The CBD process was carried out by varying cycles (1, 2 and 3 cycles) of deposition. The formed samples were annealed at 80 °C for 30 min.

The structure, surface morphology, and optical characterization of the deposited thin film indicated a strong relationship between the number of deposition cycles. The scanning electron microscope (SEM) showed a uniform morphology with randomly oriented nano-grains of the copper sulfide film at varying deposition cycles (Fig.1). The thin film morphology uniformly covers the PP substrate and shows a smooth surface. Additionally, the films prepared by CBD with 3 cycles were found quite dense with good crystallinity and no holes, homogenous surface, adhesion to the substrate, compact, and improved in grain size compared to copper sulfide films prepared with 2 cycles (Fig. 1.).

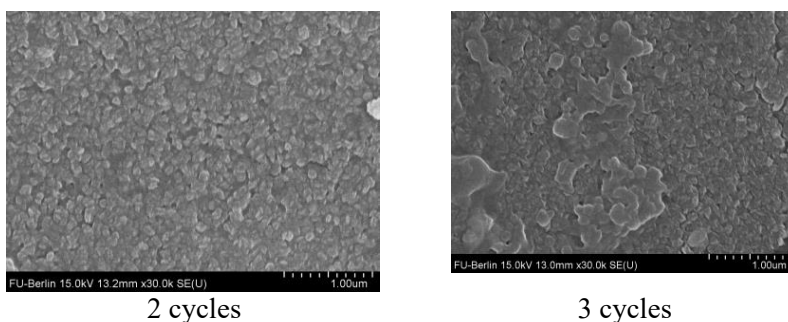


Fig. 1. Surface morphology of Cu_xS thin films prepared at different cycles

Analysis of Cu_xS thin films also was performed using X-ray diffraction analysis, ultraviolet-visible (UV-VIS) spectroscopy, and Raman after each deposition cycle. The electrical result of the thin films shows that resistivity decreases, while conductivity increases as the CBD cycle increases.

References

1. J. Cardoso et al, *Semicond. Sci. Technol.*, **16** (2001) 123-127.
2. M. T. S. Nair and P. K. Nair, *Semicond. Sci. Technol.*, **4** (1989) 191-199.
3. A. Galdikas et al, *Sensors Actuators B Chem.*, **67** (2000) 76-83.



BOOK OF ABSTRACTS

JELGAVA, LATVIA

SEPTEMBER 20-22, 2023

RAMAN ANALYSIS OF Cu_xS THIN FILMS DEPOSITED ON the SURFACE OF POLYPROPYLENE

Edita Paluckiene¹, Martina Gilić^{2,3}, Neringa Petrasauskiene¹

¹Department of Physical and Inorganic Chemistry, Kaunas University of Technology, Kaunas, Lithuania

²Institute of Experimental Physics, Freie Universität Berlin, Berlin, Germany

³Institute of Physics Belgrade, Belgrade, Serbia

Polypropylene (PP) is one of the most widely used thermoplastic polymers with great chemical, physical and mechanical properties. In this work, the preparation of electrically conductive $\text{Cu}_x\text{S}/\text{PP}$ films by deposition of copper sulfide from an aqueous solution onto a polypropylene film surface via chemical bath deposition method (CBD). Copper sulfide layers were deposited using a mixture of 0.05 M CuCl_2 and 0.05 M $\text{Na}_2\text{S}_2\text{O}_3$ solutions. The CBD process was carried out from 1 to 3 cycles at room temperature. The duration of each cycle was 16 hours.

In order to find the optimal technological conditions for the Cu_xS deposition process, the influence of deposition cycles was studied. Analysis of this material included studies of structure, morphology and electrical surface conductivity.

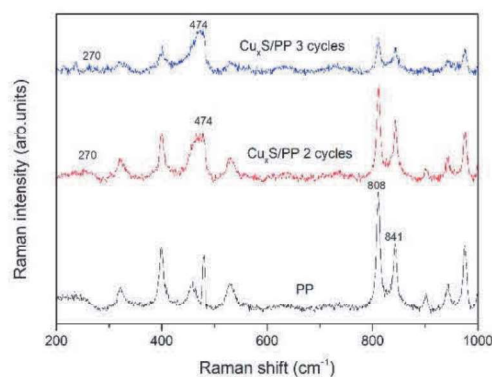


Fig. 1. Raman spectra of the $\text{Cu}_x\text{S}/\text{PP}$ thin films

Raman Spectroscopy is a non-destructive chemical analysis technique which provides detailed information about chemical structure, phase and polymorphy, crystallinity and molecular interactions of materials. Raman spectrum of PP 6 (Fig. 1) shows $\text{C}-\text{C}$ stretching at 808 cm^{-1} and 972 cm^{-1} , band at 841 cm^{-1} is related to rocking CH_2 , rocking at 972 cm^{-1} and 998 cm^{-1} corresponds to CH_3 vibrations [1]. As shown in Fig. 1, the typical Raman spectra copper sulfide film samples (deposited at 2 and 3 cycles) exhibit similar peak positions. The spectrum reveals a pronounced peak at 474 cm^{-1} , which is assigned to vibrational (stretching) modes from the covalent $\text{S}-\text{S}$ bonds [2] and a much weaker peak at about 270 cm^{-1} attributed to the $\text{Cu}-\text{S}$ bond vibration [2]. Therefore, the main attention was paid to the analysis of the intensity of the most intense Raman mode at 474 cm^{-1} . Raman analysis confirms the composition of the copper sulfide on the surface of PP films.

References

1. H. Tadokoro, M. Kobayashi, M. Ukita, K. Yasufuku, S. Murahashi. Normal Vibrations of the Polymer Molecules of Helical Conformation. V. Isotactic Polypropylene and Its Deuteroderivative // *J Chem Phys.* – 1965. – Vol. 42, P.1432.
2. Ishii M.; Shibata K.; Nozaki H. Anion Distributions and Phase Transitions in $\text{CuS}_{1-x}\text{Se}_x$ ($x = 0-1$) Studied by Raman Spectroscopy // *J. Solid State Chem.* – 1993. – Vol. 105 – P. 504–511.

ANALYSIS OF Cu_xS THIN FILM DEPOSITED ON SURFACE OF POLYAMIDE – RAMAN SPECTROSCOPY

Neringa Petrasauskiene¹, Martina Gilić², Edita Paluckiene¹

¹Department of Physical and Inorganic Chemistry, Kaunas University of Technology, Kaunas, Lithuania

²Institute of Experimental Physics, Freie Universität Berlin, Berlin, Germany

³Institute of Physics Belgrade, Belgrade, Serbia

The preparation of electrically conductive $\text{Cu}_x\text{S}/\text{PA}$ films by deposition of copper sulfide from an aqueous solution onto a polyamide film surface is reported in this paper.

Copper sulfide (Cu_xS) layers were deposited on the surface of polyamide via the chemical bath deposition method (CBD) at room temperature using a mixture of 0.05 M CuCl_2 and 0.05 M $\text{Na}_2\text{S}_2\text{O}_3$ solutions for 16 h. The CBD process was carried out by varying the number of cycles (1, 2 or 3 cycles) of deposition. The influence of deposition cycles was studied to determine the optimum condition for the deposition process. The analysis of this material included studies on the structure, morphology and electrical surface conductivity.

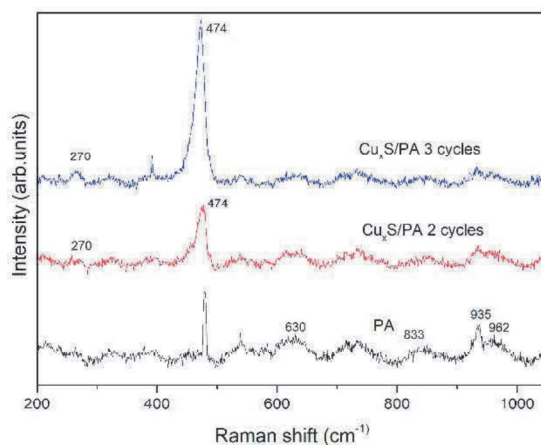


Fig. 1. Raman spectra of the $\text{Cu}_x\text{S}/\text{PA}$ thin films

Raman spectroscopy is a useful spectroscopic technique to study the crystal phase, crystallinity and vibrational properties of the films. Raman spectrum of pure PA 6 (Fig. 1) shows $C-C$ deformation mode at 630 cm^{-1} , band at 833 cm^{-1} is related to rocking CH_2 , while stretching mode of CH_2 is at 935 cm^{-1} , and 962 cm^{-1} corresponds to CO-NH vibrations [1]. As shown in Fig. 1, the Raman spectra of copper sulfide film samples (deposited at 2 and 3 cycles) exhibit similar peak positions. The spectrum reveals a pronounced peak at 474 cm^{-1} , which is assigned to vibrational (stretching) modes from the covalent S-S bonds [2] and a much weaker peak at about 270 cm^{-1} attributed to the Cu-S bond vibration [2]. Therefore, the main attention was paid to the analysis of the Raman intensity of the most intense mode at 474 cm^{-1} . Raman analysis confirms the composition of the copper sulfide on the surface of PA films.

References

6. Ferreiro V., Depecker C., Laureyns J., Coulon G. Structures and morphologies of cast and plastically strained polyamide 6 films as evidenced by confocal Raman microspectroscopy and atomic force microscopy // *Polymer*. – 2004. – Vol. 45, – P. 6013–6026.
7. Ishii M.; Shibata K.; Nozaki H. Anion Distributions and Phase Transitions in $\text{CuS}_{1-x}\text{Se}_x$ ($x = 0-1$) Studied by Raman Spectroscopy // *J. Solid State Chem.* – 1993. – Vol. 105 – P. 504–511.

Boosting Surface-Enhanced Raman Scattering by Ultrathin Golden Film on Bio-Photonic Crystals

Martina Gilic, Mohamed Ghobara, Louisa Reissig

Institute of Experimental Physics, Freie Universität Berlin, Arnimallee 14, 14195 Berlin, Germany
martina.gilic@fu-berlin.de

Abstract: Hybrid substrates based on three structurally distinct diatom biosilica coated with ultrathin uniform gold were utilized in SERS. The comparative analysis showed that substrates containing cylindrical *Aulacoseira sp.* valves achieved the enhancement up to 8-folds. © 2022 Gilic et al.

1. Introduction

Surface-enhanced Raman spectroscopy (SERS) is an outstanding tool for qualitative and quantitative analysis, with a sensitivity that enables the analyte detection down to a single-molecule level. In the core of this technique are the plasmonic active substrates that could couple the incoming laser light and free electrons within, which launches surface plasmon polaritons in case of a planar surface or localized surface plasmon resonance in case of nanoparticles [1,2]. Additional enhancement could be obtained through utilizing hybrid substrates that include photonic crystals (PCs) or resonant gratings, which leads to the coupling, *for instance*, of guided-mode resonance (GMR) with the surface plasmonic resonance and thus additionally increases SERS [2]. Diatoms are unicellular aquatic algae whose exoskeleton represents one of the exquisite examples of natural 2D photonic crystals. To the best of our knowledge, a few diatom species, mainly *Pinnularia*, have been used to fabricate hybrid substrates for SERS coated with either silver or gold NPs or rarely non-uniform thin films [3]. It has been suggested that diatom valves mainly contribute to the SERS through GMR [3, 4], but also with concentrating analyte molecules as well as nanoparticles on their surface and pore rims. However, coating the valves with nanoparticles or non-uniform golden films creates the hotspots without homogeneity for the SERS signal over the entire valve surface.

In this work, we aim to experimentally evaluate SERS enhancement and homogeneity obtained by hybrid substrates consisting of ultrathin uniform golden film (10 nm) coating the biosilica valves of three different diatom species of distinct structural features. The obtained results were supplemented by theoretical calculations.

2. Experimental work

The diatom monolayers of *Coscinodiscus radiatus* (CR), *Gomphonema parvulum* (GP), and *Aulacoseira sp.* (Aula) on glass substrates were coated with 10 nm golden film via physical vapor deposition, after applying a self-assembled monolayer of 3-mercaptopropyl trimethoxy silane to assure the thickness homogeneity. Scanning electron microscopy was obtained with Hitachi SU8030. Raman measurements were obtained on Horiba XploRA with 638nm laser line. Theoretical calculations were done with COMSOL 5.5 using the frequency domain method.

3. Main results and discussion

The uniformity of Au layer and fine structure of hybrid substrates were characterized with SEM. As can be seen from Fig. 1a, the gold is evaporated uniformly over the sample creating a smooth film with no signs of dewetting or voids. The 3 chosen valves differ significantly in terms of size, shape, and parameters. The GP (Fig.1b) has small 7 μm long oval valves, with rows of 0.1 μm pores with spacing 0.2 μm within a row. Aula has cylindrical valves of 15 μm diameter with a flat top surface, pore size of 0.3 μm , and pore spacing within a range of 0.6 – 1 μm (Fig.1c). Finally, CR has large circular valves of 100 μm and 3 pore layers, where the largest pore size is 1.2 μm (Fig.1d).

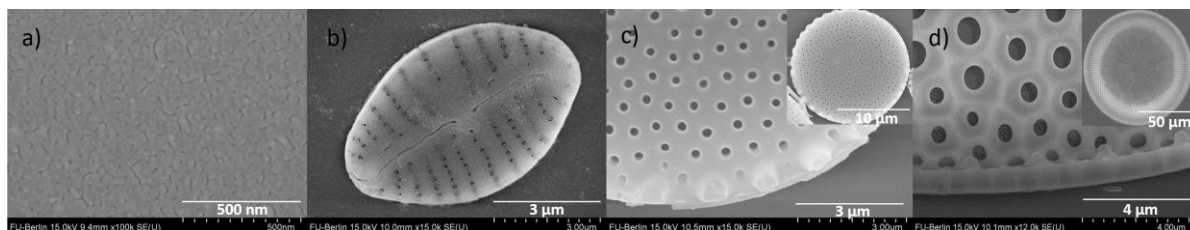


Fig. 1. SEM of the valves with the golden thin film. a) gold, b) *Gomphonema parvulum*, c) *Aulacoseira sp.*, d) *Coscinodiscus Radiatus*. Insets in (c) and (d) show the whole valve.

The SERS spectra of a dried drop of 10^{-3} M Rhodamine 6G (R6G) in ethanol obtained on different substrates are presented in Fig 2a. All three diatom valves give a significant enhancement compared to golden film without biosilica - the signal enhancement of the spectrum obtained on GP was 5.5x, on CR 6.8x, and finally on Aula 8.4x. Raman mapping of intense mode of R6G at 1360 cm^{-1} (marked with *) obtained on the golden coated Aula valves is shown in Fig.2b. The mapping image corresponds the optical image and no doubt the signal is homogeneously stronger on the valve than the surrounding substrate. The pore size and spacing are the key parameters in considering the valve as a photonic crystal-like structure, and within the three valves they are comparable to the laser λ_{exc} . In such dielectric structures, the occurring of GMR is expected at specific wavelengths and can be coupled to the plasmonic resonance to enhance electromagnetic (EM) fields close to the surface. In case of Aula valve, pore spacing partially matches the λ_{exc} , while pore size approximates $\lambda_{\text{exc}}/2$.

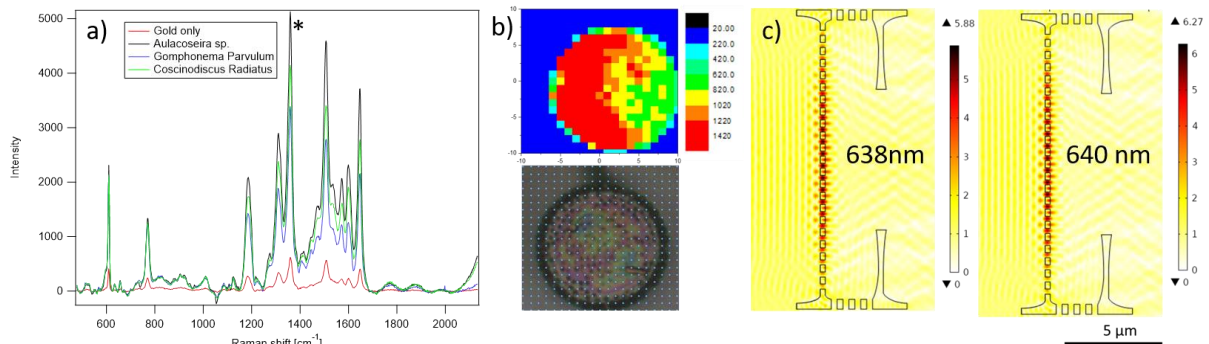


Fig. 2. a) Raman spectra of R6G obtained on four different substrates; b) Raman mapping of 1360 cm^{-1} mode on *Aulacoseira sp.* valve; c) The EF enhancement in 2D CS in Aula valve model coated with 10 nm gold on the top at λ_{exc} and λ_{GMR} . The EF was initiated from the left with an input strength of 1 V/m.

The theoretical calculations were carried out on statistically representative selected 2D cross-sections (CS) to investigate the possible contribution of GMR in the three hybrid substrates to the observed enhancement in SERS with the presence of the gold thin film. The observed GMR of 2D CS in GP valve model was studied extensively in our previous work [5], however no modes were observed at λ_{exc} under normal incidence in the air. The same conclusion was obtained for the 2D CS of CR valves. For Aula 2D CS, GMR maximum on 640 nm is found for the pore spacing set to be $0.61\text{ }\mu\text{m}$, and on 638nm (λ_{exc}) electromagnetic field (EF) intensity insignificantly drops from 6.27 to 5.88 V/m (Fig. 2c). During the GMR, a higher EF intensity was observed within the pores. However, the λ_{GMR} shows a red shift with increasing pore spacing, and for instance, for spacing of $0.75\text{ }\mu\text{m}$ λ_{GMR} appears at 778nm. Thus, it requires more effort in future work to find out the possible explanations besides the GMR for the enhancement, including the concentration of analyte on the hybrid substrates.

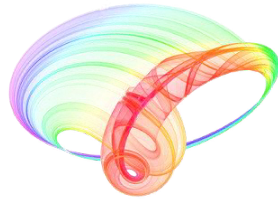
4. Conclusion

The ability of the obtained hybrid structures to significantly and uniformly enhance SERS was proved experimentally and showed different enhancements depending on the fine structure of the substrates. The theoretical analysis suggests that, in case of some diatom species, GMR might be partially responsible for the SERS enhancement.

REFERENCES

- [1] R.R. Jones, D. C. Hooper, L. Zhang, D. Wolverson, and V.K. Valev, "Raman techniques: Fundamentals and frontiers," *Nanos. Res. Lett.* **14**, 231 (2019).
- [2] A. Wang and X. Kong, "Review of recent progress of Plasmonic Materials and nano-structures for surface-enhanced Raman scattering," *Materials* **8**, 3024–3052 (2015).
- [3] E. De Tommasi and A. C. De Luca, "Diatom biosilica in plasmonics: Applications in sensing, diagnostics and therapeutics [invited]," *Biom. Opt. Express* **13**, 308-3101 (2022).
- [4] F. Ren, J. Campbell, D. Hasan, X. Wang, G.L. Rorrer, A.X. Wang, Enhancing surface plasmon resonances of metal nanoparticles by diatom biosilica, *Opt. Express* **21**, 15308-15313 (2013).
- [5] M. Ghobara, C. Oschatz, P. Fratzl, and L. Reissig, "Light modulation by a small pennate diatom valve: The case of *Gomphonema Parvulum*," in *IEEE Photonics Conference* (2021).

Book of abstracts



PHOTONICA2021

VIII International School and Conference on Photonics

& HEMMAGINERO workshop

23 - 27 August 2021,

Belgrade, Serbia

Editors

Mihailo Rabasović, Marina Lekić and Aleksandar Krmpot

Institute of Physics Belgrade, Serbia

Belgrade, 2021

Boosting surface plasmon resonances of thin golden film by bio photonic crystals

M. Gilic¹, M. Ghobara¹ and L. Reissig¹

¹*Institute for Experimental Physics, Freie Universität Berlin, Arnimallee 14, 14195 Berlin
martina.gilic@fu-berlin.de*

Diatoms are unicellular biomineralized algae which possess a biosilica shell with a 2D periodic pore structure. Due to their unique physical, chemical and photonic properties, diatoms found numerous application in biochemical sensors contributing to their ultra-high sensitivity [1, 2]. As substrates for Surface Enhanced Raman Spectroscopy (SERS) they proved to be capable of concentrating analyte molecules on their surface as well as assembling metal nanoparticles at pore rims which lead to more controllable hot spot creation. It has been suggested that diatoms enhance the SERS signal additionally with guided mode resonance due to their photonic crystal – like properties. However, current studies are limited to coating diatoms with noble nanoparticles or non-uniform golden films, which hampers interpretation regarding their photonic structure contribution and leads to unsatisfactory reproducibility. Here we present biosilica substrates based on diatom frustules coated with a uniform 10nm thick layer of gold as a candidate for highly reproducible SERS substrates with high enhancement factors. The uniform films spread over the periodic frustule structure enable the study of photonic properties of periodical pore arrays and their role in enhancing optical sensitivity. Rhodamine 6G is used as a typical Raman probe molecule. Our results show that substrates with a gold film over diatom monolayers improve SERS detection of R6G by several times compared to substrates with a gold film on glass. The reproducibility of the measurement was verified with Raman mapping. Surface morphology and the fine structure of the diatoms were investigated with Scanning Electron Microscopy, confirming structural integrity for an expanded analytical study.

REFERENCES:

- [1] K. Squire, K. Sivashanmugan, B. Zhang, J. Kraai, G. Rorrer, A. Wang, ACS APPLIED NANO MATERIALS 3, 1656 (2020).
- [2] S. Manago, G. Zito, A. Rogato, M. Casalino, E. Esposito, A. De Luca, E. De Tommasi, ACS Appl. Mater. Interfaces 10, 12406 (2018).

15th Photonics Workshop 2022
Kopaonik, Serbia, March 13-16, 2022

Institute of Physics Belgrade, Pregrevica 118, 1080 Belgrade, Serbia
Phone +381 11 3713 000 Fax: +381 11 3162 190, email fotonika@ipb.ac.rs
<http://www.photonicsworkshop.ipb.ac.rs>

Dr. Martina Gilic

Institute for Experimental Physics

Freie Universität Berlin

Arnimallee 14

14195 Berlin

On behalf of the Organizing Committee of the “**15th Photonics Workshop 2022**” we are pleased to invite you to the workshop scheduled from **March 13-16, 2022 in Kopaonik, Serbia**. This conference will be organized by the **Institute of Physics Belgrade** and **Optical Society of Serbia**.

It is our special pleasure to invite you to attend the meeting and present an **invited lecture (20 min)**. The lecture is expected to contain an introduction to be appreciated by graduate students and offer a review and up-to-date progress in your field of research.

Should you have any question please don't hesitate to contact us by e-mail.

Yours sincerely,



Dr Marina Lekić
Chair of the Organizing Committee
email: lekic@ipb.ac.rs, fotonika@ipb.ac.rs

RATE COEFFICIENTS FOR Ar^+ IN Ar/BF_3 MIXTURESŽ. NIKITOVIĆ¹, M. GILIĆ², J. MITRIĆ³ and Z. RASPOPOVIĆ⁴^{1,2,3,4}*Institute of Physics, University of Belgrade, Pregrevica 118, 11080 Belgrade, Serbia*¹zeljka@ipb.ac.rs²martina@ipb.ac.rs³jmitric@ipb.ac.rs⁴zr@ipb.ac.rs

Abstract. In this paper we present most probable reactions of Ar^+ ion with Ar/BF_3 mixtures. Appropriate gas phase enthalpies of formation for the products were used to calculate scattering cross section as a function of kinetic energy. These data are needed for modeling in numerous applications of technologically important BF_3 discharges. Results for transport coefficients as a function of E/N (E - electric field; N - gas density), specially rate coefficients were obtained by using the Monte Carlo technique.

1. INTRODUCTION

Cold plasmas are frequently used in new technologies where they open up the possibilities of non-intrusive production or modification of various substances (Makabe et al. 2006.). These plasmas have a high electron temperature and low gas temperature so non-equilibrium behavior of a large number of species becomes important (Robson et al. 2005.). Current computer resources allow studies of complex global models (Murakami et al. 2013.) which describe the behavior of such plasmas by taking into account a very large number of particles. The knowledge of ion-neutral reactions is generally available (see https://nl.lxcat.net/data/set_type.php) although the effects of reactions on transport parameters of particular ions are much less studied due to non-detectability of rapidly vanishing ionic fluxes. This especially holds for ions whose transport is affected by fast reactions (Stojanović et al. 2014. and Nikitović et al. 2016.).

In this paper we firstly selected the most probable reactions of Ar^+ with BF_3 gases for thermodynamic threshold energies below about 15 eV.

2. CROSS SECTION SETS

Complete cross section sets for ion transport are scarce in spite of a broad range of specific methods relevant for quantification of particular cross sections. The main problem in heavy particle scattering, easily and precisely selecting the state of the projectile and target before the collision, is still very complicated for a range of conditions, so databases for ion scattering (Murakami et al. 2013. and https://nl.lxcat.net/data/set_type.php) are still devoid of such data. Phelps established the first worldwide accessible database with cross section sets (see <https://nl.lxcat.net/cache/5b33772b61cf9/>) tested for each particular case either for swarm conditions of spatially resolved measurements of emission or ion mobility values. In order to focus on effects of reactive processes introduced by BF_3 we neglected all but these two components of the $\text{Ar}^+ + \text{Ar}$ cross section set. Complete cross section sets used in this work are shown in Figure 1.

Appropriate gas phase enthalpies of formation for the products (Table 1) were used to calculate thermodynamic thresholds.

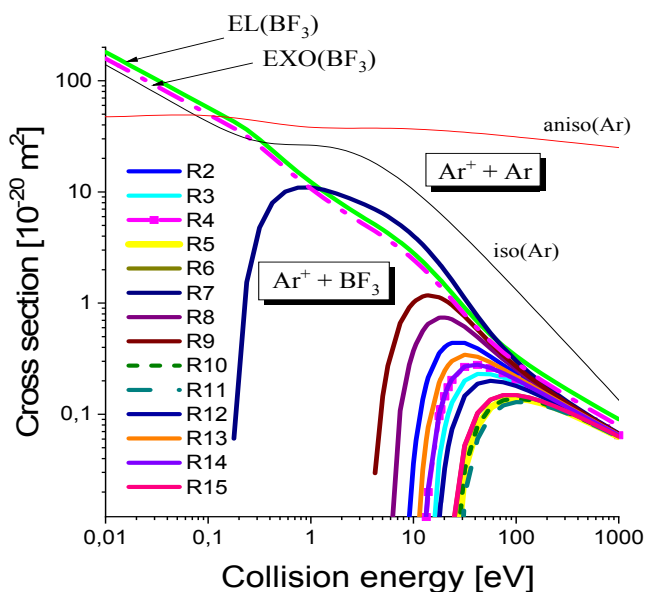


Figure 1: Cross section sets for Ar^+ in BF_3 .

Ion/neutral	$\Delta H_f(\text{ion})$ kJ/mol (room temperature)	$\Delta H_f(\text{neutral})$ kJ/mol (room temperature)
Ar^+/Ar	1520.57	0
$\text{Ar}_2^+/\text{Ar}_2$	1398.1	-1.01
B^+/B	1363.3	562.7
BF^+/BF	957	-115.8
$\text{BF}_2^+/\text{BF}_2$	314	-589.9
$\text{BF}_3^+/\text{BF}_3$	364.3	-1137.0
F^+/F	1760.2	79.4
F_2^+/F_2	1514.5	0

 Table 1: Heats of formation $\Delta_r H^0$ at 298 K (kJ/mol).

3. DISCUSSION AND RESULTS

Monte Carlo Simulations (MCS) have many applications for analysis of the transport of charged particles in plasmas. MCS provide swarm data with the only the uncertainty due to statistical fluctuations and uncertainties in the cross sections. In addition, MCS is the basis of hybrid models of plasmas allowing easy and accurate representation of the end effects and of the non-local high energy groups of particles which are essential in production of plasmas and treatment of surfaces. The MC code used in our analysis is based on the null collisions method.

In Figure 2 we show rate coefficients for reactions of Ar^+ ions with Ar/BF_3 mixtures at $T=300\text{K}$, calculated by Monte Carlo simulations. Rate coefficients are important for applications of the global model to Ar/BF_3 mixtures. We are presenting reaction products and thermodynamic thresholds for $\text{Ar}^+ + \text{BF}_3$ (Nikitović et al. 2019.) formation a) total attachment and b) attachment for endothermic and exothermic reaction products.

4. CONCLUSION

In addition to presenting the data we show here the effects of non-conservative collisions to ion transport. Data for swarm parameters for ions are needed for hybrid and fluid codes and the current focus on liquids or liquids in the mixtures with rare gases dictates the need to produce data compatible with those models.

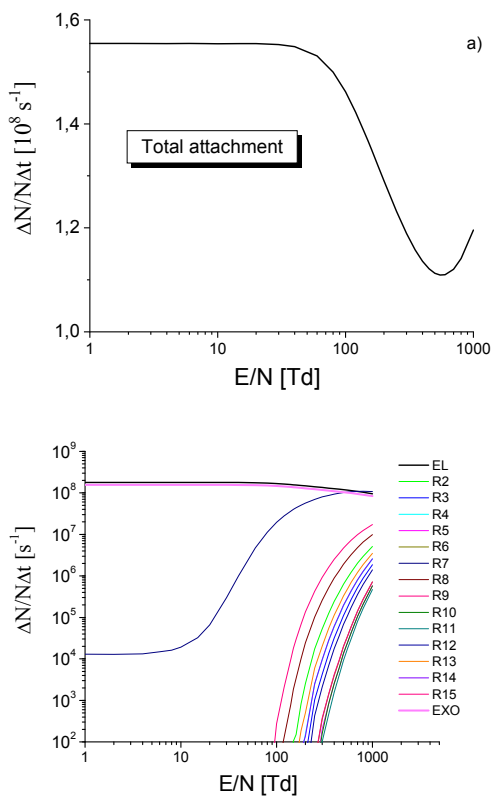


Figure 2: Rate coefficients of Ar^+ in Ar/BF_3 mixtures.

References

- Makabe, T., Petrović, Z. : 2006, *Plasma Electronics: Applications in Microelectronic Device Fabrication* Taylor and Francis, New York: CRC Press.
- Murakami, T., Niemi, K., Gans, T., O'Connell, D., Graham, W. G. : 2013, *Plasma Sources Sci. Technol.*, **22**, 015003.
- Nikitović, Ž., Gilić, M., Raspopović, Z., Stojanović, V. : 2016, *EPL*, **116**, 15002.
- Nikitović, Ž., Raspopović, Z., Stojanović, V. : 2019, *EPL*, **128**, 15001.
- Robson, R. E., White, R. D., Petrović, Z. Lj. : 2005, *Rev. Mod. Phys.*, **77**, 1303.
- Stojanović, V., Nikitović, Ž., Raspopović, Z., Jovanović, J. : 2014, *Acta Physica Polonica*, **A125**, 46.

Photonic crystal behavior of biosilica – influence of frustule's morphology on SERS sensitivity

Martina Gilic¹, Mohamed Ghobara¹, Louisa Reissig¹

¹*Institute for Experimental Physics, Freie Universität Berlin, Arnimallee 14, 14195 Berlin*

Contact: M. Gilic (martina.gilic@fu-berlin.de)

Abstract. Hybrid substrates for Surface Enhanced Raman Spectroscopy (SERS) based on diatom biosilica frustules covered with thin uniform gold films have been investigated. The observed increased sensitivity has been linked to the resemblance of diatom frustules to 2D photonic crystals and associated unique optical properties, such as guided mode resonance (GMR) [1, 2]. In this work the enhancement of three structurally distinct diatom biosilica species were compared – *Aulacosira sp.*, *Coscinodiscus sp.* and *Gomphonema Parvulum*. Uniform and well controlled thin layers of gold could be deposited onto the biosilica utilizing physical vapour deposition and a self-assembled (SAM) monolayer adhesion layer leading to accurate and reproducible SERS enhancement factors without creating artificial hot-spots. Those could hamper interpretation regarding the contribution of the frustules intrinsic photonic structure and lead to unsatisfactory reproducibility. The in the samples occurring distinct structural parameters, obtained from scanning electron microscope (SEM) analysis, such as pore size, spacing and other lattice parameters, allow us to study the influence of chosen laser excitation lines on coupling of GMR and Surface Plasmon Resonance (SPR), theoretically (using COMSOL multiphysics) as well as experimentally. We demonstrate that SERS enhancement strongly depends on the frustules morphology, and thus its photonic properties. The greatest SERS enhancement factor (of more than 3, compared to gold on flat glass) of Rhodamine 6G was obtained on frustules from *Coscinodiscus sp.*, with dominant structural parameters in the range of the excitation line. The reproducibility of the measurements was verified with Raman mapping. The results suggest that high emphasis should be given to the detailed analysis of lattice parameters of the several 100k diatom species and increasing our understanding of the structural relationship of the enhancement, for selecting best target materials for future bio-sensor application.

REFERENCES

[1] J. Kraai, A. Wang, G. Rorrer, Adv. Mater. Interfaces 7 (2020) 2000191.

[2] G. Perozziello, P. Candeloro, M. Coluccio, G. Das, L. Rocca, S. Pullano, A. Fiorillo, M. De Stefano, E. Di Fabrizio, Appl. Sci. 8 (2018) 668.



Martina Gilic

Institut of Physics Belgrade

	All	Since 2020
Citations	582	415
h-index	14	11
i10-index	22	14

6 articles

11 articles

not available

available

Based on funding mandates

TITLE	CITED BY	YEAR
<p>Optical properties of CdS thin films</p> <p>M Gilic, J Trajic, N Romcevic, M Romcevic, DV Timotijevic, G Stanisic, ... Optical Materials 35 (5), 1112-1117</p>	62	2013
<p>Raman spectroscopy of optical properties in CdS thin films</p> <p>J Trajić, M Gilić, N Romčević, M Romčević, G Stanišić, B Hadžić, ... Science of Sintering 47 (2), 145-152</p>	56	2015
<p>Optical properties and fluorescence of quantum dots CdSe/ZnS-PMMA composite films with interface modifications</p> <p>RM Abozaid, ZŽ Lazarević, I Radović, M Gilić, D Šević, MS Rabasović, ... Optical Materials 92, 405-410</p>	51	2019
<p>Structural properties and luminescence kinetics of white nanophosphor YAG: Dy</p> <p>MS Rabasovic, D Sevic, J Krizan, MD Rabasovic, S Savic-Sevic, M Mitric, ... Optical Materials 50, 250-255</p>	42	2015
<p>Optical properties of CuSe thin films-band gap determination</p> <p>M Petrović, M Gilic, J Ćirković, M Romčević, N Romčević, J Trajic, I Yahia Science of Sintering 49 (2), 167-174</p>	33	2017
<p>Structural and optical properties of CuSe₂ nanocrystals formed in thin solid Cu–Se film</p> <p>M Gilić, M Petrović, R Kostić, D Stojanović, T Barudžija, M Mitrić, ... Infrared Physics & Technology 76, 276-284</p>	27	2016
<p>Yttrium orthoferrite powder obtained by the mechanochemical synthesis</p> <p>ZŽ Lazarević, Č Jovalekić, M Gilić, V Ivanovski, A Umićević, D Sekulić, ... Science of Sintering 49 (3), 277-284</p>	26	2017
<p>Characterization and luminescence kinetics of Eu³⁺ doped YVO₄ nanopowders</p> <p>D Sevic, MS Rabasovic, J Krizan, S Savic-Sevic, M Mitric, M Gilic, ... Materials Research Bulletin 88, 121-126</p>	18	2017
<p>Determination of magneto-optical quality and refractive index of bismuth germanium oxide single crystals grown by Czochralski technique</p> <p>ZŽ Lazarević, P Mihailović, S Kostić, MJ Romčević, M Mitrić, S Petričević, ... Optical Materials 34 (11), 1849-1859</p>	18	2012

TITLE	CITED BY	YEAR
<p>Isotope-like effect in $\text{YVO}_4:\text{Eu}^{3+}$ nanopowders: Raman spectroscopy</p> <p>J Mitrić, U Ralević, M Mitrić, J Ćirković, G Križan, M Romčević, M Gilić, ... Journal of Raman Spectroscopy 50 (6), 802-808</p>	17	2019
<p>Raman spectroscopy of bismuth silicon oxide single crystals grown by the Czochralski technique</p> <p>Z Lazarević, S Kostić, V Radojević, M Romčević, M Gilić, ... Physica Scripta 2013 (T157), 014046</p>	17	2013
<p>Optical properties of CdTe/ZnTe self-assembled quantum dots: Raman and photoluminescence spectroscopy</p> <p>M Gilic, N Romcevic, M Romcevic, D Stojanovic, R Kostic, J Trajic, ... Journal of alloys and compounds 579, 330-335</p>	16	2013
<p>Composition, structure and potential energy application of nitrogen doped carbon cryogels</p> <p>A Kalijadis, N Gavrilov, B Jokić, M Gilić, A Krstić, I Pašti, B Babić Materials Chemistry and Physics 239, 122120</p>	15	2020
<p>Optical properties of layered III–VI semiconductor $\gamma\text{-InSe}$: M (M= Mn, Fe, Co, Ni)</p> <p>A Milutinović, ZŽ Lazarević, M Jakovljević, B Hadzić, M Petrović, M Gilić, ... Journal of Physics and Chemistry of Solids 89, 120-127</p>	14	2016
<p>Spectroscopic characterization of YAG and Nd: YAG single crystals</p> <p>S Kostić, Z Lazarević, M Romčević, V Radojević, A Milutinović, G Stanišić, ... Physica Scripta 2014 (T162), 014026</p>	12	2014
<p>Synthesis and characterization of monophasic $\text{CaO-TiO}_2\text{-SiO}_2$ (sphene) based glass-ceramics</p> <p>J Maletaškić, B Todorović, M Gilić, M Marinović-Cincović, K Yoshida, ... Science of Sintering 52 (1), 41-52</p>	11	2020
<p>Phonon properties of $\text{ZnSnSb}_2 + \text{Mn}$ semiconductors: Raman spectroscopy</p> <p>M Romcevic, M Gilic, L Kilanski, W Dobrowolski, IV Fedorchenko, ... Journal of Raman Spectroscopy 49 (10), 1678-1685</p>	11	2018
<p>The Bridgman method growth and spectroscopic characterization of calcium fluoride single crystals</p> <p>IH Elswie, ZŽ Lazarević, V Radojević, M Gilić, M Rabasović, D Šević, ... Science of Sintering 48 (3), 333-341</p>	11	2016
<p>Optical properties of the mechanochemically synthesized $\text{Cu}_2\text{FeSnS}_4$ (stannite) nanocrystals: Raman study</p> <p>J Trajic, M Romcevic, M Petrovic, M Gilic, P Balaz, A Zorkovska, ... Optical Materials 75, 314-318</p>	10	2018

TITLE	CITED BY	YEAR
Low-temperature photoluminescence of CuSe₂ nano-objects in selenium thin films M Gilić, M Petrović, J Ćirković, N Paunović, S Savić-Sević, Ž Nikitović, ... Processing and Application of Ceramics 11 (2), 127-135	10	2017

My Web of Science



Researcher Search > Author Profile



Profile



My researcher profile

EDIT

My records



Publications

+ ADD

Grants

+ ADD

Peer reviews

+ ADD

Editor records

+ ADD

Editorial board memberships

+ ADD

Pending records

Profile notifications



Share



Export CV

Metrics

[Open dashboard](#)

Profile summary

- 43** Total documents
- 43** Publications indexed in Web of Science
- 43** Web of Science Core Collection publications
- 0** Preprints
- 0** Dissertations or Theses
- 0** Non-indexed publications
- 2** Verified peer reviews
- 0** Verified editor records
- 0** Awarded grants

Web of Science Core Collection metrics ⓘ

12
H-Index

43
Publications

405
Sum of Times Cited

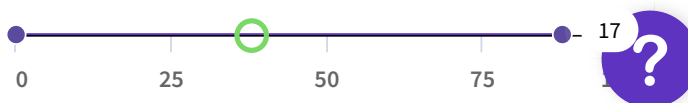
381
Citing Articles

0
Sum of Times Cited by Patents

0
Citing Patents

[View citation report](#)

Author Impact Beamplot Summary ⓘ





Freie Universität Berlin, Fachbereich Physik
Arnimallee 14, 14195 Berlin

Fachbereich Physik
Institut für Experimentalphysik
AG Reissig

Prof. Louisa Reissig
Arnimallee 14
14195 Berlin

Telefon +49 30 838- 63531
Fax +49 30 838- 453337
E-Mail louisa.reissig@fu-berlin.de
Internet www.fu-berlin.de

01.09.2023

Arbeitszeugnis

Frau Dr. Martina Gilic war vom 25.09.2020 bis zum 31.07.2023 in der AG Reissig am Institut für Experimentalphysik der Freien Universität Berlin als erfahrene wissenschaftliche Mitarbeiterin (senior Postdoc) tätig. AG Reissig ist eine Nachwuchsgruppe, die sich mit der Implementierung biologischer Materialien in opto-elektronischen und photonischen Bauteilen beschäftigt und diese mit herkömmlichen Materialien vergleicht. Um die Materialien optimal einzusetzen beruht die Forschung zum einen auf einer genauen Untersuchung der optischen und strukturellen Eigenschaften, aber auch einem fundiertem Verständnis des Aufbaus der anvisierten Bauteile, sowie ihrer Anpassung und Optimierung, mit dem Ziel von dem Einsatz der biologischen Materialien bestmöglich zu profitieren. Dr. Gilic war eine wichtige Mitarbeiterin für die erfolgreiche Durchführung des DFG Projektes "Die Frustule der Diatomeen als Natur-gestaltete Bauscheine in photonischen Anwendungen", war aber auch an anderen Forschungsprojekten beteiligt.

Das Aufgabengebiet von Frau Dr. Gilic umfasste u.a. folgende Tätigkeiten:

- Planung der Forschungsstrategien zur Umsetzung der Projektziele
- Herstellung der Proben als dünne Schichten (Rotationsbeschichtung, Arbeiten mit Vakuum und inerte Atmosphäre).
- Charakterisierung der optischen und strukturellen Eigenschaften (u.a. SERS Raman-Spektroskopie, UV-Vis-Spektroskopie, Rasterelektronenmikroskopie REM, optische Nahfeldmikroskopie SNOM))
- Analyse und Interpretation der erhaltenen Forschungsergebnisse (u.a. mit Hilfe von Software IGOR Pro und Origin)
- Ergänzung der experimentellen Ergebnisse durch Simulationen (COMSOL Multiphysics)
- Umfangreiche Literaturrecherche
- Veröffentlichung wissenschaftlicher Ergebnisse in renommierten Zeitschriften
- Präsentation der Ergebnisse auf internationalen Konferenzen und internen Seminaren
- Unterstützung bei der Organisation der Arbeitssicherheit in den Bereichen Erste Hilfe, Chemikalieninventur und Erstellung der Chemikaliensicherheitsblätter.
- Vertretung der Teamleitung bei Bedarf (auch längerfristig) mit Übernahme der Leitung der Gruppenseminare und Anleitung der übrigen MitarbeiterInnen.
- Etablierung interner und externer Kollaborationen
- Lehre als Tutorin in der Nebenfachvorlesung Physik (Bachelorstudium, Deutsch)

Dr. Martina Gilic ist eine erfahrene Wissenschaftlerin mit hervorragenden Kenntnissen experimenteller Techniken der physikalischen Chemie und einer fundierten Erfahrung wissenschaftliche Studien systematisch durchzuführen und Teilstudien anzuleiten. Sie besitzt ein hervorragendes Grundwissen in den Bereichen der physikalischen Chemie, und exzellente Voraussetzungen dieses auch in modernen interdisziplinären Bereichen der Wissenschaft einzusetzen. Sie war stets bereit ihr Wissen mit anderen zu teilen, und auch in Themen, an denen sie selbst nicht gearbeitet hat, mit Rat und Erfahrung beiseite zu stehen. Frau Dr. Gilic zeigte gleichzeitig eine sehr große Bereitschaft sich in neue Themengebiete einzuarbeiten, und den Austausch mit anderen WissenschaftlerInnen in unserem Team, innerhalb der Universität aber auch extern zu suchen, eine Voraussetzung für die erfolgreiche Bearbeitung interdisziplinärer Themengebiete.

Dr. Matrina Gilic ist eine sehr zuverlässige und gewissenhafte Wissenschaftlerin, die gestellte Aufgaben stets erfolgreich zu Ende bringt, sowie sich mit Neugier und Begeisterungsfähigkeit mühelos in neue Gebiete auch unter Zeitdruck einarbeitet. Dies gelingt ihr vor allem durch ihr sehr gutes und effektives Projektplanungstalent und ihre beeindruckende Fähigkeit effektiv zu priorisieren und klar zu kommunizieren. Durch ihr großes Durchhaltevermögen, auch bei unerwarteten Schwierigkeiten, hält sie Abgabetermine stets ein, oder bietet frühzeitig einen gut durchdachten und unterlegten Alternativplan. Auch in Zeiten äußerer erschwelter Bedingungen (wie während der Corona-Pandemie oder Übernahme längerer Vertretungsaufgaben) fand Frau Dr. Gilic stets einen Lösungsweg. Ihre Positivität, Flexibilität und Bodenständigkeit erlaubten es ihr sich auf neue Situationen ideal einzulassen, um die erwarteten Aufgaben zu erledigen. Sie scheute sich nie Verantwortung zu übernehmen und erfüllte alle Aufgaben stets zur vollsten Zufriedenheit.

Ihr Verhalten gegenüber Vorgesetzten, Gruppenmitgliedern, KollegInnen und Externen war stets ausgezeichnet. Martina wurde für ihre umsichtige und respektvolle Art von allen MitarbeiterInnen der FU sowie externen BesucherInnen unserer AG geschätzt. Sie war, von Anfang an, ein wichtiger Faktor für den Zusammenhalt unserer kleinen AG, war den jüngeren Gruppenmitgliedern ein Vorbild und stand immer mit Rat zur Seite. Als Tutorin war sie bei den Studierenden aufgrund ihrer offenen und ermutigenden Art und ihrer stets ausgezeichneten Vorbereitung, sowie ihrer Bereitschaft zur Anwendung moderner Lehrmethoden sehr geschätzt.

Obwohl Englisch an der FU im Wissenschaftsbereich die Lingua Franca ist, war Martina bereit auch in ihrer privaten Zeit ihre Deutschkenntnisse stets zu verbessern (auch über den Besuch an Kursen), um die Kommunikation mit den sonstigen Mitarbeitern am Fachbereich und in der Verwaltung zu erleichtern, und ihren Einsatz in der Lehre zu ermöglichen.

Mit dem Projektende zum 31.07.2023 lief der befristete Vertrag von Dr. Gilic aus. Wir danken Frau Dr. Gilic für den hervorragenden Einsatz, sowohl im wissenschaftlichen als auch lehrenden Bereich. Wie bedauern es sehr sie als wissenschaftliche Mitarbeiterin und Kollegin in unserer AG zu verlieren. Mit Interesse werden wir ihren weiteren wissenschaftlichen und beruflichen Werdegang verfolgen, und würden uns freuen, wenn sich wieder eine Art der Zusammenarbeit bietet. Auf jeden Fall, wünschen wir ihr für ihren weiteren Berufs- und Lebensweg alles Gute und viel Erfolg.



Prof. Louisa Reissig (verheiratet Dalglesch)

Optics of Diatom Frustules

Toward Applications and Photobiology

Dissertation

zur Erlangung des Grades eines
Doktors der Naturwissenschaften
(Dr. rer. nat.)

am Fachbereich Physik
der Freien Universität Berlin

vorgelegt von

Mohamed Ghobara

Berlin

2024

Acknowledgments

First, I would like to thank **Prof. Dr. Louisa Reissig**, who supervised, encouraged, and helped me a lot during the first three years of my PhD. She also helped me a lot while transitioning from biology to physics and gave me the proper training on experimental and numerical techniques, enabling me to conduct the research work successfully. I would also like to thank her for the countless fruitful discussions, comments, and positive criticism that encouraged me to make more effort. Thanks also for her helpful comments and suggestions on earlier versions of my thesis.

I would like to express my sincere gratitude to my supervisor **Prof. Dr. Paul Fumagalli** for accepting me as a PhD student in his group upon the recommendation of Prof. Dr. Louisa Reissig. I am really grateful for his kindness, wisdom, knowledge, and unlimited support, and for guiding me through difficult times to reach the final steps in my thesis. Without his help, this thesis will not be there. He also helped me develop more toward physics. On a personal level, I learnt from his wisdom and leadership many lessons. I would also like to thank him very much for his helpful comments and suggestions on different versions of my thesis.

I would like to appreciate and thank **Prof. Dr. Stephanie Reich**, my second supervisor, for her help, understanding of the challenges I faced during my PhD journey, and the fruitful discussions and suggestions at different stages of my thesis.

I am deeply grateful to **Dr. Martina Gilic** and would like to thank her very much for all the work that we did together during her PostDoc in the department and all fruitful discussions. She has also helped me to learn more about Raman spectroscopy and SERS substrates. She also helped me with many SEMs images she captured during our research work. She was really a good friend who advised me during the hard times I faced in my PhD journey. I am really grateful for her help.

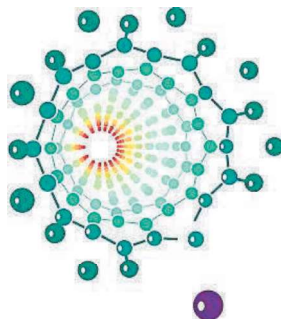
I am really grateful to **Dr. Yasser Shokr** for all the mental support, discussions, and advice he offered during my PhD. He was more than a brother and helped me settle in Berlin.

I would like to thank all my colleagues from **AG Fumagalli** and **AG Reissig**, whom I enjoyed discussions with. I would also like to thank people from other research groups in the department who gave me access to their labs and equipment during my PhD time, including **AG Heberle**, **AG Bolotin**, and **AG Reich**. My sincere thanks also go to the administrative members of the department, **Mrs Badow**, **Mrs Endrias**, and **Mrs Cech** for their unlimited help and support.

My sincere thanks also go to **Dr. Cathleen Oschatz** (Max Planck Institute of Colloids and Interfaces, Potsdam, Germany) for collaboration through providing

Универзитет у Београду

Факултет за физичку хемију



Јелена М. Митрић

**СТРУКТУРНА И ОПТИЧКА СВОЈСТВА
ПОЛУПРОВОДНИЧКИХ НАНОМАТЕРИЈАЛА:
ГАДОЛИНИЈУМ – ЦИРКОНАТА И ИТРИЈУМ
– ВАНАДАТА ДОПИРАНИХ ЕУРОПИЈУМОМ,
КАДМИЈУМ – ТЕЛУРИДА И ЦИНК – ОКСИДА
МОДИФИКОВАНОГ РУТЕНИЈУМОВИМ
КОМПЛЕКСИМА**

Докторска дисертација

Београд, 2020.

ЗАХВАЛНИЦА

Велику захвалност дугујем својим менторима,

др Ивани Стојковић Симатовић, ванредном професору, на несебичној помоћи и свим корисним саветима и сугестијама током израде ове дисертације;

а посебно др Небојши Ромчевићу, научном саветнику, из чијих идеја је и настала ова докторска дисертација. Хвала Вам на великој подршци, свим саветима и дискусијама током протеклих година.






Такође, искористићу прилику да се посебно захвалим својим колегама из Института за физику:

Др Маји Ромчевић, за свако прво читање радова које сам написала и за све сугестије које су их учиниле квалитетнијим; др Мартини Гилић, за бројна тумачења добијених резултата и заједничке месеце проведене у лабораторији за раманску спектроскопију; др Бранки Хаџић, експерту за цинк – оксид, за помоћ око тумачења добијених резултата и бројне дискусије; др Бориславу Васићу и др Урошу Ралевићу за помоћ при мерењима на микроскопу атомских сила; др Новици Пауновићу, за исцрпна мерења инфрацрвених спектра.

Хвала и др Данијелу Доброволском, са Института за физику Пољске академије наука и др Ибрахиму С. Јахији, са Кинг Калид Универзитета у Саудијској Арабији, на заједничком раду на танким филмовима кадмијум – телурида; као и колегама Фернандез – Искјердо и Хименез – Хернандез из Лабораторије за неорганску и општу хемију Универзитета у Хавани, Куба, на заједничком раду на наноплочицама цинк – оксида.

Хвала и свим осталим колегама, екипи из студентске канцеларије Института за физику, који су ми улепшали докторске студије, као и својим пријатељицама, Тањи, Јеленици и Магдаленчици, на подршци током рада на овој дисертацији.

На крају, желим да се захвалим мојој породици, мом брату, мајци и оцу, за најчвршћи ослонац и највећу подршку коју сам имала током свог школовања. Ову докторску дисертацију посвећујем вама.

Folders	Subject [Biosensors] Manuscript ID: biosensors-2806696 - Acknowledgement - Review Received
Inbox	From biosensors@mdpi.com 
Drafts	To Martina Gilić 
Sent	Cc biosensors@mdpi.com 
Junk	Reply-To Lottie Wang  , Biosensors Editorial Office 
Trash	Date Fri 12:22
	<p>Dear Dr. Gilić,</p> <p>Thank you for submitting your review of the following manuscript:</p> <p>Manuscript ID: biosensors-2806696 Title: A 3D hydrophobic SERS sensor by silver-coated PTFE membrane for direct trace-detection of molecules in water Authors: Guanwei Tao, Jiajun Li, Yunyun Mu, Xinping Zhang *</p> <p>We are continuously working to improve the services we offer and would greatly appreciate receiving feedback about your experiences through the short survey below. Click here to start the survey: https://www.research.net/r/Reviewer_Survey_2023</p> <p>We encourage you to register an account on our submission system and bind your ORCID account (https://susy.mdpi.com/user/edit). You are able to deposit the review activity to your ORCID account manually via the below link: https://susy.mdpi.com/user/reviewer/status/finished</p> <p>We also invite you to contribute to Encyclopedia (https://encyclopedia.pub), a scholarly platform providing accurate information about the latest research results. You can adapt parts of your paper to provide valuable reference information for others in the field.</p> <p>Kind regards, Ms. Lottie Wang Assistant Editor Email: lottie.wang@mdpi.com Biosensors (http://www.mdpi.com/journal/biosensors/)</p> <p>MDPI Branch Office, Beijing Building 2, Courtyard 4, Guanyinan North Street, Tongzhou District, 101101 Beijing, China</p> <p>Biosensors Editorial Office E-Mail: biosensors@mdpi.com http://www.mdpi.com/journal/biosensors</p> <p>Disclaimer: The information and files contained in this message are confidential and intended solely for the use of the individual or entity to whom they are addressed. If you have received this message in error, please notify me and delete this message from your system. You may not copy this message in its entirety or in part, or disclose its contents to anyone.</p> <p>*** This is an automatically generated email ***</p>
	Message 6 of 3358

Folders



Inbox

Drafts

Sent

Junk

Trash

Subject [Coatings] Manuscript ID: coatings-2703809 - Acknowledgement - Review Received**From** coatings@mdpi.com **To** Martina Gilić **Cc** Coatings Editorial Office , Anna Krzykawska **Reply-To** Anna Krzykawska , Coatings Editorial Office **Date** 2023-10-31 19:40

Dear Dr. Gilić,

Thank you for submitting your review of the following manuscript:

Manuscript ID: coatings-2703809

Title: Optimalization of the Electrophoretic Deposition Parameters and Mechanism of Formation of Ag-TiO₂ Nanocoating on a NiTi Shape Memory Alloy: Part I

Authors: Karolina Dudek *, Mateusz Dulski *, Jacek Podwórny, Magdalena Kujawa, Patrycja Rawicka

We are continuously working to improve the services we offer and would greatly appreciate receiving feedback about your experiences through the short survey below.

Click here to start the survey:

https://www.research.net/r/Reviewer_Survey_2023We encourage you to register an account on our submission system and bind your ORCID account (<https://susy.mdpi.com/user/edit>). You are able to deposit the review activity to your ORCID account manually via the below link:<https://susy.mdpi.com/user/reviewer/status/finished>We also invite you to contribute to Encyclopedia (<https://encyclopedia.pub>), a scholarly platform providing accurate information about the latest research results. You can adapt parts of your paper to provide valuable reference information for others in the field.

Kind regards,

Dr Anna Krzykawska

Assistant Editor, MDPI Poland

E-Mail: krzykawska@mdpi.com

al.Jana Pawła II43a, 31-864, Krakow, Poland

www.mdpi.com

Submit your papers to journal Coatings

<https://susy.mdpi.com/user/manuscripts/upload/?journal=coatings>

Disclaimer: MDPI recognizes the importance of data privacy and protection. We treat personal data in line with the General Data Protection Regulation (GDPR) and with what the community expects of us. The information contained in this message is confidential and intended solely for the use of the individual or entity to whom they are addressed. If you have received this message in error, please notify me and delete this message from your system. You may not copy this message in its entirety or in part, or disclose its contents to anyone.

*** This is an automatically generated email ***

**REVIEWER
CERTIFICATE**

This certificate is awarded to

M. Gilić

in recognition of their contribution to

1 manuscript in 2024 for

Plasmonics

04 November 2024



REVIEW CONFIRMATION CERTIFICATE

We are pleased to confirm that

Martina Gilić

has reviewed 2 papers for the following MDPI journals in 2023:

Biosensors, Coatings

Shu-Kun Lin

Dr. Shu-Kun Lin, Publisher and President
Basel, 2 January 2024



MDPI is a publisher of open access, international, academic journals. We rely on active researchers, highly qualified in their field to provide review reports and support the editorial process. The criteria for selection of reviewers include: holding a doctoral degree or having an equivalent amount of research experience; a national or international reputation in the relevant field; and having made a significant contribution to the field, evidenced by peer-reviewed publications.